

Christian-Albrechts-Universität zu Kiel  
Institut für Theoretische Physik und Astrophysik

---

---

Density Functional Calculations of Self-Diffusion and  
Au Island Nucleation on Au(001) in the Presence of a Cl  
Adlayer

---

---

DISSERTATION

ZUR ERLANGUNG DES DOKTORGRADES  
DER MATHEMATISCH-NATURWISSENSCHAFTLICHEN FAKULTÄT  
DER CHRISTIAN-ALBRECHTS-UNIVERSITÄT ZU KIEL

VORGELEGT VON

ALEXANDRA CELINDA DÁVILA LÓPEZ

KIEL, 2020

Erster Gutachter: Prof. Dr. Eckhard Pehlke  
Institut für Theoretische Physik und Astrophysik,  
Christian-Albrechts-Universität zu Kiel,  
Leibnizstraße 15,  
24098 Kiel,  
Deutschland

Zweiter Gutachter: Prof. Dr. Olaf M. Magnussen  
Institut für Experimentelle und Angewandte Physik  
Christian-Albrechts-Universität zu Kiel  
Leibnizstraße 19,  
24098 Kiel,  
Deutschland

Tag der mündlichen Prüfung: 28.10.2020

Zum Druck genehmigt:

gez.

---

Dekan

# Abstract

Homoepitaxy on metal surfaces at electrochemical environment has been adopted as model system to investigate the dependence of growth modes on sample potential and metal deposition rate as well as the influence of anions *e.g.* halides. In *operando* surface X-ray scattering (SXS) experiments at the interface between an Au(001) electrode and HCl + H<sub>2</sub>AuCl<sub>4</sub> containing electrolyte Krug *et al.* have observed that the growth mode depends on the electrode potential and Au ion concentration. Transitions from 3D to layer-by-layer and to step-flow growth mode were observed at sample potentials, where the unreconstructed substrate surface is stable. To understand the morphology and differences of growing structures during electrodeposition model calculations for atomistic processes accounting for coadsorbed atoms are required.

In this work density functional theory (DFT) calculations have been employed to investigate self-diffusion of a Au adatom and nucleation of Au islands on Cl covered unreconstructed Au(001) terraces. As step-flow growth mode involves rapid mass transport on flat terraces, diffusion mechanisms of a Au adatom on  $c(\sqrt{2} \times 2\sqrt{2})R45^\circ$ -Cl and  $c(2 \times 2)$ -Cl Au(001) surfaces have been calculated with Cl coverage of 1/2 and in the presence of a Cl vacancy in the adlayer structure. A prerequisite for calculating diffusion mechanisms is the search of global energy minimum configurations, our DFT calculations have shown that the Au<sub>ad</sub>Cl<sub>2</sub> complex stays stable at different Cl coverages. It has been found that in case of the fully Cl covered Au(001) surfaces the diffusion energy barriers are  $\geq 0.44$  eV. In the presence of a neighboring Cl vacancy the diffusion barriers are drastically reduced to about half of the value for the fully Cl covered surface. Thus, Au self-diffusion on covered surfaces is promoted by Cl vacancies.

DFT calculations addressing the initial steps toward Au island nucleation on  $c(2 \times 2)$ -Cl covered Au(001) surfaces have been carried out. The atomic geometry of Au<sub>n</sub> adatom structures for  $n \leq 4$ , as well as their stability as a function of Cl chemical potential has been determined. A weakly bonded (AuCl<sub>2</sub>)-chain as the most stable structure has been identified in case of Cl chemical potentials such that Cl vacancies are suppressed. In the range of Cl chemical potential, where Cl vacancies occur in equilibrium with the adlayer and bind to a Au adatom structure, significant changes in regard to the Au<sub>ad</sub>-structure are induced. Moreover, the formation of a dimer from two monomers is accompanied by an energy gain between 0.06 – 0.23 eV. For the formation of Au trimer and tetramer structures the calculations suggest a similar tendency. Results indicate that on  $c(2 \times 2)$ -Cl covered Au(001) surfaces the Au<sub>ad</sub>-island nucleation is supported by the presence of vacancies in the Cl adlayer.

The dependence of the diffusion energy barriers on sample potential is estimated from the variation of the dipole moment along the diffusion path. However, for more reliable estimations the double layer capacity and the potential of zero charge for the Au(001)/electrolyte interface are required.

---

This work reveals the complex influence of the coadsorption of Cl atoms on the self-diffusion of Au adatom and the nucleation of Au islands. Our results refer to intralayer processes and nucleation on Cl covered terraces. The Cl adlayer strongly modifies the adsorption properties and energies of small Au clusters, which results in different diffusion mechanisms and Au cluster equilibrium structures compared to the clean surface. The concentration of halide vacancies in the Cl adlayer may play a decisive role for the self-diffusion and for the energetics of island nucleation.

# Kurzfassung

Homoepitaxie auf Metalloberflächen in elektrochemischer Umgebung wurde als Modellsystem angenommen, um die Abhängigkeit der Wachstumsmodi von einem angelegten Probenpotential zu untersuchen. Ebenso wurde der Einfluss von Anionen (z.B. Halogeniden) auf Metallabscheidungsrate analysiert. Bei *operando* Oberflächen-Röntgenstreuexperimenten (SXS) an der Grenzfläche zwischen einer Au(001)-Elektrode und einem HCl + HAuCl<sub>4</sub> Elektrolyt, haben Krug *et al.* beobachtet, dass der Wachstumsmodus vom Elektrodenpotential und der Au-Ionenkonzentration abhängt. Übergänge vom 3D- über das Layer-by-Layer- hin zum Step-Flow-Wachstumsmodus wurden bei Probenpotentialen, bei denen die unrekonstruierte Substratoberfläche stabil ist, beobachtet. Für ein detaillierteres Verständnis der Morphologie und der Unterschiede der wachsenden Strukturen während der Elektrodeposition sind Modellrechnungen für atomistische Prozesse unter Berücksichtigung ko-adsorbierter Atome erforderlich.

In dieser Arbeit wurden Dichtefunktionaltheorie (DFT) basierte Rechnungen verwendet, um die Selbstdiffusion des Au-Adatoms und die Nukleation der Au-Insel auf Cl-bedeckten, unrekonstruierten Au(001)-Terrassen zu untersuchen. Für den Step-Flow-Wachstumsmodus ist ein schneller Massentransport auf flachen Terrassen erforderlich. Diffusionsmechanismen von Au Adatomen auf  $c(\sqrt{2} \times 2\sqrt{2})R45^\circ$ -Cl und  $c(2 \times 2)$ -Cl bedeckten Au(001)-Oberflächen – gleichbedeutend einer Cl-Bedeckung von 1/2 – wurden für vollständige, sowie mit Vakanzen durchsetzte Cl-Adlage berechnet. Eine Voraussetzung für die Berechnung von Diffusionsmechanismen ist das Bestimmen von globalen Energieminima-Konfigurationen. Die in dieser Arbeit durchgeführten DFT-Berechnungen haben gezeigt, dass der Au<sub>ad</sub>Cl<sub>2</sub> Komplex bei verschiedenen Cl-Bedeckungen stabil bleibt. Es hat sich gezeigt, dass im Falle der vollständig mit Cl bedeckten Au(001)-Oberflächen die Diffusionsenergiebarrieren  $\geq 0.44$  eV sind. Bei einer Cl-Vakanz sinken die Diffusionsbarrieren drastisch auf etwa die Hälfte des Wertes für die vollständig mit Cl bedeckte Oberfläche. Somit wird die Au-Selbstdiffusion auf bedeckten Oberflächen durch Cl-Vakanzen gefördert.

Weiterhin wurden DFT basierte Rechnungen zu den ersten Schritten der Au-Insel-Nukleation auf  $c(2 \times 2)$ -Cl-bedeckten Au(001)-Oberflächen durchgeführt. Auch die atomare Geometrie von Au<sub>n</sub>-Adatomstrukturen für  $n \leq 4$ , sowie ihre Stabilität als Funktion des chemischen Cl-Potentials wurde bestimmt. Es wurde eine schwach gebundene (AuCl<sub>2</sub>)-Kette als stabilste Struktur identifiziert. Im Bereich des Cl-chemischen Potentials, wo Cl-Vakanzen im Gleichgewicht mit der Adlage auftreten und an eine Au-Adatom-Struktur binden, werden signifikante Veränderungen in Bezug auf die Au-Adstruktur induziert. Darüber hinaus wird die Bildung eines Dimers aus zwei Monomeren begleitet von einem Energiegewinn zwischen 0.06 – 0.23 eV. Für die Bildung von Au-Trimer- und Tetramerstrukturen deuten die Berechnungen auf eine ähnliche Tendenz. Die Ergebnisse zeigen, dass auf  $c(2 \times 2)$ -Cl bedeckten Au(001)-Oberflächen die Nukleation von Au Inseln durch Vakanzstellen in die Cl Adlage unterstützt wird.

---

Die Potentialabhängigkeit der Diffusionsenergiebarrieren und der Bindungsenergien wird aus der Dipolmomentänderung des Systems während des Diffusionsprozesses berechnet. Für zuverlässigere Schätzungen sind die Doppelschichtkapazität und das Nullladungspotential für die Au(001)/Elektrolyt-Grenzfläche erforderlich.

Diese Arbeit macht den komplexen Einfluss der Koadsorption von Cl-Atomen auf die Selbstdiffusion von Au Adatomen und auf die Keimbildung von Au-Inseln deutlich. Unsere Ergebnisse beziehen sich auf Intralayer Prozesse und Nukleation auf Cl bedeckten Terrassen. Die Cl-Adlage modifiziert die Adsorptionseigenschaften und -energien von kleinen Au-Clustern deutlich. Dies führt zu – im Vergleich zu sauberen Oberflächen – anderen Diffusionsmechanismen und Au-Cluster-Gleichgewichtsstrukturen. Weiterhin kann die Konzentration der Halogenid-Leerstellen in der Cl-Schicht eine entscheidende Rolle für die Selbstdiffusion und für die Energetik der Inselkernbildung spielen.

# Contents

<b>1. Introduction</b>	<b>1</b>
<b>2. Theoretical Background</b>	<b>9</b>
2.1. Density Functional Theory . . . . .	9
2.1.1. Hohenberg-Kohn Theorems . . . . .	9
2.1.2. Kohn-Sham Equations . . . . .	10
2.1.3. Approximate Exchange-Correlation Energy Functionals . . . . .	11
2.1.4. Van der Waals Interaction . . . . .	13
2.2. Computational Approach . . . . .	14
2.2.1. Periodic Supercell with a Plane Wave Basis Set . . . . .	14
2.2.2. Pseudopotentials . . . . .	17
2.2.3. The QUANTUM ESPRESSO Software Distribution . . . . .	17
2.3. Diffusion . . . . .	19
2.3.1. Transition State Theory . . . . .	19
2.3.2. The Nudged Elastic-Band Method . . . . .	22
2.3.3. Metadynamics . . . . .	25
2.3.4. Diffusion of Halide Atoms on Coinage (001)-Metal Surfaces . . . . .	26
2.4. Epitaxial Growth . . . . .	30
2.4.1. Thermodynamic and Kinetic Growth Modes . . . . .	30
2.4.2. Atomic Processes and Rate Equations . . . . .	31
2.4.3. Nucleation . . . . .	32
2.5. Double Layer Structure . . . . .	34
<b>3. Halide Adlayer Structure on Au(001)</b>	<b>39</b>
3.1. Surface Structure of Au(001) . . . . .	44
3.2. Cl Adlayer on Au(001) . . . . .	45
3.2.1. Exchange-Correlation Energy and Solvation Effects . . . . .	47
3.3. Br Adlayer on Au(001) . . . . .	48
3.4. I Adlayer on Au(001) . . . . .	51
<b>4. Self-Diffusion of Au Adatom on Cl Covered Au(001) Surface</b>	<b>53</b>
4.1. Au-Cl Complexes on Au(001) . . . . .	53
4.1.1. Stability of Au-Cl Complexes . . . . .	54
4.1.2. Diffusion of Au-Cl Complexes . . . . .	55
4.2. Self-Diffusion of Au <sub>ad</sub> on Cl Covered Au(001) at $\Theta = 1/2$ . . . . .	57
4.2.1. Diffusion of Au <sub>ad</sub> on $c(2 \times 2)$ -Cl Au(001) . . . . .	58
4.2.2. Diffusion of Au <sub>ad</sub> on $c(\sqrt{2} \times 2\sqrt{2})R45^\circ$ -Cl Au(001) . . . . .	66

---

4.3.	Self-Diffusion of Au <sub>ad</sub> on Cl Covered Au(001) in the Presence of a Cl Vacancy	68
4.3.1.	Diffusion of Au <sub>ad</sub> on $c(2 \times 2)$ -Cl Au(001) Surface	70
4.3.2.	Diffusion of Au <sub>ad</sub> on $c(\sqrt{2} \times 2\sqrt{2})R45^\circ$ -Cl Au(001) Surface	70
4.4.	Self-Diffusion of Au <sub>ad</sub> on Cl Covered Au(001) in the Presence of an Additional Cl Atom	74
4.4.1.	Diffusion of Au <sub>ad</sub> on $c(2 \times 2)$ -Cl Au(001) Surface	75
4.5.	Discussion of Induced Dipole Moments and the Effect of an Adsorbed Water Layer	78
4.5.1.	Clean Au(001) Surface	78
4.5.2.	$c(2 \times 2)$ -Cl Au(001) Surface	81
4.6.	Publication J. Chem. Phys. 151, 064709 (2019), Copyright (2019) by AIP Publishing	84
<b>5.</b>	<b>Initial Steps Toward Au<sub>ad</sub> Island Nucleation on a <math>c(2 \times 2)</math>-Cl Au(001) Surface</b>	<b>97</b>
5.1.	Au <sub>ad</sub> Small Clusters on $c(2 \times 2)$ -Cl Au(001)	97
5.1.1.	Au <sub>ad</sub> Monomer	99
5.1.2.	Au <sub>ad</sub> Dimer	100
5.1.3.	Further Clusters of Au <sub>ad</sub>	104
5.1.4.	Discussion of Induced Dipole Moments	106
5.2.	Diffusion of Au <sub>2</sub> Cl Dimer on Clean Au(001)	107
5.3.	Publication J. Chem. Phys. 152, 084701 (2020), Copyright (2020) by AIP Publishing	111
<b>6.</b>	<b>Summary and Outlook</b>	<b>121</b>
<b>A.</b>	<b>Appendix</b>	<b>125</b>
A.1.	Au-Cl Complex on Clean Unreconstructed Au(001)	125
A.2.	Supplementary Material from Publication J. Chem. Phys. 151, 064709 (2019), Copyright (2019) by AIP Publishing	128
A.3.	Molecular Dynamics Trajectories	148
A.4.	Adsorption Configurations of Au <sub>ad</sub> on $c(2 \times 2)$ -Cl Au(001) with an Additional Cl Atom	154
A.5.	Au <sub>2</sub> Cl <sub>n</sub> Complex on Clean Unreconstructed Au(001)	155
A.6.	Supplementary Material from Publication J. Chem. Phys. 152, 084701 (2020), Copyright (2020) by AIP Publishing	157
A.7.	Au <sub>4</sub> Cl <sub>n</sub> Complex on Clean Unreconstructed Au(001)	179
	<b>Bibliography</b>	<b>185</b>



## Acronyms

<b>STM</b>	scanning tunneling microscopy
<b>DFT</b>	density functional theory
<b>NEB</b>	nudged elastic-band
<b>TST</b>	transition state theory
<b>EAM</b>	embedded atom method
<b>GGA</b>	generalized gradient approximation
<b>LDA</b>	local density approximation
<b>MD</b>	molecular dynamics
<b>PES</b>	potential energy surface
<b>QMC</b>	Quantum Monte Carlo
<b>UHV</b>	ultra high vacuum
<b>vdW</b>	van der Waals
<b>vdW-DF</b>	van der Waals density functional
<b>SXS</b>	surface X-ray scattering



# 1. | Introduction

Electrodeposition is utilized in a wide variety of technical fields, ranging from metallurgy to microelectronics and nanotechnology. Metal or metal-alloy deposition are commonly used for electrical contacts, in electronics for solder bumps in printed circuit boards (PCB), for chip interconnections (damascene copper electroplating [1]) and for multilayered coating to modify surface properties *e.g.* corrosion resistance or wettability [2]. Currently, it is being applied for the development of new Li-Based batteries *e.g.* synthesis of new electrode materials, fabrication of 3D current collectors (CCs) to enhance the performance of the battery [3]. The advantage of electrodeposition relies on the capability to tune reactions by an external electric circuit, enabling the fine and easy control over material deposition. Therefore, electrodeposition offers a promising way to advance in the direction of renewable energy sources and storage technologies. To accomplish this an understanding of deposit morphology evolution is essential, along with the atomic-scale processes involved during crystal growth and film roughening.

## Homoepitaxial Growth under UHV Conditions

Homoepitaxial growth far from equilibrium is determined by the rate of atom deposition on the surface, and the rates of different atomistic processes encountered by adatoms on the surface such as mass transport across terraces or over steps [4, 5]. In heteroepitaxial systems further kinetic effects play a role *e.g.* the effect of strain on terrace, as well as on interlayer diffusion [6], and the formation of quantum dots driven by strain [7]. Experiments for metal homoepitaxy under ultrahigh vacuum (UHV) have identified three growth modes: step-flow, layer-by-layer and multilayer growth modes, which depend on relative rates along with temperature and surface orientations. For example, prior studies of homoepitaxy on clean Ag(001) [8, 9] and Ag(111) [10] surfaces by means of reflection high-energy electron-diffraction (RHEED) evidenced noticeable different growth behavior. RHEED intensity oscillation patterns are found for Ag(001) in a temperature range from 200 to 480 K, which proves a layer-by-layer growth mode. Above 500 K the oscillation patterns disappear and a intensity is reached, which indicates the transition to the step-flow mode [9]. In case of Ag(111) RHEED intensities showed no oscillations within the temperature range of 225 to 575 K, intensity curves indicated a transition from multilayer to step-flow growth mode at increasing temperature [10]. To clarify this anisotropy Yu and Scheffler employed density functional theory (DFT) to study the self-diffusion of Ag adatoms on flat and stepped Ag(001) surfaces [11]. They found out that for Ag(001) there is no additional barrier to

descend from an upper to a lower terrace *i.e.* good interlayer mass transport giving rise to a smooth surface, while the additional step barrier on Ag(111) supports the multilayer growth mode [11]. Furthermore, authors reported that the equilibrium island shape should be octagonal very close to a square with predominately {111}-faceted steps [12] in accordance with experimental findings [13]. Moreover, homoepitaxial growth on Au(001) is a complex process due to the quasihexagonal reconstruction of the substrate, which has been inferred as a  $(5 \times 20)$  structure from low energy electron diffraction (LEED) patterns [14]. Scanning tunneling microscopy (STM) experiments under UHV conditions by Günther *et al.* have shown a layer-by-layer growth mode with strongly anisotropic effects, specifically the rectangular shape of the island (island shape anisotropy) and strongly anisotropic diffusion [15]. Theoretical studies addressing these anisotropic effects [16, 17] were carried out by means of effective medium theory (EMT) and many-atom potential [18] using large super unit cells (in the order of  $10^4$  atoms in Ref. [17]). Within these studies two hexagonal superstructures,  $(1 \times 5)$  in Ref. [16] and  $(28 \times 5)$  in Ref. [17]), were evaluated. Long-time molecular dynamics (MD) simulations [17] revealed that reconstructed rectangular islands with a quantized number  $(6n + 1)$ , where  $n$  is natural number) of rows are energetically preferable as shown in Ref. [15]. Regarding diffusion, authors pointed out that adatoms move via long-range exchange diffusion process along the reconstruction rows rather than via hopping mechanisms [17]. In the long-range process, adatoms come into the hexagonal island or substrate resulting in local distortions and excessive tensile strain which is released by cooperative motion of atoms along the reconstruction rows [17].

To investigate the spatial and temporal evolution of epitaxial growth theoretical studies have employed kinetic Monte Carlo (KMC) method. The main idea of KMC is to describe stochastic processes by their rates  $\nu_j \exp(-E_{\text{act},j}/k_B T)$ , where  $\nu_j$  and  $E_{\text{act},j}$  are the corresponding attempt frequency and activation barrier for a given process  $j$ , respectively. Activation barriers for relevant processes can be derived by means of DFT calculations, and hence the corresponding diffusion rates. This methodology has been successfully applied in several theoretical studies, for example *ab initio* KMC study of homoepitaxial growth on Al(111) surface in Ref. [19], and island growth on the reconstructed GaAs(001) in Ref. [20]. Besides, rates can be also calculated on the fly during simulation for a given potential *e.g.* Al(100) crystal growth [21] in combination with an embedded atom potential [22]. On covered surfaces relevant processes are not easily to be determined and extensive calculations are required, therefore KMC studies including coadsorbates on the substrate are scarce. To obtain an atomic-scale insight of nucleation and growth processes on covered surfaces, DFT has been the method of choice for many studies in the literature *e.g.* growth of Pt oxide chains at an oxygen coverage  $\Theta \leq 0.75$  ML [23], CuO growth and diffusion mechanisms on  $c(2 \times 2)$ -O Cu(100) surface [24]. Further DFT calculations in conjunction with ReaxFF molecular dynamics simulations have been carried out to unravel film growth processes *e.g.* metal oxidation at high temperatures [25, 26], but results are limited by the quality of the force field employed [26]. Therefore, in the present work DFT is the method of choice.

---

## Atomistic Processes in the Electrochemical Interface

Catalytic reactions, which are technological relevant, occur at the electrode/liquid interface. Therefore, the understanding of the structure of electrified interfaces represents the core of many electrochemistry studies. The whole array of charged species and oriented dipoles existing at the metal-solution interface is called the electrical double layer, which can be described as an arrangement of layers [27–29]. The layer closest to the electrode is called the inner Helmholtz plane (IHP), where specifically adsorbed ions reside. The outer Helmholtz plane (OHP) is the plane of the closest approach of solvated ions to the electrode surface. These ions are said to be nonspecifically adsorbed, which are distributed from the OHP into the bulk of the solution (the so-called diffuse layer). Several continuum models were proposed to describe the electric double layer [27, 30] *e.g.* Gouy-Chapman-Stern model yields a sequence of a linear and exponential potential drop within the double layer region. However, the continuum models do not include the structure of interfacial water and its impact on the profile of potential drop [31, 32]. Furthermore, the nature of ions and the local electric field are not accounted for. Current computational *ab initio* models target an aspect of electrochemical systems, such as the electrostatic double layer, the electronic structure at the electrode–electrolyte interface, the electron or ion transfer processes taking place at constant electrode potential, the ion diffusion in electrolyte [31–33]. But, a unifying approach, able to cover the statistical mechanics and thermodynamics as well as material science or electronic structure of these complex systems, is still missing [31–33].

### Chemisorbed Adsorbates and Surface Dynamics

Electrolyte species with weakly bound solvation shells can chemisorb on electrode surfaces *e.g.*  $(\text{SO}_4)^{2-}$  on Au(111) [34]. In particular, halides are well-known to form closed-packed ordered adlayer structures on metal surfaces depending on the sample potential applied [35]. For example, a  $c(2 \times 2)$ -Cl adlayer on Cu(001) has been observed for sample potential above  $-0.4 V_{\text{Ag}/\text{AgCl}}$  while for more negative potentials  $(1 \times 1)$  phase has been found [36]. In case of Au(001) surface, the adsorption of Cl starts at sample potential, where the hexagonal reconstruction of the substrate is stable [37]. The lifting of the reconstruction (hex  $\rightarrow (1 \times 1)$  transition) occurs at  $0.08 V_{\text{Ag}/\text{AgCl}}$  in  $\text{Cl}^-$  containing solution [38]. Within the potential range, where the unreconstructed Au(001) surface is stable a  $c(\sqrt{2} \times 2\sqrt{2})$ -Cl adlayer has been reported in surface X-ray scattering (SXS) experiments [35]. A defective  $c(2 \times 2)$ -Cl has been observed in STM images within a sample potential regime from 0 to  $0.4 V_{\text{Ag}/\text{AgCl}}$  [38], while the surface Cl coverage rises steeply at this potential range [37]. To estimate theoretically the equilibrium coverage of halides on metal electrodes DFT calculations within a thermodynamic approach, the so-called Computational Hydrogen Electrode (CHE) [39], has been successfully employed in several studies [40, 41]. The CHE method is based on the idea to express the chemical potential of proton-electron pair through the corresponding chemical potential of gas-phase  $\text{H}_2$  molecules, using the standard hydrogen electrode (SHE). Therefore, the explicit treatment of solvated protons is avoided. However, the application of this method to halides/Ag and halides/Au systems is still an open problem [41–44].

Surface mobility of adsorbates can be enhanced by electrolyte species chemisorbed on

metal surfaces. The influence of adsorbate-adsorbate interaction on surface transport has been investigated by in situ video-STM for several systems on halide covered metal surfaces. One of these experiments was performed on the  $c(2 \times 2)$ -Cl covered Cu(100) surface, in which low coverage of sulfur was embedded *i.e.* sulfur atoms were used as tracer atoms [45, 46]. It was observed, that the activation barrier was lowered linearly with increasing sample potential [45, 46]. This strong dependence on sample potential was ascribed to an electrostatic energy term arising from the interaction of the change of dipole moment during diffusion and the electric field in the interface as proposed by Giesen *et al.* within a thermodynamic condition (surfaces held at constant potential) in Ref. [47]. This interpretation was also adopted by Rahn *et al.* [48] to explain experimental data for hopping diffusion of S atoms on a  $c(2 \times 2)$ -Br covered Cu(100)-surface. Interestingly, Rahn *et al.* found out an inverted dependence of the activation barrier on sample potential compared to the Cl covered Cu(100) surface. To understand this difference the authors presented DFT calculations of  $S_{ad}$  hopping diffusion in both halide covered surfaces. Results suggested a way for the inversion of potential dependence of  $S_{ad}$  diffusion on  $c(2 \times 2)$ -Br as compared to  $c(2 \times 2)$ -Cl covered Cu(100) by a change in the mechanism of the elementary hopping process.

## Electrodeposition processes

Studies of electrochemical deposition have revealed a notable influence of the electrode potential and coadsorbed anions (from electrolyte) on homepitaxial growth of metals [49–53], while temperature and deposition rate are kept constant. For diffusion-limited deposition the rate of ions from a solution (with a given concentration) is independent of the chosen sample potential. Regarding coinage metal systems, experiments for Cu(001) and Au(001) homoepitaxy in  $Cl^-$  containing electrolyte were conducted employing surface X-ray diffraction (SXRD) [50, 51]. Structural information of the interface between coinage metal(001) electrodes and the  $Cl^-$  containing electrolyte as a function of sample potential and metal deposition rate revealed that both systems exhibit an opposite dependence of growth modes on sample potential. Homoepitaxial growth of Cu(001) in electrolytes containing chloride proceeds from step-flow to layer-by-layer (2D), and to multilayer (3D) with increasing sample potential *i.e.* the surface grows rough [51, 52]. The step-flow growth appears at sample potential range, where the Cl adlayer is disordered [52]. In case of Au(001), the growth mode changes from multilayer to layer-by-layer over the sample potential range toward negative values, where the hexagonal reconstruction of Au(001) surface is stable. Along this potential range strong anisotropic effects during homoepitaxial growth have been demonstrated by means of STM experiments [54], which is in agreement with previous work under UHV conditions [15]. Furthermore, dynamics of hexagonal stripes have been observed by video-STM experiments [55]. In the regime of unreconstructed Au(001) surface transitions from 3D to 2D, and finally to step-flow growth mode with increasing sample potential have been determined from scattered X-ray intensities [50, 56]. The dependence of Ehrlich-Schwöbel barrier on sample potential has been claimed as responsible for the 3D–2D growth transition. Moreover, the emergence of step-flow mode growth has been attributed to the rapid diffusion of adatoms on terraces. However, also other quantities

---

such as the dependence of binding properties of a kink site on an island edge on sample potential [57], as well as the dependence of the binding properties of a critical nucleus on sample potential may play a role. The latter process compete against the self-diffusion on the terrace. In case of detachment from an island edge, the interaction between the electric field in the double layer and the change in dipole moment during the migration from a kink site to the terrace leads to an electrostatic energy contribution to the activation barrier [57, 58]. Theoretical DFT studies addressed this issue disregarding the presence of coadsorbates, which yield a positive change in dipole moment *i.e* a decrease in the activation barrier with the sample potential [58].

The difference of growth behaviors for both coinage metal(001) surfaces as a function of sample potential highlight the complex relation between the deposited adatoms with its local environment. In the presence of metal atoms experimental data of the Cl adlayer during homoepitaxial Cu(001) growth has shown a mutual interaction between Cu growth and the Cl adlayer [52]. The reduction of Cu surface mobility has been attributed to the  $c(2 \times 2)$ -Cl adlayer. Moreover, the presence of Cu adatoms affect the Cl ordering dynamics. Similar studies regarding the Cl adlayer structure during Au electrodeposition are not available to date. From the structural investigations discussed so far, the surrounding chloride adlayer (structure and surface density) plays a decisive role in growth behavior. Concerning theoretical studies, Mesgar *et al.* investigated by means of DFT the effect of Cl on self-diffusion of Au adatom on clean and stepped Au(001) surfaces at low Cl coverage [59, 60]. On terraces diffusion mechanisms of Au-Cl complexes on the clean Au(001) surface were calculated, which yield 0.15 and 0.34 eV for  $\text{Au}_{\text{ad}}\text{Cl}_2$  and  $\text{Au}_{\text{ad}}\text{Cl}$ , respectively. In Ref. [60] diffusion paths along a step and during the detachment from a step were accounted in the presence of a Cl adatom. Furthermore, Mesgar *et al.* have investigated the effect of chlorine on Au island ripening by means of KMC approach [59]. In order to consider a large number of diffusion scenarios, Mesgar *et al.* have trained a ReaxFF AuCl-forcefield by considering DFT diffusion energy barriers of  $\text{Au}_{\text{ad}}\text{Cl}$  complex on the clean Au substrate [59, 60]. These investigations focused in the dissociation of a  $\text{Au}_{\text{ad}}\text{Cl}$  complex from stepped surfaces and the diffusion of  $\text{Au}_{\text{ad}}\text{Cl}$  complex disregarding the effect of the Cl adlayer and its coverage. Therefore, important questions remain in the Cl-Au(001) system during Au deposition which some were assessed within work: What is known about the adsorption positions of metal adatoms on Cl covered surfaces? Which diffusion mechanism do Au adatoms follow on Cl covered terraces? How does the Cl adlayer influence step-edge barrier of metal adatoms? How does nucleation of metal adatoms proceed on Cl covered metal surfaces?

## Overview

The aim of this work is to investigate nucleation and growth for Au(001) homoepitaxial electrodeposition in Cl containing electrolytes from first principles calculations. Due to the extensive scope of this topic the attention is focused on the diffusion mechanism of  $\text{Au}_{\text{ad}}$  and initial steps on Au island nucleation on Cl covered unreconstructed Au(001) terraces. Contrary to nucleation and growth on clean surfaces, the presence of Cl coadsorbates yields

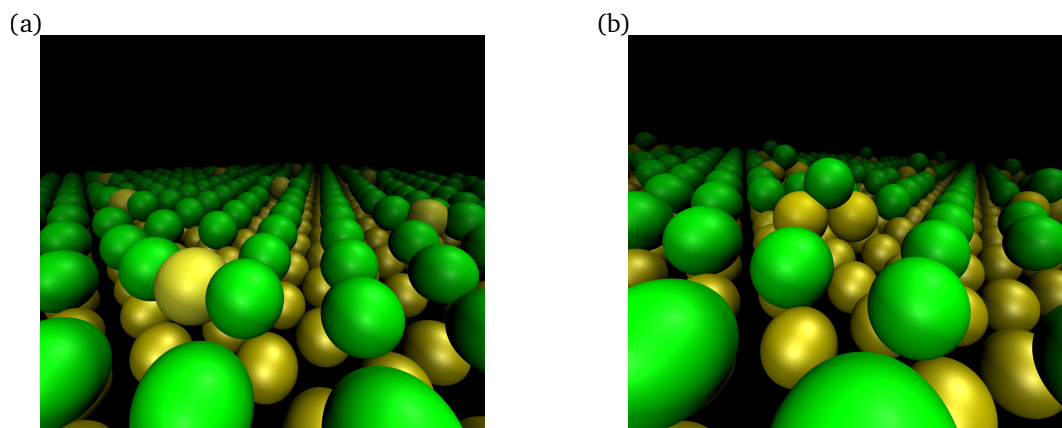


Figure 1.1.: Periodic repeated atomic configurations for (a) Au adatom, (b) Au ad-dimer on the  $c(2 \times 2)$ -Cl Au(001) surface.

a large number of possible adsorption configurations. Therefore, extensive DFT calculations have been carried out to identify the local binding topology of Au adatom and small clusters with the Cl adlayer.

The organization of this thesis is as follows:

- In Chapter 2, a theoretical background of density functional theory is presented, as well as the relevant concepts regarding the metal-solution interface and growth kinetics with atomic surface processes.
- In Chapter 3, the equilibrium Cl coverage and adsorption structures on the unreconstructed Au(001) surface are identified as a function of Cl chemical potential. Thus, ranges of Cl chemical potential, in which Cl adlayer structure are stable, are established. Particularly, the stability range corresponding to Cl coverage of 1/2 is regarded as a reference. Further halides (Br, I) adlayer structures on the unreconstructed Au(001) surface are discussed.
- In Chapter 4, the diffusion mechanisms of a Au adatom on Cl covered unreconstructed Au(001) surfaces attributed to the experimentally observed step-flow growth mode are investigated with Cl coverage of 1/2, and in the presence of a Cl vacancy and an additional Cl atom. To pursue this goal, a detailed analysis of the structure and chemical bonding of a Au adatom on Cl covered Au(001) surfaces has been carried out. A comparison between adsorption of Au at high coverages and Au-Cl complexes on the clean Au(001) surface is presented.
- In Chapter 5, the results regarding initial steps toward Au island nucleation are presented. The equilibrium structures as well as binding energies of Au dimer on the  $c(2 \times 2)$ -Cl covered Au(001) surface are presented as a function of Cl chemical potential. Several local Cl coverages have been considered in the calculations. Furthermore, qualitative characteristics of small Au cluster adsorbed on the  $c(2 \times 2)$ -Cl covered Au(001) surface are discussed.



- 
- Finally, in Chapter 6, the results and perspectives obtained from this work are summarized.

Chapters 4 and 5 consist of original published work by the author in a peer reviewed journal.



# 2. | Theoretical Background

In the last decades first principle methods in conjunction with the advancement of computer power have provided rapid and reliable results for a wide range of issues in material science e.g. microelectronics, energy storage or prediction of new functional materials. First principle methods pursue to solve the Schrödingers equation, which governs the behavior of the electrons in a system. Density Functional Theory (DFT) solves efficiently this problem with a simple description of the quantum effects of exchange and correlation, and provides information of the ground state electronic structure of a system for a relatively low computational cost compared to other techniques such as Quantum Monte Carlo. Therefore, DFT has become a remarkably successful tool in a wide range of disciplines.

This section summarizes briefly the theoretical framework which the calculations of the present work are based on, and the relevant concepts regarding the metal-solution interface and growth kinetics with atomic surface processes.

## 2.1. Density Functional Theory

The total energy of a many-body system is given by the eigenvalue of the corresponding Hamiltonian, using the many-body wave function of the electronic ground state. The calculation of such eigenvalue for solid or surfaces is intractable by means of the wave-function approach. To overcome this drawback Hohenberg, Kohn and Sham developed a theory called *Density Functional Theory* (DFT), which allows to determine the ground state of a system of many interacting particles by using the electron density as a basic variable in place of the many-body wave function. In 1964, Hohenberg and Kohn derived two theorems for a non-degenerate ground state [61], which constitute the fundamental basis of DFT. Later on both theorems have been generalized for degenerate ground states, spin densities and time dependence. More detailed information is to be found in Ref. [62] and references therein.

### 2.1.1. Hohenberg-Kohn Theorems

Considering a system of interacting particles in an external potential  $V_{\text{ext}}(\mathbf{r})$ , including any problem of electrons and fixed nuclei, where the Hamiltonian can be written as (using

Hartree atomic units):

$$\hat{H} = -\frac{1}{2} \sum_i \nabla_i^2 + \sum_i V_{\text{ext}}(\mathbf{r}_i) + \frac{1}{2} \sum_{i \neq j} \frac{1}{|\mathbf{r}_i - \mathbf{r}_j|}. \quad (2.1)$$

In case of atoms, molecules and solids the external potential is caused by the nuclei. The last term of Eq. (2.1) denotes the electron-electron interaction.

The first theorem of Hohenberg and Kohn states:

**Hohenberg-Kohn Theorem I:** *For any system of interacting particles, the external potential  $V_{\text{ext}}(\mathbf{r})$ , and hence the total energy, is (to within a constant) a unique functional of the ground state electron density  $n_0(\mathbf{r})$ .* [62]

With this theorem Hohenberg and Kohn establish a one-to-one mapping of the external potential to the ground state density, to within an additive constant. Since all internal energies, kinetic energy and electron-electron interaction potential, are uniquely determined if the electron density  $n(\mathbf{r})$  is specified, one can define the Hohenberg-Kohn functional  $F_{\text{HK}}$ :

$$F_{\text{HK}} \equiv T[n] + E_{\text{int}}[n]. \quad (2.2)$$

$F_{\text{HK}}$  is a unique functional of the electron density for non-degenerate and degenerate ground states [63].

The second theorem of Hohenberg and Kohn reads as follows:

**Hohenberg-Kohn Theorem II:** *If  $n_0(\mathbf{r})$  is the ground state density that correspond to  $V_{\text{ext}}$ , every density  $n(\mathbf{r})$  in the  $E_{V_{\text{ext}}}[n]$  ( $V$ -representable) follows:*

$$E_0 = E_{V_{\text{ext}}}[n_0] \leq E_{V_{\text{ext}}}[n]. \quad (2.3)$$

In other words, the ground state energy can be obtained without the explicit knowledge of the many-electron wave function, but from the minimization of an energy functional which depends on the electron density alone.

### 2.1.2. Kohn-Sham Equations

In 1965 Kohn and Sham presented a self-consistent scheme based on the Hohenberg-Kohn theorems to provide the ground state density of an interacting system [64]. Their approach basically consists in replacing the interacting many-body system with an auxiliary non-interacting system in an effective potential with the same electron density as the real system. The total energy functional of the interacting many-body system can be written as follows:

$$E_{KS}[n] = T_{KS}[n] + \int d\mathbf{r} V_{\text{ext}}(\mathbf{r})n(\mathbf{r}) + E_{\text{Hartree}}[n] + E_{xc}[n]. \quad (2.4)$$

Here  $T_{KS}[n]$  is the kinetic energy of the non-interacting system and  $V_{\text{ext}}$  is the external potential due to the nuclei.  $E_{\text{Hartree}}$  is the classical coulomb interaction of the electron density with itself.

$$E_{\text{Hartree}}[n] = \frac{1}{2} \iint d\mathbf{r}' d\mathbf{r} \frac{n(\mathbf{r})n(\mathbf{r}')}{|\mathbf{r} - \mathbf{r}'|}. \quad (2.5)$$

All many-body particle effects of exchange and correlation as well as kinetic energy are represented by  $E_{xc}[n]$ , the so-called exchange-correlation energy functional. The  $E_{xc}[n]$  is not known exactly, and needs to be approximated. In terms of the Hohenberg-Kohn functional  $F_{KS}$  the  $E_{xc}[n]$  can be written as :

$$E_{xc}[n] = F_{KS}[n] - (T_{KS}[n] + E_{\text{Hartree}}[n]). \quad (2.6)$$

The variational principle applied to Eq. (2.4) yields to:

$$\begin{aligned} \frac{\delta E_{KS}}{\delta n(\mathbf{r})} &= \frac{\delta T_{KS}}{\delta n(\mathbf{r})} + V_{\text{ext}}(\mathbf{r}) + \frac{\delta E_{\text{Hartree}}}{\delta n(\mathbf{r})} + \frac{\delta E_{xc}}{\delta n(\mathbf{r})}, \\ &= \frac{\delta T_{KS}}{\delta n(\mathbf{r})} + V_{\text{ext}}(\mathbf{r}) + V_{\text{Hartree}}(\mathbf{r}) + V_{xc}(\mathbf{r}), \\ &= \frac{\delta T_{KS}}{\delta n(\mathbf{r})} + V_{KS}(\mathbf{r}) = \mu, \end{aligned} \quad (2.7)$$

where  $\mu$  is the Lagrange multiplier associated with the requirement of constant number of particles, and corresponds to the chemical potential.  $V_{KS}(\mathbf{r})$  is the effective one-body potential. Equation 2.7 leads to the one-body Kohn-Sham Schrödinger-like equations:

$$H_{KS} \psi_i = -\frac{1}{2} \nabla^2 \psi_i + V_{KS}(\mathbf{r}) \psi_i = \epsilon_i \psi_i, \quad (2.8)$$

where the  $\epsilon_i$  are the eigenvalues of the effective hamiltonian  $H_{KS}$ . The electron density can be calculated as:

$$n(\mathbf{r}) = \sum_i f_i |\psi_i(\mathbf{r})|^2 \quad (2.9)$$

The functions  $\psi_i$  are the Kohn-Sham orbitals, and the occupation numbers  $f_i$  which are the Fermi-Dirac function. Considering the degeneracy of spin up and spin down fermions,  $f_i$  varies between 0 and 2. The Kohn-Sham equations have to be self-consistently solved together with  $V_{KS}(\mathbf{r})$  and  $n(\mathbf{r})$ .

Although the exact exchange-correlation energy-functional is not known, the success of DFT is attributed to the approximated models along with the Kohn-Sham equations which have rendered accurate results for different materials.

### 2.1.3. Approximate Exchange-Correlation Energy Functionals

In principle if the exchange-correlation energy-functional  $E_{xc}[n]$  were known, the exact ground state electron density and energy of the many-body system could be found by solving the Kohn-Sham equations. As it is not the case, approximations of the  $E_{xc}[n]$  are unavoidable, these approximations will determine the accuracy of the calculation.

A large and ever-growing number of approximate functionals with different levels of complexity have been proposed in the last decades, an overview of the pool of existing functionals up-to-date can be found in references [65–67]. The hierarchy of energy functionals is represented by Perdew and Schmidt's "Jacob's Ladder" of xc-functionals [68], which connects the Hartree world of non-interacting particles to heaven of chemical accuracy.

Along this ladder, additional terms constructed by the density or the Kohn-Sham orbitals are introduced into the electron density to overcome several deficiencies *e.g.* description of long-range dispersion interactions or highly correlated electron systems. The search for more robust energy-functionals is a highly active field, which nowadays combined with statistical techniques such as machine learning [69, 70] gives new perspectives to the field.

### Local and Semi-Local Functionals

- **Local-Density Approximation (LDA)**

LDA occupies the lowest rung of the “Jacob’s Ladder” and it is based on the exchange-correlation per particle of the homogeneous electron gas  $\epsilon_{xc}^{hom}$ . The total exchange-correlation energy of the system can be written as:

$$E_{xc}^{LDA} = \int d\mathbf{r} n(\mathbf{r}) \epsilon_{xc}^{hom}(n(\mathbf{r})) \quad (2.10)$$

The term  $\epsilon_{xc}^{hom}(n(\mathbf{r}))$  can be partitioned into exchange and correlation energies of the homogeneous gas,  $\epsilon_x^{hom} + \epsilon_c^{hom}$ . The exchange energy is given by the analytic form  $\epsilon_x^{hom} = -\frac{3}{4}(\frac{3}{\pi})^{1/3}n(\mathbf{r})^{1/3}$ , this result was derived by Dirac [71] for the Thomas-Fermi-Dirac model. For the correlation energy  $\epsilon_c^{hom}$  there is not explicit expression known. However, it has been accurately calculated by means of quantum Monte Carlo simulations by Ceperly and Alder [72], and parameterized by Perdew and Zunger [73]. The main idea of LDA is to consider an inhomogeneous system as a set of many small systems with a locally constant density.

Despite of being based on the homogeneous electron gas, LDA proved to give accurate results for solid-state materials *e.g.* bulk lattice constants within 3% error with respect to experimental values [74, 75]. However, one limitation of LDA is an overbinding tendency. This has been observed in molecular system *e.g.* rare-gas dimers [76], transition metal complexes [77], as well as, in solid systems. For example, the cohesive energies for Cu and Ge are overestimated by about 23% [74, 78]. In case of chemical reactions LDA underestimates activation energy barriers of biomolecular reactions by 0.4 – 0.9 eV [77]. But LDA reproduces experimental diffusion barriers for the system Ag on Pt(111) with very high accuracy [79]

- **Generalized Gradient Approximation (GGA)**

To improve the systematic errors from LDA, the gradient of the density  $\nabla n$  was included to account for the non-homogeneity of the electron density. Therefore, GGAs are often called semi-local functionals. With the dependency on  $\nabla n$  several improvements on the quality of DFT calculations for atoms, molecules, bulk solids, and surfaces were achieved. The GGA exchange-correlation energy-functional takes the form:

$$E_{xc}^{GGA} = \int d\mathbf{r} n(\mathbf{r}) \epsilon_{xc}(n, |\nabla n|) \quad (2.11)$$

There are several different types of GGAs in the literature, but it is possible to distinguish two main lines. The first one was initially proposed by Becke [80], and is based

on numerical fitting procedures involving large molecular training sets. This type of functionals have provided accurate results for mostly molecular systems [81, 82]. The second group is anchored in more fundamental arguments of quantum mechanics such as the fulfillment of the exact relations on the exchange and correlation hole. Among these functionals, the functionals proposed by Perdew and Wang (PW91) [83] and Perdew, Burke and Enzerhof (PBE) [84] are widely used. For all calculations in this work the PBE-GGA functional has been used.

GGA functionals overcome the issue of overbinding. In case of molecular systems several studies of transition metal complexes [85–87] have shown that the results with GGA functionals (BP86,PBE) yield for bondlengths within 0.01 Å from experimental data. A detailed assessment of bulk properties (lattice constants and cohesive energies) for alkali, alkaline-earth and transition metals by Schimka *et al.* [88] have shown that for lattice constants PBE-GGA render accurate results for 3d elements. They observed that for 4d or 5d elements the lattice constant is systematically overestimated. In case of cohesive energies PBE-GGA performs remarkably good, errors with respect to experimental data are always close to zero and hardly ever exceed 0.5 eV *e.g.* for Au the absolute error amounts to 0.78 eV. A detailed study of surface properties such as surface energies, work functions and interlayer surface relaxations for a large set of metals and (111), (110) and (001) surface planes have been performed by Patra *et al.* [89]. They have found that PBE-GGA tends to underestimate both surface energies (of about 24%) and work functions (in case of Au(001) surface the uncertainty is about 3%, see Table 3 in Ref. [89]). On the other side, GGA fails describing van der Waals bonds. For long range dispersion forces, GGA binding energies are found to be very small or even nonexistent [90].

#### 2.1.4. Van der Waals Interaction

The van der Waals (vdW) interactions between atoms and molecules play an important role in various systems such as surfaces, soft matter and biomolecules *e.g.* the double-helix stability in DNA [91]. vdW interactions are long-range interactions, that are quantum mechanical in origin and arise from induced dipoles [92]. The vdW interaction is non-local, inter-particle separations can exceed 10 nm *e.g.* bilayer graphene [93]. Therefore, local and semi-local functionals are not able to describe dispersion interactions. Different approaches have been proposed for studies of vdW system, see Refs. [91, 94] and references therein. Three main types of approaches can be identified: (i) explicit density functionals, (ii) DFT extended with atom-pair potentials *e.g.* DFT-D2, D3 by Grimme *et al.* [95, 96] and DFT-TS by Tkatchenko and Scheffler [97], and (iii) perturbation theory, typically in the random-phase approximation. The general form of the non-local correlation energy involves a six dimensional integral via

$$E_c^{\text{nl}} = \frac{1}{2} \int d^3r d^3r' n(\mathbf{r})\Phi(\mathbf{r}, \mathbf{r}')n(\mathbf{r}'), \quad (2.12)$$

where  $\Phi$  is a so-called non-local kernel that describes the non-local correlation. The non-local correlation energy functional  $E_c^{\text{nl}}$  is only one part of the xc-energy functional. There

are also the local correlation and the semilocal exchange.

The first universal non-local functional (the so-called vdW-DF) was proposed by Dion *et al.* in their seminal paper [98]. In their approach, the correlation energy,  $E_c[n]$ , was divided into two parts,  $E_c^{0,\text{nl}}[n] + E_c^{\text{nl}}[n]$ . The first term accounts for the short range contribution of the correlation energy in LDA. The second term is a full potential approximation, which is exact ( $r^{-6}$  dependence) at large separations between any two molecules. This formalism has been applied for a wide variety of systems from bulk to molecules physisorbed on infinite surfaces *e.g.* naphthalene on graphite [99]. Following [98] the vdW-DF is evaluated as post-processing perturbation, which uses the prior calculated charge density. Thonhauser *et al.* derived the exchange correlation potential for the vdW-DF, which allowed to perform a fully self-consistent calculation using vdW and calculate the Hellmann-Feynman forces [100]. A direct evaluation of the non-local contribution to the exchange-correlation energy is computationally very demanding as it requires to solve the six dimensional spatial integral, Eq. (2.12), and the computation of the non-local potential  $v_c^{\text{nl}}(\mathbf{r})$  [100] that involves a three dimensional integral for each point  $\mathbf{r}$ . To overcome this issue Román-Pérez and Soler rewrote the kernel  $\Phi$  and implemented a method based on fast Fourier transforms [101]. The application of this method results in similar computation times as for GGA functionals. Various modifications of vdW-DF have been proposed *i.e.* vdW-DF2 by Lee *et al.* [102] and the opt functionals (optPBE-vdW, optB88-vdW, and optB86b-vdW) where the exchange functionals were optimized for the correlation part [103]. Ambrosetti *et al.* investigated the role of long-range correlation in the cohesive properties of Au, Ag, and Cu bulk noble metals by applying different vdW-corrected density functional theory methods [104]. They found out that the vdW-corrected DFT methods, based on genuine nonlocal functionals, overestimate the lattice constants and underestimate the cohesive energy and the bulk modulus [104]. Similar results were also obtained by Park *et al.* [105]. Furthermore, Patra *et al.* [89] observed a variation of about 0.2 eV for the work function of the unreconstructed Au(001) surface between PBE (5.07 eV) and SCAN+rVV10 (5.28 eV). The SCAN+rVV10 includes realistic intermediate- and long-range vdW interactions.

## 2.2. Computational Approach

### 2.2.1. Periodic Supercell with a Plane Wave Basis Set

One method to practically solve the Kohn-Sham equations consists in expanding the KS orbitals  $\psi_{i,\mathbf{k}}$  in term of a set of functions. Many types of functions can be used as basis set [62]. But their performance depends on the physics of the problem of discussion, and the computational cost for an accurate description of the density functional. For these reasons plane waves have been used in all calculations in this thesis.

According to Bloch's theorem the wave function in a periodic system can be written as the product of the wave part and the  $u_{i,\mathbf{k}}$ , which has the periodicity of the crystal. Here the index  $\mathbf{k}$  represents the wave vector within any primitive cell of the periodic lattice in reciprocal space, at each  $\mathbf{k}$  there are a discrete number of bands  $i$ .

$$\psi_{i,\mathbf{k}}(\mathbf{r}) = e^{i\mathbf{k}\cdot\mathbf{r}} \frac{1}{\sqrt{N_{\text{cell}}}} u_{i,\mathbf{k}}(\mathbf{r}), \quad (2.13)$$



where  $N_{\text{cell}}$  number of primitive cells. The expansion of the functions  $u_{i,\mathbf{k}}$  by a plane wave basis set is written as

$$u_{i,\mathbf{k}}(\mathbf{r}) = \frac{1}{\sqrt{\Omega_{\text{cell}}}} \sum_m c_{i,m}(\mathbf{k}) e^{i\mathbf{G}_m \cdot \mathbf{r}}, \quad (2.14)$$

where  $\mathbf{G}_m$  is a vector of the reciprocal space and  $\Omega_{\text{cell}}$  is the volume of a primitive cell.

In a crystal the effective potential  $V_{KS}$  is periodic and can be expressed as Fourier series.

$$V_{KS}(\mathbf{r}) = \sum_m v_{KS}(\mathbf{G}_m) e^{i\mathbf{G}_m \cdot \mathbf{r}}. \quad (2.15)$$

In this way, the Kohn-Sham orbitals  $\psi_{i,\mathbf{k}}$  are expressed as a linear combination of plane waves

$$\psi_{i,\mathbf{k}}(\mathbf{r}) = \frac{1}{\sqrt{\Omega}} \sum_m c_{i,m}(\mathbf{k}) e^{i(\mathbf{k}+\mathbf{G}_m) \cdot \mathbf{r}}, \quad (2.16)$$

with  $\Omega = N_{\text{cell}}\Omega_{\text{cell}}$ , and leads to

$$n_{i,\mathbf{k}}(\mathbf{r}) = \frac{1}{\Omega} \sum_{m,m'} c_{i,m'}^*(\mathbf{k}) c_{i,m}(\mathbf{k}) e^{i(\mathbf{G}_m - \mathbf{G}_{m'}) \cdot \mathbf{r}}. \quad (2.17)$$

In case of the electron density, it is expressed by

$$n(\mathbf{r}) = \frac{1}{N_{\text{group}}} \sum_{R_n} \sum_{\mathbf{k}}^{\text{IBZ}} w_{\mathbf{k}} \sum_i f(\varepsilon_{i,\mathbf{k}}) n_{i,\mathbf{k}}(R_n \mathbf{r} + \mathbf{t}_n), \quad (2.18)$$

where  $R_n$  are the symmetry operations of the crystal (or surface), and  $f(\varepsilon_{i,\mathbf{k}})$  denotes the occupation function e.g. Fermi-Dirac. In metallic systems at zero temperature occupations drop from 1 (or 2 for spin unpolarized) to zero as the eigenvalues become larger than the fermi energy, therefore a smeared occupancy distribution must be used. In this work all calculations have been carried out with Methfessel-Paxton smearing [106]. Furthermore, the sum over the Brillouin zone (BZ) can be reduced by meanings of symmetry operations to the sum over the  $k$ -points in the irreducible Brillouin zone (IBZ), such points are weighted by  $w_{\mathbf{k}}$  in Eq. (2.18). In case of metals the bands are partially filled, thus dense meshes of  $k$ -points are necessary to sample the Fermi surface. There are several methods to choose special finite sets of  $k$ -points in the IBZ, along this work the method proposed by Monkhorst-Pack [107] has been used.

As the basis is orthonormal, the Kohn-Sham equations can be written as a matrix equation

$$\frac{1}{2} |\mathbf{k} + \mathbf{G}_m|^2 c_{i,m}(\mathbf{k}) + \sum_{m'} v_{KS}(\mathbf{G}_m - \mathbf{G}_{m'}) c_{i,m'}(\mathbf{k}) = \varepsilon_{i,\mathbf{k}} c_{i,m}(\mathbf{k}). \quad (2.19)$$

To truncate the number of reciprocal vector  $\mathbf{G}'_m$ , a particular cut-off energy  $E_{\text{cut-off}}$  is chosen in form of the maximal kinetic energy of the plane waves

$$\frac{1}{2} |\mathbf{k} + \mathbf{G}_{\text{max}}|^2 \leq E_{\text{cut-off}} \quad (2.20)$$

Convergence tests are necessary to find an adequate value of  $E_{\text{cut-off}}$  that compute the physical properties of the system with the required accuracy. Besides the single control parameter  $E_{\text{cut-off}}$ , employing plane wave basis sets provides several advantages *e.g* independence of atom positions and species (unbiased), direct application of the Hellmann-Feynman theorem [108, 109] for forces on atoms (no Pulay forces [110]), and efficient FFT algorithms to transform between  $\mathbf{r}$ -space and  $\mathbf{G}$ -space representations. On the other hand, a disadvantage of this basis is that very large cut-off energies are required to obtain an adequate description of the potential and wave function close to the nucleus. A solution to this issue is the pseudopotential approximation, which replaces core electrons and the strong Coulomb potential by a weaker pseudopotential that acts on a set of pseudo wavefunctions or the so-called *frozen core approximation*, this will be briefly discussed in Sec. 2.2.2.

In practice, the use of plane waves as a basis set is suitable for systems with three dimensional translation symmetry. In case of a surface, only two dimensional periodicity are presented. To simulate a surface, we use a periodically repeated supercell. A supercell is formed by two parts: a slab, which contains a finite number of parallel atomic layers, and a vacuum region, which eliminate the unwanted interactions between the periodic slabs. Additionally, the slabs may have an asymmetric or symmetric configuration with respect to the XY plane, which are defined by the adsorption of atoms or molecules in one or both sides of the slab. When using an asymmetric slab, a dipole correction [111, 112] should be applied with regard to the different work functions of the top and the bottom of the slab. A schematic representation of a supercell is depicted in Fig. 2.1.

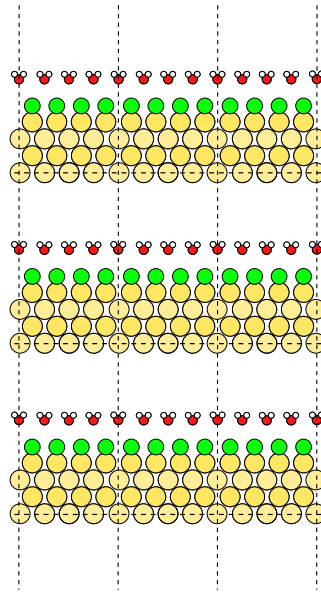


Figure 2.1.: Schematic representation of a periodically repeated supercell, in which the adsorbates and molecules reside on one side of the surface *i.e* asymmetric configuration.

### 2.2.2. Pseudopotentials

In a calculation, the wavefunctions of the core electrons and the rapid oscillations of the wavefunction of the valence electrons close to the nucleus would require very large plane wave basis sets *i.e.* they are computational demanding. However, the valence electrons are mostly responsible for the chemical bonding. Therefore, a way to tackle this problem is to replace the strong Coulomb potential of the nucleus and the chemical inert frozen core electrons by an effective potential, which will eliminate the rapid oscillations of the valence electrons wavefunctions in the core region. This can be done via pseudopotentials (PP).

Pseudopotentials must fulfill a list of requirements to be a “good” such as to correctly describe the scattering properties of the atom, to be transferable *i.e.* to give reliable results in different chemical environments. Furthermore, their corresponding pseudo wavefunctions should be smooth and soft within a core region  $R_c$  and ideally agree with the all-electron wave function outside the core region.

The most well-known DFT-based PPs are norm-conserving (NCP) [113], ultrasoft [114] and projector augmented wave (PAW) [115] pseudopotentials. Along this work all atoms were represented by ultrasoft pseudopotentials [114] from the open-source GBRV library [116].

#### Ultrasoft Pseudopotentials

In 1990, Vanderbilt proposed soft self-consistent (ultrasoft) pseudopotentials [114], within his approach the norm conserving property and the condition that the integrated charge inside the core region must be the same as in the all-electron wave function are not anymore enforced. Thus, it becomes possible to choose  $R_c$  larger than for a norm-conserving PP, and reduce significantly the plane wave cut-off energy. For this charge deficit localized atom-centered augmentation charges are introduced, which are defined as the difference of densities between the all-electron wave function and the pseudo electron wave function. Due to the augmentation charges, the pseudo wavefunction are the solutions of the generalized eigenvalue problem

$$[\hat{H} - \epsilon_i \hat{S}] \tilde{\psi}_i = 0, \quad (2.21)$$

where  $\hat{S}$  is an overlap operator, which enforce the orthonormality of the pseudo wave functions  $\tilde{\psi}_i$

$$\langle \tilde{\psi}_j | \hat{S} | \tilde{\psi}_i \rangle = \delta_{i,j}. \quad (2.22)$$

Ultrasoft pseudopotentials are especially used for 3d transition-metals due to the low computational cost and its accuracy.

### 2.2.3. The QUANTUM ESPRESSO Software Distribution

All DFT calculations in this work have been carried through with the QUANTUM ESPRESSO (*opEn Source Package for Research in Electronic Structure, Simulation, and Optimization*) software distribution [117–120], which is released under the GNU General Public License [121]. The open-source software distribution performs electronic structure calculations

based on DFT or many-body perturbation theory using plane wave basis sets and pseudopotentials. QUANTUM ESPRESSO is based on two core packages, PWscf and CP performing self-consistent and molecular-dynamics calculations, and on additional packages for more advanced calculations as well as on post-processing (PP) tools. For a full list of packages see Ref. [117, 118, 120]. In this work DFT calculations have been performed using the PWscf package (v.5.4.0), and using PP package to extract selected quantities *e.g.* charge densities.

PWscf performs many different kinds of self-consistent (scf) calculations of electronic structure properties within the DFT framework. Detailed reviews of the algorithms implemented in PWscf have been published in Ref. [117]. Here, the basic idea behind the employed self-consistency cycle involved in a ground state calculation for a given external potential (atomic coordinates) is summarized. Each iteration begins with a trial charge density  $\rho^{(\text{in})}$  and trial Kohn-Sham wave functions. These input quantities are either obtained from a previous iteration or they are an initial guess. The latter is usually built from a superposition of atomic charges, constructed from pseudopotential data. After the effective potential has been calculated from  $\rho^{(\text{in})}$ , the Kohn-Sham wave functions and eigenvalues can be found via an iterative procedure. In PWscf a block Davidson algorithm and an alternative algorithm based on band-by-band minimization using conjugate gradient are implemented [117]. Mixing algorithms find the optimal linear combination of a few  $\rho^{(\text{in})}$  from previous iterations, that minimizes the scf norm defined by  $\|\rho^{(\text{out})} - \rho^{(\text{in})}\|$  [117]. This dictates how the charge density is changed from step to step towards self-consistency, which is achieved when the energy changes are below a given threshold. Once a self-consistent solution is reached for a given atomic geometry, the Hellmann-Feynman forces on the atoms can be calculated.

In summary, PWscf can be applied:

- (i) to calculate the ground-state energy and one-electron (Kohn-Sham) orbitals, atomic forces, stresses;
- (ii) to perform structural optimization and molecular dynamics on the Born-Oppenheimer surface, also with variable cell;
- (iii) to calculate minimum energy paths (MEPs), activation energies, and transition states uses the nudged elastic band (NEB) method;
- (iv) to calculate the free energy surface at fixed cell through metadynamics, if patched with PLUMED [122];
- (v) to calculate solvation energies through continuum models, if patched with Environ [123].

A detailed description of the main computational parameters and a summary of convergence properties (dimension of the super-cell, cut-off energy,  $k$ -point sampling) are given in the Appendix.

## 2.3. Diffusion

Surface diffusion of adsorbed species (*e.g.* atoms, molecules, vacancies, small clusters) plays a determinant role in many processes under UHV conditions or at electrochemical interfaces, which have significant technological applications. For example, diffusion of adatoms influences the nucleation and growth processes in electrochemical deposition *e.g.* Damascene electroplating [1]. Furthermore, it also affects the dynamics behavior in adsorbate layers *e.g.* 2D ordered adlayers as well as in electrocatalytic processes, where diffusion over steps occurs.

### 2.3.1. Transition State Theory

When atoms coming from the gas phase or ions from the electrolyte are adsorbed on the surface, new electronic states are formed due to the bonding to the surface. Specifically, the binding energy changes with the lateral position due to the substrate lattice. To exemplify this, let us denote the degrees of freedom of an adatom and a surface by  $\mathbf{R}_{\text{ad}}$  and  $\mathbf{R}_{\text{surf}}$  respectively. The total energy of the electronic ground state of the adatom-surface  $V(\mathbf{R}_{\text{ad}}, \mathbf{R}_{\text{surf}})$ , to simplify  $V(\mathbf{R})$ , is known as the potential energy surface (PES). If the substrate consist of  $N$  atoms  $\mathbf{R}_{\text{surf}} = (R_i)_{i=1\dots 3N}$  and the atomic coordinates of the adsorbate are  $\mathbf{R}_{\text{ad}} = (x, y, z)$ , then the PES is a  $3N + 3$  dimensional function. The global minima of  $V(\mathbf{R})$  are called adsorption configurations. The position of the adatom on the surface is named “adsorption site”. The diffusion of an adatom from an adsorption site to another involves a transition state, which is energetically less favorable. The minimum energy scale between two adsorption sites is the activation energy barrier  $E_{\text{act}}$ , which is the energy difference between the transition state and the global minima.

Thermally activated diffusion processes can be classified in two types, if the activation energy barrier is much larger than the thermal energy,  $k_{\text{B}}T \ll E_{\text{act}}$ , an adatom hops randomly from one adsorption site to another. Along this motion, adatoms remain vibrating in an potential well associated to a certain adsorption site until they accumulate the sufficient energy to overcome the  $E_{\text{act}}$ . Therefore, the jumps are considered independent from each other *i.e.* Markov process. In the other case of  $k_{\text{B}}T \geq E_{\text{act}}$ , the diffusion of adatoms is described as a 2D Brownian motion. There is no confinement of the adatoms to adsorption sites, hence they move freely on the surface. Most of the experiments of our interest have been performed in the regime of  $k_{\text{B}}T \ll E_{\text{act}}$ . Theoretical studies have suggested that for diffusion via hopping activation energy barriers hold  $5 k_{\text{B}} T_{\text{room}} (0.13 \text{ eV}) \leq E_{\text{act}}$ .

A simple theoretical framework for surface diffusion regards the migration of an adatom as a two dimensional random walk on the lattice adsorption sites. Considering the diffusion of an adatom by nearest-neighbor hops on a (001) substrate lattice, the mean square displacement grows linearly with the time according to [124]

$$\langle (\mathbf{r}(t) - \mathbf{r}(0))^2 \rangle = \langle (\Delta \mathbf{r})^2 \rangle = \langle (\Delta \mathbf{x})^2 \rangle + \langle (\Delta \mathbf{y})^2 \rangle = 4 D t = 4 \Gamma a^2 t, \quad (2.23)$$

where  $D$  denotes the surface diffusion coefficient,  $\Gamma$  is the hopping rate, and  $a$  is the nearest-neighbor distance in the (001) substrate. This expression does not hold for other crystal

planes, the extension is straight forward. In the zero coverage limit the diffusion coefficient coincides with the collective diffusion coefficient  $\tilde{D}$ , which is defined through Fick's laws.

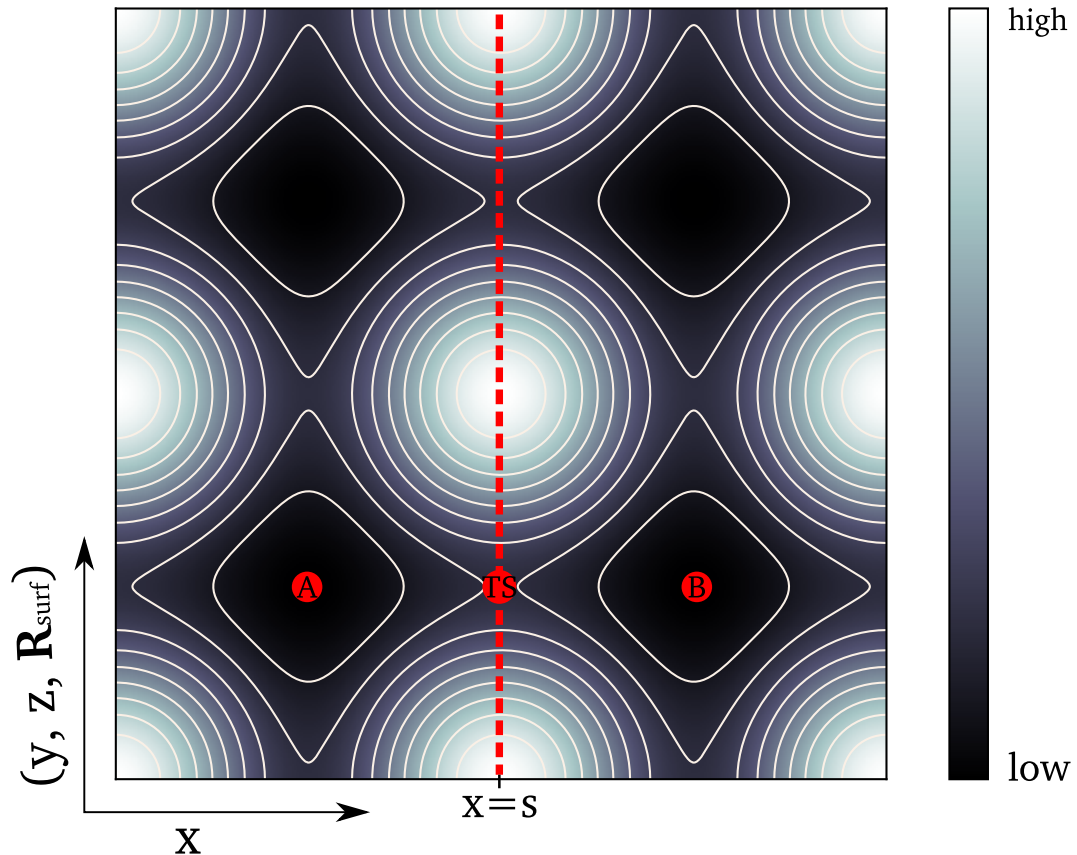


Figure 2.2.: Cut through a  $3N + 3$  dimensional PES with coordinate labels  $(x, y, z, \mathbf{R}_{\text{surf}})$ . Two minima are denoted by A and B, the transition state for the hopping diffusion from A to B is labeled by TS. The red dashed line represents the hyper-plane  $P_{TS}$  for  $x = s$ .

The derivation of an expression for the hopping rate  $\Gamma$  has been an active research area since Arrhenius published his well-known empirical relation for temperature dependence of reaction rates [125]. Several methods [126–129] for calculating  $\Gamma$  have been developed along the years with different levels of complexity, the most widespread (and simplest) approach is *Transition State Theory* (TST). Within TST quantum effects such as tunneling are neglected, this assumption does not hold when temperature becomes low enough [28]. For example, considering the PES  $V(\mathbf{R})$  which corresponds to an adsorbate on a surface, see Fig. 2.2. A and B are two minima points of the PES. The highest point along the minimum energy path from the point A (initial configuration) to the next stable (or meta-stable) point B (final configuration) is the saddle point TS. The activation energy barrier of this path amounts to  $E_{\text{act}} = V(\mathbf{R}_{TS}) - V(\mathbf{R}_A)$ . To separate the regions around A and B it is defined a  $3N + 2$  dimensional hyper-plane, denoted by  $P_{TS}$ , which passes through the point TS and

is orthogonal to all constant  $V$  hyper-surface everywhere else [126]. The hyper-plane  $P_{TS}$  is given by the condition  $x = s$  in Fig. 2.2. Under the assumption that  $TS$  is a point of no return, every configuration on  $P_{TS}$  with a positive velocity component perpendicular to  $P_{TS}$  lead to the diffusion from  $A$  to  $B$ . As TST is a statistical mechanical theory, the hopping rate is determined by ensemble averages [126, 128, 130]:

$$\Gamma_{TST}^{A \rightarrow B} = \frac{\langle v_x \Theta(v_x) \delta(x - s) \rangle}{\langle \Theta(s - x) \rangle}, \quad (2.24)$$

where  $v_x$  is the velocity along the diffusion direction, in this case  $x$  axis.  $\Theta$  is the Heaviside function. The ensemble averages are calculated over the canonical probability density  $Z^{-1} \exp(-\mathcal{H}/k_B T)$ ,  $\mathcal{H}$  denotes the Hamiltonian of the system. Let  $Z_A$  and  $Z_{TS}$  be the canonical partition function of the system, respectively for the initial and the transition state. By evaluating Eq. (2.24), the hopping rate is given by

$$\Gamma_{TST}^{A \rightarrow B} = \frac{k_B T}{2\pi\hbar} \frac{Z_{TS}}{Z_A} \quad (2.25)$$

$$= \frac{k_B T}{2\pi\hbar} \exp(-\Delta F/k_B T), \quad \Delta F = F(\mathbf{R}_{TS}) - F(\mathbf{R}_A). \quad (2.26)$$

The canonical expression for the Helmholtz free energy,  $F = -k_B T \ln Z$ , has been used. Within the harmonic approximation the potential may be expanded near the point  $A$  by a Taylor series to second order, similarly for the point  $TS$  within the constraining hyper-plane  $P_{TS}$ . Consequently, the expression for the hopping rate  $\Gamma_{TST}^{A \rightarrow B}$  and the free energy difference  $\Delta F$  result in [130]:

$$\Gamma_{TST}^{A \rightarrow B} = \frac{2k_B T}{h} \frac{\prod_{i=1}^{3N+3} \sinh \frac{h\nu_i^A/2}{k_B T}}{\prod_{i=1}^{3N+2} \sinh \frac{h\nu_i^{TS}/2}{k_B T}} \exp(-E_{\text{act}}/k_B T), \quad (2.27)$$

and

$$\Delta F = E_{\text{act}} + \Delta F_{\text{vib}} \quad (2.28)$$

$$= E_{\text{act}} + \int \ln \left[ 2 \sinh \left( \frac{h\nu}{2k_B T} \right) \right] \Delta n(\nu) d\nu, \quad (2.29)$$

where  $E_{\text{act}}$  is the activation energy barrier, this quantity is accessible through DFT calculations.  $\Delta n(\nu)$  is the difference between the vibrational densities at the points  $TS$  and  $A$ , which can be computed by the dynamical matrix. As the PES is expected to be convex upward at  $TS$ , one of the eigenvalues  $\nu_{TST}^2$  is negative. For the vibration density, this value is not taken into account, which leads to

$$\int_0^\infty \Delta n(\nu) d\nu = -1 \quad (2.30)$$

In the classical limit, where  $\frac{h\nu_{\max}}{k_B T} \ll 1$ , Eq. (2.27) can be written as [130]

$$\Gamma_{TST}^{A \rightarrow B} = \frac{\prod_{i=1}^{3N+3} \nu_i^A}{\prod_{i=1}^{3N+2} \nu_i^{TS}} \exp(-E_{\text{act}}/k_B T) \quad (2.31)$$

$$= \nu_0 \exp(-E_{\text{act}}/k_B T). \quad (2.32)$$

$\Gamma_{TST}$  reduces to an Arrhenius expression with a pre-exponential factor of  $\nu_0$ , which is also referred as *attempt frequency*. Generally,  $\nu_0$  is considered to be between  $10^{12}$ – $10^{13}$   $s^{-1}$ , which is a typically phonon frequency. By means of DFT the pre-exponential factor  $\nu_0$  and the activation energy barrier  $E_{\text{act}}$  (see Sec. 2.3.2) can be calculated. In the low temperature limit the activation energy should be corrected by the zero-point energy  $\Delta E_{zpe} = \sum_{i=1}^{3N+2} \frac{h\nu_i^{TS}}{2} - \sum_{i=1}^{3N+3} \frac{h\nu_i^A}{2}$ , for temperatures lower than the critical temperature quantum effects should be accounted [131]. In case of  $\nu_0$ , they are evaluated by the density matrix at the initial configuration and transition state [79, 132]. For some systems [79, 132] it has been demonstrated that  $\nu_0$  follows the Meyer-Neldel compensation rule [133],  $\nu_0$  is correlated to the corresponding activation energy barrier. Beyond harmonic TST, it is known that the hopping rate  $\Gamma_{TST}$  is an upper bound to the true hopping rate [127, 128]. As an example Sharia and Henkelman [134] have shown that harmonic TST can overestimate the true rate by as much as 50% for an adatom diffusion on Al(100) surface.

### 2.3.2. The Nudged Elastic-Band Method

To obtain activation energy barriers and to calculate hopping rates using TST, it is necessary to locate the transition state (TS) on a configuration space path between the minima in the PES. Along the way, local minima (intermediate states) may occur. The path of least resistance is the so-called minimum energy path (MEP). Several algorithms on TS optimization have been proposed. Generally, they can be divided into two groups: single-ended and double-ended saddle point search methods [135].

The single-ended algorithms start from an initial configuration on the PES, which is in most cases a minimum. Two methodologies can be used, uphill approach or molecular dynamics (MD). The uphill approach determines the direction where the potential is a local maximum, and minimizes the potential in the space perpendicular to that direction. Within this approach the lowest curvature mode, which is calculated by diagonalizing the Hessian matrix, is chosen as the maximization direction. The need for the Hessian matrix at each step can become computationally expensive, specially for large systems. Further methodologies *e.g.* dimer [136] or Lanczos [137] methods do not calculate the full Hessian matrix, only the lowest non zero eigenvalue and the corresponding eigenvector. Molecular dynamics simulations (using force fields or *ab-initio*) can predict and quantify rare events *e.g.* diffusion of a cluster on a surface. But simulating rare events is often prohibitive. Typically energy barriers of several  $k_B T_{\text{room}}$  need to be overcome, thus the transition state region will be visited only a few times (if it does) in such simulations due to the computational



limitations or slow kinetics. To tackle this issue, a wide variety of algorithms have been developed to accelerate these long time scales processes. Most of these approaches require an appropriate choice (some prior knowledge of the reaction) of collective variables to bias the free energy surface. Examples of algorithms in this class are umbrella sampling [138, 139], blue moon [140, 141] and metadynamics [142] (see Sec. 2.3.3). Current research is focused on methodologies for cases with lack of prior knowledge [143, 144].

A second class of transition state search methods is the doubled-ended approach. These methods find the transition state configuration between specified initial and final configurations, and with it, the activation energy barrier. The most widely applied method is the Nudged elastic band (NEB) [145–147], which uses a string of images (or replicas) to describe the diffusion pathway. Adjacent images are connected by a harmonic spring interaction, altogether mimics an elastic band. The minimization of the forces acting on the images leads to the MEP. The key feature of the NEB method is that only the projections of the spring and true forces (from the PES) are taken into account for the minimization, thus the convergence of the NEB to the MEP is ensured. The initial set-up for the string of images has been typically constructed by a linear interpolation (LI) between the given initial and final configurations. In some cases LI yields images with small interatomic distances. This can be avoided by using an interpolation of pairwise distances at each image along the path, this approach is known as *image dependent pair potential* (IDPP) method [148].

In an elastic band with  $N + 1$  images, let  $\mathbf{R}_i$  be the atomic coordinates of  $i$ -th image and  $k$  be a spring constant.  $\mathbf{R}_0$  and  $\mathbf{R}_N$  correspond to the (fixed) initial and final configuration, respectively. To form an elastic band, artificial harmonic spring forces between the images are introduced. The total force acting on an intermediate image is the sum of the spring and true forces

$$\mathbf{F}_i = -\nabla V(\mathbf{R}_i) + \mathbf{F}_{\text{spring},i} \quad (2.33)$$

$$= -\nabla V(\mathbf{R}_i) - k(\mathbf{R}_i - \mathbf{R}_{i+1}) + k(\mathbf{R}_{i-1} - \mathbf{R}_i). \quad (2.34)$$

Employing the plain *elastic band* force  $\mathbf{F}_i$  can deliver some deviations in the region close to the transition state [147]. For example, the component of the spring force which is perpendicular to the path can lead to *corner-cutting* *i.e.* the band can not follow a curved MEP and the activation energy is overestimated, or intermediate states tend to slide away from the saddle point region due to  $\nabla V$  along the path. To tackle these issues, in the NEB method the force in the image  $i$ -th becomes

$$\mathbf{F}_i^{\text{NEB}} = -\nabla V(\mathbf{R}_i) + (\nabla V(\mathbf{R}_i) \cdot \hat{\boldsymbol{\tau}}_i) \hat{\boldsymbol{\tau}}_i + (\mathbf{F}_{\text{spring},i} \cdot \hat{\boldsymbol{\tau}}_i) \hat{\boldsymbol{\tau}}_i, \quad (2.35)$$

where  $\hat{\boldsymbol{\tau}}_i$  is the normalized tangent vector in the image  $i$ -th. The definition of  $\boldsymbol{\tau}_i$  plays a crucial role to determine the MEP. Originally, the tangent vector  $\boldsymbol{\tau}_i$  was derived from the bisection of two unit vectors adjacent to the  $i$ -th image

$$\hat{\boldsymbol{\tau}}_i = \boldsymbol{\tau}_i / \|\boldsymbol{\tau}_i\|, \quad \boldsymbol{\tau}_i = \frac{\mathbf{R}_i - \mathbf{R}_{i-1}}{|\mathbf{R}_i - \mathbf{R}_{i-1}|} + \frac{\mathbf{R}_{i+1} - \mathbf{R}_i}{|\mathbf{R}_{i+1} - \mathbf{R}_i|} \quad i \in \{1 \dots N - 1\}. \quad (2.36)$$

However, following Eq. (2.36) calculations for some systems yield to not converged results and kinks along the diffusion path. To overcome this issue, a new tangent  $\boldsymbol{\tau}_i$  has been

proposed by Henkelman and Jónsson

$$\hat{\boldsymbol{\tau}}_i = \boldsymbol{\tau}_i / \|\boldsymbol{\tau}_i\|, \quad \boldsymbol{\tau}_i = \begin{cases} \boldsymbol{\tau}_i^+ = \mathbf{R}_{i+1} - \mathbf{R}_i & \text{if } V(\mathbf{R}_{i+1}) > V(\mathbf{R}_i) > V(\mathbf{R}_{i-1}) \\ \boldsymbol{\tau}_i^- = \mathbf{R}_i - \mathbf{R}_{i-1} & \text{if } V(\mathbf{R}_{i+1}) < V(\mathbf{R}_i) < V(\mathbf{R}_{i-1}). \end{cases} \quad (2.37)$$

If the energy of image  $i$ -th is either a local minimum or a transition state, the tangent vector is taken to be a weighted average of the adjacent vectors  $\boldsymbol{\tau}_i^+$  and  $\boldsymbol{\tau}_i^-$ . The switch between the two adjacent vectors becomes smooth at extrema points along the MEP. The tangent estimate is calculated as:

$$\hat{\boldsymbol{\tau}}_i = \boldsymbol{\tau}_i / \|\boldsymbol{\tau}_i\|, \quad \boldsymbol{\tau}_i = \begin{cases} \boldsymbol{\tau}_i^+ \Delta V_i^{\max} + \boldsymbol{\tau}_i^- \Delta V_i^{\min} & \text{if } V(\mathbf{R}_{i+1}) > V(\mathbf{R}_{i-1}) \\ \boldsymbol{\tau}_i^+ \Delta V_i^{\min} + \boldsymbol{\tau}_i^- \Delta V_i^{\max} & \text{if } V(\mathbf{R}_{i+1}) < V(\mathbf{R}_{i-1}), \end{cases} \quad (2.38)$$

where

$$\begin{aligned} \Delta V_i^{\max} &= \max(|V(\mathbf{R}_i) - V(\mathbf{R}_{i-1})|, |V(\mathbf{R}_i) - V(\mathbf{R}_{i+1})|) \\ \Delta V_i^{\min} &= \min(|V(\mathbf{R}_i) - V(\mathbf{R}_{i-1})|, |V(\mathbf{R}_i) - V(\mathbf{R}_{i+1})|). \end{aligned}$$

With this improved way for calculating the tangent vector, which regard all possible cases for  $V(\mathbf{R}_i)$ , the elastic band converges smoothly to the MEP with a sufficient number of images.

Furthermore, to ensure that all intermediate states of the elastic band are equally spaced (if all spring constants are equal to  $k$ ) the spring force  $\mathbf{F}_{\text{spring},i}$  is calculated as [146]

$$\mathbf{F}_{\text{spring},i} \cdot \hat{\boldsymbol{\tau}}_i = k (\|\mathbf{R}_{i+1} - \mathbf{R}_i\| - \|\mathbf{R}_i - \mathbf{R}_{i-1}\|) \quad (2.39)$$

This modification of the spring force achieves equally spaced intermediate states even in regions with high curvature, with this the sampling of the intermediate images is improved. Nevertheless, the resolution of the MEP close to the transition state is not sharp enough, and leads to activation energy barriers with large uncertainties. A way of converging the highest energy image to the saddle point is achieved by modifying the force at this point, the so-called Climbing Image NEB (CI-NEB) [145]. Let  $i_{\max}$  be the intermediate configuration with the highest energy on the band, the CI-NEB force on this image is given by [145]

$$\mathbf{F}_{i_{\max}}^{\text{CI-NEB}} = -\nabla V(\mathbf{R}_{i_{\max}}) + 2(\nabla V(\mathbf{R}_{i_{\max}}) \cdot \hat{\boldsymbol{\tau}}_{i_{\max}}) \hat{\boldsymbol{\tau}}_{i_{\max}}. \quad (2.40)$$

In comparison to Eq. (2.35), the above equation does not contain the term corresponding to the spring force. This term has been replaced by the inverse tangent component of the true force, therefore the  $i_{\max}$  state can ascend to the saddle point. In combination with CI-NEB further improvements for  $\hat{\boldsymbol{\tau}}_{i_{\max}}$  can be achieved by setting variable spring constants [146].

Different modifications have been proposed to the NEB method [149–151] *e.g.* AutoNEB [151] algorithm which reduces the number of force evaluations. Furthermore, Garrido Torres *et al.* implemented an algorithm for NEB calculations using a surrogate machine learning model [152], in which the cost of converging the elastic band no longer scales with the number of moving images on the path.

In this work, the CI-NEB method was used to determine the activation energy barriers as well as transition states and diffusion paths. For the creation of a set-up of images the IDPP method was employed as implemented in the Atomic Simulation Environment (ASE) [153, 154].

### 2.3.3. Metadynamics

Metadynamics [142, 155, 156] is an enhanced sampling method, which explores the free energy surface (FES) and accelerate the search of rare events. The method is based on a dimensional reduction, the high dimensional configuration space is reduced by a projection to a set of collective variables (CV) which must be identified previously. Within this approach, the sampling is accelerated by a history-dependent bias potential constructed in the CV space.

The collective variables are functions of the atomic coordinates of the system  $\mathbf{R}$ , and the dimensionality of the CV's is reduced to  $d$  degrees of freedom.

$$\mathbf{s}(\mathbf{R}) = (S_1(\mathbf{R}), \dots, S_d(\mathbf{R})).$$

Examples of CV's used in molecular dynamics are geometry related, such as distance, angles and dihedrals. The Helmholtz free energy as a function of these CV's is defined as

$$F(\mathbf{s}') = -\frac{1}{k_B T} \ln \left( \int d\mathbf{R} \exp(-\beta V(\mathbf{R})) \prod_{i=1}^d \delta(s'_i - S_i(\mathbf{R})) \right) + C \quad (2.41)$$

where  $C$  is an arbitrary constant. At a time  $t$  an external bias potential  $V_G(S(R), t)$  is added to the Hamiltonian of the system. The external potential  $V_G(S(R), t)$  is given by a sum of Gaussian functions, which have been added at a given time interval  $\tau_G$

$$V_G(\mathbf{s}(\mathbf{R}), t) = \sum_{t'=\tau_G, 2\tau_G, \dots} \frac{W}{\tau_G} \prod_{i=1}^d \exp \left( -\frac{(s_i(\mathbf{R}) - s_i(\mathbf{R}(t')))^2}{2\sigma_i^2} \right), \quad (2.42)$$

$W/\tau_G$  and  $\sigma_i$  are the height and width, respectively, of the Gaussian function for the  $i$ -th CV. The addition of consecutively Gaussian functions to the Hamiltonian forces the system to escape to another minimum state on the PES.

The basic assumption [155] of metadynamics is that at sufficiently long time  $V_G$  provides an estimate of the free energy

$$\lim_{t \rightarrow \infty} V_G(\mathbf{s}, t) = -F(\mathbf{s}) + C \quad (2.43)$$

The choice of CV's is crucial for an adequate description of the rare events from one to another local minimum states. CV's should measure the progress of the transition between two minima and at the same time provide an understanding of the dynamical progress, altogether makes the choice of the CV's non trivial.

In this work metadynamic AIMD simulations at finite temperature have been performed with the aim to find further stable configurations of a Au adatom at Cl covered Au(001) surfaces, particularly for Cl coverage equal to 1/2 and in the presence of a Cl vacancy. For this reason calculations have been carried out with large Gaussian function, thus the FES could be explored at fast pace. Calculations have been carried out using the PLUMED [122] plugin in combination with PWscf [117] at a reduced cutoff energy of 25 Ry.

### 2.3.4. Diffusion of Halide Atoms on Coinage (001)-Metal Surfaces

Anion adsorption on metal surfaces can modified the surface morphology and electronic structure and chemical reactivity. Particularly, at solid-liquid interfaces co-adsorbed halides are known to strongly affect interface processes in solution *e.g.* metal electrodeposition, which have important technological applications [1]. Understanding halide diffusion on metal surfaces is a prerequisite as the diffusivity is a decisive factor for, *e.g.* nucleation and growth in electrochemical deposition processes. If the halide coverage on the surface is high, adsorbate-adsorbate interactions can modify the adsorbate dynamic [48, 157, 158].

In this section, we will briefly discuss the results of previous studies on halide (Cl, Br, I) diffusion. We focus on the unreconstructed (001) face of coinage metals (Cu, Ag and Au). Results for low halide coverage are summarized in Tab. 2.1. For a broad overview, the reader is referred to the review by Andryushechkin *et. al* [159] and the references therein.

The adsorption takes place on specific sites on the (001) surface. Halides occupy the four-coordinated hollow site on Cu(001) and Ag(001) surfaces [48, 159–163]. But on Au(001) surface the two-coordinated bridge site is preferred for Cl and Br [59, 60, 163]. At low coverages DFT calculations for I have shown only marginal differences (below the accuracy) between both sites on Au(001) substrate, in this case the preferable site is hollow. The difference of adsorption sites on Cu(001), Ag(001) and Au(001) surfaces has been ascribed to the balance between electronic and core-core contributions by Wang and Rikvold [163]. They have found that for Br/Au(001) the electronic energy difference between hollow and bridge sites ( $E_{hollow}^{el} - E_{bridge}^{el}$ ) partially compensates the energy difference of the core-core Coulomb interaction ( $E_{hollow}^{cc} - E_{bridge}^{cc}$ ). As a result, the bridge configuration is lower in total energy than the hollow configuration for Br/Au(001). Similar reasoning applies for adsorption of Cl on Au(001) surface. The top site is the least favorable position for halides on coinage (001)-metal surfaces. Table 2.1 lists the values of adsorption energy  $E_{ads}$  for each system. For a given halide, it is found that  $E_{ads}$  follows the trend  $Cu < Ag < Au$  [164].

The diffusion of halides on metals occurs via hopping mechanism. For Cu(001) and Ag(001) surfaces the transition state geometry of the halides resides above the bridge site, see Fig. 2.3. By contrast, on Au(001) surface the transition state position is not a high-symmetry site as shown in Fig. 2.3. Inspection of Table 2.1 shows that for Cu(001) and Ag(001) surfaces the activation energy barrier  $E_{act}$  decreases in the order  $I > Br > Cl$ . The activation barriers range from 0.06 eV ( $\approx 2.3 k_B T$ ) to 0.20 eV ( $\approx 7.7 k_B T$ ). This values are larger in comparison to  $E_{act}$  on (111) face of Cu and Ag metals, which ranges between 0.06 eV ( $\approx 2.3 k_B T$ ) to 0.08 eV ( $\approx 3.1 k_B T$ ) [165–167]. For Au(001)  $E_{act}$  decreases in the (vice versa) order  $Cl > Br > I$ , and varies from 0.01 eV ( $\approx 0.4 k_B T$ ) to 0.11 eV ( $\approx 4.3 k_B T$ ). Similarly values have been found on Au(111) surface [166, 168]. It should be noted that for both faces (001) and (111) the trend for  $E_{act}$  on Au surface is the opposite way to the trends on Cu and Ag surfaces. Regarding to the dipole moments, from Tab. 2.1 it is observed that the dipole moment change is of the same order for Cu(001) and Ag(001) surfaces. On Au(001) substrate the magnitude of  $\Delta\mu_z$  is about 10% – 20% of the values for Cu(001) or Ag(001) surfaces. By contrast, the corresponding sign of  $\Delta\mu_z$  is positive on Au(001) substrate, with the exception of Cl/Au(001) at  $\Theta = 1/4$ . The positive sign of  $\Delta\mu_z$  for Cl/Au(001) and Br/Au(001) has been attributed to z coordinate of the halide along the diffusion path. At the transition state the difference between the z

coordinate of the adatom relative to its adsorption site ranges from  $-0.2$  to  $-0.1$  Å. At  $\Theta = 1/4$   $\Delta z$  for Cl amounts to  $-0.05$  Å, this may be ascribed to the halide-halide interaction and its chemical nature. An anomalous behavior of I on metal surfaces has been reported in the literature [164, 169, 170]. For I/Au(001) the dipole moment at hollow site is positive, while for Cl,Br/Au(001) the total dipole moment is negative. Furthermore, the dipole moment for I/Au(001) follows the trend reported in Ref. [170], it decreases or even becomes negative at larger coverage.

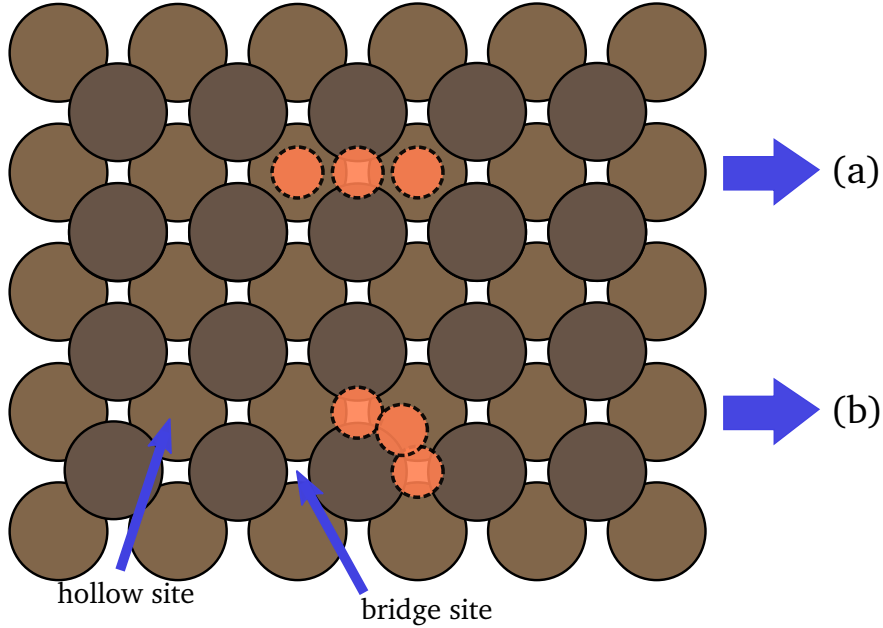


Figure 2.3.: The four-fold coordinated hollow site and the two-fold coordinated bridge site on a fcc(001) crystal surface. Schematic diffusion paths for a single halide on a fcc(001) crystal surface: (a) hollow – hollow occurs via bridge site for a single halide on Cu(001) and Ag(001) surfaces, (b) bridge – bridge diffusion for a single halide on Au(001) surface.

Up to now, we have discussed the diffusion of halides on the metal-vacuum interface. At electrochemical interfaces the adsorbates interact with the electric field in the double layer, which is the electrified interface between the electrode and electrolyte [29, 30]. Following thermodynamical arguments [47, 173], in a first-order approximation at constant electrode potential ( $\phi$ ) the change in the adsorbate's dipole moment ( $\Delta\mu_z$ ) during diffusion leads to an electrostatic energy contribution for the activation energy barrier of [47, 173]

$$E_{\text{act}}(\phi) = E_{\text{act}}^0 - \Delta\mu_z \frac{\sigma(\phi)}{\epsilon_0} \quad , \quad \text{where } \sigma : \text{charge density of defect-free surface.} \quad (2.44)$$

This energy contribution could be interpreted as the electrostatic interaction of a dipole on an electric field  $\mathcal{E}_z = \sigma/\epsilon_0$ . However, within this approach  $\sigma$  is a macroscopic charge density on the electrode. In the potential range, where the double layer capacity ( $C_d$ ) can be

Table 2.1.: Adsorption energies and activation energy barriers for halide/metal systems.  $E_{\text{act}}$  is the activation energy barrier. For halide/Cu(001), halide/Ag(001) and I/Au(001) systems  $E_{\text{act}}$  is estimated from the total energy difference between a halide atom at a bridge and hollow sites. For Cl/Au(001) and Br/Au(001)  $E_{\text{act}}$  is evaluated by NEB method. Adsorption energies  $E_{\text{ads}}$  with reference to a spin-polarized atom at hollow site (for halide/Cu(001), halide/Ag(001), I/Au(001) systems) and at bridge site (for Cl/Au(001), Br/Au(001) systems). Dipole moment change  $\Delta\mu_z$  between the transition state and the adsorption site.

Halide	Surface	$\Theta$	$E_{\text{act}} / \text{eV}$	$E_{\text{ads}} / \text{eV}$	$\Delta\mu_z / \text{e}\text{\AA}$	Reference
Cl	Cu(001)	1/8	-	-3.45	-	[164]
		1/18	0.06	-3.51 (-3.55)	-0.10	[48], [164]
	Ag(001)	1/4	0.11	-3.29	-	[161]
		1/8	-	-3.24	-	[164]
		1/16	0.11	-3.18	-	[171]
		1/18	0.11	-3.21	-0.13	[172]
	Au(001)	1/4	0.13 (0.17 <sup>a</sup> )	-2.54	-0.01 (0.0 <sup>a</sup> )	This work
		1/16	0.12 (0.16 <sup>a</sup> )	-2.64	0.02 (0.03 <sup>a</sup> )	This work
		1/36 <sup>a</sup>	0.11	-2.80	0.04	[59, 60]
	Br	Cu(001)	1/8	-	-3.17	-
1/18			0.13	-3.24 (-3.26 <sup>[164]</sup> )	-0.10	[48], [164]
Ag(001)		1/18	0.14	-2.97	-0.12	[172]
Au(001)		1/4	0.07 (0.08 <sup>a</sup> )	-2.34	0.02 (0.03 <sup>a</sup> )	This work
		1/16	0.07 (0.1 <sup>a</sup> )	-2.43	0.04 (0.05 <sup>a</sup> )	This work
I	Cu(001)	1/8	-	-2.92	-	[164]
		1/18	0.20	-2.99	-0.11	[172]
	Ag(001)	1/4	0.18	-2.70	-	[162]
		1/8	-	-2.73	-	[164]
		1/18	0.17	-2.69	-0.14	[172]
	Au(001)	1/4	0.02	-2.20	-0.06	This work
		1/8	-	-2.29	-	[164]
		1/16	0.01	-2.27	-0.09	This work

a:  $E_{\text{act}}$  and  $\Delta\mu_z$  are calculated between a halide at hollow and bridge sites.

considered a constant quantity, Eq. (2.44) can be written as

$$E_{\text{act}}(\phi) = E_{\text{act}}^0 - \Delta\mu_z \frac{C_d (\phi - \phi_{\text{pzc}})}{\epsilon_0}, \quad \text{where } \phi_{\text{pzc}} : \text{potential of zero charge.} \quad (2.45)$$

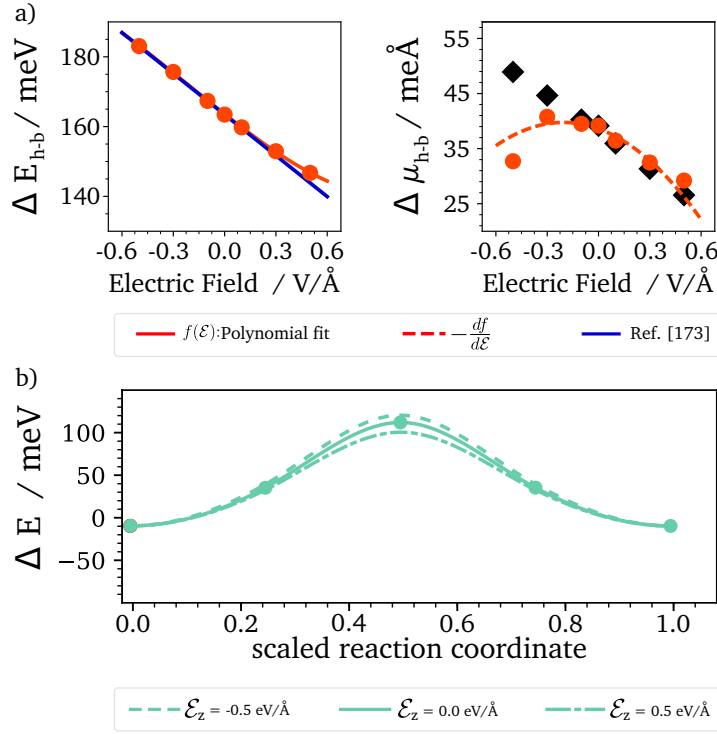


Figure 2.4.: a: Energy differences as well as dipole moment change for Cl/Au(001) at  $\Theta = 1/16$  between hollow –h– and bridge –b– sites as a function of an external homogeneous electric field, which is perpendicular to the surface. Red markers denote fully relaxed calculations at a fixed  $\mathcal{E}_z$ , black markers denote electronically relaxed calculations with frozen atomic coordinates at  $\mathcal{E}_z = 0.0$  eV/Å. b: Variation of energy along the diffusion path under homogeneous electric field for Cl/Au(001) at  $\Theta = 1/16$ .

From Eq. (2.45), the activation energy under electrochemical conditions depends linearly on the electrode potential. STM studies of  $S_{ad}$  tracer diffusion on Cl covered Cu(001) surface by Tansel and Magnussen [45] have shown almost a perfectly linear dependency between the  $E_{act}$  and the electrode potential. Additionally, numerous *in situ* STM studies of tracer surface diffusion on halide covered metal electrodes in electrochemical environment have been performed in the group of O. M. Magnussen [49], which have also shown a linear dependency of  $E_{act}$  with respect to the electrode potential. In experimental studies of coarsening of Au islands on Au(001) using electrochemical STM in chloride containing electrolytes as well as sulfuric acid solution Pichardo-Pedrero *et al.* have found that the linear relationship between the adatom formation energy from a kink site in the island edge plus the activation energy barrier on the terrace and the electrode potential is only achieved for small potentials [57]. To simulate the electrode/electrolyte by means of first principles is a very challenging task. It requires to account the liquid nature and electronic structure of the electrolyte. The presence of ions in the electrolyte, co-adsorbed water molecules and the charged interface

pose additional difficulties to the atomistic simulations. Particularly, accounting the effects of the local electric field by means of DFT has been reported in the literature [174–179] which mostly requires high computational costs. To gain a first insight into the influence of electric field on the PES for halide/metals, following [180] an external electric field has been applied and results have been compared to Eq. (2.45). The system in discussion is Cl/Au(001) with coverage  $\Theta = 1/16$ , calculations include nonlinear effects of the external electric field and atomic relaxation in the field. Energy difference between hollow and bridge site  $\Delta_{h-b}$  as a function of an external electric field is plotted in Fig. 2.4(a). The variation of energy  $\Delta E$  along the diffusion path under homogeneous electric field  $\mathcal{E}_z = -0.5, 0.0, +0.5 \text{V/\AA}$  is shown in Fig. 2.4(b). Energy difference  $\Delta E_{h-b}$  variates approximately 20% in the range of electric field from  $-0.5$  to  $+0.5 \text{ V/\AA}$ , and only 15% in case of  $E_{\text{act}}$ . Nonlinear effects on  $\mu$  are significant, but the influence on the PES is smaller than  $0.01 \text{ eV}$ . For this reason, the linear approximation proposed by Giesen *et al.* [47] is sufficient to describe halide/metal systems. In case of I/Au(001) depending on the electric field its PES is modified, *e.g.* at  $0.5 \text{ \AA}$  the bridge site becomes the preferred due to its large dipole moment  $\Delta\mu_z = -0.09 \text{ e\AA}$ . To this point, the impact of the electric field at the interface has been estimated by varying the external electric field in DFT calculations. Electric fields only slightly affects energy differences and activation energy barriers, as pointed out by Karlberg *et al.* for oxygen reduction reactions (ORR) [180]. It is known that water molecules have a strong polarization close to the metal electrode [181, 182], but how they will affect the dipole moment of adsorbed halide on metal surfaces, and hence its diffusion, is still an open question for further research.

## 2.4. Epitaxial Growth

### 2.4.1. Thermodynamic and Kinetic Growth Modes

Different surface morphologies are required for technological applications *e.g.* smooth films in the production magnetic storage devices, rough films with well defined islands for heterogeneous catalysis. To manipulate the morphology of epitaxially grown films, the control of the growth mode is necessary. A classification of epitaxial growth modes based on thermodynamic conditions was proposed by Bauer in 1958 [183], and it is applicable to thin films close to equilibrium. Three growth modes can be distinguished according to the balance of the surface energies of the substrate  $\gamma_S$ , deposit or film surface  $\gamma_D$  and the interface of the film and substrate  $\gamma_{\text{int}}$  as follows

$$\Delta\gamma = \gamma_D + \gamma_{\text{int}} - \gamma_S. \quad (2.46)$$

For the case  $\Delta\gamma > 0$  the area covered by the deposit (atoms or molecules) is minimized *i.e.* the interaction between the atoms or molecules are more strongly bound to each other than to the substrate. In this case three dimensional clusters are formed, growth mechanism proceeds via *Volmer-Weber* growth (3D-island growth). On the other hand, if  $\Delta\gamma < 0$  the energy balance requires to maximize the area covered by the deposit *i.e.* the interaction between the deposit and substrate is stronger. At initial stage the films will grow smoothly, this means one atomic layer at a time. This process continues until a certain film thickness is



reached, where the inequality does not hold anymore due to the elastic energy contributions. Subsequently, 3D-islands will be formed. The growth proceeds via the *Stranski-Krastanov* growth mode, which predominantly occurs in heteroepitaxial systems due to the mismatch in the lattice structures. In homoepitaxial growth systems the condition  $\Delta\gamma = 0$  holds. Films grow via layer-by-layer growth (or *Frank-van der Merwe* growth), ideally the growth of a layer only starts after the previous one is completed.

Under far from equilibrium conditions *e.g.* growth by molecular-beam epitaxy (MBE) the morphology of a growing film is a result of the interaction of different atomic diffusion processes, which occur on a time scale set by the deposition flux. The thermodynamic and kinetic limit provide different descriptions of film growth. Nevertheless, in real systems a clear separation between the energetic and kinetic effects can not be always achieved. The simplest model to study the basic kinetic growth mechanisms is the homoepitaxial systems, which according to thermodynamic concepts proceed via layer-by-layer growth mode. Therefore, the occurrence of a different growth mode is only attributed to kinetic effects. In the spirit of a simple picture two different diffusion processes are considered to occur on the crystal surface, diffusion of a single adatom on a flat terrace (intralayer transport) and diffusion of a single adatom across a step to a lower terrace (interlayer transport). According to the rates of both latter processes three kinetic growth modes can be observed in homoepitaxy, which are known as step-flow growth, layer-by-layer growth and multilayer growth [5]. Step-flow growth appears when intralayer transport is so rapid that adatoms reach the nearest steps and are captured there before they could form a stable nuclei [5, 184]. This mechanism usually occurs close to the equilibrium. When the system is far from equilibrium, growth proceeds via nucleation of adatoms on the terraces and hence growth of adatom islands. In this case, the interlayer transport becomes determinant for the growth mode which proceeds via two extreme cases: layer-by-layer growth or multilayer growth. Ideally, within the layer-by-layer mode every deposited adatom over an island reaches one of its step edge and jump to a lower layer. If the deposited adatoms remain bonded to the island and further nucleation takes place over the islands, the multilayer growth mode takes place.

### 2.4.2. Atomic Processes and Rate Equations

The growth of a crystal starts with the arrival of atoms through a potential gradient from vapor or liquid phase to the crystal surface, then deposited atoms become adsorbed on the substrate. Different atomistic processes are encountered by adatoms on the surface, which is usually not perfectly flat but contains imperfections *e.g.* steps. After deposition an adatom may diffuse on a flat terrace from one adsorption site to the next one by crossing over intermediate steps, this topic has been discussed in Sec. 2.3. In contrast to flat terraces, there is a numerous variety of diffusion mechanisms in the presence of surface defects. This is ascribed to the larger number of active sites *e.g.* kink sites. When an adatom has been captured by an already existing ad-island or step-edge, it may migrate along the edge, across it or even detach from it. In those cases, diffusion proceeds via hopping or an exchange mechanism. For example, diffusion of an Al adatom along the  $\langle 110 \rangle / \{111\}$  step on Al(111) proceeds via an exchange mechanism with  $E_{\text{act}} = 0.4$  eV [185], while along the  $\langle 110 \rangle / \{111\}$

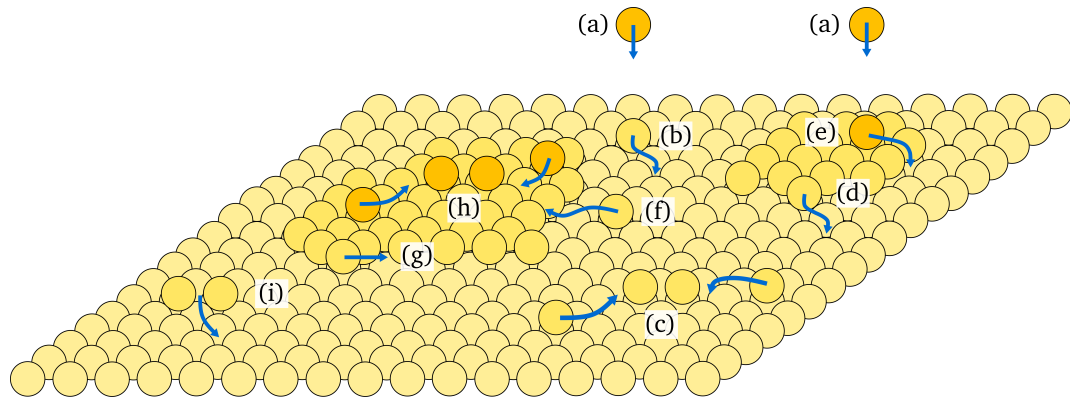


Figure 2.5.: Ball model of atomistic processes for adatoms on a clean surface: (a) deposition, (b) diffusion on a terrace, (c) nucleation of an island, (d) detachment from an island, (e) diffusion across a step, (f) diffusion toward a step, (g) diffusion over a step, (h) nucleation of an island on top of an existing island, and (i) diffusion of a dimer. This diagram was inspired by Fig. 1.3 in Ref. [4] and Fig. 2 in Ref. [19].

step on Al(111) an Al adatom diffuses via hopping with  $E_{\text{act}} = 0.3$  eV [185]. The authors have concluded that the difference on energy barriers and prefactors for diffusion along both step orientations can lead to temperature dependent ad-island shapes [185]. Pötting *et al.* have presented a detailed study on self-diffusion on perfect and imperfect Au(100) surfaces, they found out that detachment processes have low rates due to bond breaking [186]. Diffusion across a step involves the motion of an adatom at the step-edge to a lower terrace, the adatom must overcome the so-called Ehrlich-Schwöbel (ES) barrier [187, 188]. Some authors [189, 190] pointed out that the ES barriers may depend on the step thickness. These barriers can strongly influence crystal growth in the kinetic regime [12, 185, 191–193] *e.g.* large step barriers support multilayer growth when thermodynamics predict layer-by-layer growth. Eventually, during diffusion an adatom can be reached by another adatom and form stable dimers, trimers or larger clusters, which may migrate [194–197] or even coalesce [198]. The number of possible diffusion processes for islands increases tremendously with their size, therefore new approaches have been proposed to tackle this problem such as Self-Learning Kinetic Monte Carlo (SLKMC) [199], which has been applied on heteroepitaxy systems [200, 201].

### 2.4.3. Nucleation

The atomic processes form the basis of phenomenological rate equations for kinetic growth on a flat surface. Considering that adatoms are the only diffusive species *i.e.* dimers and cluster are immobile, the Equations 2.47 and 2.48 describe the time evolution of the areal

concentrations<sup>1</sup>  $n_s$  of cluster containing  $s$  adatoms [4].

$$\frac{dn_1}{dt} = F - 2\kappa_1 n_1^2 - n_1 \sum_{s>1} \kappa_s n_s + 2\gamma_2 n_2 + \sum_{s>2} \gamma_s n_s, \quad (2.47)$$

$$\frac{dn_s}{dt} = n_1 (\kappa_{s-1} n_{s-1} - \kappa_s n_s) - \gamma_s n_s + \gamma_{s+1} n_{s+1}. \quad (2.48)$$

The number adatoms is increased by the deposition rate  $F$ . The second and third term from Eq. (2.47) account for the loss of adatoms through dimer at rate  $\kappa_1$  formation and attachment to larger clusters at rate  $\kappa_s$ . While the last two terms of Eq. (2.47) are sources of adatoms, they appear as a result of dimer dissociation and detachment from an island  $n_j$  at a rate  $\gamma_j$ . Eq. (2.48) results from the growth of islands of size  $j - 1$  and the decay of islands of size  $j + 1$ . Desorption from the surface is neglected in Eq. (2.47) and (2.48). In general, Eq. (2.47) and (2.48) provide a complete picture of nucleation process. But, they contain a large number of coefficient rates  $\kappa_s$  and  $\gamma_s$ , which mostly remain unknown. One way around this issue is to distinguish between stable and unstable clusters with sizes  $s \geq i^* + 1$  and  $2 \leq s \leq i^*$  respectively.  $i^*$  is known as the critical cluster size, which depends on the flux as well as the temperature within this framework. The unstable clusters are assumed to decay faster than their net rate, this establishes thermodynamic equilibrium among the clusters. This means that the density of unstable clusters is stationary, and the concentration of unstable clusters can be written as function of  $n_1$  (Walton relation) [4].

$$\omega n_s \approx (\omega n_1)^s \exp\left(\frac{E_s}{k_B T}\right) \quad \text{for } 2 \leq s \leq i^*, \quad (2.49)$$

where  $E_s$  is the binding energy of a cluster of size  $s$ ,  $\omega$  denotes the area of an adsorption site. The stable clusters of sizes  $s \geq i^* + 1$  can increase by attachment, but they are assumed to not decay. Under this assumption, Eq. (2.48) becomes

$$\frac{dn_s}{dt} = n_1 (\kappa_{s-1} n_{s-1} - \kappa_s n_s) \quad , \quad \text{with } s \geq i^* + 1. \quad (2.50)$$

If we considered only the stable clusters, the total density of stable ad-islands follows

$$N = \sum_{s=i^*+1}^{\infty} n_s, \quad (2.51)$$

and evolves in time according to

$$\frac{dN}{dt} = \sum_{s=i^*+1}^{\infty} n_1 (\kappa_{s-1} n_{s-1} - \kappa_s n_s) = \kappa_{i^*} n_1 n_{i^*}. \quad (2.52)$$

The average of captured adatoms by stable ad-islands is defined by

$$\bar{\kappa} = N^{-1} \sum_{s=i^*+1}^{\infty} \kappa_s n_s \quad (2.53)$$

<sup>1</sup>Density of cluster averaged over a region containing a large number of clusters.

In thermal equilibrium Eq. (2.47) becomes

$$\frac{dn_1}{dt} = F - \kappa_{i^*} n_1 n_{i^*} - n_1 \bar{\kappa} N. \quad (2.54)$$

The solution of the coupled equations are far from trivial [4]. Two temporal regimes can be obtained: transient nucleation and steady state nucleation. In the first regime the loss of adatoms is negligible at very early stages. Therefore, the density of adatoms increases linearly with the time and the total density of stable ad-islands grows as  $\sim n_1^{i^*+2}$ . At the steady regime the number of deposited adatoms is balanced by the number of adatoms which are captured by stable ad-islands, this results in  $n_1 \approx \frac{F}{\bar{\kappa}N}$ . Solving Eq. (2.52), it is derived that the density of stable clusters scales  $N$  as [4, 19]

$$N \sim \left( \frac{F}{D} \right)^{(i^*/(i^*+2))}, \quad (2.55)$$

where  $D$  is the diffusion coefficient of an adatom on the flat surface. This relation can be used to obtain kinetic parameters such as activation energy barriers from experimental measurements *e.g.* growth of Ag on Pt(111) by Brune *et al.* [6]. The equation rates here are restricted to low coverages, cluster mobility and coalescence have been neglected.

## 2.5. Double Layer Structure

In an electrochemical cell the potential difference between the electrodes (anode and cathode) creates a variation in the electrostatic potential through the cell [27–29]. In the electrolyte there is no electric field due to the fact that it is an ionic conductor. Therefore, the potential variation occurs at the interface between the electrode surfaces and the electrolyte which creates large field gradients in the order of  $\sim 10^7$  V/cm [33, 202, 203]. Although the interfacial region remains overall neutral, either side of the electrode becomes charged to an equal and opposite extent, forming the so-called electric double layer [27, 28]. The core problem in electrochemical studies is to unravel the functional relationship and the effect of the field at the electrode/electrolyte interface.

One of the earliest model of the electric double layer is attributed to Helmholtz [204], who stated that two layers of opposite charge formed at the electrode/electrolyte interface and were separated by small distance  $d$ , see Fig. 2.6 (a). Thus, the structure of the Helmholtz model is described as a dielectric capacitor with

$$C_H = \frac{\varepsilon \varepsilon_0}{d}, \quad (2.56)$$

where  $\varepsilon$  is the dielectric constant of the medium,  $\varepsilon_0$  is the permittivity of free space. The corresponding potential presents a linear behavior as a function of the separation relative to the electrode.

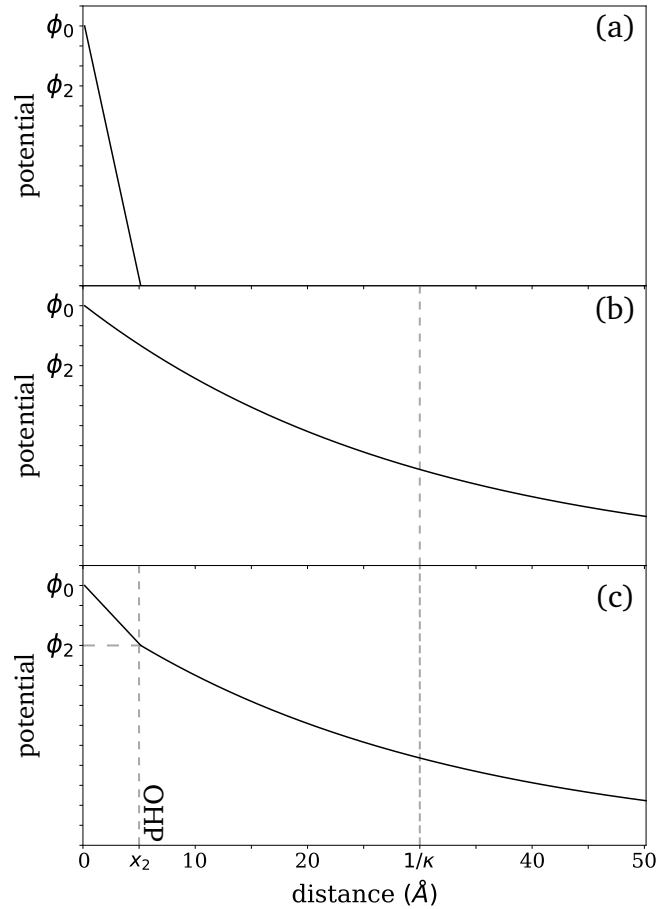


Figure 2.6.: Potential drop across the interface as proposed in (a) Helmholtz model, (b) Gouy-Chapman model, which is the solution of Eq. (2.61) for  $z e \phi(x)/k_B T \ll 1$ , and (c) Stern model. The plane at  $x_2$  is the so-called *outer Helmholtz plane* (OHP).  $1/\kappa$  is the Debye length, which denotes the thickness of the diffuse layer.

### Gouy-Chapman Model

The charge on the electrode is confined to the surface, but the same is not necessarily true of the solution. Particularly at low concentrations of electrolyte, one has a phase with a relatively low density of ions. The Gouy-Chapman model [205, 206] involves a diffuse layer of charge in the solution, in which a largest concentration of excess charge resides close to the electrode and a smaller concentration is found at largest distances relative to the electrode. The concentration of charged ions (cations and anions) in the electrolyte can be described with help of Boltzmann statistics. Considering the coordinate perpendicular to the electrode, the total charge density in the electrolyte can be written by [27, 30]

$$\rho(x) = \sum_i z_i e n_{0,i} \exp(-z_i e \phi(x)/k_B T), \quad (2.57)$$

where  $n_{0,i}$  is the bulk concentration of ion  $i$ , and  $|z_i e|$  denote the absolute charge on ion  $i$ .  $\phi$  is the potential relative to the bulk solution, at distances far from the electrode the potential and the corresponding field vanish. The potential  $\phi(x)$  is to be calculated from Poisson's equation

$$\frac{d^2\phi}{dx^2} = -\frac{\rho(x)}{\varepsilon\varepsilon_0}, \quad (2.58)$$

substituting Eq. (2.57) into Eq. (2.58)

$$\frac{d^2\phi}{dx^2} = -\frac{1}{\varepsilon\varepsilon_0} \sum_i z_i e n_{0,i} \exp(-z_i e \phi(x)/k_B T). \quad (2.59)$$

Eq.(2.59) is the so-called Poisson-Boltzmann equation [27, 30]. Multiplying by  $2\frac{d\phi}{dx}$  to Eq. (2.59) and integrating over  $x$

$$\left(\frac{d\phi}{dx}\right)^2 = \frac{2k_B T}{\varepsilon\varepsilon_0} \sum_i n_{0,i} \left[ \exp(-z_i e \phi(x)/k_B T) - 1 \right]. \quad (2.60)$$

In case of an electrolyte, in which cation and anion species have the same absolute charge e.g. HCl, Eq. (2.60) can be written as

$$\frac{d\phi}{dx} = -\sqrt{\frac{8n_0 k_B T}{\varepsilon\varepsilon_0}} \sinh\left(\frac{|ze|\phi(x)}{2k_B T}\right), \quad (2.61)$$

thus, the surface charge density on the metal is

$$\sigma = \sqrt{8n_0 k_B T \varepsilon\varepsilon_0} \sinh\left(\frac{|ze|(\phi - \phi_{pzc})}{2k_B T}\right). \quad (2.62)$$

$\phi_{pzc}$  refers to the potential when the electrode carries no charge. The corresponding differential capacitance of the diffuse layer is

$$C_{GC} = \varepsilon\varepsilon_0 \kappa \cosh\left(\frac{|ze|(\phi - \phi_{pzc})}{2k_B T}\right), \quad \kappa = \sqrt{\left(\frac{2(ze)^2 n_0}{\varepsilon\varepsilon_0 k_B T}\right)} : \text{Debye inverse length} \quad (2.63)$$

$C_{GC}$  has a V-shaped form [27] as shown in Fig. 2.7. There is a minimum at the  $\phi_{pzc}$  and a steep rise on either side.

A short-coming of this model is that counter-ion concentrations close to charged interfaces, calculated from Eq. (2.57) can become unreasonably high, even for only moderate values of surface potential [27, 30]. Moreover, measured capacitances at certain interfaces can be much lower than those predicted by the model [27, 30].

### Gouy-Chapman-Stern Model

Since the Gouy-Chapman model is only valid for low electrolyte concentrations Otto Stern [207] proposed a combination of the Helmholtz-model and the Gouy-Chapman models,

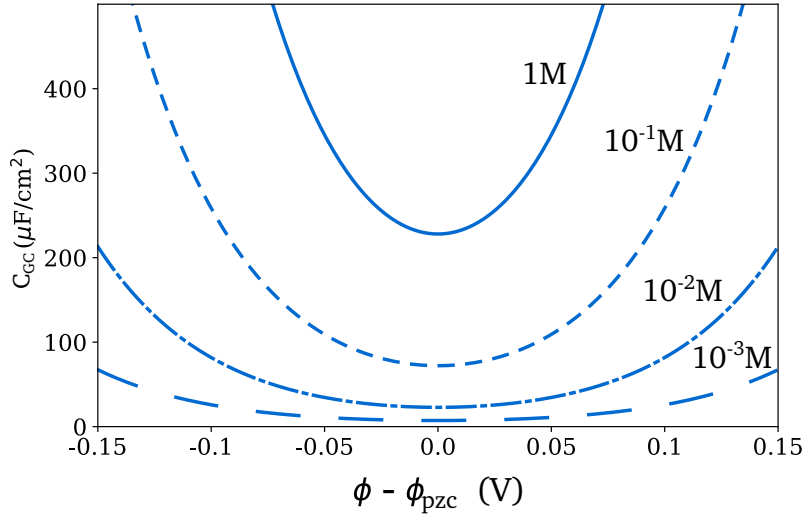


Figure 2.7.: Differential capacitances from the Gouy-Chapman theory as shown in Eq. (2.63) at 25°C for different values of electrolyte concentrations.

which results in a sequence of linearly and exponentially decreased potentials. The model is illustrated in Fig. . The plane at  $x = x_2$  is called the outer Helmholtz plane (OHP), which presents the closest approach of hydrated ions to the surface. Within this model the Poisson-Boltzmann equation (Eq. 2.59) and its solution still apply at distances  $x \leq x_2$ , see the potential drop in Fig. 2.6 (c). As the Gouy-Chapman capacitance lies in series with the capacitance of the Stern-layer the total capacitance is given by

$$\frac{1}{C} = \frac{1}{C_H} + \frac{1}{C_{GC}}. \quad (2.64)$$

The capacitance  $C$  is governed by the smaller value of the two components. For this reason close to  $\phi_{pzc}$  in systems with low electrolyte concentration  $C$  is expected to be V-shaped [27, 30] as shown in Fig. 2.7.

This model yields a phenomenological description of the solid/liquid interface. For further continuum models the reader is referred to Ref. [208]. Still as a continuum model it does not take the atomistic structure of the interface into account *e.g.* specific and quasispecific adsorption of ions, see Fig. 2.8. Specifically adsorbed ions reside at the inner Helmholtz plane (IHP). These ions are chemically bonded to the surface and (partially) discharged. Quasispecific adsorption of ions describes the mediation of the adsorption process by another species. Furthermore, the ion-ion correlation effects as well as strong nonspecific interactions of the ions with the surface charge on the electrode should be considered.

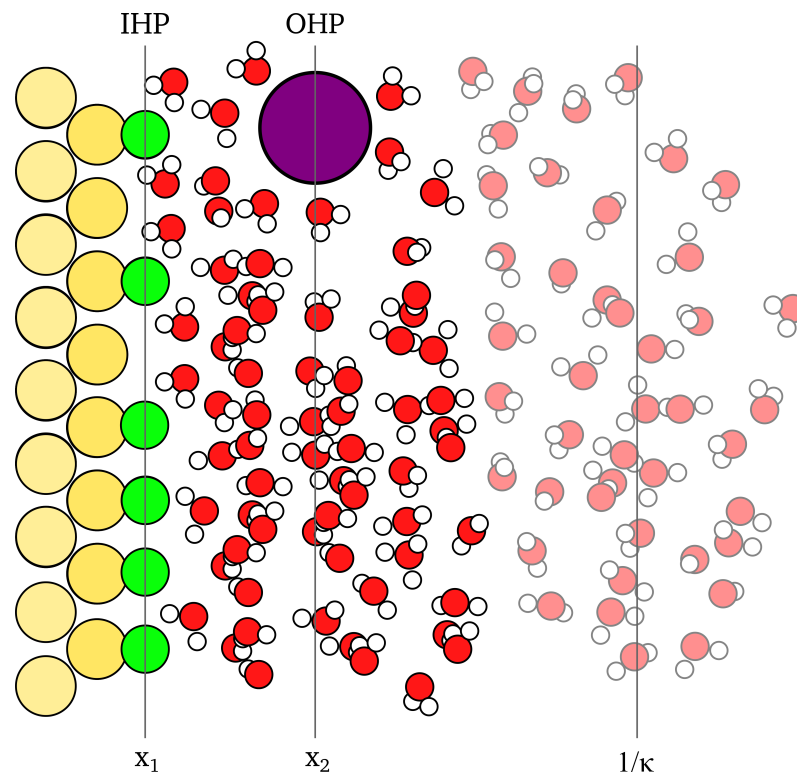


Figure 2.8.: Schematic atomistic diagram of the metal/electrolyte interface, showing specific and nonspecific adsorption. Specifically adsorbed ions reside in the inner Helmholtz plane (IHP), which is the plane at  $x_1$ . The outer Helmholtz plane (OHP), which is the plane at  $x_2$ , is the closest layer of solvated ions to the surface. This diagram was inspired by Fig. 1 in Ref. [29] and Fig. 3 (b) in Ref. [203].



# 3.

## Halide Adlayer Structure on Au(001)

To understand and characterize the kinetics and reaction mechanisms of interfacial charge transfer reactions occurring in an electrochemical environment it is necessary the knowledge of the physicochemical properties of the reactants as well as the atomic scale structure of the respective interface *e.g.* metal/electrolyte interface. Electrolyte species such as anions can chemisorb on electrode surfaces *e.g.*  $(\text{SO}_4)^{-2}$  on Au(111) [34]. Particularly, halides are known to form closed-packed ordered adlayer structures on metal surfaces depending on the sample potential applied [35]. They will attract or repulse other adsorbates, resulting in modified binding energies and diffusion mechanisms as well as the corresponding activation barriers.

Theoretically, ab initio thermodynamics approach [209–211] addresses the stability of surface configurations *e.g.* ordered adlayer phases by considering reservoirs which can interchange species (adsorbates) with the surface. The free energy per surface atoms,  $N_{\text{site}}$ , is compared among the different calculated configurations which contained a variety number of adsorbates. The most stable surface structure is obtained by minimizing the free energy per surface atom

$$\mathcal{G}(N_i, N_{\text{site}}, \mu_i) = \frac{G(N_i, N_{\text{site}}) - G_{\text{clean}}(N_{\text{site}}) - N_i \mu_i}{N_{\text{site}}}, \quad (3.1)$$

where  $G(N_i, N_{\text{site}})$  is the Gibbs free energy of a particular surface containing  $N_i$  adsorbates, and  $G(0, N_{\text{site}})$  is the Gibbs free energy of the clean surface, and  $\mu_i$  is the chemical potential of the corresponding reservoir of specie  $i$ . In Eq. (3.1) the reservoir for the specie  $i$  needs to be defined.

The Gibbs free energy can be divided into the total energy, vibrational/configurational contributions and the expansion term  $pV$ . DFT total energies are evaluated for a certain volume  $V$  of a unit cell at zero temperature and neglecting zero-point vibrations.

The vibrational component is given by

$$F_{\text{vib.}}(T, N_i, N_{\text{site}}) = \int d\omega \mathcal{F}_{\text{vib.}}(T, \omega) \sigma(\omega), \quad (3.2)$$

$$\approx N_i \sum_{j=1}^3 \mathcal{F}_{\text{vib.}}(T, \omega_j) \quad (3.3)$$

where  $\sigma(\omega)$  is the phonon DOS. Following the Einstein model  $F_{\text{vib.}}(T, N_i, N_{\text{site}})$  can be approximated to the summation over all the degrees of freedom ( $x, y, z$ ) per adsorbate. From the harmonic partition function the frequency dependent function  $\mathcal{F}_{\text{vib.}}(T, \omega)$  is written as

$$\mathcal{F}_{\text{vib.}}(T, \omega) = \frac{\hbar\omega}{2} + k_B T \ln(1 - \exp(-\hbar\omega/k_B T)). \quad (3.4)$$

Assuming that adsorption occurs at fixed sites and the interaction between adsorbed particles can be neglected, the configurational entropy can be written as [30]

$$S_{\text{conf.}}(N_i, N_{\text{site}}) = k_B \ln \left( \frac{N_{\text{site}}!}{(N_{\text{site}} - N_i)! N_i!} \right), \quad (3.5)$$

$$\approx k_B N_{\text{site}} \left[ \ln(N_{\text{site}}/N_i) + \frac{N_{\text{site}} - N_i}{N_{\text{site}}} \ln(N_i/(N_{\text{site}} - N_i)) \right]. \quad (3.6)$$

$N_i$  and  $N_{\text{site}}$  correspond to the occupied and total adsorption sites on the surface. Denoting the surface coverage as  $\Theta = \frac{N_i}{N_{\text{site}}}$ ,  $S_{\text{conf.}}$  yields

$$S_{\text{conf.}}(N_i, N_{\text{site}}) \approx k_B N_{\text{site}} \left[ -\ln(\Theta) + (1 - \Theta) \ln(\Theta/1 - \Theta) \right]. \quad (3.7)$$

It should be noted that Eq. (3.7) is not directly applicable to our high-coverage configurations due to the interaction between the coadsorbates.

### Gas phase chemical potential

At gas/solid interfaces, the stability of the different adsorption structures depends on the surrounding gas phase conditions. Assuming that the molecule of specie  $i$  is diatomic in gas phase, the chemical potential is given by

$$\mu_i(T, p) = \frac{1}{2} \mu_{\text{Mol.}i}(T, p). \quad (3.8)$$

The surrounding gas phase is described as an ideal gas reservoir. For an ideal gas of  $N$  indistinguishable particles which do not interact with each other, the chemical potential at a given temperature  $T$  and volume  $V$  is defined by

$$\mu_{\text{Mol.}i}(T, V) = \left( \frac{\partial F(T, V, N)}{\partial N} \right)_{V, T} = \left( \frac{\partial -k_B T \ln Z}{\partial N} \right)_{V, T}, \quad (3.9)$$

and the pressure can be written as

$$p = -\frac{\partial F(T, V, N)}{\partial V}. \quad (3.10)$$

The partition function  $Z$  of the system is

$$Z = \frac{1}{N!} (z_{\text{elec.}} z_{\text{trans.}} z_{\text{vib.}} z_{\text{rot.}} z_{\text{nucl.}})^N, \quad (3.11)$$

where  $z$  correspond to the partition function of one particle. The nuclear partition  $z_{\text{nucl}}$  has been considered equal to the unity, spin effects in Eq. (3.11) have been disregarded. The electronic, translation, vibrational and rotational contributions can be evaluated using statistical thermodynamics. For the electronic term we consider only the ground state energy of the molecule  $z_{\text{elec.}} = e^{-E_i/k_B T}$ . The contribution from translation in the volume  $V$  is given by

$$z_{\text{trans.}} = \frac{V}{\lambda_{\text{DB}}^3}, \quad \lambda_{\text{DB}} = \left( \frac{2\pi\hbar^2}{Mk_B T} \right)^{1/2}. \quad (3.12)$$

The vibrational motion of a diatomic molecule involves only one degree of freedom, and is determined by one-dimensional oscillator

$$z_{\text{vib.}} = \frac{e^{-\frac{1}{2}\hbar\omega/k_B T}}{1 - e^{-\hbar\omega/k_B T}}. \quad (3.13)$$

Considering the quantum energy levels of a rigid rotator, at high temperatures the  $z_{\text{rot.}}$  can be written as

$$z_{\text{rot.}} = \frac{T}{T_{\text{rot}}}, \quad T_{\text{rot}} = \frac{\hbar^2}{2Ik_B T} \quad \text{where } I : \text{moment of inertia.} \quad (3.14)$$

In case of symmetrical diatomic molecules it should be accounted the fact of quantum identical particles.

Using results from Eq. (3.12)–(3.14) in Eq. (3.11), we obtain

$$Z = \frac{1}{N!} e^{-N E_i/k_B T} \left( \frac{V}{\lambda_{\text{DB}}^3} \right)^N \left( \frac{e^{-\frac{1}{2}\hbar\omega/k_B T}}{1 - e^{-\hbar\omega/k_B T}} \right)^N \left( \frac{T}{T_{\text{rot}}} \right)^N, \quad (3.15)$$

$$F = Nk_B T \left\{ \frac{E_i}{k_B T} - \ln \frac{Ve}{N\lambda_{\text{DB}}^3} + \ln \left( e^{\frac{1}{2}\hbar\omega/k_B T} - e^{-\frac{1}{2}\hbar\omega/k_B T} \right) - \ln \frac{T}{T_{\text{rot}}} \right\}, \quad (3.16)$$

$$p = \frac{Nk_B T}{V} \quad (3.17)$$

Thus, we can write the  $\mu_{\text{Mol.}i}$  as a function of pressure and temperature

$$\mu_{\text{Mol.}i}(T, p) = E_i + k_B T \left\{ -\ln \frac{k_B T}{p\lambda_{\text{DB}}^3} + \ln \left( e^{\frac{1}{2}\hbar\omega/k_B T} - e^{-\frac{1}{2}\hbar\omega/k_B T} \right) - \ln \frac{T}{T_{\text{rot}}} \right\}. \quad (3.18)$$

Therefore, the chemical potential of the gas phase molecule can be separated into the DFT total energy of the isolated gas phase specie and a remaining part containing all temperature and pressure terms.

$$\mu_{\text{Mol.}i}(T, p) = E_i + \Delta\mu_i(T, p). \quad (3.19)$$

where the term  $\Delta\mu_i(T, p)$  can be expressed as

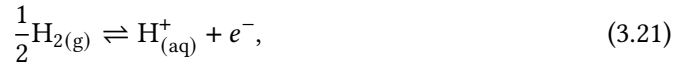
$$\begin{aligned} \Delta\mu_i(T, p) &= \Delta\mu_i(T, p^\ominus) + k_B T \ln \left( \frac{p}{p^\ominus} \right), \\ &= \Delta H(T, p^\ominus) - T\Delta S(T, p^\ominus) + k_B T \ln \left( \frac{p}{p^\ominus} \right). \end{aligned} \quad (3.20)$$

The temperature change of the enthalpy and entropy is given by  $\Delta H(T, p^\ominus) = H(T, p^\ominus) - H(0K, p^\ominus)$  and  $\Delta S(T, p^\ominus) = S(T, p^\ominus) - S(0K, p^\ominus)$  respectively. The temperature dependence is obtained from the differences of enthalpy and entropy with respect  $T = 0$  K limit. For standard pressure the enthalpy and entropy can be taken from thermochemical tables [212]. Furthermore, the elemental phase of the specie for the total energy  $E_i$  and  $\Delta\mu_i(T, p)$  should be taken into account. For molecules experimental free enthalpy values in the gas phase are used from [212]. The reference state  $\ominus$  is the standard state *i.e.*  $p^\ominus = 1$  atm.

### Chemical potential in electrochemical systems

At liquid/solid interfaces the electrochemical environment is considered as a reservoir, in which the atoms (cations and anions) are solvated by the electrolyte. Besides the electrode material, the sample potential and macroscopic parameters of the electrolyte such as pH and concentration of ions govern the surface composition. Altogether, the interrelations between the chemical potential, sample potential, ion activities and the electric field at the interface are necessary, but this is still a challenge for the theory.

To achieve a fully ab initio treatment, several first-principles methods have been proposed [39, 213–219]. Among them a computational inexpensive method is the so-called Computational Hydrogen Electrode (CHE) proposed by Nørskov *et al.* [39]. This technique avoids the calculation of solvated protons. Here, one takes advantage of the equity of the chemical potential of saturated vapor and liquid under given conditions. At standard conditions (zero pH) the reaction

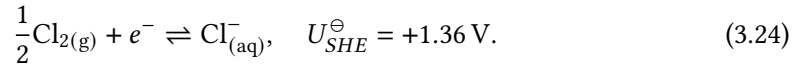


is in equilibrium at zero potential vs. the standard hydrogen electrode (SHE). In fact, the electrochemical potential of a proton-electron pair  $\tilde{\mu}_{\text{H}_{(\text{aq})}^+} + \tilde{\mu}(e^-)$  is equal half of the chemical potential of gaseous hydrogen  $\mu_{\text{H}_{2(\text{g})}}/2$ . At finite pH and sample potential the electrochemical potential of the proton-electron pair can be written as a function of the sample potential by standard thermodynamic relation  $\Delta G_{\text{rxn}} = -eU_{\text{SHE}}$ , where  $e$  is the absolute value of the electron charge and  $U_{\text{SHE}}$  is the sample potential.

$$\mu_{\text{H}} = \tilde{\mu}_{\text{H}_{(\text{aq})}^+} + \tilde{\mu}_{e^-}, \quad (3.22)$$

$$= \frac{1}{2}\mu_{\text{H}_{2(\text{g})}}(T, p^\ominus) - eU_{\text{SHE}} + k_{\text{B}}T \ln(10)\text{pH}. \quad (3.23)$$

With Eq. (3.23) the chemical potential scale can be converted into a sample potential scale. This reasoning can be used for other redox couples, for example in case of chlorine  $\text{Cl}_{(\text{aq})}^-$  is in equilibrium with  $\mu_{\text{Cl}_{2(\text{g})}}/2 + e^-$  under standard conditions at the potential of standard chlorine electrode [220]



Similarly to Eq. (3.23), the chemical potential of Cl is given by

$$\mu_{\text{Cl}} = \frac{1}{2}\mu_{\text{Cl}_{2(\text{g})}}(T, p^\ominus) + e(U_{\text{SHE}} - U_{\text{SHE}}^\ominus) + k_{\text{B}}T \ln(a_{\text{Cl}}^-), \quad (3.25)$$

where  $a_{\text{Cl}}^-$  is the activity of chlorine in the electrolyte. The chemical potential of the gas phase species at standard conditions can be written as  $E(i) + \Delta\mu_i(T, p^\ominus)$ . Particularly, for chlorine the chemical potential can be written as

$$\mu_{\text{Cl}} = E_{\text{Cl}_2}/2 + \Delta\mu_{\text{Cl}_2}(T, p^\ominus)/2 + e(U_{\text{SHE}} - U_{\text{SHE}}^\ominus) + k_{\text{B}}T \ln(a_{\text{Cl}}^-). \quad (3.26)$$

within this approach the effect of the electric field at the interface is disregarded [39].

The CHE has been successfully applied to various systems in the literature [39–41]. This approach assumes that the charge of an ion is fully neutralized during adsorption. In fact, this assumption is still an open question in the theory. The screening by solvent molecules gives origin to the so-called partial charge transferred by the adsorbate to the electrode [221–224]. The partial charge transfer can not be measured [223], but the thermodynamic (macroscopic) quantity *electrosorption valency*  $\gamma$ , which is defined as the charge flowing to the electrode per one adsorbate at a constant electrode potential [221–223, 225], can be determined. The *electrosorption valency* is defined as

$$\gamma = -\frac{1}{F} \left( \frac{\partial \sigma_{\text{M}}}{\partial \Gamma_{\text{ad}}} \right)_U, \quad (3.27)$$

where  $\sigma_{\text{M}}$  is the charge density on the metal electrode,  $\Gamma_{\text{ad}}$  is the surface concentration of the specifically adsorbed ions,  $F$  is the Faraday constant. Equivalently, the *electrosorption valency* can be defined through

$$\gamma = \frac{1}{F} \left( \frac{\partial \mu_{\text{S}}}{\partial U} \right)_{\Gamma_{\text{ad}}}, \quad (3.28)$$

where  $\mu_{\text{S}}$  is the chemical potential of the adsorbed specie in the bulk solution.

Concerning *electrosorption valency*, Monte Carlo simulations using an equilibrium lattice-gas model to investigate halide electrosorption on Ag(100) have been reported in the literature [42–44, 226]. The energy associated to a configuration of adsorbates on the surface has been described by a grand canonical effective Hamiltonian, in which the chemical potential of the halide is related to the *electrosorption valency*  $\gamma$  by the term  $\int_{U_0}^U \gamma(U') dU'$ ,  $U_0$  is a reference potential [42–44, 226]. Fitting the simulated isotherms to chronocoulometry experiments,  $\gamma$  as well as the next-nearest neighbor lateral interaction energy have been obtained. Within this approach and accurate experimental data description of the critical properties of the continuous order/disorder phase transition within the halide adlayer on Ag(001) can be provided as a function of the sample potential. Furthermore, calculations by other authors have been carried out to determine the *electrosorption valency* by means of first principles in combination with continuum electrolyte theory [227, 228]. In particular, Jinnouchi *et al.* have calculated the *electrosorption valency* for sulfate and bisulfate as a function of sample voltage on a Pt(111) electrode by performing a quadratic fit of the Gibbs free energy to sample voltage [227]. They noticed that there is variation of  $\gamma$  at different anion coverages. For halides on Au(001) surface *electrosorption valency* values either from ab initio calculations or experiments are not known to date.

Altogether, the partial charge transfer and the *electrosorption valency* are to our knowledge an open question. Therefore, we have not converted the chemical potential as a function of

electrode potential. Thus, we stay with  $\Delta\mu$  as a variable. In Sec. the chemical potential of the halide is written by

$$\mu_i = E_{\text{ref.}} + \Delta\mu_i, \quad (3.29)$$

where  $E_{\text{ref.}}$  is one half of the total energy of the isolated molecule for Cl and Br, in case of I  $E_{\text{ref.}}$  refers to the bulk energy of  $\text{I}_2$  per atom. DFT results for Cl adlayers have been published in Ref. [229].

### 3.1. Surface Structure of Au(001)

Early UHV studies have shown that clean Au(001) surfaces develops a contracted quasihexagonal (hex) top layer on the  $(1 \times 1)$  square lattice [14, 230, 231]. Historically, a superstructure  $(5 \times 1)$  has been inferred from LEED patterns by Fedak and Gjostein [230], later the same authors identified a  $(5 \times 20)$  superstructure [14]. With more sensitive techniques other superstructures have been reported in the literature, recently Hammer *et al.* have shown that the Au(001) reconstruction consists of two rotational domains of a commensurate  $c(28 \times 48)$  surface unit cell [232]. Regarding theory, Havu *et al.* [233] have investigated superstructures  $(5 \times N)$  for  $N \approx 20 - 30$  by means of DFT. They found out that denser reconstructions *e.g.*  $(5 \times 20)$  are energetically favored over the  $(5 \times 1)$  by roughly  $0.03 \text{ eV}/(1 \times 1)$ .

In electrochemical environment the gold surface resembles the UHV hexagonal reconstruction. The stability range of the Au(001)-hex depends on the electrolyte *e.g.* in 0.01 M  $\text{HClO}_4$  up to about  $0.55 \text{ V}_{\text{SCE}}$ , and in 0.01 N  $\text{H}_2\text{SO}_4$  up to  $0.30 \text{ V}_{\text{SCE}}$  [234]. STM experiments were able to observe the structural transition (hex) $\rightarrow(1 \times 1)$  of Au(001) at increasing electrode potentials [234–237]. The presence of strong specific adsorption plays a determinant role in the lifting of Au(001)-hex *e.g.* halide containing electrolytes. But for weakly adsorbing electrolytes *e.g.*  $\text{HSO}_4$  electrolyte the interaction between the surface dipole and the double layer constitutes the driving force for the lifting of the reconstruction [238]. Regarding this topic, theoretical studies by Feng *et al.* [239] and Jacob *et al.* [240, 241] have studied the potential-induced surface reconstruction of Au(001) without specific ion adsorption by means of DFT. In order to introduce the presence of an electrode potential a variable electric field has been applied perpendicular to the surperstructure  $(5 \times 1)$  and  $(1 \times 1)$ . To convert the surface charge to electrode potential scale experimental results *e.g.* double layer capacitance [239], cyclic voltammogram (CV) curves [240, 241] have been used. They conclude that electronic effects due to surface charging plays a major role in lifting the reconstruction. Recent work by Hörmann *et al.* [242] using a grand canonical simulation based on DFT in a continuum electrolyte have reproduced the transition (hex) $\rightarrow(1 \times 1)$  in the absence of adsorbates. But calculated potential zero charge showed a difference of about  $\approx 0.4 \text{ V}$  with respect to experimental values, the authors attributed this in part to low density of Au atoms on the  $(5 \times 1)$  [233].

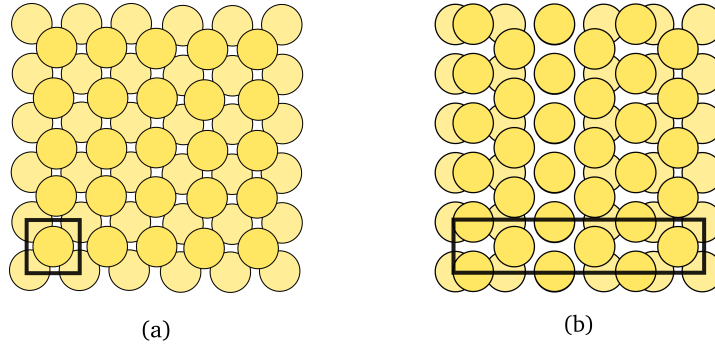


Figure 3.1.: Atomic geometry of the Au(001) substrate. (a) unreconstructed Au(001)-(1 × 1)(001), (b) the top layer is in reconstructed hexagonal structure with (5 × 1) periodicity as calculated in References [233, 239, 240]. Black squares denote the surface unit cells used in the calculations.

### 3.2. Cl Adlayer on Au(001)

In  $\text{Cl}^-$  containing electrolyte the lifting of the reconstruction is about  $0.08 V_{\text{Ag}/\text{AgCl}}$  (0.01M HCl solution) [38], this corresponds to an anodic peak in the CV curve [35, 38, 57, 243]. A low coverage of Cl has been measured on Au(001)-hex by Al-Shakran *et al.* [37]. For the unreconstructed Au(001) substrate a  $c(\sqrt{2} \times 2\sqrt{2})\text{R}45^\circ$  has been reported in surface X-ray scattering (SXS) [35]. Moreover, in situ high-speed STM studies [38] have shown a defective  $c(2 \times 2)$  structure in the potential regime from 0 to  $0.4 V_{\text{Ag}/\text{AgCl}}$ . At more positive sample potential a transition to a uniaxially compressed incommensurate  $c(\sqrt{2} \times p)\text{R}45^\circ$  structure has been observed [35, 38, 243].

To identify the equilibrium chlorine coverage and the Cl adsorption structure as a function of  $\Delta\mu_{\text{Cl}}$ , DFT calculations for several Cl structures on Au(001)-(1 × 1) have been performed with coverage  $\Theta$  ranging from 0.063 to 0.63. Electrolyte effects as well as electric field interactions have not been included in the calculations. In Fig. 3.2 four Cl adlayers are depicted: (a)  $c(2 \times 2)$  adlayer with  $\Theta = 0.5$ , (b)  $c(2\sqrt{2} \times \sqrt{2})\text{R}45^\circ$  with  $\Theta = 0.5$ , (c)  $p(3\sqrt{2} \times \sqrt{2})\text{R}45^\circ$  at  $\Theta = 0.33$ , and (d)  $p(8 \times \sqrt{2})$  at  $\Theta = 0.63$ , further structures are listed in Appendix A.6.

The total energy of a configuration will be denoted by

$$E(m, \mathcal{C}, N_{\text{site}}). \quad (3.30)$$

$m$  is the number of Cl adatoms in the unit cell,  $N_{\text{site}}$  denotes the number of Au atoms per layer in the (1 × 1) – Au surface. Thus, the coverage is defined as the ratio of  $m/N_{\text{site}}$ . The various possible configurations at a given  $(m, N_{\text{site}})$  are listed by  $\mathcal{C}$ . For example in Appendix A.6 four different configurations at  $(m = 16, N_{\text{site}} = 36)$  are shown. The minimum of  $E(m, \mathcal{C}, N_{\text{site}})$  with respect all configurations  $\mathcal{C}$  at a given  $\Theta$  and  $N_{\text{site}}$  will be only taken into account.

$$E_0(m, N_{\text{site}}) = \min_{\mathcal{C}} E(m, \mathcal{C}, N_{\text{site}}). \quad (3.31)$$

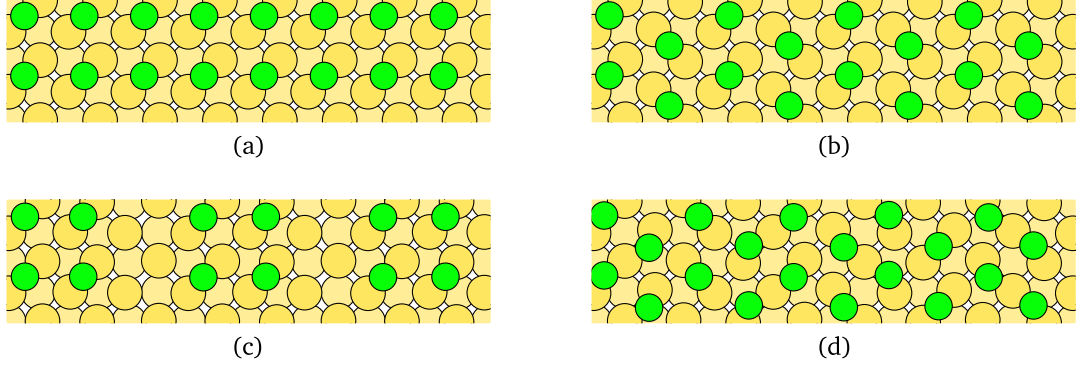


Figure 3.2.: Atomic structures of the Cl/Au(001) interface. (a)  $c(2 \times 2)$ -Cl adlayer at  $\Theta = 0.5$  simulated in a  $c(2 \times 2)$  SUC, (b)  $c(\sqrt{2} \times 2\sqrt{2})R45^\circ$ -Cl adlayer at  $\Theta = 0.5$  simulated in a  $p(2\sqrt{2} \times \sqrt{2})$  SUC, (c)  $p(3\sqrt{2} \times \sqrt{2})R45^\circ$ -Cl with  $\Theta = 0.33$  simulated in a  $p(6 \times 6)$  SUC, (d) Cl adlayer with  $\Theta = 0.63$  simulated in a  $p(8\sqrt{2} \times \sqrt{2})$  SUC. The coverage is determined by the ratio of the number adsorbed adatoms to the number of gold atoms in the surface.

The stability of different adsorption structures is compared with respect to the clean Au(001) surface by

$$E_{\text{ads}}(\Theta, \Delta\mu_{\text{Cl}}) = \left[ E_0(m, N_{\text{site}}) - E_{\text{clean}}(N_{\text{site}}) - m(E_{\text{Cl}_2}/2 + \Delta\mu_{\text{Cl}}) \right] \frac{1}{N_{\text{site}}}. \quad (3.32)$$

Following ab initio thermodynamics approach  $\mathcal{G}$  from Eq. (3.1) should be calculated [40, 209–211], in fact the adsorption energy per  $N_{\text{site}}$   $E_{\text{ads}}$  is an approximation. The configurational entropy and the contribution of differently adsorbed Cl atoms to vibrational free energy have been neglected. The contribution regarding zero point energy and vibrational free energy would be of the order of 0.040 eV for high-coverage configurations, which can be incorporated into the chemical potential term resulting in a shift in the value of  $\mu_{\text{Cl}}$ .

$E_{\text{ads}}(\Theta, \Delta\mu_{\text{Cl}})$  vs.  $\Delta\mu_{\text{Cl}}$  is shown in Fig. 3.3. The stable Cl structure for a given  $\Delta\mu_{\text{Cl}}$  results from the minimization of  $E_{\text{ads}}$  over all coverages. To consider the hex-reconstruction as a first approach, we calculate the surface energy per  $N_{\text{site}}$  of  $(5 \times 1)$  with respect to  $(1 \times 1)$  disregarding the Cl adsorbates. This value amounts to -0.042 eV ( $\sim -0.037$  eV [233]). Considering the surface energy of  $(5 \times 1)$  with respect to  $(1 \times 1)$  we determine the range of stability for the hex-Au reconstruction  $\Delta\mu_{\text{Cl}} < \sim -1.03$ . However, it should be noticed that this number is uncertain for two main reasons: (a) the reconstruction of Au surface and the neglect of electric fields, and (b) the limited number of Cl configurations with  $\Theta < 0.5$ . From Fig. 3.3 we observed three stable Cl structures in the unreconstructed range:

- $p(3\sqrt{2} \times \sqrt{2})R45^\circ$  with  $\Theta = 0.33$  for  $-1.03 < \Delta\mu_{\text{Cl}} < -0.94$ ,
- $c(2 \times 2)$  with  $\Theta = 0.33$  for  $-0.94 < \Delta\mu_{\text{Cl}} < -0.35$ ,
- $p(8 \times \sqrt{2})$  with  $\Theta = 0.63$  for  $\Delta\mu_{\text{Cl}} > -0.35$ .



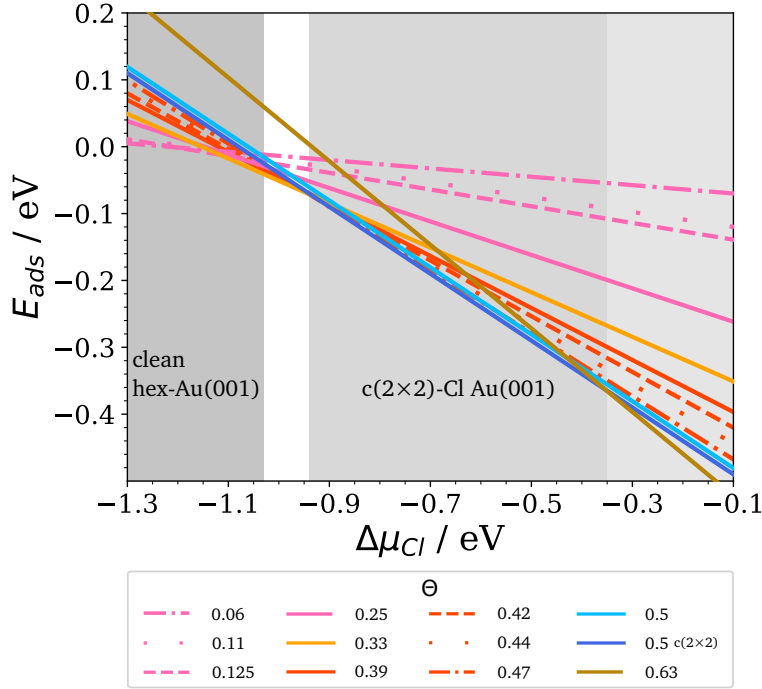


Figure 3.3.: Adsorption energy per  $N_{\text{site}}$   $E_{\text{ads}}$  at given values of  $\Theta$  as a function of  $\Delta\mu_{\text{Cl}}$ .

The  $p(3\sqrt{2} \times \sqrt{2})R45^\circ$  structure is characterized by vacancy-chains parallel to the [010] direction of the substrate. Iwai *et al.* have inferred similar structures *e.g.*  $p(5\sqrt{2} \times \sqrt{2})R45^\circ$  from LEED patterns at low temperature [244]. The chains are oriented in the [010] (or the [100]) direction of the Au substrate [244], which is identical to the direction of the vacancy chains in our calculation. At saturation coverage Iwai *et al.* have identified a  $c(2 \times 2)$ -Cl adlayer from LEED pattern at low and room temperature. In the electrochemical environment at  $T_{\text{room}}$  the experiments in Ref. [37] yield a smooth variation of the Cl coverage as a function of sample potential. It is expected that at  $T_{\text{room}}$  the vacancy chain configurations will show small statistical weight. Thus, the smoothness of  $E_{\text{ads}}$  can be recovered at  $T_{\text{room}}$ .

In Chapters 4 and 5, we restrict our discussions to values of  $\Delta\mu_{\text{Cl}}$  in  $[-0.94, -0.35]$  eV, where the  $c(2 \times 2)$  is stable within the calculated configurations.

### 3.2.1. Exchange-Correlation Energy and Solvation Effects

In order to obtain a measure of the effect related to the exchange-correlation functional  $E_{\text{xc}}[n]$ , we compare  $E_{\text{ads}}(1/2, 0)$  for  $c(2 \times 2)$ -Cl adlayer with respect to  $E_{\text{ads}}(1/2, 0)$  for  $c(2\sqrt{2} \times \sqrt{2})R45^\circ$ -Cl adlayer within the local-density approximation (LDA), general-gradient approximation (GGA) for PBE [84] and revPBE [245], and nonlocal van Waals (vdW) functional for vdW-DF [98, 100, 246]. A continuum solvation model, which models solvent as a dielectric material, have been applied by using the self-consistent solvation (SCCS) method [123].

DFT calculations have been performed within a  $c(2 \times 2)$  and  $p(\sqrt{2} \times 2\sqrt{2})$  SUC for  $c(2 \times 2)$

and  $c(2\sqrt{2} \times \sqrt{2})R45^\circ$  Cl adlayers, respectively. The computational parameters described in Appendix A.6 have been applied. Atoms are represented by pseudopotentials from PSLibrary [247], the chosen pseudopotentials have been generated with the same (or a close) functional. Regarding the continuum solvation calculations, the parameterization fit03+ $\beta$  [123, 248] has been employed.

From Tab. 3.1  $\Delta E$  amounts approximately to  $-0.01$  eV independently of the exchange-correlation functional. Therefore, a shift of the value of  $\mu_{\text{Cl}}$  is expected for Fig. 3.3 if a exchange-correlation functional from Tab. 3.1 is chosen.

Table 3.1.: Energy difference  $\Delta E$  of  $E_{\text{ads}}(1/2, 0)$  for  $c(2 \times 2)$ -Cl adlayer relative to the value for  $c(2\sqrt{2} \times \sqrt{2})R45^\circ$ -Cl adlayer using different exchange-correlation energy functionals.  $\Delta E$  has been calculated using PBE [84] and the self-consistent solvation (SCCS) method [123]. The parameterization fit03+ $\beta$  [123, 248] has been used for the continuum solvation calculations. Each system has been fully relaxed using the corresponding lattice constant  $c$ .

	Functional				Method
	LDA	GGA		GGA+NL	
	LDA [73]	PBE [84]	revPBE [245]	vdW-DF [98, 100, 246]	
$c$ (Å)	4.065 4.053 [104]	4.156 4.159 [249]	4.204 4.191 [250]	4.236 4.249 [104]	
$E_{\text{ads}}(1/2, 0)$ (eV) $c(2 \times 2)$	-0.72	-0.54	-0.44	-0.57	
$\Delta E$ (meV)	-8	-9	-8	-7	-8

### 3.3. Br Adlayer on Au(001)

In  $\text{Br}^-$  containing electrolyte the lifting of the hex-reconstruction and the formation of the  $(1 \times 1)$  phase has been reported to occur at  $-0.15$  V<sub>SCE</sub> [251]. Two ordered bromide adlayer have been found on the unreconstructed Au(100)- $(1 \times 1)$  surface. A  $c(\sqrt{2} \times 2\sqrt{2})R45^\circ$ -Br adlayer with coverage  $\Theta = 0.5$  has been reported by using STM [243] as well as in SXS experiments [251, 252]. Cuesta and Kolb have observed the  $c(\sqrt{2} \times 2\sqrt{2})R45^\circ$ -Br structure from 0.10 to 0.48 V<sub>SCE</sub> [243]. A incommensurate phase  $c(\sqrt{2} \times p)R45^\circ$  is formed at more positive potentials ( $\geq 0.48$  V<sub>SCE</sub>), in which the coverage increases from  $\Theta = 0.5$  to  $\Theta = 0.57$  [243, 252].

The equilibrium bromide coverage and the Br adsorption structure as a function of  $\Delta\mu_{\text{Br}}$  have been investigated. DFT calculations for Br structures on Au(001)- $(1 \times 1)$  have been carried out with coverage  $\Theta$  ranging from 0.063 to 0.58. As in Sec. 3.2  $c(2 \times 2)$ -Br adlayer surfaces with 1, 2 and 6 Br vacancies have been calculated within a  $p(6 \times 6)$  SUC,

corresponding to Br coverage  $\Theta = 0.47, 0.44$  and  $0.33$ . Additionally,  $c(\sqrt{2} \times 2\sqrt{2})R45^\circ$ -Br adlayer with 1, 2 and 4 Br vacancies have been calculated within a  $c(8 \times 8)$  SUC, corresponding to  $\Theta = 0.47, 0.44$  and  $0.38$ . The latter Br structure with  $\Theta = 0.38$  is depicted in Fig. 3.4 (b). A Br adlayer with  $\Theta = 0.58$ , which is shown in Fig. 3.4 (c), has been calculated within a  $p(12\sqrt{2} \times \sqrt{2})$  SUC.

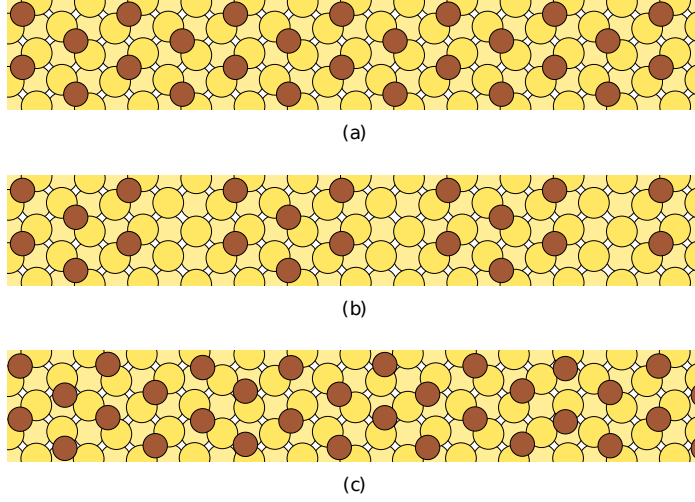


Figure 3.4.: Atomic structures of the Br/Au(001) interface. (a)  $c(\sqrt{2} \times 2\sqrt{2})R45^\circ$ -Br adlayer at  $\Theta = 0.5$  simulated in a  $p(2\sqrt{2} \times \sqrt{2})$  SUC, (b)  $p(4\sqrt{2} \times \sqrt{2})R45^\circ$ -Br with  $\Theta = 0.38$  simulated in a  $c(8 \times 8)$  SUC, (c) Br adlayer with  $\Theta = 0.58$  simulated in a  $p(12\sqrt{2} \times \sqrt{2})$  SUC.

Following Eq. (3.32), the stability of different Br adsorption structures is compared with respect to the clean Au(001) surface by

$$E_{\text{ads}}(\Theta, \Delta\mu_{\text{Br}}) = \left[ E_0(m, N_{\text{site}}) - E_{\text{clean}}(N_{\text{site}}) - m(E_{\text{Br}_2}/2 + \Delta\mu_{\text{Br}}) \right] \frac{1}{N_{\text{site}}}. \quad (3.33)$$

Fig. 3.5 shows  $E_{\text{ads}}(\Theta, \Delta\mu_{\text{Br}})$  as a function of  $\Delta\mu_{\text{Br}}$ . The adsorption energy corresponding to the equilibrium coverage is given by the lower envelope of the curves. Considering the clean Au(001)-hex surface, the Br covered Au(001) surfaces are cut-off at about  $-0.99$  eV.

The energy difference between  $E_{\text{ads}}$  for  $c(2 \times 2)$ -Br and  $E_{\text{ads}}$  for  $c(\sqrt{2} \times 2\sqrt{2})R45^\circ$ -Br adlayer is less than 5 meV, which is below the accuracy of the calculated DFT adsorption energies. Therefore, both Br adlayers are considered to be degenerate. Both structures stay stable for values of  $\mu_{\text{Br}}$  from  $-0.78$  to  $-0.15$  eV as shown in Fig. 3.5. Interestingly, Bertel and Netzer [253] have inferred from LEED patterns a  $c(2 \times 2)$ -Br structure at low temperature (180 K) and room temperature. If the  $\text{Br}_2$  dosing is continued, the authors observed a transformation of  $c(2 \times 2)$ -Br into  $c(\sqrt{2} \times 2\sqrt{2})R45^\circ$ -Br, which occurs via an intermediate structure identified as  $(\sqrt{2} \times 4\sqrt{2})R45^\circ$ -Br [253]. In the electrochemical environment at  $T_{\text{room}}$  only the  $c(\sqrt{2} \times p)R45^\circ$ -Br for  $p \leq 2\sqrt{2}$  has been observed [243, 251, 252]. The presence of water molecules and cations in the DFT calculations could be decisive factor to determine which of both structure is more stable.

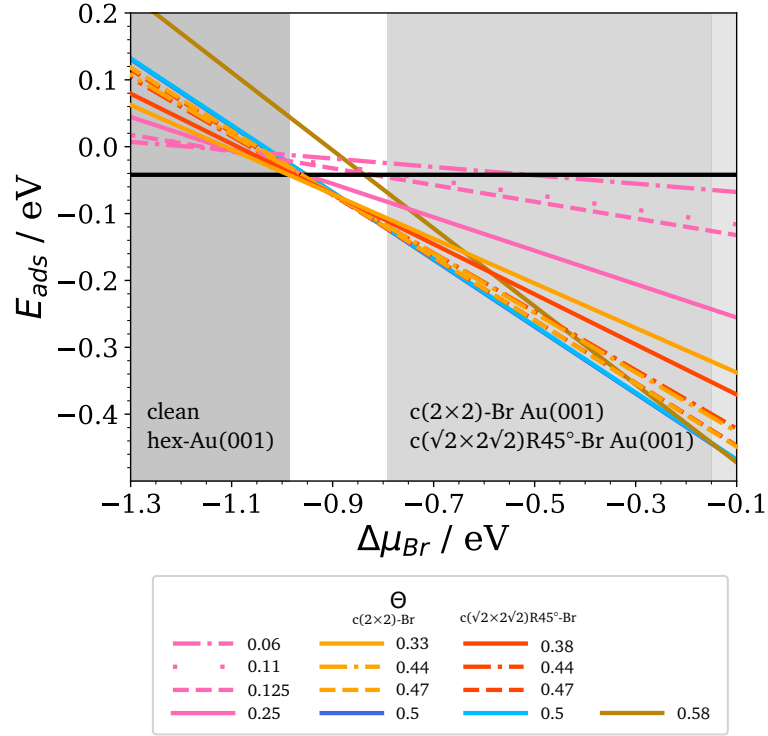


Figure 3.5.: Adsorption energy per  $N_{\text{site}}$   $E_{\text{ads}}$  at given values of  $\Theta$  as a function of  $\Delta\mu_{\text{Br}}$ .

For values of  $\mu_{\text{Br}} \geq -0.15$  eV a  $c(\sqrt{2} \times p)\text{R}45^\circ\text{-Br}$  with  $\Theta > 0.5$  becomes stable. The calculated structure (Fig. 3.4 (c)) has a coverage of about 0.58. It should be noted that some Br adatoms are located close to the hollow site due to compression in the  $[100]$  direction of the substrate. The next nearest-neighbor separation ranges from 3.80 to 4.32 Å, while at  $\Theta = 0.5$  the corresponding separation amounts to 4.64 Å.

Among those calculated structures, for value of  $\mu_{\text{Br}}$  below  $\sim -0.80$  eV a  $c(2 \times 2)\text{-Br}$  and  $c(\sqrt{2} \times 2\sqrt{2})\text{R}45^\circ\text{-Br}$  adlayer with vacancies become stable, but only for a small range of  $\Delta\mu_{\text{Br}}$ . In contrast to  $\text{Cl}/\text{Au}(001)$ , the formation energy of straight vacancy chains are smaller *e.g.* 4 meV per vacancy for 6  $\text{Vac}_{\text{Br}}$ -chain and 17 meV for 6  $\text{Vac}_{\text{Cl}}$ -chain [229]. In the electrochemical environment at  $T_{\text{room}}$  the experiments in Ref. [251] yield a smooth variation of the Br coverage as a function of sample potential. We expect that the smoothness of  $E_{\text{ads}}$  can be recovered by assessing larger number of configurations.

### 3.4. I Adlayer on Au(001)

The potential-dependent ordered halide adlayer for the Au(001) substrate in  $\Gamma^-$  containing electrolyte has been investigated by means of in situ STM by Gao *et al.* [254]. They found out that the lifting of the hex-reconstruction occurs at  $-0.6 \text{ V}_{\text{SCE}}$ . A compressible incommensurate  $c(p \times 2\sqrt{2})\text{R}45^\circ\text{-I}$  structure with  $\Theta \approx 0.46\text{--}0.49$  as well as a commensurate  $c(\sqrt{2} \times 2\sqrt{2})\text{R}45^\circ\text{-I}$  with  $\Theta = 0.5$  have been observed [254].

To address the equilibrium iodine coverage and the I adsorption structure as a function of  $\Delta\mu_{\text{I}}$ , DFT calculations have been performed for several I adlayer configurations with coverage ranging from 0.063 to 0.5. Besides the calculated structures with  $\Theta \leq 0.5$  in Sec. 3.3, here an I adlayer with  $\Theta = 0.46$  has been calculated within a  $p(12\sqrt{2} \times 2\sqrt{2})$  SUC as shown in Fig. 3.6 (c).

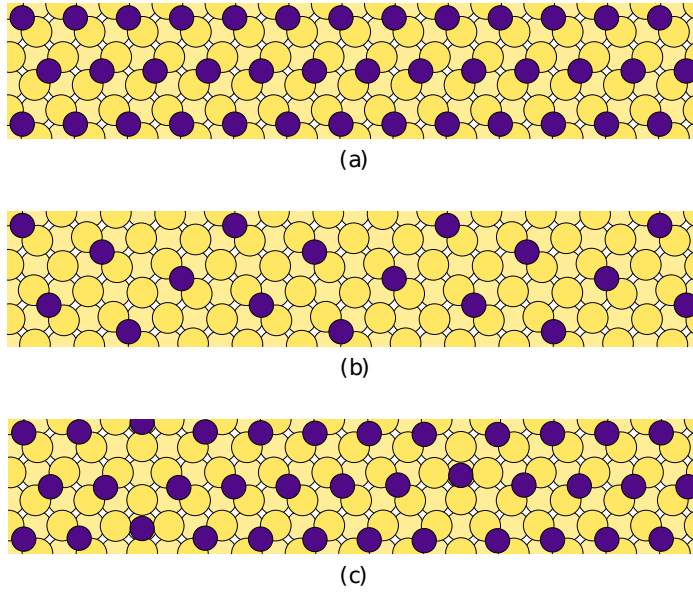


Figure 3.6.: Atomic structures of the I/Au(001) interface. (a)  $c(\sqrt{2} \times 2\sqrt{2})\text{R}45^\circ\text{-I}$  adlayer at  $\Theta = 0.5$  simulated in a  $p(2\sqrt{2} \times \sqrt{2})$  SUC, (b)  $c(4 \times 2)\text{-I}$  with  $\Theta = 0.25$  simulated in a  $p(4 \times 2)$  SUC (configuration from Ref. [255]), (c) I adlayer with  $\Theta = 0.46$  simulated in a  $p(12\sqrt{2} \times 2\sqrt{2})$  SUC.

Following Eq. (3.32), the stability of different I adsorption structures is compared with respect to the clean Au(001) surface by

$$E_{\text{ads}}(\Theta, \Delta\mu_{\text{Br}}) = \left[ E_0(m, N_{\text{site}}) - E_{\text{clean}}(N_{\text{site}}) - m(E_{\text{I,bulk}} + \Delta\mu_{\text{I}}) \right] \frac{1}{N_{\text{site}}}. \quad (3.34)$$

In this equation, the bulk energy of  $\text{I}_2$  is considered as the natural state of  $\text{I}_2$  is solid rather than gas.

Fig. 3.7 shows  $E_{\text{ads}}(\Theta, \Delta\mu_{\text{I}})$  as a function of  $\Delta\mu_{\text{I}}$ . The adsorption energy corresponding to the equilibrium coverage is given by the lower envelope of the curves. Considering the clean Au(001)-hex surface, the I covered Au(001) surfaces are cut-off at about  $-0.78 \text{ eV}$ .

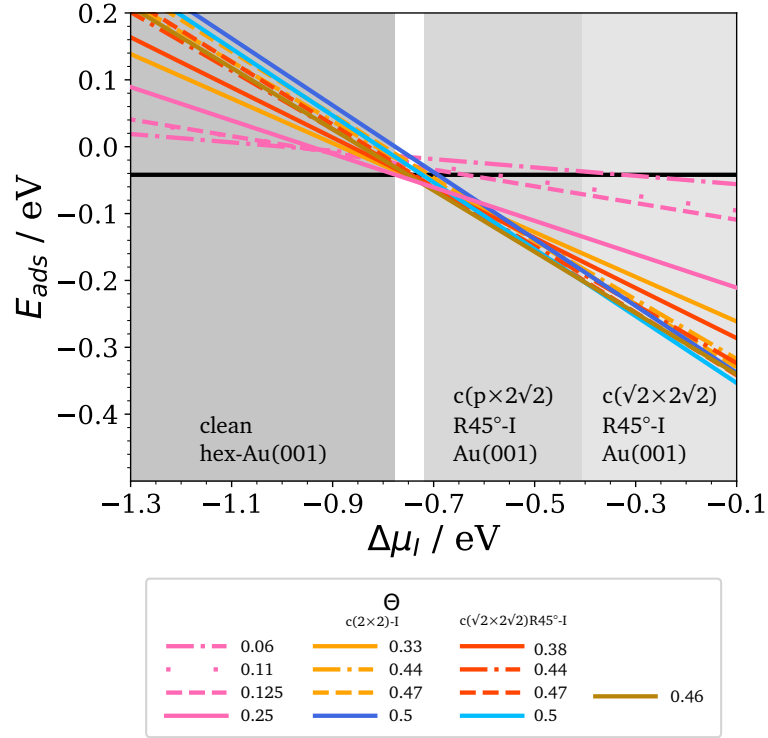


Figure 3.7.: Adsorption energy per  $N_{\text{site}}$   $E_{\text{ads}}$  at given values of  $\Theta$  as a function of  $\Delta\mu_I$ .

Among the calculated structures for low coverage, only the  $c(4 \times 2)$  with  $\Theta = 0.25$  appears stable for  $\Delta\mu_I$  from  $-0.78$  to  $-0.72$  eV, see Fig. 3.7 and the I adlayer in Fig. 3.6 (b). It should be pointed out that this structure has not been observed either in electrochemical environment or in UHV conditions. In fact, a  $c(6 \times 2)$ -I with  $\Theta \approx 0.33$  has been reported from LEED experiments at low temperature under certain adsorption/cooling conditions [256], this structure has not been here considered. For values of  $\mu_I$  from  $-0.72$  to  $-0.41$  eV a  $c(p \times 2\sqrt{2})R45^\circ$  with  $\Theta = 0.46$  becomes stable. In Ref. [254, 256] a similar structure model has been proposed, in which I adatoms are located at top and hollow sites, and at positions in between both sites. The authors pointed out that the different adsorption sites of I adatoms result in a long range periodic modulation [254, 256]. Conversely, in Fig. 3.6 (c) I adatoms occupy bridge or hollow sites of the substrate, which not reproduce the observed modulation as the difference of  $z$  coordinate between hollow and bridge site are smaller. For  $\mu_I > -0.41$  eV the  $c(\sqrt{2} \times 2\sqrt{2})R45^\circ$  with  $\Theta = 0.5$  is found to be stable. In this case, the formation of  $c(\sqrt{2} \times 2\sqrt{2})R45^\circ$  adlayer rather than a  $c(2 \times 2)$  could be attributed mainly to the strongly repulsive interactions among the adsorbed I adatoms.

The experimentally observed  $c(p\sqrt{2} \times 2\sqrt{2})R45^\circ$ -I adlayers with  $\Theta \leq 0.5$  have been found to be stable within this approach. But, further studies would be needed to assess low coverage configurations such as the  $c(6 \times 2)$ -I adlayer [256] and I adlayer reconstruction with high coverage  $\Theta > 0.5$ . Moreover, further structures as shown in Fig. 3.6 (c) are required to investigate the observed topographical corrugation in STM images of I adlayers [254, 256].

# 4.

## Self-Diffusion of Au Adatom on Cl Covered Au(001) Surface

On the nanoscale the diffusion of atoms and molecules along surfaces and interfaces plays a crucial role in electrodeposition or dissolution. The transport of this species can be tuned by the presence of a layer of other adsorbates on the surface [32, 257]. Especially, in the case of a high coverage of adsorbates the attraction or repulsion between each other modifies the migration paths, and hence the energy barriers of the diffusing specie. Experiments carried out under UHV conditions or at the electrochemical interface in conjunction with theoretical studies [48, 59, 157, 258] have revealed the complexity of this situation, particularly the chemical nature of the adsorbates can entirely determine the surface dynamic behavior of a adatom diffusion [48].

In the present Chapter Density Functional Theory (DFT) studies were performed to investigate the local binding topology of the Au adatom on a fully Cl covered Au(001) surface at a chlorine coverage  $\Theta = 1/2$ , as well as, the relevant diffusion mechanisms. In addition, the diffusion energy barriers have been compared with the corresponding in systems containing a chlorine vacancy and with an additional adsorbed chlorine adatom in the vicinity of the Au adatom. DFT results from Sec. 4.1, 4.2 and 4.3 have been published in Ref. [158].

### 4.1. Au–Cl Complexes on Au(001)

Although our primary interest and focus are on the atomistic description of the self-diffusion of a Au adatom on a Cl covered Au(001) surface at high coverage, it is instructive to climb up the ladder of complexity starting with Au adatom at low Cl coverage. Therefore, calculations have been carried through for Au adatom,  $\text{Au}_{\text{ad}}\text{Cl}$ ,  $\text{Au}_{\text{ad}}\text{Cl}_2$  and  $\text{Au}_{\text{ad}}\text{Cl}_4$  complexes on clean  $(1 \times 1)$ -Au(001) surface by means of DFT, our results are compared to the literature.

The adsorption configurations of Au–Cl complexes adsorbed on clean  $(1 \times 1)$ -Au(001) are listed in Appendix A.1. The lowest energy configurations for a given number of Cl atoms bonded to the Au adatom are selected from Appendix A.1. The  $\text{Au}_{\text{ad}}\text{Cl}$  complex adsorbs at the hollow site of the substrate, while the Cl atom bonds at the top of the Au adatom [59, 60]. In case of the  $\text{Au}_{\text{ad}}\text{Cl}_2$  complex, the Au adatom adsorbs at bridge site of the substrate with the Cl adatoms close to Au bridge positions [60]. The  $\text{Au}_{\text{ad}}\text{Cl}_4$  complex adsorbs at the hollow site of the substrate with Cl atoms occupying the Au top positions. Fig. 4.1 displays

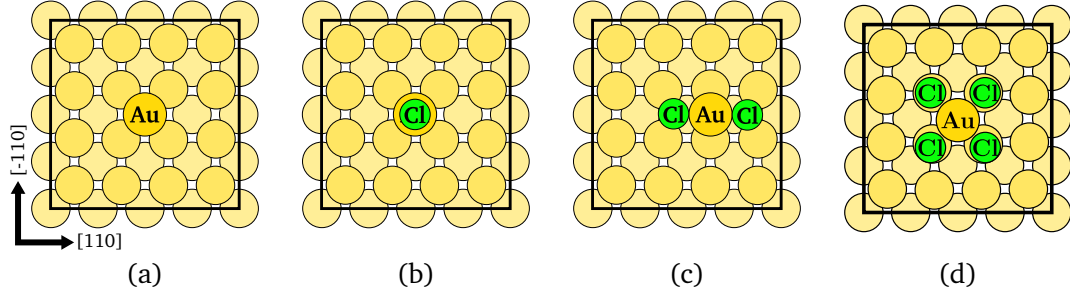


Figure 4.1.: The lowest calculated energy configurations for Au–Cl complexes adsorbed on the clean unreconstructed Au(001) surface. The black squares represent the  $p(4 \times 4)$  surface unit cell used in the calculation. Details regarding the computation are to be found in Appendix A.1.

the lowest energy configurations for Au–Cl complexes.

#### 4.1.1. Stability of Au–Cl Complexes

As a very first step, we discuss the stability of Au–Cl complexes as a function of Cl chemical potential. In order to obtain such dependency, a Cl reservoir is assumed with the  $\mu_{\text{Cl}}$ . The stable complexes are selected by minimizing

$$E_{\text{diff},1}(n_{\text{Cl}}, \mu_{\text{Cl}}) = E_0(n_{\text{Cl}}, N_{\text{site}}) - E_0(0, N_{\text{site}}) - n_{\text{Cl}}(E_{\text{Cl}_2}/2 + \mu_{\text{Cl}}), \quad (4.1)$$

with respect  $n_{\text{Cl}}$ , which denotes the number of Cl atoms bonded to the Au adatom.  $N_{\text{site}}$  is the number of Au atoms per layer.  $E_0(n_{\text{Cl}}, N_{\text{site}})$  is the total energy of the system Au–Cl complex with  $n_{\text{Cl}}$  atoms on Au(001), see Fig. 4.1.  $E_0(0, N_{\text{site}})$  is chosen as a reference energy and corresponds to a single Au adsorbed on Au(001) as shown in Fig. 4.1 (a).

Fig. 4.2 shows  $E_{\text{diff},1}$  as a function of  $\mu_{\text{Cl}}$  for  $n_{\text{Cl}} = 0, 1, 2$  and 4. At equilibrium state between the Cl adatoms and the reservoir the value of  $\mu_{\text{Cl}}$  depends on the coverage *e.g.* at  $\Theta = 1/16$   $\mu_{\text{Cl}}$  amounts to -1.21 eV. For the  $\text{Au}_{\text{ad}}\text{Cl}$  complex  $E_{\text{diff},1}$  at  $\mu_{\text{Cl}} = -1.21$  eV amounts to only -0.01 eV. The negative sign suggests that there is an energy gain if a Cl atom is adsorbed on the top site of the  $\text{Au}_{\text{ad}}$  rather than on the terrace, but the absolute value is below the accuracy of our DFT calculations. At  $\mu_{\text{Cl}} = -1.21$  eV  $E_{\text{diff},1}$  amounts to +0.14 eV (0.13 eV [60]) and +1.57 eV for  $\text{Au}_{\text{ad}}\text{Cl}_2$  and  $\text{Au}_{\text{ad}}\text{Cl}_4$ , respectively.

From Chapter 3 the  $c(2 \times 2)$ -Cl adlayer at  $\Theta = 1/2$  is stable for the values of  $\mu_{\text{Cl}}$  from -0.94 to -0.35 eV. Along this range we observe from Fig. 4.2 that the  $\text{Au}_{\text{ad}}\text{Cl}_2$  and  $\text{Au}_{\text{ad}}\text{Cl}_4$  complexes are stable. In fact,  $\text{Au}_{\text{ad}}\text{Cl}_2$  complex remains stable from -0.94 to -0.50 eV approximately, which is equivalent to 75% of the range of  $c(2 \times 2)$ -Cl adlayer. Therefore, in Sec. 4.1.2 we focus on the diffusion of  $\text{Au}_{\text{ad}}\text{Cl}_2$  complex. We compare the activation energy barriers of  $\text{Au}_{\text{ad}}\text{Cl}_2$  with the diffusion barrier of Au and  $\text{Au}_{\text{ad}}\text{Cl}$ .



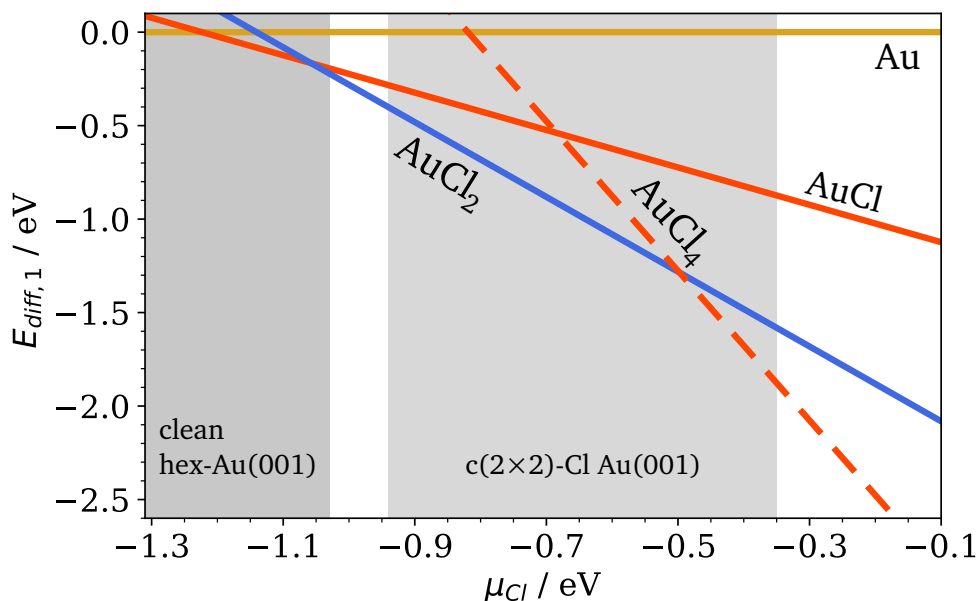


Figure 4.2.:  $E_{\text{diff},1}$  is plotted as a function of  $\mu_{\text{Cl}}$  for Au-Cl complexes depicted in Fig. 4.1. Grey regions denote the stability range of the clean hex-Au(001) and  $c(2 \times 2)$ -Cl covered Au(001) with  $\Theta = 1/2$ .

#### 4.1.2. Diffusion of Au-Cl Complexes

##### Au<sub>ad</sub>

The diffusion of a single Au adatom on clean unreconstructed Au(001) surface has been investigated in detail by DFT [59, 60, 186, 194, 259]. According to these studies the Au adatom diffuses via exchange mechanism. In comparison to Cu/Cu(001) and Ag/Ag(001), which diffuse via hopping over the bridge site, the tensile surface stress lowers the energy of the transition state for the exchange mechanism on Au(001) [259]. Results from the literature are summarized in Tab. 4.1.

##### Au<sub>ad</sub>Cl

Mesgar et al. [59, 60] investigated the diffusion of Au<sub>ad</sub>Cl complex on clean unreconstructed Au(001) by step-wise movement of the adatom along the pathways [59, 60]. They found that exchange mechanism is favorable for Au<sub>ad</sub>Cl complex with an energy barrier of 0.34 eV, while the activation energy via hopping amounts to 0.5 eV [59, 60].

##### Au<sub>ad</sub>Cl<sub>2</sub>

The MEP for the lowest energy diffusion path for Au<sub>ad</sub>Cl<sub>2</sub> complex which we have identified is shown in Fig. 4.3 and atomic geometries are shown in Fig. 4.4. Along this path the Au<sub>ad</sub>Cl<sub>2</sub> complex performs a rotation and a translation at the same time. The diffusion barrier is calculated to be 0.07 eV. Along the MEP a local minimum is encountered as depicted in

Fig. 4.3 and denoted by LM, which is energetically unstable by only 0.05 eV with respect the start configuration. Mesgar [60] calculated diffusion paths in which the  $\text{Au}_{\text{ad}}\text{Cl}_2$  complex moves toward the perpendicular and collinear direction of the complex, obtaining energy barriers about of 0.15 eV and 0.18 eV respectively [60].

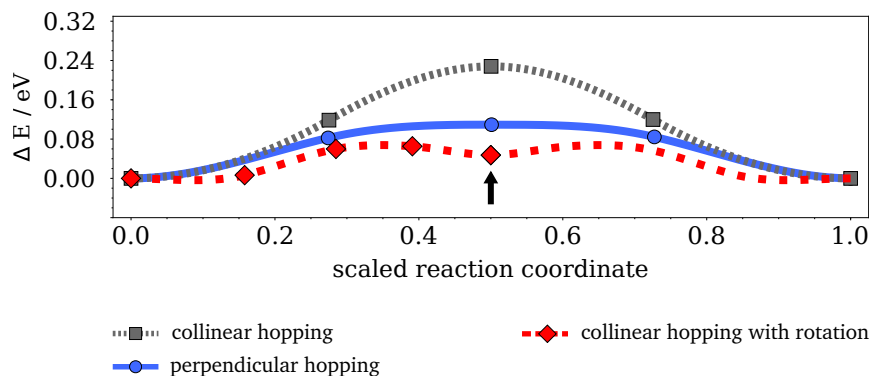


Figure 4.3.: Variation of energy along the diffusion, with the adsorption minimum (Fig. 4.1 (c)) taken as reference. Diffusion along  $[110]$  Calculations have been performed in a  $p(4 \times 4)$  SUC, slabs have been modeled by 4 Au layers.

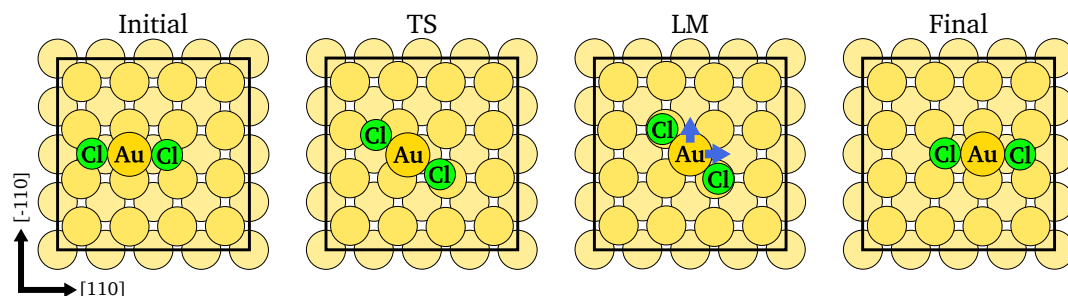


Figure 4.4.: Atomic geometries of local minimum (LM) and transition state (TS) configurations along the MEP with the lowest energy barrier in Fig. 4.3. The  $\text{Au}_{\text{ad}}\text{Cl}_2$  can diffuse to any adsorption site. NEB calculations have been carried on with 4 layer slabs.

Among the Au–Cl complexes here considered, the  $\text{Au}_{\text{ad}}\text{Cl}_2$  is the most stable within the range of  $\mu_{\text{Cl}}$  of  $[-0.94, -0.50]$  eV and possesses the lowest energy barrier. The effect of adsorbate-adsorbate interactions on the diffusion of  $\text{Au}_{\text{ad}}$  will be accounted in Sec. 4.2, 4.3 and 4.4.

Table 4.1.: Comparison with theoretical studies of activation barriers  $E_{\text{act}}$  (eV) and variation of dipole moment  $\Delta \mu$  (eÅ) at transition state for  $\text{Au}$ ,  $\text{Au}_{\text{ad}}\text{Cl}$  and  $\text{Au}_{\text{ad}}\text{Cl}_2$  on clean  $(1 \times 1)\text{-Au}(001)$ .

Complex	Mechanism	$E_{\text{act}}$ (eV)		$\Delta \mu$ (eÅ)	
		This work	Ref.	This work	Ref.
$\text{Au}_{\text{ad}}$	Hopping	0.62	0.58 [259]	0.015	0.004 [60]
			0.86 [194]		
	Exchange	0.27	0.70 [186]	-0.08	-0.11 [60]
			0.40 [259]		
$\text{Au}_{\text{ad}}\text{Cl}$	Hopping	-	0.50 [59, 60]	-	-0.11 [60]
	Exchange	-	0.34 [59, 60]	-	+0.41 [60]
$\text{Au}_{\text{ad}}\text{Cl}_2$	Perpendicular hopping	0.11	0.15	-0.07	-0.10 [60]
	Collinear hopping	0.23	0.18	-0.05	-0.17 [60]
	Collinear hopping with rotation	0.07	-	-0.12	-

## 4.2. Self-Diffusion of $\text{Au}_{\text{ad}}$ on Cl Covered $\text{Au}(001)$ at $\Theta = 1/2$

So far, however, little is known about the detailed diffusion mechanisms of a Au adatom embedded in a halide coadsorbed structure. Therefore, the overall goal of the presented work is to investigate the chlorine chemical bonding near the Au adatom, as well as, the diffusion mechanisms. Special attention will be focused on the variation of dipole moment  $\Delta \mu$  along the diffusion paths, because according Giesen *et al.* [47] positive  $\Delta \mu$  would imply a decrease on the energy barrier within the sample voltage. Sections 4.2.1 and 4.2.2 will deal with a  $(1 \times 1)\text{-Au}(001)$  surface that is entirely covered by a Cl adlayer. Two experimentally observed adlayer reconstructions,  $c(2 \times 2)$  [38] and  $c(2\sqrt{2} \times \sqrt{2})$  [35] Cl adlayers, have been considered.

Adsorption configurations chosen by chemical intuition have been ionically relaxed. Beside relaxation, a set of local configurations have been investigated by BOMD and metadynamic-BOMD, see Appendix A.3. The atomic configurations and energies of  $\text{Au}_{\text{ad}}$  adsorbed on Cl covered surfaces with  $\Theta = 1/2$  here considered are listed in Appendix A.2, which has been published in the Supplementary Material of Ref. [158].

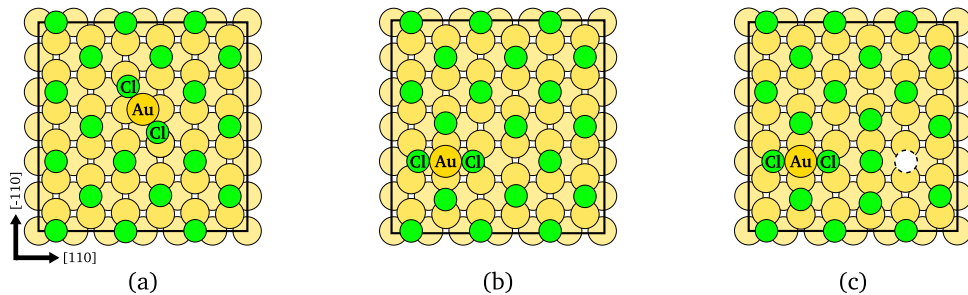


Figure 4.5.: Selected adsorption configurations of  $\text{Au}_{\text{ad}}$  on  $c(2 \times 2)$ -Cl Au(001) surface. (a) Lowest energy configuration. Energy difference  $\Delta E$  with respect to structure (a) amounts to: (b)  $\Delta E = 0.37$  eV, (c)  $\Delta E = 1.15$  eV. Dotted circle in (c) highlights the displacement of a Cl adatom from the  $c(2 \times 2)$  sublattice. The black squares represent the  $p(6 \times 6)$  surface unit cell used in the calculation.

#### 4.2.1. Diffusion of $\text{Au}_{\text{ad}}$ on $c(2 \times 2)$ -Cl Au(001)

DFT calculations for  $\text{Au}_{\text{ad}}$  adsorbed on the  $c(2 \times 2)$ -Cl Au(001) surface, see Appendix A.2, yield the most energetically favorable structure as shown in Fig. 4.5 (a). The Au adatom is adsorbed at bridge site of the surface, and binds to two Cl adatoms. The  $\text{Au}_{\text{ad}}\text{-Cl}$  bond length is about 2.31 Å on clean and  $c(2 \times 2)$ -Cl Au(001) surfaces, while the optimized bond length for the neutral and ionic  $\text{Au}_{\text{ad}}\text{Cl}_2$  molecule in vacuum [260] is 2.18 and 2.28 Å respectively. The formed  $\text{Au}_{\text{ad}}\text{Cl}_2$  complex is arranged along the [100] (or [010]) direction of the substrate. If the  $\text{Au}_{\text{ad}}\text{Cl}_2$  complex lies parallel to [110] direction of the substrate as depicted in Fig. 4.5 (b), the local minimum configuration is 0.37 eV more unstable than the lowest total energy configuration. The energy difference can increase significantly, if the distance between Cl adatoms is smaller than the lattice constant. For example, the energy difference between structure from Fig. 4.5 (c) (analog to configuration in Ref. [60]) and the lowest total energy configuration amounts to 1.15 eV.

The discussion regarding the diffusion of  $\text{Au}_{\text{ad}}$  will start with a process that involve the dissociation of  $\text{Au}_{\text{ad}}\text{Cl}_2$  complex to  $\text{Au}_{\text{ad}}\text{Cl}$  complex and Cl adatom, continue with the rotation of the  $\text{Au}_{\text{ad}}\text{Cl}_2$  complex and the neighboring Cl adatoms. Additionally, two further diffusion paths will be discussed. One is characterized by the formation of a  $\text{Au}_{\text{ad}}\text{Cl}_3$ -like structure, and the last involves an exchange process between the  $\text{Au}_{\text{ad}}$  and a Au atom of substrate.

#### Hopping via Hollow Site

The translation of  $\text{Au}_{\text{ad}}$  by  $a$  (nearest-neighbor distance) to an equivalent neighboring position preferentially proceeds via the MEP depicted in Fig. 4.6 with the corresponding atomic geometries depicted in Fig. 4.7. The activation barrier amounts to 0.44 eV in Fig. 4.6. The hopping via hollow site promotes only the  $[\bar{1}10]$  direction of diffusion, in which the dissociation and formation of  $\text{Au}_{\text{ad}}\text{Cl}_2$  complex occurs. Similarly, Mesgar proposed a diffusion path based on the transition of  $\text{Au}_{\text{ad}}\text{Cl}_2$  to  $\text{Au}_{\text{ad}}\text{Cl}$  with an energy barrier of 0.69 eV in Ref. [60].

There are two main differences between both diffusion paths. First of all,  $Au_{ad}Cl_2$  complexes are arranged differently in the initial configurations as shown in Fig. 4.5 (a) and (c). Secondly, the diffusion of  $Au_{ad}$  proceeds along the  $[110]$  direction of the substrate in Ref. [60], while in our path the  $Au_{ad}$  moves toward the  $[\bar{1}10]$  direction.

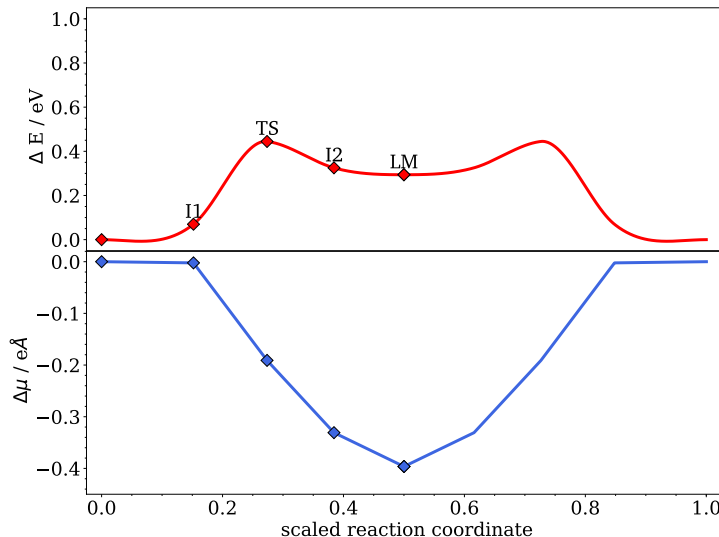


Figure 4.6.: Variation of energy  $\Delta E$  and dipole moment  $\Delta \mu$  along the diffusion path of a  $Au_{ad}$  via hollow site (see Fig. 4.7) in a fully covered  $c(2 \times 2)$ -Cl  $Au(001)$  surface. A Nudged Elastic Band (NEB) calculation has been carried out for the 4 layers  $Au$  slabs. Diamonds denote the calculated configurations, the red line is an interpolation of the energies along the path. Half of the path is derived from symmetry operations.

The migration of  $Au_{ad}$  starts with:

1. the diffusion to the next hollow site. During this step one of the Cl atoms from the complex raises up the top of  $Au_{ad}$ , see side-view of Fig. 4.7. At this point the system arrives to a local minimum (LM) configuration, which is less energy favorable by about 0.3 eV with respect to the initial configuration.
2. In the next half of the path the  $Au_{ad}$  diffuses from hollow site to the next bridge site. This part is identical to step 1 by mirror symmetry.

Concerning the dipole moment, the elevation of one Cl atom from the  $Au_{ad}Cl_2$  complex is correlated with the strong negative variation of dipole moment  $\Delta \mu$ , which is calculated with respect to the initial configuration. At the transition state (TS) the difference between the  $z$  coordinate of the elevated Cl relative to the  $z$  coordinate of a  $Cl_{ad}$  far from the complex amounts roughly to 1.2 Å and its  $\Delta \mu$  is -0.19 eÅ. Similarly, at the local minimum (LM) the difference between  $z$  coordinates amounts to 2.1 Å, which yields a more negative  $\Delta \mu$  -0.40 eÅ. Following the formula by Giesen *et al.* [47], a negative  $\Delta \mu$  at the transition state implies an increase in the energy barrier with the sample voltage.

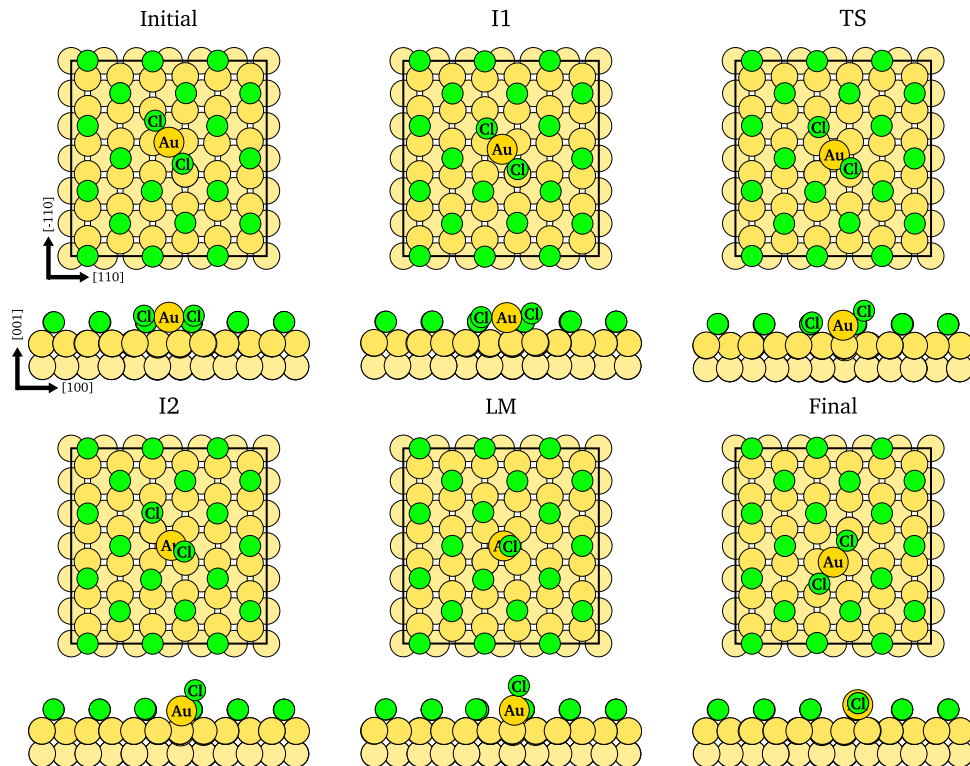


Figure 4.7.: Initial and final position for the diffusion of  $\text{Au}_{\text{ad}}$  on a completely  $c(2 \times 2)$ -Cl covered Au(001) surface as well as the intermediate configurations for the hopping via hollow. Along the path a local minimum is encountered, which is denoted as LM, and the transition states is denoted by TS. The remaining intermediate configurations along the path are denoted as I. The  $p(6 \times 6)$  surface unit cell used in the calculation is indicated by black squares. For sake of better visualization of the  $\text{Au}_{\text{ad}}$  diffusion some Cl atoms are not shown in the side-view representations.

### Rotation of $\text{Au}_{\text{ad}}\text{Cl}_2$ complex

In Ref. [48] Rahn *et al.* suggest two diffusion mechanisms for a  $\text{S}_{\text{ad}}$  on a halide covered Cu(100) surface. Here, of particular interest is the diffusion by rotation of  $\text{S}_{\text{ad}}$  and the halide coadsorbates. However, it is not directly applicable to our case due to the adsorption sites and the bonding between  $\text{Au}_{\text{ad}}$  and coadsorbates. In spirit of their work, a MEP of the rotation of the  $\text{Au}_{\text{ad}}\text{Cl}_2$  complex and neighboring Cl adatoms is depicted in Fig. 4.8 with the corresponding atomic geometries illustrated in Fig. 4.9. Along the reaction path two transition states are encountered, both amount to 0.52 eV. It should be noted that here the diffusion specie is the  $\text{Au}_{\text{ad}}\text{Cl}_2$  complex rather than the  $\text{Au}_{\text{ad}}$ . Additionally, the  $\text{Au}_{\text{ad}}\text{Cl}_2$  can diffuse from bridge site of the substrate to any symmetrically equivalent site.

In Fig. 4.9 the Cl atoms that participate in the diffusion path of  $\text{Au}_{\text{ad}}\text{Cl}_2$  are labeled with the numbers 1 and 2. We refer to them as *atom 1* and *atom 2*, which are initially separated

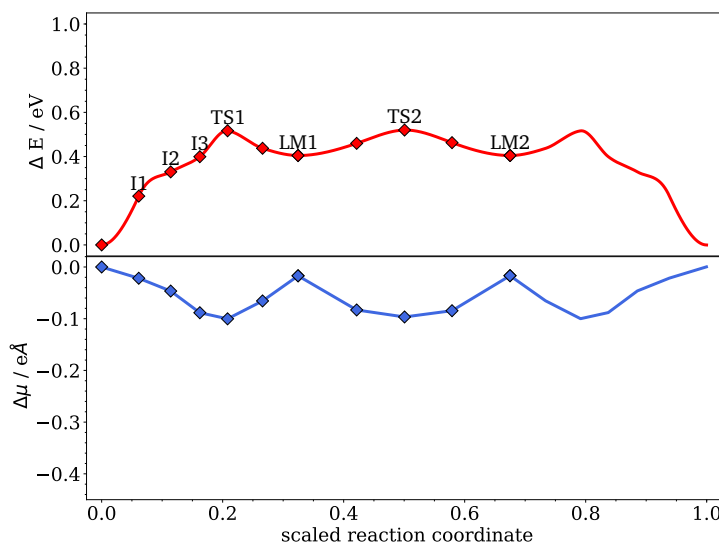


Figure 4.8.: Diffusion energy path of the  $Au_{ad}$  by rotation mechanism, see Fig. 4.9. Variation of energy  $\Delta E$  and dipole moment  $\Delta \mu$  along the diffusion path. The thickness of the Au slabs is 4 layers. Diamonds denote the calculated configurations.

by 4.08 Å ( $\approx$  lattice constant). The diffusion path proceeds as following:

1. the *atom 1* diffuses to next neighboring bridge site, this motion produces a slightly displacement of the  $Au_{ad}Cl_2$  complex and *atom 2*. Thus, the energy is increased by about 0.33 eV. See configurations I1 and I2 in Fig. 4.9, and the corresponding  $\Delta E$  in Fig. 4.8.
2. The *atom 2* moves toward the next bridge site, and arrives to a local minimum (LM1 in Fig. 4.9). The position of *atom 2* in TS1 is consistent with the transition state geometry of a single Cl adatom on Au(001) shown in Sec. 2.3.4. In LM1 structure the  $Au_{ad}Cl_2$  complex is slightly tilted with respect to the initial position. *Atoms 1* and *2* occupy energetically unfavorable positions, the separation between them is about 3.53 Å which is 20% larger than the nearest-neighbor distance. Therefore, LM1 configuration is energetically unfavorable by 0.40 eV with respect to the initial configuration.
3. The MEP between local minima (LM1 and LM2) corresponds solely to the diffusion of  $Au_{ad}Cl_2$  complex. It should be noted that LM1 and LM2 are equivalent by a symmetry operation (horizontal mirror). The corresponding energy barrier amounts to 0.12 eV with respect to LM1, this value is consistent with results for diffusion of single  $Au_{ad}Cl_2$  complex on Au(001) in Sec. 4.1.2. At TS2 configuration the  $Au_{ad}Cl_2$  complex is arranged along the  $[\bar{1}10]$  (or  $[110]$ ) direction of the substrate. Finally, *atoms 1* and *2* diffuse consecutively to next  $c(2 \times 2)$ -Cl sublattice sites.

In comparison to the previous path, here the motion of Cl adatoms is close to the surface, see side-view representations in Fig. 4.9. But, the  $Au_{ad}Cl_2$  complex as well as the surroundings Cl adatoms move along  $z$  direction up to 0.3 Å, which altogether contribute to the

dipole moment. The variation of the dipole moment at the both transition states amounts roughly to  $0.10 \text{ e}\text{\AA}$ .

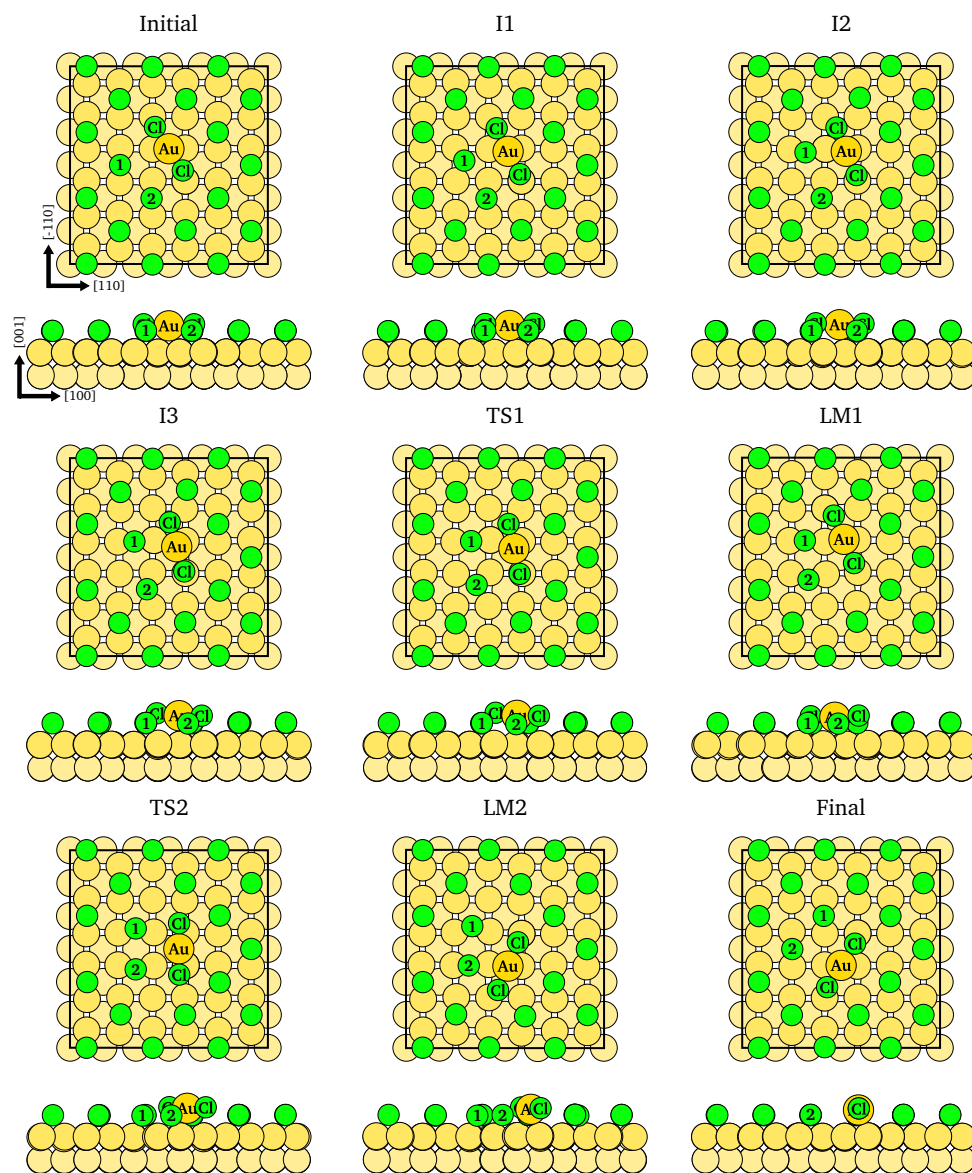


Figure 4.9.: Initial and final position for the diffusion of  $\text{Au}_{\text{ad}}$  on a completely  $c(2 \times 2)$ -Cl covered Au(001) surface as well as the intermediate configurations for the rotation mechanism. Along the paths two local minima (LM1 and LM2) and two transition states (TS1 and TS2) are encountered. The remaining intermediate configurations along the path are denoted as I. The thickness of the Au slab is 4 layers. The squares represent the  $p(6 \times 6)$  surface unit cell used in the calculation.



### Hopping via Bridge Site

The MEP for a translation of Au adatom from a bridge position via bridge site is depicted in Fig. 4.10 and atomic geometries are shown in Fig. 4.11. The diffusion specie in Fig. 4.11 is solely the Au adatom. The activation barrier for this path amounts to 0.81 eV, which is 45% larger than the hopping via hollow. However, this mechanism is still interesting since along the diffusion path a  $Au_{ad}Cl_3$ -like structure on the  $c(2 \times 2)$ -Cl Au(001) surface is identified.

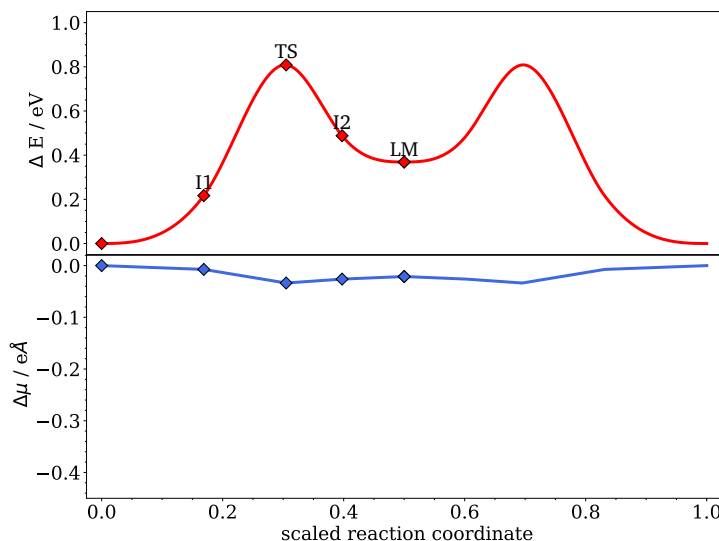


Figure 4.10.: Hopping of the  $Au_{ad}$  via bridge site. Variation of energy  $\Delta E$  and dipole moment  $\Delta \mu$  along the diffusion path.

In Fig. 4.11 the Cl adatoms that will bind to  $Au_{ad}$  are labeled with the numbers **1** and **2**. We refer to them as *atom 1* and *atom 2*. The  $Au_{ad}Cl_2$  complex is initially arranged along the  $[100]$  direction of the substrate in Fig. 4.11. The  $Au_{ad}$  moves toward bridge position in the  $[0\bar{1}0]$  direction of the substrate, while the Cl atoms of the complex and *atom 1* are slightly displaced from their initial positions. At the transition state a Y-shaped  $Au_{ad}Cl_3$ -like structure is formed. The  $Au_{ad}$  resides close to the bridge site of the substrate, thus the  $Au_{ad}Cl_2$  bonds are stretched from 2.31 Å to 2.63 and 2.37 Å and the separation between  $Au_{ad}$  and *atom 1* has reduced from 4.62 Å to 2.73 Å. Adsorption structures of  $Au_{ad}Cl_3$  adsorbed on clean  $(1 \times 1)$ -Au(001) surface have not been reported so far. But, Lee *et al.* have found no stable  $AuS_3$  complex on clean unreconstructed Au(111) by means of DFT [261].

After the energy barrier has been surmounted, the system arrives to an intermediate local minimum (LM) configuration as shown in Fig. 4.11. The  $Au_{ad}Cl_2$  complex is arranged along the  $[110]$  direction, which is energetically unfavorable by 0.37 eV with respect to the initial configuration. This increment of energy is attributed to the displacement of Cl adatoms, which are separated by 4.65 Å but initially the separation was about 5.65 Å ( $\approx 2$  times the nearest-neighbor distance). From this position the  $Au_{ad}$  can diffuse to any lowest energy position by symmetry operations.

Concerning the dipole moment,  $\Delta \mu$  at the transition state amounts to -0.03 eÅ. The

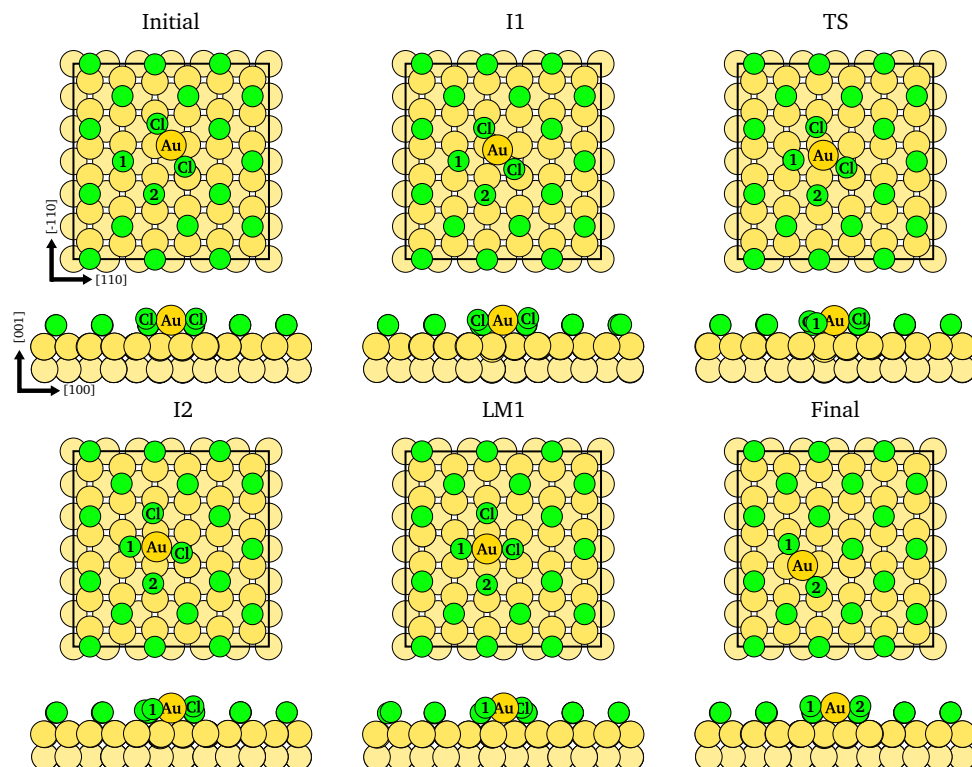


Figure 4.11.: The diffusion path of a  $\text{Au}_{\text{ad}}$  hopping from bridge site to the next lowest energy position. Along the paths a local minimum is encountered, which is denoted as LM, and the transition state is denoted as TS. The remaining intermediate configurations along the path are denoted as I.

absolute value of  $\Delta\mu$  is distinctly smaller than in the previous paths, this is ascribed to the small variations of  $z$  coordinates of Cl adatoms from  $-0.28$  to  $+0.14$  Å.

#### $\text{Au}_{\text{ad}}\text{-Au}$ Exchange

From the literature it is known that the diffusion of a single  $\text{Au}_{\text{ad}}$  on a clean Au(001) surface proceeds by exchange mechanism. In addition, further theoretical studies [194, 195, 262] concluded that the exchange process is also favorable for the diffusion of Au dimer on clean Au(001) surface. This feature of the  $\text{Au}_{\text{ad}}$  at clean Au(001) leads us to two questions: how could the  $\text{Au}_{\text{ad}}$  diffuse via exchange mechanism on a Cl covered Au(001) surface? and how large would be the corresponding activation barrier?

Keeping in mind that the  $\text{Au}_{\text{ad}}$  adsorbs at bridge site and binds to two Cl atoms, one possible exchange mechanism is between the  $\text{Au}_{\text{ad}}$  with the next nearest Au atom of the substrate. The corresponding MEP is shown in Fig. 4.12 and the atomic geometries are depicted in Fig. 4.13. The migration of the Au adatom is restricted to the [110] direction of the substrate, while on clean surface the  $\text{Au}_{\text{ad}}$  diffuses along the [100] (or [010]) direction. The activation barrier amounts to 0.89 eV, which is 66% larger than on clean Au(001) surface.

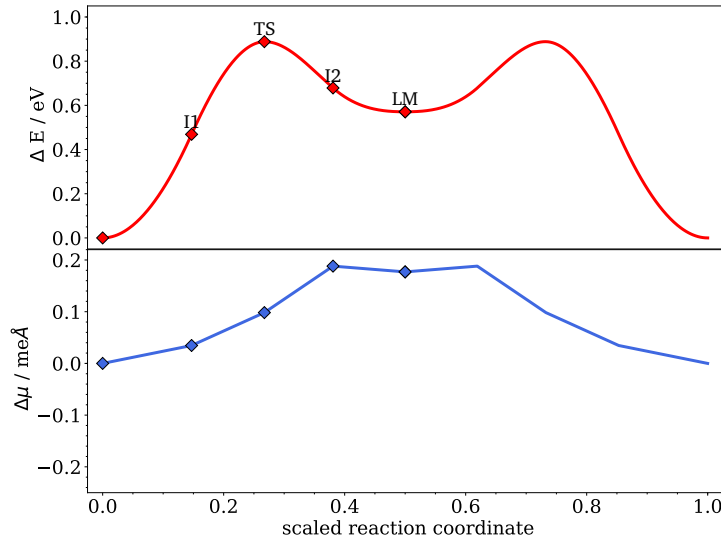


Figure 4.12.: Exchange mechanism with the  $Au_{ad}$  and a first layer Au atom. Variation of energy  $\Delta E$  and dipole moment  $\Delta \mu$  along the diffusion path.

The increment of energy can be ascribed to the atomic geometries along the path *e.g.* the orientation of Au dimer, the separation between Cl and Au atom from the substrate. In fact, the difference between  $z$  coordinate of the Au atoms amounts to  $1.1 \text{ \AA}$  at the transition state, while on clean  $(1 \times 1)\text{-Au}(001)$  the Au atoms are found at the same  $z$  coordinate. Furthermore, the  $Au_{ad}$  is only coordinated to one Au atom of the substrate, but on clean surface the  $Au_{ad}$  is fivefold coordinated at the transition state [259].

The variation of dipole moment at the transition state is  $+0.10 \text{ e\AA}$ , which means a decrease of the energy barrier with the sample potential. However, this path is rather unlikely due to its high energy barrier.

A further exchange mechanism between  $Au_{ad}$  and a Au atom of the substrate, which are separated from each other by about  $4 \text{ \AA}$ , along the  $[100]$  direction of the substrate leads to a similarly large energy barrier, therefore will not be further discussed.

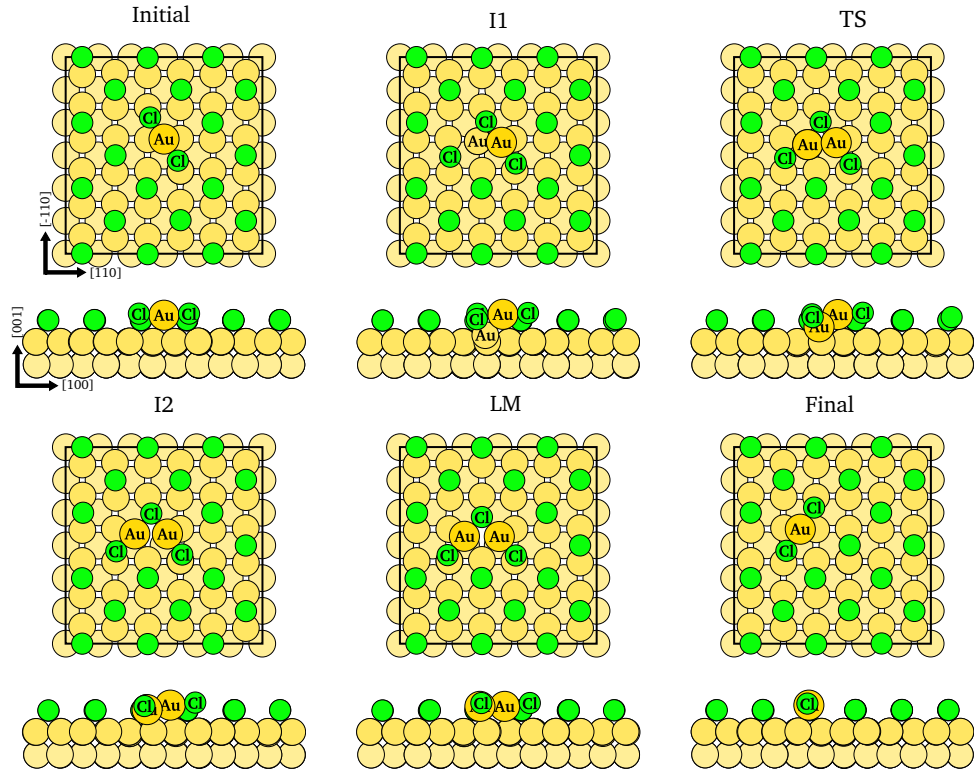


Figure 4.13.: The diffusion path of a  $\text{Au}_{\text{ad}}$  by an exchange process. The  $\text{Au}_{\text{ad}}$  exchanges with a first layer Au atom.

#### 4.2.2. Diffusion of $\text{Au}_{\text{ad}}$ on $c(\sqrt{2} \times 2\sqrt{2})R45^\circ\text{-Cl Au}(001)$

In Ref. [51] the diffusion of  $\text{Au}_{\text{ad}}$  on a  $c(\sqrt{2} \times 2\sqrt{2})R45^\circ$  Au(001) surface is expected to proceed from a hollow position to next neighbor via a bridge site. A low deformation of the Cl adlayer in the presence of Au adatom was assumed due to the spacing between neighboring Cl adatoms in the sublattice. In fact, Golks *et al.* conjectured that at the bridge site the variation of dipole moment could be positive. This argumentation would explain the potential dependence of  $\text{Au}_{\text{ad}}$  on Au(001) surface in the electrochemical environment.

To investigate the hypothesis proposed by Golks *et al.* [51], we have investigated the chemical bonding near  $\text{Au}_{\text{ad}}$  on  $c(\sqrt{2} \times 2\sqrt{2})R45^\circ\text{-Cl Au}(001)$  at  $\Theta = 1/2$ . The adsorption configurations of  $\text{Au}_{\text{ad}}$  adsorbed on Cl covered Au(001) are listed in Appendix A.2. Among the calculated structures Fig. 4.14 (a) depicts the lowest energy configuration. Similarly to the lowest energy position of  $\text{Au}_{\text{ad}}$  on  $c(2 \times 2)\text{-Cl Au}(001)$ , the  $\text{Au}_{\text{ad}}$  is located at bridge site of the substrate surface in Fig. 4.14 (a). This result does not match the hypothesis proposed in Ref. [51] based on the diffusion of  $\text{Au}_{\text{ad}}$  from a hollow position via a bridge site. In fact, if the  $\text{Au}_{\text{ad}}$  resides at hollow site, the adsorption configuration is energetically unfavorable by 0.37 eV with respect to the structure in Fig. 4.14 (a). These results will have interesting consequences on the self-diffusion of  $\text{Au}_{\text{ad}}$  on Cl covered surfaces.

In the lowest energy configuration the  $\text{Au}_{\text{ad}}\text{Cl}_2$  complex appears tilted with respect to

[110] (or  $[\bar{1}10]$ ) direction of the substrate. Regarding the interatomic distances, the  $Au_{ad}-Cl$  bond and  $Au_{ad}-Au_{substrate}$  amount to 2.31 and 2.88 Å in Fig. 4.14 (a), similar values have been obtained in the case of the  $c(2 \times 2)$ -Cl adlayer [158]. In the local minima configuration shown in Fig. 4.14 (b), which is energetically unfavorable by 0.08 eV, the  $Au_{ad}Cl_2$  complex is arranged along the [110] (or  $[\bar{1}10]$ ) direction with the  $Au_{ad}$  located close to the top site of the substrate. The  $Au-Cl$  bond remains unaltered, the  $Au_{ad}-Au_{substrate}$  distance amounts to 2.74 Å.

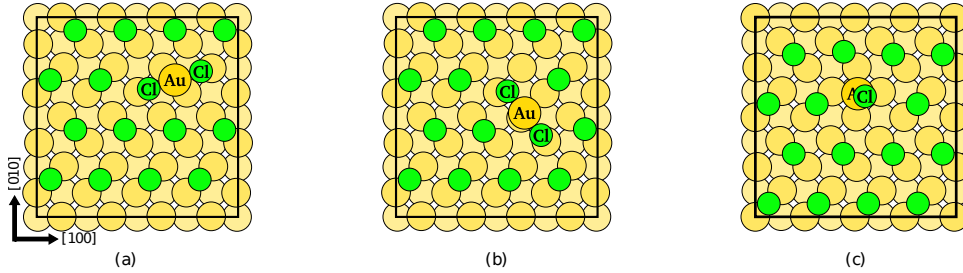


Figure 4.14.: Selected adsorption configurations of  $Au_{ad}$  on  $c(\sqrt{2} \times 2\sqrt{2})R45^\circ$ -Cl Au(001). (a) Lowest energy configuration. Energy difference  $\Delta E$  with respect to structure (a) amounts to: (b)  $\Delta E = 0.08$  eV, (c)  $\Delta E = 0.37$  eV. The black squares represent the  $c(8 \times 8)$  surface unit cell.

Regarding diffusion, a MEP for  $Au_{ad}$  on  $c(\sqrt{2} \times 2\sqrt{2})R45^\circ$ -Cl Au(001) as well as the corresponding atomic geometries are shown in Fig. 4 in Ref. [158]. The diffusion is performed solely by the  $Au_{ad}$  and proceeds via top site with an activation barrier of about 0.77 eV. Similarly to Sec. 4.2.1, the transition state geometry is characterized by a  $AuCl_3$ -like structure with  $Au_{ad}-Cl$  bond distance of 2.37 and 2.61 Å.

Table 4.2.: Comparison of activation barriers  $E_{act}$  (eV) and variation of dipole moment  $\Delta \mu$  (eÅ) at transition state for  $Au_{ad}$  on Cl covered  $(1 \times 1)$ -Au(001) with  $\Theta = 1/2$ .

Cl Adlayer	Mechanism	$E_{act}$ (eV)	$\Delta \mu$ (eÅ)
$c(2 \times 2)$	Hopping via hollow	0.44	-0.20
	$Au_{ad}Cl_2$ rotation	0.52	-0.10
	Hopping via bridge	0.81	-0.03
	Exchange	0.89	+0.10
$c(\sqrt{2} \times 2\sqrt{2})R45^\circ$	Hopping via top	0.77	-0.09

Up to now, calculations have revealed that the Cl adlayers modifies strongly the adsorption properties and energies of the Au adsorbed on Au(001), hence the diffusion paths proceeds in a more complex way as on clean  $(1 \times 1)$ -Au(001) surface. The main effect of the Cl specific adsorption is the location of the  $Au_{ad}$  in the global minimum configuration. The  $Au_{ad}$  adsorbs on bridge site of the substrate rather than the hollow site, and forms a complex

with the neighboring Cl atoms of the adlayer.

Activation energy barriers and corresponding variation of dipole moments for all diffusion paths of Au<sub>ad</sub> on Cl covered Au(001) with  $\Theta = 1/2$  are summarized in Tab. 4.2. The activation barriers are larger by about 0.17 eV (or more depending on the mechanism) than the diffusion barrier of a single Au<sub>ad</sub> on clean surface. Furthermore, we observe that  $\Delta\mu$  for the lowest energy diffusion path on Cl covered Au(001) surfaces are negative. This would imply an increase in the energy barrier with the sample potential following Ref. [47], which is not in agreement with the experiment [50, 57]. A discussion is presented in Sec. 4.5. To explore further the influence of Cl coverage on activation barriers and variation of dipole moments, we investigate the adsorption properties and energies of the Au adsorbed on Cl covered Au(001) in the presence of a Cl vacancy and of an additional Cl atom in Sec. 4.3 and 4.4, respectively.

### 4.3. Self-Diffusion of Au<sub>ad</sub> on Cl Covered Au(001) in the Presence of a Cl Vacancy

Vacancy-mediated surface diffusion has been invoked since the last decades to explain diffusion of impurity atoms in the surface [263–265] and ripening of adatom islands [266]. Furthermore, recently experiments at electrochemical environment [267] evidenced the interaction of adsorbates with metal vacancies *i.e.* vacancy-mediated diffusion underneath the coadsorbed adlayer. First-principles studies of this interactions are not available in the literature, but diffusion mechanisms assisted by vacancies in the coadsorbed adlayer have been investigated within the DFT-framework [48, 268, 269].

Within the potential range of step-flow growth mode [50] Al-Shakran *et al.* [37] showed that the Cl coverage increases with a constant slope, this means Cl vacant sites are present on the surface. Indeed, it is feasible to find a Cl vacancy site next close to a Au<sub>ad</sub>Cl<sub>2</sub> complex. Hence, the presence of Cl vacancies was considered, when studying the self-diffusion of Au adatoms at the electrochemical interface.

The aim is to elucidate the chemical bonding topology of the Au<sub>ad</sub> in the presence of a Cl vacancy, and its role in the diffusion mechanisms. Therefore, a total of 30 configurations have been relaxed to local total energy minima. Structures have been inspired by the calculated adsorption configurations of Au<sub>ad</sub> at  $\Theta = 1/2$  presented above, and local minima structures of Cl adlayer with a vacant site shown in Ref. [158]. The atomic configurations and energies of Au<sub>ad</sub> adsorbed on Cl covered surfaces in the presence of a Cl vacancy are listed in Appendix A.2, results have been published in the Supplementary Material of Ref. [158].

The calculations reveal that the potential energy surface exhibits a topology with many local minima. In case of the  $c(2 \times 2)$ -Cl adlayer the energy of local minima configurations are within a range of roughly 0.2 eV of the lowest energy configuration, while for the  $c(\sqrt{2} \times 2\sqrt{2})R45^\circ$ -Cl adlayer local minima are within a range of 0.34 eV. For both Cl adlayer reconstructions the lowest energy configurations remain characterized by a Au adatom adsorbed on bridge site of the substrate binding with two Cl adatoms as depicted in Fig. 4.15 (a) and (d). It should be noted that a Cl adatom is displaced by  $c/2$  from the  $c(\sqrt{2} \times 2\sqrt{2})R45^\circ$ -Cl adlattice site in Fig. 4.15 (d). Interatomic distances and Bader charges

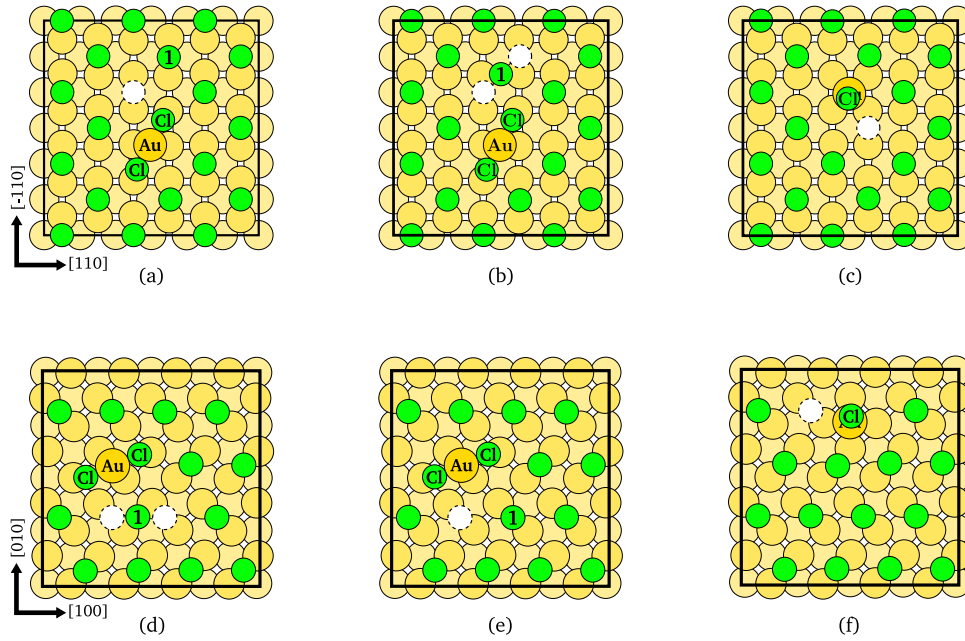


Figure 4.15.: Ground state total energy configurations for  $c(2 \times 2)$ -Cl (a-c) and  $c(\sqrt{2} \times 2\sqrt{2})R45^\circ$ -Cl (d-f) adlayer reconstructions. Lowest energy configurations are (a) and (d) for  $c(2 \times 2)$  and  $c(\sqrt{2} \times 2\sqrt{2})R45^\circ$ , respectively. The energy difference  $\Delta E$  with respect to structure (a) amounts to: (b)  $\Delta E = 0.04$  eV, (c)  $\Delta E = 0.19$  eV. The energy difference  $\Delta E$  with respect to structure (d) amounts to: (e)  $\Delta E = 0.06$  eV, (f)  $\Delta E = 0.29$  eV. White circles denote position of the vacancies. In (b) and (e) an additional circle is shown to highlight the fact that a Cl adatom is displaced.

of the  $Au_{ad}Cl_2$  do not suffer any appreciable change by the vacant site in the adlayer.

Most of the local minima configurations here considered are characterized by the displacement of either a Cl adatom or  $Au_{ad}Cl_2$  complex. In Fig. 4.15 two local minima for each Cl adlayer reconstruction are shown, for convenience Cl adatoms are denoted by the number 1, to which we refer as *atom 1*. Fig. 4.15 (b) depicts a local minimum, in which *atom 1* is displaced to the next bridge site. The displacement increases the energy by 0.04 eV with respect to the lowest energy configuration. If  $Au_{ad}Cl$  complex adsorbs on hollow site of the substrate as show in Fig. 4.15 (c), the energy difference  $\Delta E$  amounts to 0.19 eV with respect to the lowest energy configuration. This value can be 0.25 eV larger, if the  $Au_{ad}$  adatom does not bind to any Cl atom. Similar values of  $\Delta E$ , 0.06 eV for Fig. 4.15 (e) and 0.29 eV for Fig. 4.15 (f), are found for the  $c(\sqrt{2} \times 2\sqrt{2})R45^\circ$  adlayer.

Altogether, the migration mechanisms will proceeds via subsequent elementary diffusion events involving the Cl vacancy and the  $Au_{ad}Cl_2$  complex separately, resulting in a complicated walking like motion.

### 4.3.1. Diffusion of Au<sub>ad</sub> on $c(2 \times 2)$ -Cl Au(001) Surface

Fig. 4.16 and Fig. 4.17 show the atomic geometries corresponding to two diffusion mechanisms for Au<sub>ad</sub> on  $c(2 \times 2)$ -Cl Au(001) in the presence of a Cl vacancy, to which we will refer as *Path I* and *Path II*. It should be noted that along each diffusion step the Au<sub>ad</sub> forms the Au<sub>ad</sub>Cl<sub>2</sub>. We refer to the highest energy barrier along the MEP leading from one configuration to a symmetrically equivalent (and hence iso-energetic). The activation barriers which govern the transition rates amount to 0.26 and 0.25 eV for *Path I* and *Path II*, respectively. In fact, the activation barriers are about 4 times the diffusion of Au<sub>ad</sub>Cl<sub>2</sub> complex on clean surface. Conversely, the lowest diffusion energy barrier for Au<sub>ad</sub> with  $\Theta = 1/2$  amounts to 0.44 eV, which is approximately 70% larger than the activation barriers in the presence of Cl vacant site. Therefore, the main effect of a Cl vacancy is the reduction of the activation barriers.

*Path I* leads to a translation of Au<sub>ad</sub>Cl<sub>2</sub> complex by  $c$  (lattice constant) along the  $[\bar{1}00]$  direction of the substrate, while with *path II* Au<sub>ad</sub>Cl<sub>2</sub> complex is translated by a lattice constant along the  $[010]$  direction of the substrate. With aid of both paths the Au<sub>ad</sub>Cl<sub>2</sub> complex can move to any adsorption site. It should be noted that *path II* involves mostly diffusion steps performed by the neighboring Cl adatoms, see Fig. 4.17. In this way, a Cl vacant site will be created close to Au<sub>ad</sub>Cl<sub>2</sub> complex.

### 4.3.2. Diffusion of Au<sub>ad</sub> on $c(\sqrt{2} \times 2\sqrt{2})R45^\circ$ -Cl Au(001) Surface

Fig. 4.18 shows the atomic geometries corresponding to a diffusion mechanism for Au<sub>ad</sub> on  $c(\sqrt{2} \times 2\sqrt{2})R45^\circ$ -Cl Au(001) in the presence of a Cl vacancy. Similarly to the  $c(2 \times 2)$  adlayer, diffusion steps involve the movement of Cl adatoms and Au<sub>ad</sub>Cl<sub>2</sub> complex, separately. Cl adatoms that participate in the diffusion mechanism are denoted by numbers in Fig. 4.18. The activation barrier amounts to 0.35 eV, which is approximately 50% of the energy barrier at  $\Theta = 1/2$ . Thus, the reduction of the energy barriers by the presence of a Cl vacant site is independent of the Cl adlayer.

In Fig. 4.18 the Au<sub>ad</sub>Cl<sub>2</sub> complex is transported by a lattice constant along  $[\bar{1}00]$  direction of the substrate. Due to the quasi-hexagonal lattice, along some diffusion steps the distance between Cl adatoms is equivalent to nearest-neighbor Au–Au separation. In this case the energy will increase substantially by about 0.35 eV with respect to the lowest energy configuration, and the system will be in an unstable state *i.e.* transition state.

A further diffusion mechanism is shown in Ref. [158], in which the Au<sub>ad</sub>Cl<sub>2</sub> complex is translated by  $-c(1/2, 1, 0)$  with respect the initial position. Each path promotes only one direction of diffusion separately.

The difference of electric dipole moment at the transition state relative to the adsorption site comes out negative for all the calculated MEP's with  $\Theta = 1/2$  and containing a Cl vacancy, see Tab. 4.3. As a consequence, an increase of the energy barrier height with the sample potential will result from the equation by Giesen et al. in Ref. [47]. In this case the diffusion of a Au<sub>ad</sub> on a Cl covered Au(001) terrace would not be sufficient to explain the acceleration of Au island coarsening with the sample potential [57] as well as the transition between layer-by-layer and step-flow growth mode as a function of sample potential [50].



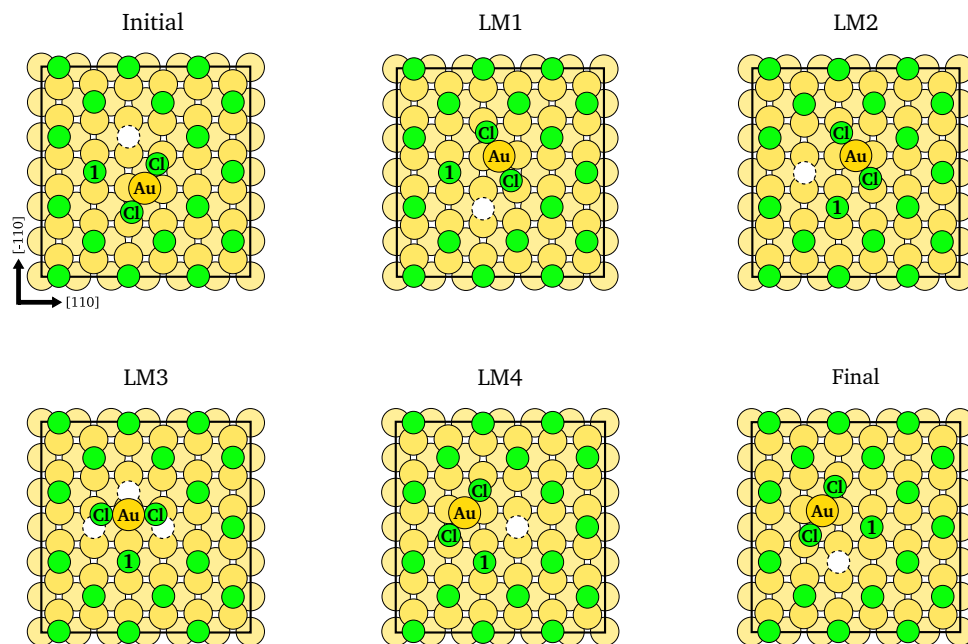


Figure 4.16.: Atomic geometries of local minima (LM) configurations along the diffusion path with the lowest energy barrier for a translation of  $Au_{ad}Cl_2$  complex in the  $[\bar{1}00]$ . Some local minima, which involve elemental diffusion steps of *atom 1*, have been omitted. In LM3 additional circles are shown to highlight the displacement of the Cl adatoms from the  $c(2 \times 2)$  lattice sites. In text we refer to this mechanism as *path I*.

Alternative explanations for such effects would be to include *e.g.* the water environment [248, 270–273], the energy barrier for the detachment of Au step [58], and the sample potential dependency for island nucleation.

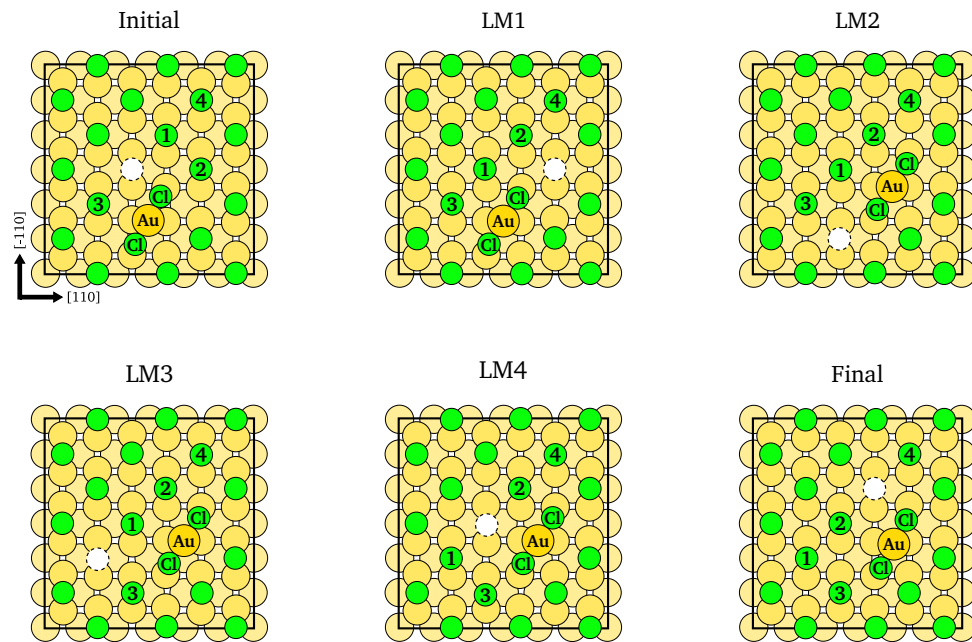


Figure 4.17.: Atomic geometries of local minima configurations along the diffusion path with the lowest energy barrier for a translation of  $\text{Au}_{\text{ad}}\text{Cl}_2$  complex in the  $[010]$ . Some local minima, which involve elemental diffusion steps of *atom 1-3*, have been omitted. In text we refer to this mechanism as *path II*.

Table 4.3.: Comparison of activation barriers  $E_{\text{act}}$  (eV) and variation of dipole moment  $\Delta\mu$  (eÅ) at transition state for  $\text{Au}_{\text{ad}}$  on Cl covered  $(1 \times 1)$ -Au(001) surfaces with  $\Theta = 1/2$  and containing one Cl vacancy and for  $\text{Au}_{\text{ad}}\text{Cl}_2$  on clean  $(1 \times 1)$ -Au(001) surface.  $\text{vac}_{\text{Cl}}$  refers to one Cl vacancy.

Au(001) surface			$E_{\text{act}}$ (eV)	$\Delta\mu$ (eÅ)	
$\text{Au}_{\text{ad}}\text{Cl}_2$	clean	Fig. 4.4	0.07	-0.12	
$\text{Au}_{\text{ad}}$	$c(2 \times 2)\text{-Cl}$	No $\text{vac}_{\text{Cl}}$	Fig. 4.7	0.44	-0.20
		$\text{vac}_{\text{Cl}}$	Fig. 4.16	0.26	-0.08
	$c(\sqrt{2} \times 2\sqrt{2})\text{R}45^\circ\text{-Cl}$	No vac.	Fig. 3 in Ref. [158]	0.77	-0.09
		$\text{vac}_{\text{Cl}}$	Fig. 4.18	0.35	-0.09
		Fig. 8 (b) in Ref. [158]	0.34	-0.06	

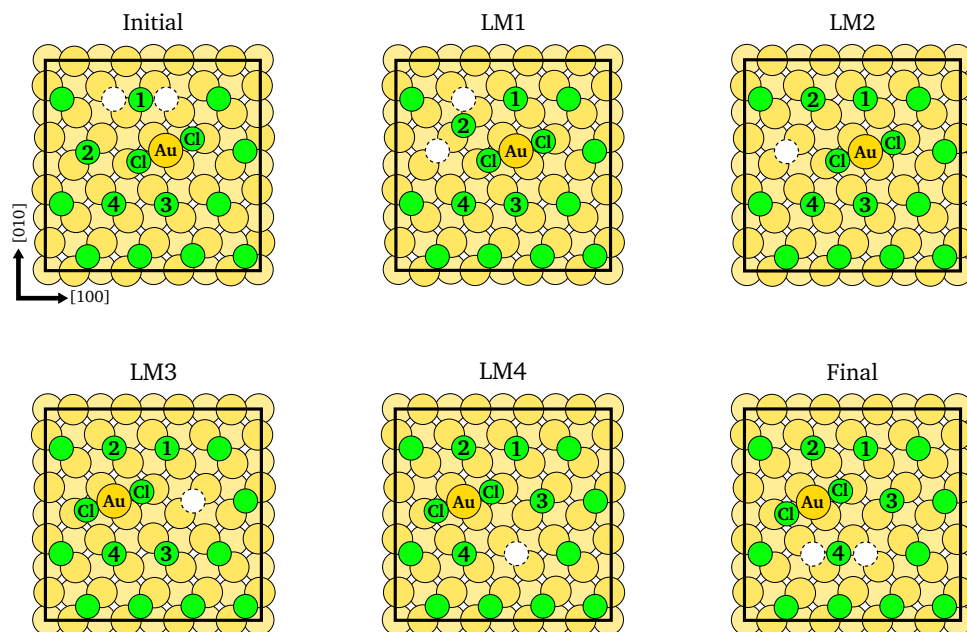


Figure 4.18.: Atomic geometries of local minima (LM) configurations along the diffusion path with the lowest energy barrier for a translation of  $Au_{ad}Cl_2$  complex in the  $[\bar{1}00]$  direction of the substrate. Some local minima, which involve elemental diffusion steps of *atoms*, have been omitted. Additional circles are shown to highlight the displacement of the Cl adatoms from the  $c(\sqrt{2} \times 2\sqrt{2})$  lattice sites. An additional diffusion mechanism, in which the  $Au_{ad}Cl_2$  complex is transported by  $-c(1/2, 1)$  with an energy barrier of 0.34 eV, is shown in Ref. [158].

#### 4.4. Self-Diffusion of Au<sub>ad</sub> on Cl Covered Au(001) in the Presence of an Additional Cl Atom

Complementary to Sections 4.2 and 4.3, we discuss the local binding topology of a Au<sub>ad</sub> as well as diffusion mechanism on the  $c(2 \times 2)$ -Cl Au(001) surface in the presence of an additional Cl atom on the adlayer. Analogously to Sec. 4.3, structures have been inspired by the calculated adsorption configurations of Au<sub>ad</sub> at  $\Theta = 1/2$ . Structures have been relaxed to local total energy minima. The atomic configurations and energies of Au<sub>ad</sub> adsorbed on  $c(2 \times 2)$ -Cl Au(001) in the presence of an additional Cl atom are listed in Appendix A.4.

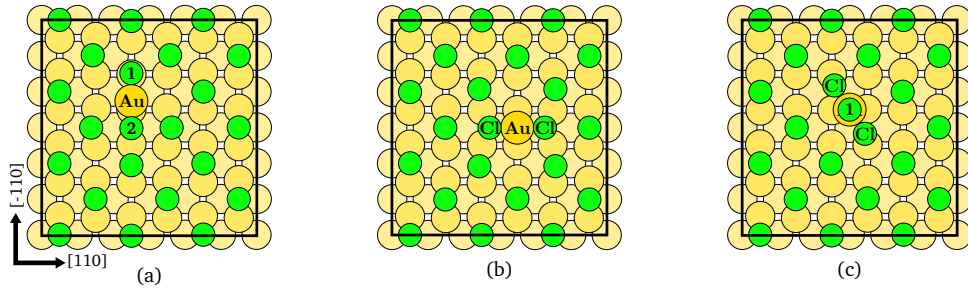


Figure 4.19.: Ground state total energy configurations for  $c(2 \times 2)$ -Cl adlayer reconstruction. Lowest energy configuration is depicted in (a). The energy difference  $\Delta E$  with respect to structure (a) amounts to: (b)  $\Delta E = 0.11$  eV, (c)  $\Delta E = 0.38$  eV.

The lowest energy configuration is characterized by a Au adatom adsorbed close to the top site of the substrate binding with two Cl adatoms, which are denoted by 1 and 2 in Fig. 4.19 (a). In contrast to Sec. 4.2 and 4.3, the Au<sub>ad</sub>Cl<sub>2</sub> complex is arranged along  $[\bar{1}10]$  direction of the substrate. The difference between the  $z$  coordinate of *atom 2* relative to *atom 1* amounts to 0.61 Å, this is ascribed to the additional repulsion in *atom 2* by the neighboring Cl adatoms. The Au<sub>ad</sub>-Cl bond lengths amount to 2.30 and 2.25 Å for *atom 1* and 2, respectively. Furthermore, the Bader charges amount to +0.38 e for Au<sub>ad</sub>, -0.40 and -0.28 e for *atom 1* and 2, respectively. These dissimilarities are attributed to their adsorption positions and  $z$  coordinate.

A local minimum configuration is depicted in Fig. 4.19 (b), which is energetically unstable by 0.11 eV relative to the lowest energy configuration. The Au<sub>ad</sub> is located on bridge site, and the Au<sub>ad</sub>Cl<sub>2</sub> complex is arranged along the  $[110]$  direction of the substrate. Therefore, the number of Cl adatoms within a range of a lattice constant relative to Cl atoms of the complex has increased (6 in total). The distances between *atom 1* (or *atom 2*) to the neighboring Cl adatoms amount to 3.36 Å (Cl atoms along  $[\bar{1}10]$ ) and 3.72 Å (Cl atoms along  $[110]$ ), which are 20% and 10% smaller than the lattice constant. In Fig. 4.19 (c) the *atom 1* is adsorbed on the top of the Au<sub>ad</sub> rather than on the surface. Therefore, the separations between adatoms on  $c(2 \times 2)$ -Cl adlayer are only slightly modified by about  $\sim 0.04$  Å. It should be noted that without *atom 1* the structure corresponds to the lowest energy configuration at  $\Theta = 1/2$ . The formation of a T-shaped Au<sub>ad</sub>Cl<sub>3</sub> complex is energetically unfavorable by 0.38 eV with respect to the lowest energy configuration. This evidences the preference to form Au<sub>ad</sub>Cl<sub>2</sub>

complex and to adsorb a  $\text{Cl}$  atom on the surface.

#### 4.4.1. Diffusion of $\text{Au}_{\text{ad}}$ on $c(2 \times 2)\text{-Cl Au}(001)$ Surface

As the surface is very crowded by  $\text{Cl}$  adatoms, the migration of the  $\text{Au}_{\text{ad}}\text{Cl}_2$  complex would result in high energy barriers. Consequently, the diffusion path will consist on the motion of  $\text{Au}$  and neighboring  $\text{Cl}$  adatoms. The translation of  $\text{Au}_{\text{ad}}$  by one lattice constant to an equivalent neighboring position proceeds via the MEP depicted in Fig. 4.20 with the corresponding atomic geometries depicted in Fig. 4.21. The highest energy barrier along a path to an equivalent configuration is considered as the corresponding activation barrier, which amounts to 0.73 eV.

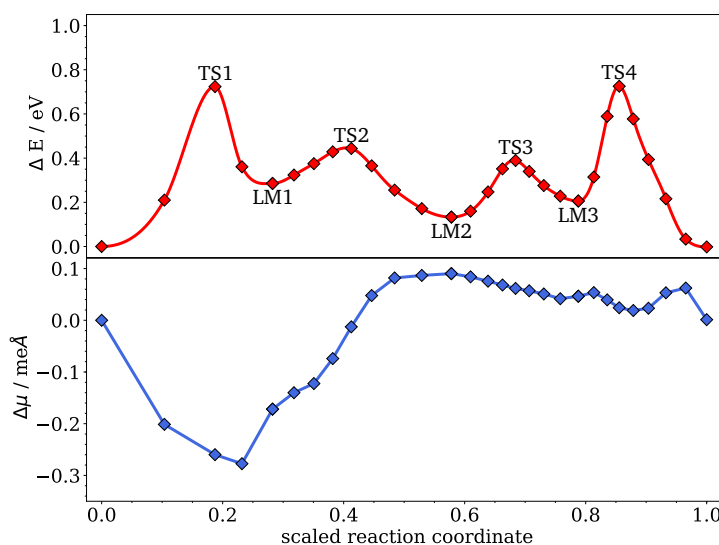


Figure 4.20.: Variation of energy  $\Delta E$  and dipole moment  $\Delta \mu$  along the MEP for a translation of  $\text{Au}_{\text{ad}}$  on  $c(2 \times 2)\text{-Cl Au}(001)$  in the presence of an additional  $\text{Cl}$  adatom. The MEP is a composition of individual CI-NEB runs connecting local minima.

In Fig. 4.21 the  $\text{Cl}$  atoms that participate in the diffusion path of  $\text{Au}_{\text{ad}}$  are labeled with the numbers. The diffusion path proceeds as following:

1. the  $\text{Au}_{\text{ad}}$  moves toward to the next hollow site, see Initial and LM1 configurations in Fig. 4.21. The transition state is characterized by a  $\text{Au}_{\text{ad}}\text{Cl}_3$ -like structure with a  $\text{Cl}$  atom close to the top of  $\text{Au}_{\text{ad}}$ . The  $\text{Au}\text{-Cl}$  bond separations amount to 2.57 (*atom 1*), 2.27 (*atom 2*) and 2.63 Å (*atom 3*). Moreover, the difference of  $z$  coordinate of *atom 2* relative to *atom 3* amounts to 2.68 Å. The dipole moment variation at TS1 amounts to  $-0.26 \text{ eÅ}$ , the negative sign and large absolute value are attributed to the elevation of *atom 2*. The energy barrier for this diffusion step amounts to 0.72 eV, similarly barriers have been obtained in Sec. 4.2.1 and 4.2.2 for MEP's with a  $\text{Au}_{\text{ad}}\text{Cl}_3$ -like structure at the transition state. In the LM1 configuration the difference of  $z$  coordinate of *atom 2* relative to *atom 3* amounts to 2.04 Å.

2. From LM1 to LM2 configurations the  $\text{Au}_{\text{ad}}\text{Cl}_2$  complex moves downward to the surface. Thus, *atoms 4 and 5* are displaced to their next neighboring bridge sites. The energy barrier for this diffusion step with respect to the lowest energy configuration amounts to 0.44 eV. At TS2 the difference of  $z$  coordinate of *atom 2* relative to *atom 3* amounts to 0.61 Å, while at the lowest energy configuration the difference of  $z$  coordinate of *atom 2* with respect to *atom 1* amounts to the same value. The variation of the dipole moment at TS2 is about -0.02 eÅ, the small absolute value of  $\Delta\mu$  is ascribed to the small displacements in  $z$  direction of the neighboring Cl adatoms rather than to the Cl atoms of the complex.
3. The diffusion step between LM2 and LM3 configurations is driven by *atom 4 and 5*, while the complex fluctuates around its position. The Cl adatoms move simultaneously to their next bridge site. The energy barrier amounts to 0.39 eV, and the corresponding variation of dipole moment is +0.06 eÅ. The variation of dipole moment continues to decrease, but still positive, to the value of +0.04 eÅ at LM3 configuration. The positive sign of  $\Delta\mu$  is attributed to the fact that Cl adatoms are closer to the surface than in the initial state.
4. In the last diffusion step the  $\text{Au}_{\text{ad}}$  moves close to the next top site. Similarly to the first step, the transition state is characterized by a  $\text{Au}_{\text{ad}}\text{Cl}_3$ -like structure. However, here all the Cl adatoms lie on the surface. This explains the fact that the variation of dipole moment is positive (+0.02 eÅ). The energy barrier amounts to 0.73 eV, only 0.01 eV larger than the first energy barrier which is beyond the accuracy of our DFT calculations.

By comparison to the diffusion of  $\text{Au}_{\text{ad}}$  on  $c(2 \times 2)$ -Cl Au(001) surface with  $\Theta \leq 1/2$ , the activation barrier  $E_{\text{act}}$  of  $\text{Au}_{\text{ad}}$  in the presence of an additional Cl atom is significantly large. The hopping rate  $\text{Au}_{\text{ad}}\text{Cl}_2$  complex in the presence of Cl vacancy (given by  $\approx \nu_0 e^{-0.26\text{eV}/k_B T}$ ) is roughly eight orders of magnitude higher than in the presence of an additional Cl atom at room temperature. From Ref. [37] coverages larger than 1/2 occur for electrode potentials above 0.5 V<sub>SCE</sub>, which are beyond the potential range of step-flow growth mode investigated in Ref. [50].

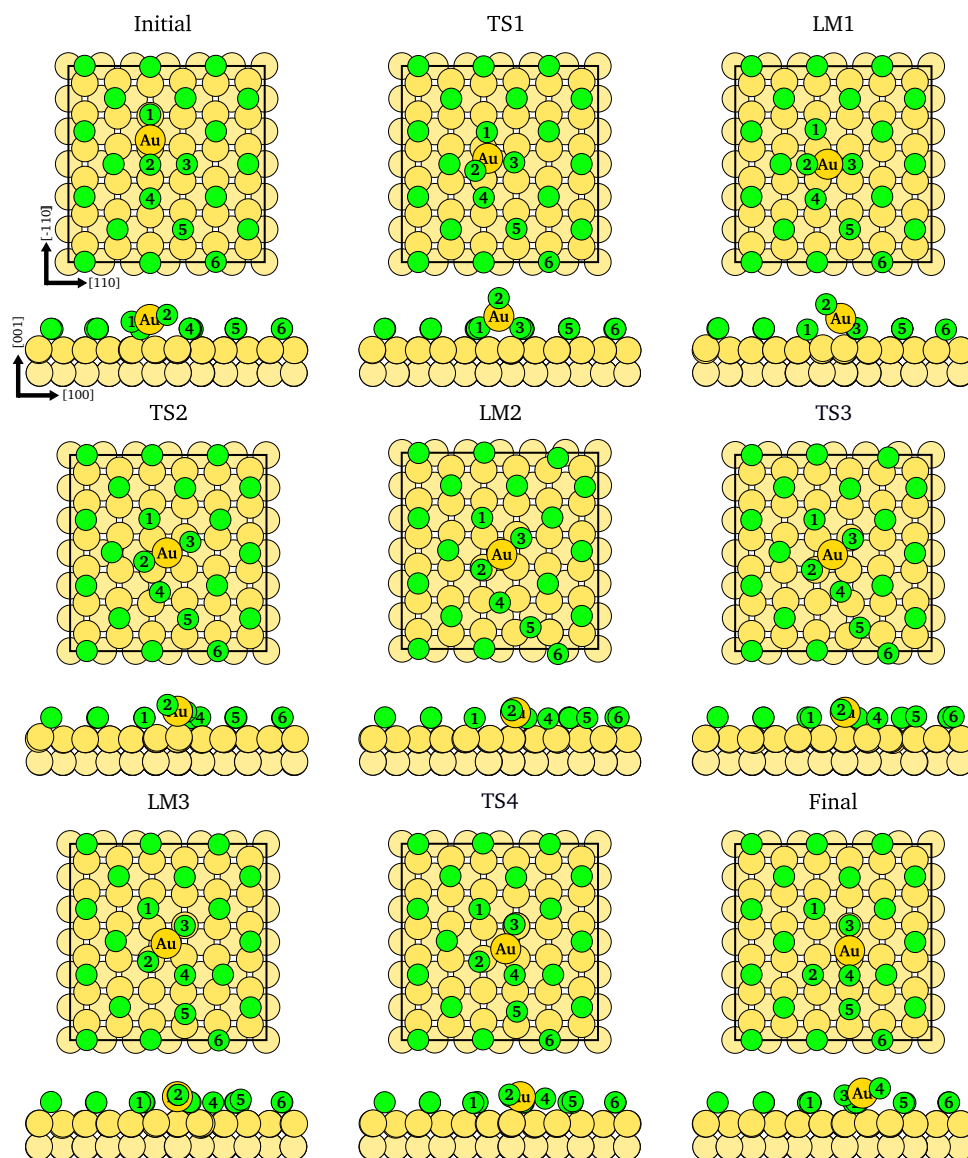


Figure 4.21.: Atomic geometries of local minima and transition state configurations along the MEP for a translation of  $Au_{ad}$  on the  $c(2 \times 2)$ -Cl  $Au(001)$  surface in the presence of an additional Cl atom.

## 4.5. Discussion of Induced Dipole Moments and the Effect of an Adsorbed Water Layer

The development of an atomistic picture of the surface electrochemical processes is far from trivial. Its complexity yield on processes occurring at the interface between the electrode surface and the electrolyte. A computational description should include water molecules as well as ions, which can be specifically adsorbed or solvated [202, 274–277]. Furthermore, it is necessary to account the liquid nature and electronic properties of the electrolyte. This could be achieved by performing ab initio molecular dynamics (AIMD) simulations at room temperature which require long time-consuming calculations. For example Sakong *et al.* have studied the structure of liquid water on Pt(111) surface during 40 ps. AIMD simulations Ref. [216]. Another difficulty is to simulate the electrode/electrolyte interface under variable potential bias. There is not a generally accepted constant potential method to quantify this dependency to date. But there are several schemes [174, 215, 218, 219, 242, 278–280] that attempt to it.

To gain an impression of the effect of an adsorbed water layer to our system of interest, in Ref. [158] a static water layer placed on clean Au(001) and on a Cl covered Au(001) surfaces were calculated disregarding the influence of the electrochemical interface and the cations from the electrolyte. Complementary to results in Ref. [158], here a discussion of the adsorption energy per H<sub>2</sub>O molecule and per water layer, as well as, the polarization effects is presented. The adsorption energies have been calculated as:

$$E_{\text{ads}}^{\text{Mol. H}_2\text{O}} = (E(n_{\text{Cl}}, n_{\text{H}_2\text{O}}) - E(n_{\text{Cl}}, 0) - n_{\text{H}_2\text{O}} E_{\text{Mol. H}_2\text{O}}) / n_{\text{H}_2\text{O}}, \quad (4.2)$$

$$E_{\text{ads}}^{\text{Layer H}_2\text{O}} = (E(n_{\text{Cl}}, n_{\text{H}_2\text{O}}) - E(n_{\text{Cl}}, 0) - E_{\text{Layer H}_2\text{O}}) / n_{\text{H}_2\text{O}}. \quad (4.3)$$

$n_{\text{Cl}}$  and  $n_{\text{H}_2\text{O}}$  are the number of Cl atoms and water molecules in the SUC, respectively.  $E(n_{\text{Cl}}, n_{\text{H}_2\text{O}})$  corresponds to the total energy of the system containing  $n_{\text{Cl}}$  atoms,  $n_{\text{H}_2\text{O}}$  molecules and the Au(001) surface. In this equations  $E(n_{\text{Cl}}, 0)$  has been chosen as reference energy. If  $n_{\text{Cl}}$  is equal to zero,  $E(0, 0)$  refers to the total energy of the clean Au(001) surface.  $E_{\text{Mol. H}_2\text{O}}$  is the total energy of an isolated water molecule.  $E_{\text{Layer H}_2\text{O}}$  is the total energy of an isolated water adlayer, atomic positions of the water molecules have been fixed at the geometries corresponding to  $E(n_{\text{Cl}}, n_{\text{H}_2\text{O}})$ .

Regarding the polarization effects, one dimensional charge density differences  $\tilde{\rho}(z)$ , which results from the integration over lateral coordinates  $x$  and  $y$  for each  $z$  plane, and the induced work function change upon water adsorption on clean and  $c(2 \times 2)$ -Cl Au(001) surfaces are discussed.

### 4.5.1. Clean Au(001) Surface

The structure of water on metallic electrode surfaces has been intensely investigated [281–283]. Particularly on (111) metal surfaces previous work by various authors has shown that the water ice-like adlayer is no stable at room temperature, but it is a good starting point [181, 284, 285]. Regarding (001) metal surfaces, Yeh and Berkowitz have found a rectangular water structure on Pt(001) by means of MD simulations with classical potentials



[286]. Lin and Groß have performed BOMD simulations for the water/Au(001) interface starting from a rectangular structure on a  $p(2 \times 2)$  SUC [287]. They found out that the rectangular structure on Au(001) is thermodynamically not stable at 140 K. Montoya *et al.* have determined an optimal water layer structure on Cu(001) within a  $p(4 \times 3)$  SUC by means of DFT, see Ref. [202] and corresponding supplementary material. The calculated water layer with  $\Theta_{\text{water}} = 2/3$  resembles the hexagonal ice-like structure. Furthermore, Ungerer *et al.* have found out that the adsorbed H<sub>2</sub>O molecules tend to form hexagonal rings on Pt(001) as  $\Theta_{\text{water}}$  increases.

In this work, a single layer of 16 water molecules on a clean surface within a  $p(4 \times 4)$  SUC has been relaxed starting from a rectangular structure as described in Ref. [287]. The relaxed rectangular water layer is depicted in Fig. 4.22 (a). Water molecules are located on (or close to) top site and form a zigzag chain. Two inequivalent water molecules are observed, one with a hydrogen atom pointing to surface, the other with a hydrogen atom above the oxygen atom. These results have been pointed out in Ref. [287]. A further water adlayer have been found by introducing a perturbation to rectangular structure. This have been achieved by placing the rectangular structure on top of a  $c(2 \times 2)$ -Cl Au(001) surface with a vacant site, which results in a hex-like water adlayer similarly as in Ref. [202]. Two relaxed hex-like water structures are shown in Fig. 4.22 (b) and (c), which differ by a translation with respect to each other. It should be noted that water molecules do not have a preferred orientation. In comparison to the rectangular structure, the hex-like structures are not flat, see side-views in Fig. 4.22 (b) and (c).

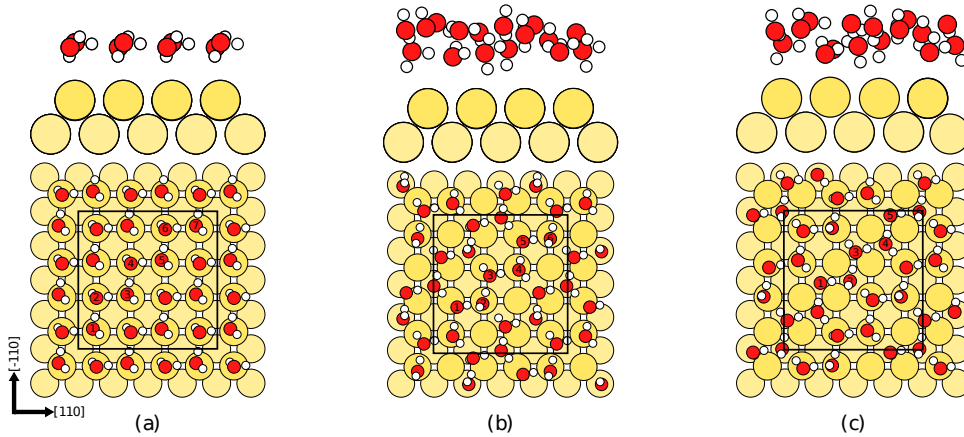
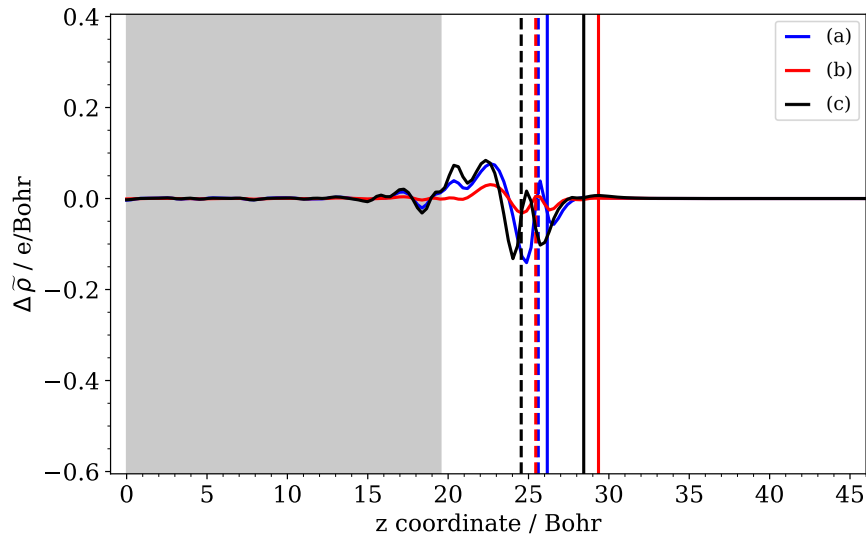


Figure 4.22.: Clean Au(001) surface in contact with a water adlayer. (a) is a rectangular water layer as calculated by Lin et. Groß [287]. (b) and (c) are hex-like water adlayers, which are displaced from each other.

Inspection of Tab. 4.4 shows that the lowest adsorption energy  $E_{\text{ads}}^{\text{Mol. H}_2\text{O}}$  corresponds to the hex-like structure (-0.52 eV), this is attributed to the higher number of H-bonds in the water layer. In case of the adsorption energy  $E_{\text{ads}}^{\text{Layer H}_2\text{O}}$ , the values for all here considered water layers are very similar and in magnitude small. This means that the water layer is weakly adsorbed to the metal surface.

Table 4.4.: Water induced work function change  $\Delta\Phi$  with respect to the clean Au(001) surface and adsorption energies for each water structure depicted in Fig. 4.22.

	H <sub>2</sub> O structure	$\Delta\Phi$ (eV)	$E_{\text{ads}}^{\text{Mol. H}_2\text{O}}$ (eV)	$E_{\text{ads}}^{\text{Layer H}_2\text{O}}$ (eV)
H <sub>2</sub> O/Au(001)	Fig. 4.22 (a)	-0.14	-0.44	-0.03
	Fig. 4.22 (b)	+0.37	-0.50	-
	Fig. 4.22 (c)	-0.28	-0.52	-0.05
		-0.09 [287]	-0.39 [287]	-


 Figure 4.23.: Charge density difference  $\Delta\tilde{\rho}(z)$  for the adsorption of a water layer on a clean Au(001) surface. The blue, red and black lines correspond to Fig. 4.22 (a), Fig. 4.22 (b) and Fig. 4.22 (c) respectively. The grey area represents the Au surface. Vertical lines represent the smallest (dashed) and largest (straight)  $z$  coordinate of oxygen atoms for each surface.

Regarding polarization effects, the induced work function amounts to +0.37 eV for Fig. 4.22 (b) and -0.28 eV for Fig. 4.22 (c). As a first sight, one would expect the same value because both structures are similar. In order to understand the electronic origin of this discrepancy, the water-induced charge density differences are shown in Fig. 4.23. In case of water adlayers from Fig. 4.22 (a),(c), the charge transfer is more pronounced than for Fig. 4.22 (b). Furthermore, the local charge rearrangement has shown that the water molecules from Fig. 4.22 (c) are more polarized than Fig. 4.22 (b). This charge rearrangement could be a consequence of the variation of  $z$  *e.g.* and the high polarizability of water molecules. For example in Fig. 4.22 (c) *atom 3* is closer to the Au surface by 0.58 Å relative to

its position in Fig. 4.22 (b).

#### 4.5.2. $c(2 \times 2)$ -Cl Au(001) Surface

To the best of our knowledge, there are no studies addressing the structure of the water layer in contact with Cl coadsorbed surfaces. But recently *Ab initio* MD-Simulations of Pt slab in contact with NaCl aqueous electrolyte performed by Khatib *et al.* [178] have observed that interfacial water is arranged in hexagonal and pentagonal water rings, which have a different densities and distributions, depending on the electrode charging.

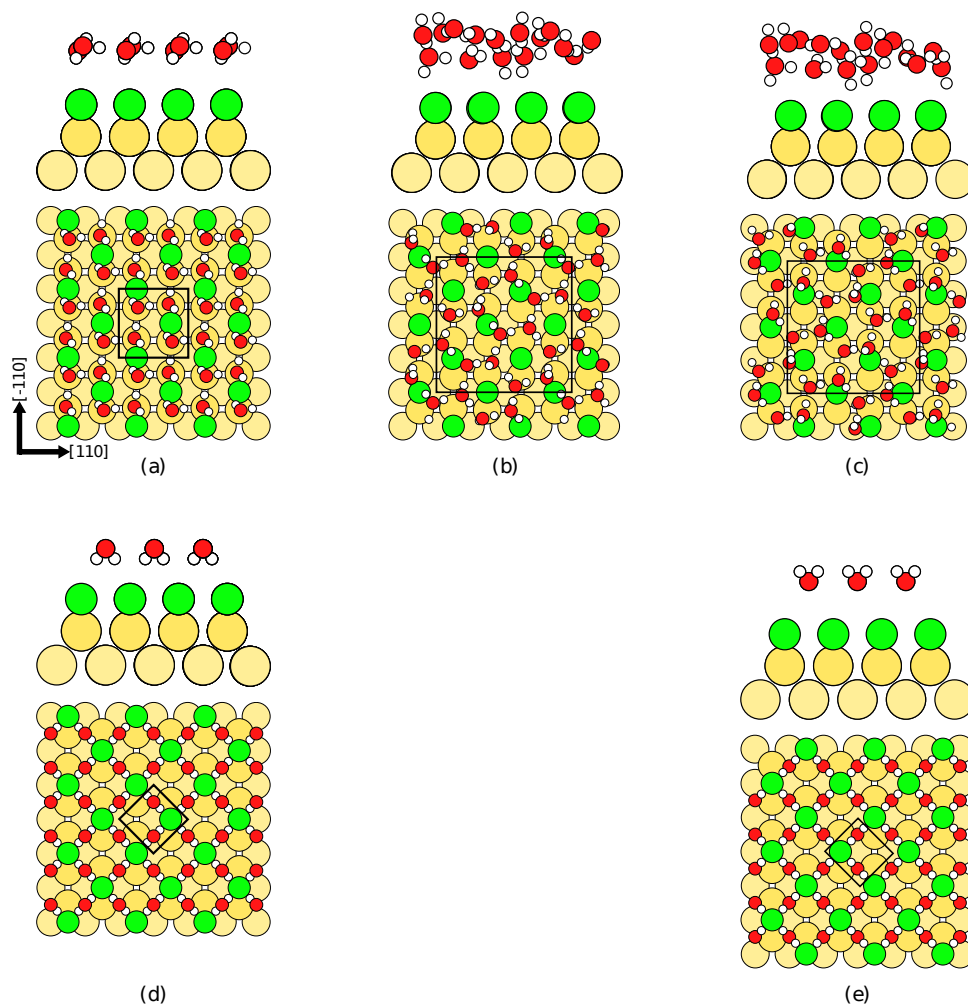


Figure 4.24.:  $c(2 \times 2)$ -Cl Au(001) surface in contact with a water adlayer. (c) is a rectangular water layer as shown in Ref. [287]. (b) and (c) are hex-like water adlayers similar to the ones calculated on clean Au(001) surface. (d) is a H-down oriented water layer as calculated in the literature [274–277]. (e) is a H-up oriented water adlayer. In all calculations the effect of cations has been neglected. Black squares represent the surface unit cell of the calculations.

To gain an impression of the static water structure four structures have been calculated on the  $c(2 \times 2)$ -Cl Au(001) surface, see Fig. 4.24. A rectangular water structure from Ref. [287] has been ionically relaxed within a  $p(2 \times 2)$  SUC. The hex-like structures have been simulated within a  $p(4 \times 4)$  SUC. The H-down and H-up water structures, Fig. 4.24 (d) and (e), have been simulated within a  $c(2 \times 2)$  SUC following the work by Keller *et al.* [288]. During the subsequent relaxation, the Cl atoms and the Au atoms in the outermost four of the layers as well as the H and O atoms of the water molecules were allowed to move. In case of H-up and H-down structures, the motion of water molecules have been restricted to an axis perpendicular to the surface.

Table 4.5.: Water induced work function change  $\Delta \Phi$  with respect to the fully covered  $c(2 \times 2)$ -Cl/Au(001) surface and adsorption energies for each water structure depicted in Fig. 4.24.

	H <sub>2</sub> O structure	$\Delta \Phi$ (eV)	$E_{\text{ads}}^{\text{Mol. H}_2\text{O}}$ (eV)	$E_{\text{ads}}^{\text{Layer H}_2\text{O}}$ (eV)
$c(2 \times 2)$ -Cl+H <sub>2</sub> O/Au(001)	Fig. 4.24 (a)	0.06	-0.42	-0.02
	Fig. 4.24 (b)	0.61	-0.48	-0.01
	Fig. 4.24 (c)	0.34	-0.49	-0.01
	Fig. 4.24 (d)	2.83	+0.43	-0.09
	Fig. 4.24 (e)	-4.21	+0.50	-0.01

In Tab. 4.5 the adsorption energy  $E_{\text{ads}}^{\text{Mol. H}_2\text{O}}$  for the hex-like structure present the lowest value (-0.49 eV) among the water adlayers here considered. In comparison to the clean surface the water molecules adsorb less strongly to the Cl covered Au(001) surface. The water-oriented molecules do not adsorb, the structures obtained from the calculations are highly artificial. The adsorption energy  $E_{\text{ads}}^{\text{Layer H}_2\text{O}}$  for Fig. 4.24 (a)-(c) are very small ( $\approx 0.01$  eV), this is ascribed to the low charge transfer between the water and Cl adlayers in Fig. 4.25. Conversely, the H-down water structure present a strong charge rearrangement in the region between the water molecules and the Cl adlayer in Fig. 4.25. Therefore, H-down structure has a large  $E_{\text{ads}}^{\text{Layer H}_2\text{O}}$  (-0.09 eV). This could be attributed to interaction between Cl and H atoms, which is supported by the fixed lateral coordinates of the water molecules.

The effect of temperature and cations on water/Cl covered Au surface is still an open question. Whether water molecules would prefer an orientation cannot be answered from our calculations. But in the water/metal interface many authors have reported that there is no preferential orientation of water molecules in the interface [216, 217, 284]. Therefore, H-down structure as shown Fig. 4.24 (d) or (e) is not expected to occurred.

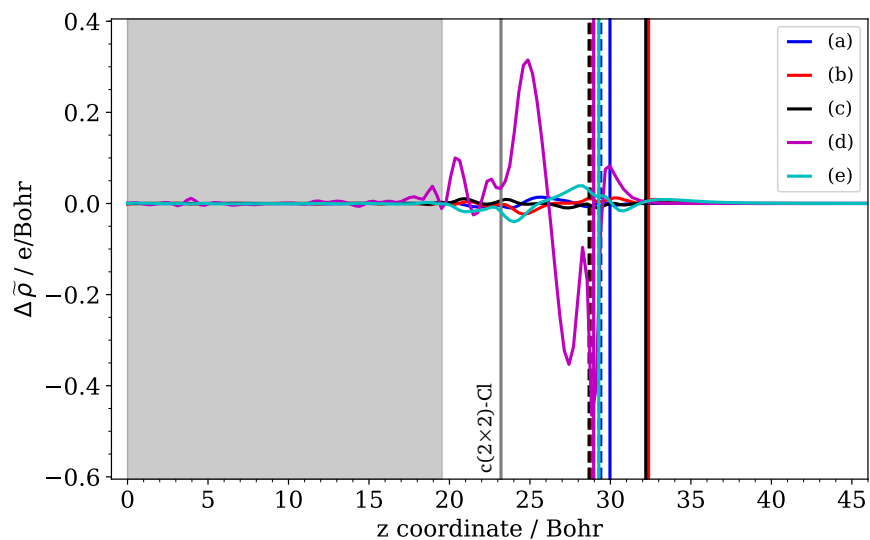


Figure 4.25.: Charge density difference  $\Delta \bar{\rho}(z)$  for the adsorption of a water layer on a  $c(2 \times 2)$ -Cl Au(001) surface. The gray area represents the Au surface, while the gray vertical line indicates the position of the Cl adlayer. Remaining vertical lines represent the smallest (dashed) and largest (straight)  $z$  coordinate of oxygen atoms for each surface.

**4.6. Publication J. Chem. Phys. 151, 064709 (2019),  
Copyright (2019) by AIP Publishing**

# DFT study of Au self-diffusion on Au(001) in the presence of a Cl adlayer

Cite as: J. Chem. Phys. 151, 064709 (2019); doi: 10.1063/1.5113965

Submitted: 10 June 2019 • Accepted: 21 July 2019 •

Published Online: 13 August 2019



View Online



Export Citation



CrossMark

Alexandra Celinda Dávila López<sup>a)</sup>  and Eckhard Pehlke<sup>b)</sup>

## AFFILIATIONS

Institut für Theoretische Physik und Astrophysik, Christian-Albrechts-Universität zu Kiel, Kiel, Germany

<sup>a)</sup>davila@theo-physik.uni-kiel.de

<sup>b)</sup>pehlke@theo-physik.uni-kiel.de

## ABSTRACT

The atomic-scale mechanism of self-diffusion on coinage metal surfaces has been investigated by density functional theory calculations before. However, the detailed role of the co-adsorbed anions and of the electrochemical interface is not yet fully understood. We present diffusion paths of a Au adatom on  $c(2 \times 2)$ -Cl and  $c(\sqrt{2} \times 2\sqrt{2})R45^\circ$ -Cl Au(001) surfaces. In the case of the fully Cl covered Au(001) surfaces, the diffusion energy barriers are  $\geq 0.44$  eV. In the presence of a neighboring Cl vacancy, the diffusion barriers are drastically reduced to about half of the value for the fully Cl covered surface. Thus, Au self-diffusion is promoted by Cl vacancies. A first estimate for the effect of water on the diffusion energy barrier of the Cl vacancy is derived by calculating the interaction of configurations along the diffusion path with a water layer.

Published under license by AIP Publishing. <https://doi.org/10.1063/1.5113965>

## I. INTRODUCTION

Processes at solid-electrolyte interfaces are affected by coadsorbed ions.<sup>1–6</sup> In particular, anions as halides form strongly chemisorbed adlayers at coinage metal surfaces<sup>7</sup> and can modify interface reactions, for example the reactivity and selectivity of electrocatalytic reactions<sup>8</sup> and nucleation and growth.<sup>9,10</sup> Recently, experimental results by Rahn *et al.*<sup>11</sup> have shown that the chemical nature of these species can entirely determine the microscopic dynamic behavior of adatom surface diffusion.

Particularly, for the Au(001)-electrolyte interface, the number of monolayer islands created by the  $(\text{hex}) \rightarrow (1 \times 1)$  transition of the Au substrate has been investigated in electrochemical annealing studies.<sup>12–15</sup> The number of islands decreases, while their size increases with time via a two-dimensional Ostwald ripening process. Using electrochemical STM in chloride containing electrolytes as well as sulfuric acid solution, Giesen and co-workers<sup>13–15</sup> have studied the coarsening of the Au islands on Au(001) as a function of electrode potential. The decay of an island requires the dissociation of an Au atom from a kink site in the island edge and the diffusion of atoms on the terrace.<sup>15</sup> Giesen *et al.* have concluded that the coarsening of the Au islands is diffusion-limited. The

decay rate increases exponentially with the sample potential, with rates for chloride containing electrolyte being larger than for sulfate containing electrolytes. Thus, chloride is assumed to enhance mobility.

Moreover, by means of surface X-ray scattering (SXS)<sup>9,16</sup> experiments at the interface between a Au(001) electrode and a  $\text{Cl}^-$  containing electrolyte, Krug *et al.* have quantitatively investigated the dependence of the growth mode on electrode potential and Au-concentration in the electrolyte. Transitions from 3D to layer-by-layer and finally to step-flow growth mode have been observed with increasing sample potential. This has been ascribed to an increase in Au surface mobility with sample potential.<sup>9</sup> The transition between the step flow-mode and layer-by-layer growth mode depends on how fast the adatom diffuses on the terraces. However, also other quantities such as the dependence of the binding properties of the critical nucleus on sample potential may play a role.

To contribute to the understanding of processes at the Au(001)-electrolyte interface, information at the atomic-scale is crucial. However, the detailed microscopic mechanisms of electrodeposition and the role of the halide adsorbates at the interface at high coverage are still not clarified. The diffusion of Au adatoms and  $\text{Au}_{\text{ad}}\text{Cl}$

without the influence of further co-adsorbates has been studied in Refs. 17–19. Müller and Ibach<sup>18</sup> have calculated activation energies and variation of dipole moment of adatoms migrating on coinage metal surfaces. Specifically, they have analyzed the reaction path involved in the dissociation of an atom from a kink site in a step, which finally results in the diffusion of the atom on the terrace. In Ref. 20, Pötting *et al.* have presented a detailed study of self-diffusion mechanisms on perfect and imperfect Au(001) surfaces. Similarly to Ref. 20, Mesgar *et al.*<sup>19,21</sup> have investigated the diffusion of an Au<sub>ad</sub>Cl complex on clean and stepped Au(001) surfaces. Additionally, in Ref. 21, a diffusion path of a Au<sub>ad</sub>Cl<sub>2</sub> complex on a Cl covered Au(001) surface is proposed for Cl coverage  $\Theta = 1/2$ . The corresponding diffusion energy barrier amounts to 0.68 eV.<sup>21</sup> Altogether, however, detailed information on the lowest energy configurations, such as the atomic and electronic structure, the diffusion paths, and the variation of the dipole moment along the diffusion paths for the Cl covered surface is still scarce.

Our aim is to reveal the local binding topology of an Au adatom on a Cl covered Au(001) surface at chlorine coverage  $\Theta = 1/2$  and to discuss the relevant diffusion mechanisms with and without a nearest-neighbor chlorine vacancy. We refer to the potential range of step-flow growth mode where the unreconstructed (1 × 1) Au(001) substrate is stable.<sup>9</sup> Computational details are described in Sec. II. We start with the diffusion of a Au<sub>ad</sub>Cl<sub>2</sub> complex on the clean Au(001) surface and compare it to the literature in Sec. III A. In Sec. III B, we address the local binding topology around the Au adatom at high Cl coverage ( $\Theta = 1/2$ ), and the corresponding lowest energy diffusion mechanisms are presented. Both adlayer structures, c(2 × 2)-Cl and c( $\sqrt{2} \times 2\sqrt{2}$ )R45°-Cl, are considered, which have been observed in STM experiments under electrochemical conditions.<sup>22,23</sup> In view of the experimental data for the surface coverage of specifically adsorbed chlorine on Au(001) as a function of sample potential, the presence of Cl vacancies has to be accounted for.<sup>24</sup> In Sec. III C, we present the Cl vacancy diffusion paths for both Cl adlayers. Furthermore, in Sec. III D, we calculate the diffusion mechanisms of a Au adatom involving a nearest-neighbor Cl vacancy on the Cl covered Au(001) surfaces. Finally, we present a rough estimate to quantify the change in energy barrier and dipole moment in the case of the diffusion of a Cl vacancy in contact with a water layer.

## II. COMPUTATIONAL DETAILS

Periodic density functional theory (DFT) calculations have been performed using PWscf from the Quantum ESPRESSO package.<sup>25,26</sup> The generalized gradient approximation by Perdew, Burke, and Ernzerhof (PBE-GGA)<sup>27</sup> is applied to the exchange correlation functional. The halogens and metal atoms are represented by ultrasoft pseudopotentials<sup>28</sup> from the open-source GBRV library.<sup>29</sup> The Au(001) surfaces were simulated by a slab geometry with 4 or 6 metal layers. Adsorbed atoms were on one side. The Au atoms in the two lowermost layers were fixed at their ideal bulk positions, and the remaining Au layers and the adsorbate layer were allowed to relax. In all calculations, the unreconstructed Au(001) (1 × 1) substrate was assumed. The slabs were separated by a vacuum region with a thickness of about 13 Å. With regard to the different work functions of the top and bottom surface of the slab, a dipole correction<sup>30,31</sup> has been used. Dipole moment changes along the reaction paths have been

derived from the dipole moments as calculated by PWscf. Geometry optimizations have been carried through at a plane-wave cutoff energy of 30 Ry until the Hellmann-Feynman forces acting on the relaxed atoms became smaller than 5 meV/Å. For the Brillouin zone integration, we have used a (4 × 4 × 1) Monkhorst-Pack grid of special *k*-points<sup>32</sup> for the p(4 × 4) surface unit cell and a (3 × 3 × 1) grid for the p(6 × 6) and for the c(8 × 8) surface unit cells. The Cl coverage is defined as the ratio of the number of adsorbed Cl adatoms to the number of gold surface atoms of the unreconstructed Au(001) surface.

Minimum energy paths and diffusion barriers have been determined with the climbing image nudged elastic band (CI-NEB) method<sup>33–35</sup> with a plane-wave cutoff energy of 30 Ry. Where applicable, additional paths have been obtained by application of suitable symmetry operations to already calculated NEB paths. In order to explore the potential energy surface (PES) of chlorine-covered Au surfaces, *ab initio* metadynamic simulation on the Born-Oppenheimer (BOMD) surface has been carried out using the PLUMED<sup>36</sup> plugin with PWscf at a reduced cutoff energy of 25 Ry.

Detailed convergence tests are presented in the [supplementary material](#). Roughly, the accuracy of energy differences along the diffusion path is estimated to be about 40 meV, and in the case of the induced dipole moments, the accuracy is between 10 and 20 meÅ.

## III. RESULTS AND DISCUSSION

### A. Diffusion of Au<sub>ad</sub>Cl<sub>2</sub> complex on Au(001) without Cl coadsorbate

The specific adsorption of chloride anions on a Au surface modifies the diffusion barriers.<sup>37</sup> Moreover, on Cl covered Au(111), a Au<sub>ad</sub>Cl<sub>2</sub> complex has been observed at chlorine coverage slightly above 0.33 ML in low-temperature STM images by Andryushechkin *et al.*<sup>38</sup> Thus, the gold halide complexes may act as the diffusion species on Cl covered Au(001).

As a very first step, we discuss the diffusion of the Au<sub>ad</sub>Cl<sub>2</sub> complex on clean unreconstructed Au(001) and compare it to the literature.<sup>19,21</sup> In agreement with previous authors, the adsorption site of the Au<sub>ad</sub>Cl<sub>2</sub> complex on Au(001) is the bridge site, with the Cl atoms pointing toward neighboring bridge sites; see Fig. 1. This is in contrast to the Au adatom and the Au<sub>ad</sub>Cl complex on Au(001) which are known to adsorb at the hollow site.<sup>18–20,39</sup> Figure 1 shows three diffusion paths for the Au<sub>ad</sub>Cl<sub>2</sub> complex. The lowest activation barrier corresponds to path C and amounts to 70 meV. The activation energy of Au<sub>ad</sub>Cl<sub>2</sub> thus corresponds to only 11% of the hopping diffusion via bridge of Au<sub>ad</sub> on the clean unreconstructed Au(001) surface and 17% of the exchange diffusion process.<sup>19,20,39</sup> It should be noted that the Au<sub>ad</sub>Cl<sub>2</sub> complex can diffuse to any adsorption site via paths of type C, while paths A and B promote only one direction of diffusion separately.

In Table I, we summarize our results for Au<sub>ad</sub>Cl<sub>2</sub> complex diffusion and compare them to the literature. Activation barriers and the corresponding variation of dipole moment for paths A and B are in good agreement with Ref. 21. With respect to the variation of dipole moment  $\Delta\mu$  at the transition state, the three proposed mechanisms are characterized by a negative  $\Delta\mu$ . This is ascribed to the elevated position of the Cl relative to Au<sub>ad</sub> along the path. In fact,



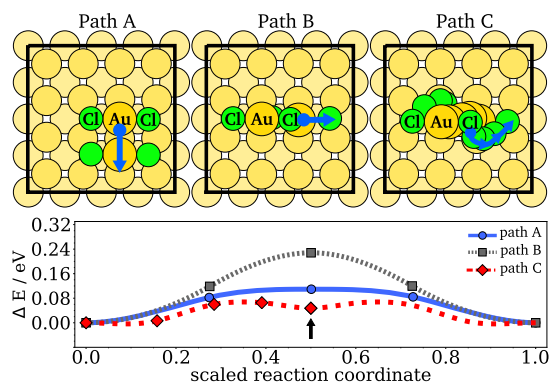


**FIG. 1.** Top: Diffusion paths for the  $\text{Au}_{\text{ad}}\text{Cl}_2$  complex on the clean Au(001) surface. Calculations were carried out with 4 layer slabs. Bottom: Variation of the energy along the diffusion path, with the adsorption minimum (bridge site) taken as reference. Along path C, a local minimum (denoted by an arrow) is encountered when the Au adatom resides at a hollow site of the substrate lattice. The first half of path C (initial to hollow site) has been calculated, while the second half has been obtained by applying a rotation by  $180^\circ$  around an axis perpendicular to the surface through the respective hollow site.

the diffusion of a single Au adatom via exchange has also a negative  $\Delta\mu$ ,<sup>18,21</sup> a sign opposite to the case of Au adatom diffusion via bridge calculated by Refs. 18 and 21.

Regarding the stability of the  $\text{Au}_{\text{ad}}\text{Cl}_2$  complex on the otherwise clean unreconstructed Au(001) surface, we note that the energy is lowered by 0.15 eV if two Cl atoms dissociate from the  $\text{Au}_{\text{ad}}\text{Cl}_2$  complex and adsorb separately on the otherwise clean surface. This result is in agreement with the result of Mesgar,<sup>21</sup> who has already pointed out this fact. Furthermore, consistent with this work, the  $\text{Au}_{\text{ad}}\text{Cl}$  complex is energetically preferable as long as the transition to the hex-reconstructed substrate is not considered. However, the  $\text{Au}_{\text{ad}}\text{Cl}_2$  complex becomes the most stable local Cl adsorption structure of  $\text{Au}_{\text{ad}}$  for the range of the more positive chemical potentials considered in this work. The effect of the specifically coadsorbed Cl atoms will be accounted for in the DFT calculations presented in Secs. III B and III D.

## B. Self-diffusion of $\text{Au}_{\text{ad}}$ on Cl covered Au(001)

The sample potential range where the Au substrate is unreconstructed ( $1 \times 1$ ) overlaps with the potential range where the

**TABLE I.** Comparison with theoretical studies by Mesgar<sup>21</sup> of diffusion barriers  $\Delta E$  (eV) and variation of dipole moment  $\Delta\mu$  (eÅ) at the transition state for  $\text{Au}_{\text{ad}}\text{Cl}_2$  diffusion on the clean Au(001) surface. High symmetry sites are denoted as t: top, b: bridge, h: hollow. e denotes the absolute value of the electron charge.

Pathway	Fig. 1	$\Delta E$ (eV)		$\Delta\mu$ (eÅ)	
		This work	Ref. 21	This work	Ref. 21
b $\rightarrow$ t $\rightarrow$ b	A	0.11	0.15	-0.07	-0.10
b $\rightarrow$ h $\rightarrow$ b	B	0.23	0.18	-0.05	-0.17
	C	0.07	...	-0.12	...

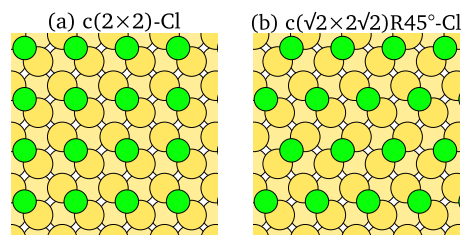


**FIG. 2.** Structure model of the metal/halide interface of Au(001). (a)  $c(2 \times 2)$ -Cl adlayer structure as observed in Ref. 22, (b)  $c(\sqrt{2} \times \sqrt{2})R45^\circ$ -Cl adlayer at coverage  $\Theta = 1/2$  as described in Ref. 23. (b) is a centered reconstruction with respect to the adlayer but not to the substrate.

$c(2 \times 2)$ -Cl adlayer structure has been observed.<sup>22</sup> Furthermore, also a  $c(\sqrt{2} \times \sqrt{2})R45^\circ$ -Cl has been found in experiment.<sup>23</sup> Figure 2 schematically shows the two experimentally observed Cl adlayer reconstructions. The schematic model proposed for the  $c(2 \times 2)$ -Cl adlayer in Ref. 22 differs from the DFT equilibrium structure with respect to the Cl adsorption sites, which is the Au-bridge site in the case of DFT,<sup>19</sup> as shown in Fig. 2.

Our DFT calculations have shown that the adsorption energy of Cl with respect to an isolated  $\text{Cl}_2$  molecule amounts to -1.08 eV for  $c(2 \times 2)$ -Cl and -1.06 eV per atom for  $c(\sqrt{2} \times \sqrt{2})R45^\circ$ -Cl. The small difference between the energies is below the accuracy of our DFT calculations. Thus, both reconstructions will be considered. Now the questions come across: what is the structure and chlorine chemical bonding near  $\text{Au}_{\text{ad}}$  on both Cl covered Au(001) surfaces? How does  $\text{Au}_{\text{ad}}$  diffuse in case of both Cl adlayer reconstructions? To answer the first question, we have first relaxed configurations chosen by chemical intuition. Furthermore, a set of local adsorption configurations were investigated with metadynamic-BOMD and BOMD simulations at finite temperature, where intermediate configurations were ionically relaxed. Different adsorption configurations are listed in the [supplementary material](#).

In the case of both  $c(2 \times 2)$ -Cl and  $c(\sqrt{2} \times \sqrt{2})R45^\circ$ -Cl adlayers with  $\Theta = 1/2$ , the  $\text{Au}_{\text{ad}}\text{Cl}_2$  complex has turned out to be the most stable structure. It is adsorbed on the bridge site; see Figs. 3 and 4. This differs from a previous suggestion in Ref. 10 and influences the argumentation for the potential dependence of Au self-diffusion on the Au(001) surface in the electrochemical environment.

Experimental observations of the  $\text{Au}_{\text{ad}}\text{Cl}_2$  complex on Cl covered Au(001) is not known to us, but a low-temperature STM study by Andryushechkin *et al.*<sup>38</sup> on Au(111) has demonstrated that after the formation of the  $(\sqrt{3} \times \sqrt{3})R30^\circ$ -Cl adlayer, the nucleation of  $\text{Au}_{\text{ad}}\text{Cl}_2$  complex takes place. Moreover, DFT calculations in Ref. 38 have confirmed that the Au atom from the  $\text{Au}_{\text{ad}}\text{Cl}_2$  complex occupies the bridge site, with the Cl atoms on-top positions on Au(111). In Table II, we compare the interatomic distances of the  $\text{Au}_{\text{ad}}\text{Cl}_2$  complex on clean and Cl covered Au surfaces. Inspection of Table II shows that the  $\text{Au}_{\text{ad}}\text{-Cl}_c$  bond lengths of the  $\text{Au}_{\text{ad}}\text{Cl}_2$  complex on clean Au(001) and Cl covered Au surfaces do not differ significantly. Another important feature is the distance between the  $\text{Au}_{\text{ad}}\text{Cl}_2$  complex and the substrate. Table II shows the distances of  $\text{Au}_{\text{ad}}$  and  $\text{Cl}_c$  to the substrate  $\text{Au}_s$  separately. The  $\text{Au}_{\text{ad}}\text{-Au}_s$  separation varies only slightly; this is attributed to the fact that the adsorption site is the same for clean Au(001) and Cl covered Au surfaces.

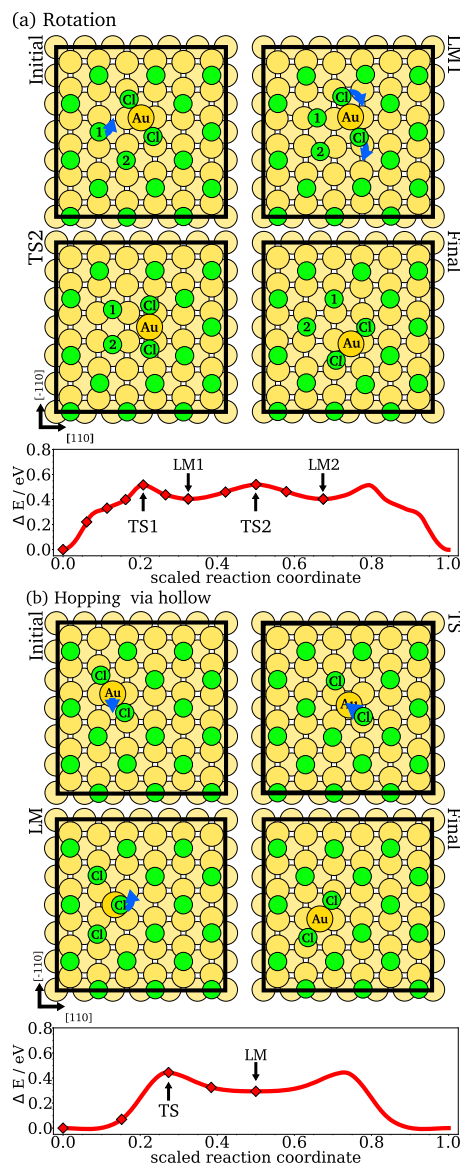


**FIG. 3.** Initial and final position for the diffusion of  $\text{Au}_{\text{ad}}$  on a completely  $c(2 \times 2)$ -Cl covered Au(001) surface as well as the intermediate configurations for the rotation mechanism (a) and hopping via hollow (b). Along the paths, local minima are encountered; they are denoted as LM, and the transition states are denoted as TS. The thickness of the Au slab is 4 layers. The squares represent the  $p(6 \times 6)$  surface unit cell used in the calculation. The diffusion path is indicated schematically by arrows. The variation of the energy along the diffusion paths is shown for paths (a) and (b). Diamonds represent the calculated configurations; the line is an interpolation of energies along the diffusion path. Parts of the paths are derived from symmetry operations.

The  $\text{Cl}_c$ -Au<sub>s</sub> separation for the clean Au(001) represents the larger variation, as to be expected.

To quantify the charge transfer from the surface to the adsorbates, we have applied Bader's analysis<sup>41</sup> using the program by the Henkelman group.<sup>42–45</sup> The charges of the chlorine atoms in the

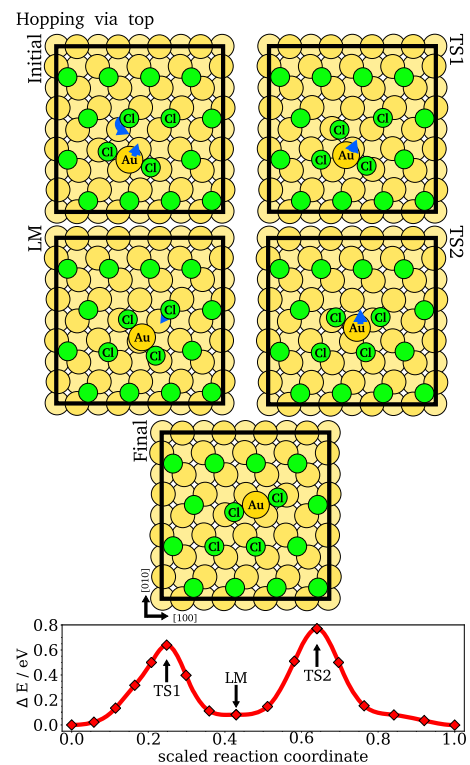


**FIG. 4.** Top: Diffusion of  $\text{Au}_{\text{ad}}$  on a completely  $c(\sqrt{2} \times \sqrt{2})R45^\circ$ -Cl covered Au(001) surface via top site. Calculations were carried out with slabs containing 4 layers Au. Bottom: The variation of energy along the diffusion path. Diamonds represent the calculated configurations along the diffusion path.

$\text{Au}_{\text{ad}}\text{Cl}_2$  complex are equal to  $-0.35 e$ , while the charge on the chemisorbed Cl atoms on Au(001) without  $\text{Au}_{\text{ad}}$  is  $-0.39 e$ . These values are consistent with the ones reported for Cl/Au(111) by Gao *et al.*<sup>46</sup> and by Andryushechkin *et al.*<sup>38</sup> Analogously to the findings for the  $\text{Au}_{\text{ad}}\text{Cl}_2$  complex on Au(111) in Ref. 38, the gold adatom  $\text{Au}_{\text{ad}}$  is positively charged with  $+0.39 e$  independent of the Cl adlayer. In contrast to  $\text{Au}_{\text{ad}}$ , the gold atoms of the first layer carry charges between  $+0.10 e$  and  $+0.15 e$ . This difference indicates that  $\text{Au}_{\text{ad}}$  from the  $\text{Au}_{\text{ad}}\text{Cl}_2$  complex and the gold atoms of the substrate have different ionicity.

To this point, we have analyzed the adsorption configurations with minimum energy for both Cl adlayers. In Secs. III B 1 and III B 2, we present the diffusion paths with lowest energy barriers.

### 1. $\text{Au}_{\text{ad}}/c(2 \times 2)$ -Cl Au(001)

Primarily, for  $c(2 \times 2)$ -Cl Au(001), we found two mechanisms: a rotation and hopping via hollow. The first mechanism is based on a rotation of the  $\text{Au}_{\text{ad}}\text{Cl}_2$  complex and the neighboring  $\text{Cl}_{\text{ad}}$ ; see Fig. 3. As a first step, the chlorine adatoms move consecutively to the next bridge sites as in the intermediate configuration. Then, the  $\text{Au}_{\text{ad}}\text{Cl}_2$  complex rotates. During the rotation, the charge of the atoms of the  $\text{Au}_{\text{ad}}\text{Cl}_2$  complex remains approximately the same, as

**TABLE II.** Interatomic distances for the  $\text{Au}_{\text{ad}}\text{Cl}_2$  complex on clean and Cl covered Au surfaces.  $\text{Au}_{\text{ad}}$ : gold adatom,  $\text{Au}_{\text{s}}$ : gold atom from the substrate,  $\text{Cl}_{\text{c}}$ : chlorine from the  $\text{Au}_{\text{ad}}\text{Cl}_2$  complex,  $\text{Cl}_{\text{ad}}$ : chlorine atom from the Cl adlayer. Schwerdtfeger *et al.*<sup>40</sup> have calculated the Au–Cl bond distance for the  $\text{Au}_{\text{ad}}\text{Cl}_2^-$  complex, which amounts to 2.34 Å. All data for Au(111) are from Ref. 38.

	Interatomic distance (Å)					
	This work					Au(111) <sup>38</sup>
	$c(2 \times 2)\text{-Cl}$		$c(\sqrt{2} \times 2\sqrt{2})\text{R}45^\circ\text{-Cl}$			$(\sqrt{3} \times \sqrt{3})\text{R}30^\circ\text{-Cl}$
Clean	No vacancy	Cl vacancy	No vacancy	Cl vacancy		
(Fig. 1)	(Fig. 2)	(Fig. 7)	(Fig. 3)	(Fig. 8)	[Fig. 5(c) in Ref. 38]	
$\text{Au}_{\text{ad}}\text{-Cl}_{\text{c}}$	2.31	2.31	2.31	2.31	2.31	2.30
$\text{Cl}_{\text{c}}\text{-Au}_{\text{s}}$	3.00	2.67	2.66	2.67	2.67	2.65
$\text{Au}_{\text{ad}}\text{-Au}_{\text{s}}$	2.84	2.88	2.88	2.88	2.87	2.94

well as the bond length between  $\text{Au}_{\text{ad}}\text{-Cl}_{\text{c}}$ . In the hopping process, the  $\text{Au}_{\text{ad}}\text{Cl}_2$  complex dissociates to  $\text{Au}_{\text{ad}}\text{Cl} + \text{Cl}_{\text{ad}}$ . The remaining Cl adatom stays at the bridge site on the surface and  $\text{Au}_{\text{ad}}$  moves to the hollow site. In contrast to the  $\text{Au}_{\text{ad}}\text{Cl}_2$  complex, the charge of  $\text{Au}_{\text{ad}}$  from  $\text{Au}_{\text{ad}}\text{Cl}$  is +0.22, close to the Au atoms of the substrate. Two further diffusion paths, one corresponding to an exchange process, where  $\text{Au}_{\text{ad}}$  exchanges with a first layer Au atom, and another one with a hopping from the bridge site to the nearest bridge site, turned out to have unfavorable energy barriers.

Energy variations  $\Delta E$  along the reaction paths are shown in Fig. 3. Path b, hopping via hollow, has the lowest activation energy for diffusion. The transition state along this path corresponds to the  $\text{Au}_{\text{ad}}\text{Cl}_2$  dissociation. The barrier amounts to 0.44 eV. Our diffusion energy barrier is lower by 0.25 eV than the energy barrier of the diffusion path proposed in Ref. 21 at a Cl coverage  $\Theta = 1/2$ . Both our [Fig. 3(b)] and Mesgar's diffusion path (Fig. 5.14 in Ref. 21) proceed via an intermediate AuCl complex; however, the Cl atoms mainly participating in the process are not lined up along a line in the [110]-direction in our case.

The variation of the dipole moment at the transition state via hollow is strongly negative,  $-0.19 \text{ eÅ}$ , due to the elevation of the negatively charged Cl along the reaction path. According to the formula by Giesen *et al.*,<sup>14</sup> a diffusion path with a negative  $\Delta\mu$  would imply an increase in the energy barrier with the sample voltage.

## 2. $\text{Au}_{\text{ad}}/c(\sqrt{2} \times 2\sqrt{2})\text{R}45^\circ\text{-Cl Au}(001)$

In the case of  $c(\sqrt{2} \times 2\sqrt{2})\text{R}45^\circ\text{-Cl}$  at  $\Theta = 1/2$ , the rotation path is energetically unfavorable. This is ascribed to the Coulomb repulsion between the halides.

The diffusion mechanism we found proceeds via a top site; see Fig. 4. Along the diffusion path, a Cl adatom attaches to the  $\text{Au}_{\text{ad}}\text{Cl}_2$  complex and, as a result, a  $\text{Au}_{\text{ad}}\text{Cl}_3$ -like transition structure is formed. The variation of energy along the path is shown in Fig. 4. The large increase in energy corresponds to the formation of the  $\text{Au}_{\text{ad}}\text{Cl}_3$ -like structures and amounts to 0.64 and 0.77 eV. Similarly, a structural model of  $\text{Au}_{\text{ad}}\text{Cl}_3$  was theoretically predicted on Cl covered Au(111) in Ref. 38. Andryushechkin *et al.* found that  $\text{Au}_{\text{ad}}\text{Cl}_3$  is less energetically favorable than  $\text{Au}_{\text{ad}}\text{Cl}_2$ , similar to our

results. However, we note that in our case, the  $\text{Au}_{\text{ad}}\text{Cl}_3$  complex lies with all Cl atoms on the surface, which differs from the structure found in Ref. 38 in the case of the Au(111) substrate where one of the Cl atoms is on top of  $\text{Au}_{\text{ad}}$ . In our calculations, at the transition state, the charge of  $\text{Au}_{\text{ad}}$  amounts to +0.39  $e$  similar to the  $\text{Au}_{\text{ad}}\text{Cl}_2$  complex.

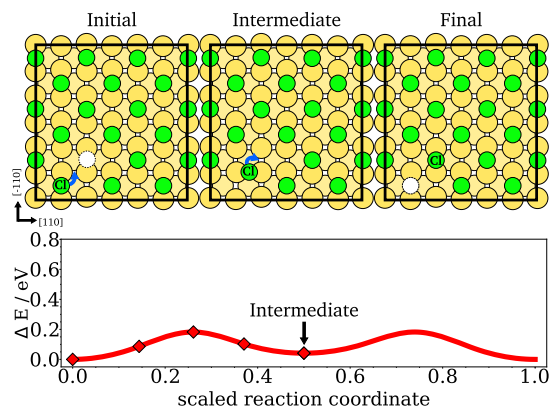
Along the diffusion path, the variation of the dipole moment  $\Delta\mu$  is negative, which would imply an increase in the energy barrier with the sample potential, the same as for  $\text{Au}_{\text{ad}}/c(2 \times 2)\text{-Cl Au}(001)$ .

## C. Cl vacancy diffusion

Experimental data on the surface chloride coverage as a function of the sample potential have been reported by Al-Shakran *et al.*<sup>24,47</sup> The surface coverage increases steeply in the sample potential regime roughly from 0.1 to 0.4 V vs SCE. At more positive potentials, the coverage attains a quasiplateau. The potential range where the  $\text{Cl}^-$  coverage increases steeply overlaps with the potential range of growth experiments by Krug *et al.*<sup>9</sup> Thus, vacancies are present on the surface in this experiment and have to be considered when studying the self-diffusion of Au adatoms at the electrochemical interface. As a first step, we discuss the diffusion paths for a Cl vacancy site on Cl covered Au(001) surfaces in Secs. III C 1 and III C 2.

### 1. Cl vacancy/ $c(2 \times 2)\text{-Cl Au}(001)$

The atomic geometry of a Cl vacancy in the  $c(2 \times 2)\text{-Cl}$  adlayer on Au(001) is depicted in Fig. 5 (denoted as initial state there). The Cl vacancy perturbs the halide adlayer. The charges of the Cl adatoms range from  $-0.36 e$  to  $-0.39 e$ , as compared to  $-0.38 e$  in case of the Cl adlayer without defect. This can be compared to the Bader charge of Cl at low coverages of  $-0.41 e$ . The difference is ascribed to halide-halide interactions. The difference between the  $z$  coordinate of the Cl adatoms on the surface relative to the  $z$  coordinate of Cl adatom on the surface with a vacancy varies from  $-0.05 \text{ Å}$  to  $+0.05 \text{ Å}$  and is correlated with the variation of the charge. The formation energy of a Cl vacancy with respect to a  $c(2 \times 2)\text{-Cl}$  with no defect and half the energy of the  $\text{Cl}_2$  molecule amounts to +0.96 eV. The sign implies the cost of energy.



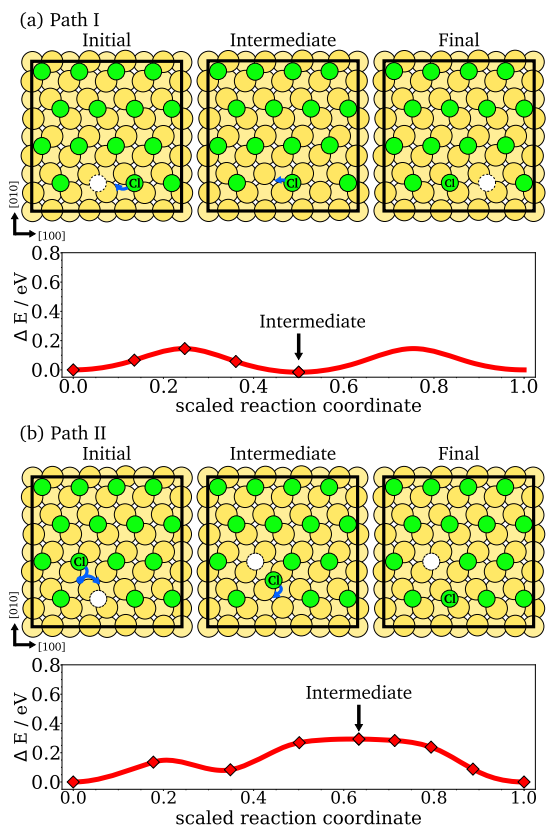
**FIG. 5.** Top: Atomic geometry of the  $c(2 \times 2)$ -Cl adlayer with a vacant site (dotted circle) in a  $(6 \times 6)$  SUC. The diffusion path of a Cl adatom hopping from the bridge site to a vacant site is denoted by a line. Along the path, a local minima (LM) occurs, corresponding to the intermediate configuration. The thickness of the Au slab is 6 layers. Bottom: Variation of energy along the diffusion path. The arrow denotes LM. Diamonds represent calculated configurations.

Figure 5 shows the diffusion path of a Cl vacancy and the variation of energy along the path. The activation energy barrier along the diffusion path amounts to 0.18 eV, comparable to the diffusion barrier of a single Cl adatom. The dipole moment variation  $\Delta\mu$  along the diffusion path is negative and amounts to  $-6$  meÅ. We note that for the single Cl adatom,  $\Delta\mu$  is positive, which correlates with the negative  $\Delta z$  along the diffusion path. The negative sign of  $\Delta\mu$  in the case of the Cl vacancy diffusion is unexpected at first glance because also in the case of the  $c(2 \times 2)$ -Cl with a Cl vacancy, the diffusing Cl adatom comes closer to the Au substrate at the transition state. In comparison with the single Cl adatom diffusion, the variation of  $z$  coordinate at the transition state is smaller. The subtle negative value of  $\Delta\mu$  is ascribed to the variation of the  $z$  coordinates of the surrounding Cl adatoms, which also contributes to  $\Delta\mu$ .

## 2. Cl vacancy/ $c(\sqrt{2} \times 2\sqrt{2})R45^\circ$ -Cl Au(001)

The atomic geometry of a Cl vacancy in the  $c(\sqrt{2} \times 2\sqrt{2})R45^\circ$ -Cl adlayer on Au(001) is shown in Fig. 6. There are two inequivalent neighboring Cl adatoms close to the Cl vacancy site. Therefore, in the case of the  $c(\sqrt{2} \times 2\sqrt{2})R45^\circ$ -Cl adlayer, there are two inequivalent diffusion paths that lead to vacancy hopping in two inequivalent directions. Path I is energetically comparable to the diffusion of a single Cl adatom. However, along path II, the energy barrier increases to 0.29 eV, and the dipole moment differences along the path vary between 0 and  $-80$  meÅ. The higher value of the energy barrier is ascribed to the repulsive interaction between the Cl adatoms and the change in the properties of the Au-Cl bond. The charge of the diffusing Cl adatom amounts to  $-0.38$  e, and the corresponding variation of its  $z$  coordinate amounts to 0.16 Å.

Table III summarizes the results of energy barriers and the corresponding variations of the dipole moment for both Cl adlayers and compares to the diffusion of a single Cl atom on an unreconstructed Au(001) surface.



**FIG. 6.** There are two inequivalent diffusion paths for a vacancy in the  $c(\sqrt{2} \times 2\sqrt{2})R45^\circ$ -Cl adlayer. (a) Path I and (b) path II. The figure shows the atomic geometries of the  $c(\sqrt{2} \times 2\sqrt{2})R45^\circ$ -Cl with a vacant site (dotted circle) in  $c(8 \times 8)$  SUC. The Au slab contains 6 layers. The variation of energy along the diffusion path for (a) and (b) is shown. Diamonds represent calculated configurations along the diffusion path.

## D. Self-diffusion of $Au_{ad}$ on Cl covered Au(001) with a Cl vacancy

Following the reasoning given above, diffusion paths for the  $Au_{ad}Cl_2$  complex in the presence of a nearest-neighbor Cl vacancy have been investigated. For both Cl adlayer reconstructions, the adsorption configuration with the lowest energy is still characterized by a  $Au_{ad}Cl_2$  complex adsorbed at the bridge site; see Figs. 7 and 8.

**TABLE III.** Comparison of diffusion barriers  $\Delta E$  (eV) and variation of dipole moment  $\Delta\mu$  (eÅ) at the transition state for the diffusion of a single Cl on clean Au(001) and Cl vacancy diffusion on Cl covered Au(001) surfaces.

	Clean	$c(2 \times 2)$ -Cl	$c(\sqrt{2} \times 2\sqrt{2})R45^\circ$ -Cl	
			Path I	Path II
$\Delta E$ (eV)	0.14	0.18	0.15	0.29
$\Delta\mu$ (meÅ)	+13	-6	-10	-65

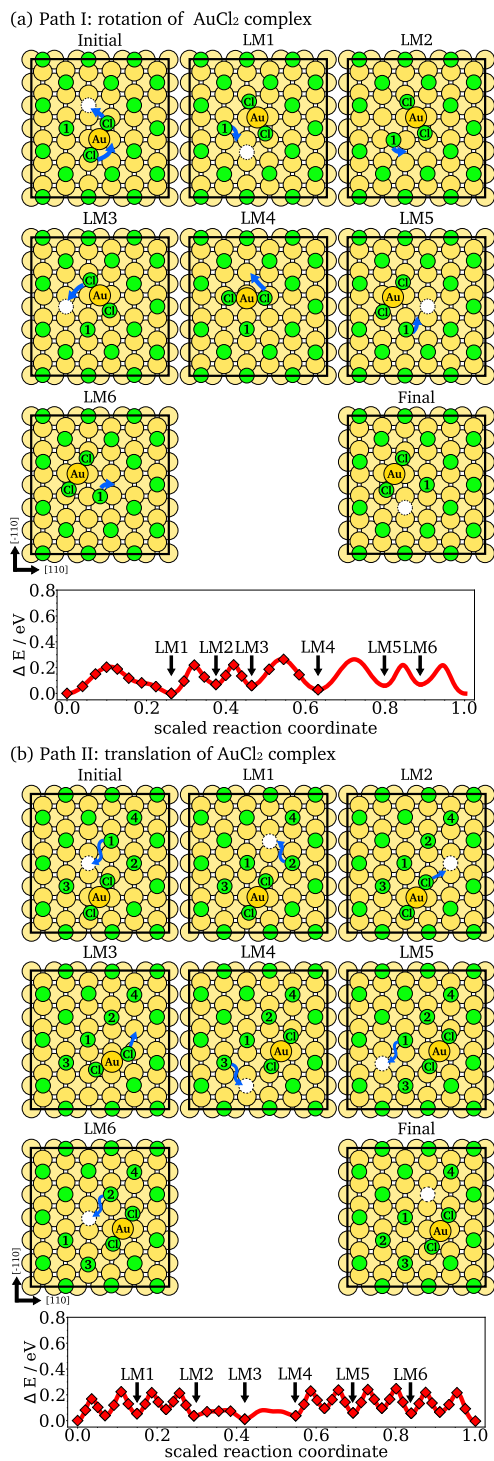


**FIG. 7.** Initial and final position for the diffusion of  $\text{Au}_{\text{ad}}$  on a  $c(2 \times 2)$ -Cl covered  $\text{Au}(001)$  surface with a Cl vacancy in the immediate neighborhood of the  $\text{Au}_{\text{ad}}\text{Cl}_2$  complex. Intermediate configurations for the rotation path (a) and the translation path (b) of the  $\text{Au}_{\text{ad}}\text{Cl}_2$  complex are shown. The Au slabs contain 4 layers. The variation of energy along the diffusion path is displayed for paths (a) and (b). Diamonds represent calculated configurations.

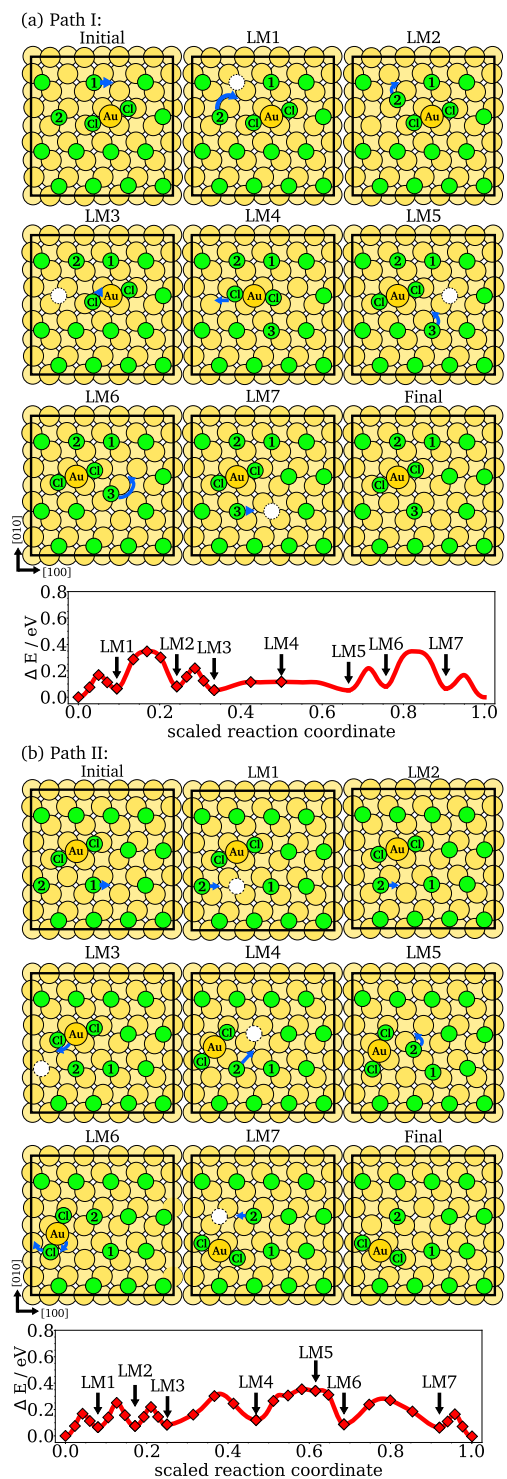


**FIG. 8.** Initial and final position for the diffusion of  $\text{Au}_{\text{ad}}$  on a  $c(\sqrt{2} \times 2\sqrt{2})\text{R}45^\circ\text{-Cl}$   $\text{Au}(001)$  surface containing a Cl vacancy. Intermediate configurations for path I (a) and path II (b) are shown. The Au slabs contain 4 layers. The variation of energy along the diffusion path is displayed for paths (a) and (b). Diamonds represent calculated configurations.

In the case of the  $c(\sqrt{2} \times 2\sqrt{2})R45^\circ$ -Cl adlayer reconstruction, the lowest energy configuration contains a Cl adatom which is not occupying an adsorption site of the original  $c(\sqrt{2} \times 2\sqrt{2})R45^\circ$  sublattice but is displaced by half a lattice constant. Hence, the position of the Cl vacancy is no longer well defined, e.g., compare initial and LM1 configurations in Fig. 8. Despite the presence of the Cl vacancy, neither the interatomic distances of the  $\text{Au}_{\text{ad}}\text{Cl}_2$  complex nor the corresponding Bader charges suffer any appreciable change; see Table II.

The diffusion paths in the presence of a nearest-neighbor halogen vacancy are characterized by elementary diffusion steps involving the Cl vacancy and the  $\text{Au}_{\text{ad}}\text{Cl}_2$  complex separately. Inevitably, this leads to longer diffusion paths, and along them many local minima (LM) are encountered. In fact, the diffusion energy barriers are similar to the diffusion energy barriers of the elementary step of a single Cl vacancy. Hence, the diffusion mechanisms mediated by a Cl vacancy have energy barriers which are approximately only half as large as those corresponding to diffusion paths without a vacancy.

### 1. $\text{Au}_{\text{ad}}/c(2 \times 2)$ -Cl Au(001) with a Cl vacancy

To reach an arbitrary adsorption site, two mechanisms are proposed: path I, characterized by the rotation of the  $\text{Au}_{\text{ad}}\text{Cl}_2$  complex, and path II, characterized by the translation of  $\text{Au}_{\text{ad}}\text{Cl}_2$ . In both mechanisms, the diffusion is accompanied by displacements of the Cl vacancy; see Figs. 7(a) and 7(b).

The first mechanism (Fig. 7) starts with a combined rotation and translation of the  $\text{Au}_{\text{ad}}\text{Cl}_2$  complex. Along this process, the Bader charges and bond length of  $\text{Au}_{\text{ad}}\text{Cl}_2$  undergo only minimal changes. The corresponding energy barrier, from initial to LM1 configurations, amounts to 0.20 eV. Then, the neighboring Cl adatom, denoted with the number 1 in Fig. 7(a), moves to the vacant site (LM1 to LM3), similar to the diffusion steps in Sec. III C. After this, another rotation is performed leading from the LM3 configuration to the LM5 configuration. It should be noted that there is a mirror symmetry that maps LM4 to itself and LM5 to LM3 as well LM2 to LM6. Consecutively, the Cl atom moves to the neighboring vacant site. At the end, the  $\text{Au}_{\text{ad}}\text{Cl}_2$  complex is translated by a lattice constant in the  $[-100]$  direction of the Au substrate with respect to the initial position. The largest activation energy barrier corresponds to the transition state between LM3 and LM4 and amounts to 0.26 eV with respect to the initial configuration.

The second mechanism is mainly composed of consecutive diffusion steps of the Cl vacancy, as seen in Fig. 7(b). From LM2 to LM4 configuration, the  $\text{Au}_{\text{ad}}\text{Cl}_2$  complex moves in the  $[010]$  direction of the substrate, with an energy barrier comparable to the diffusion of a single  $\text{Au}_{\text{ad}}\text{Cl}_2$  complex on the clean Au(001) surface (Fig. 1). With this diffusion path, the  $\text{Au}_{\text{ad}}\text{Cl}_2$  complex is translated by a lattice constant in the  $[010]$  direction of the Au substrate. The overall largest energy barrier amounts to 0.25 eV.

For both mechanisms, the variation of dipole moment at the transition state amounts to  $-0.08$  eÅ and  $-0.02$  eÅ, respectively.

### 2. $\text{Au}_{\text{ad}}/c(\sqrt{2} \times 2\sqrt{2})R45^\circ$ -Cl Au(001) with a Cl vacancy

Figure 8 displays two diffusion mechanisms that in combination can transport the  $\text{Au}_{\text{ad}}\text{Cl}_2$  complex to any other adsorption

site. Similar to  $c(2 \times 2)$ , also here the diffusion consists of  $\text{Au}_{\text{ad}}\text{Cl}_2$  and Cl vacancy diffusion steps separately. Along the proposed diffusion paths, the ionicities and geometric properties of the  $\text{Au}_{\text{ad}}\text{Cl}_2$  complex remain without significant change.

With the first mechanism, the  $\text{Au}_{\text{ad}}\text{Cl}_2$  complex is translated by a lattice constant in the  $[-100]$  direction of the Au substrate with respect to the initial configuration, see Fig. 8(a), where the translation itself occurs between the LM3 configuration and the LM5 configuration with small variation of the total energy. Similar to the Cl vacancy diffusion in Sec. III C, the activation energy barrier amounts to 0.35 eV and corresponds to the diffusion of a Cl adatom to a vacancy site (from LM1 to LM2). The Bader charge of the diffusing Cl adatom is about  $-0.39 e$  and is the largest among the Cl adatoms. With the second path, the complex is transported by  $c(\frac{1}{2}, 1)$  on the Au substrate; see Fig. 8(b). Interestingly, the activation energy barrier also corresponds to the diffusion of a Cl adatom to a vacant site (from LM4 to LM5) and amounts to 0.34 eV. As to be expected, from this observation for both mechanisms, the variation of dipole moment  $\Delta\mu$  is negative and consistent with the results for path II in Fig. 6.

### E. Discussion of induced dipole moments and the effect of an adsorbed water layer

The difference in the electric dipole moment at the transition state relative to the adsorption site (i.e., the ground state) comes out negative for all diffusion paths of the Au adatom (with attached Cl atoms) on Cl covered Au(001) surfaces (coverage  $\Theta = 0.5$ ) presented in this paper; see Table IV. If the dipole moments were unaffected by the electrolyte, this sign of the dipole moment variation would imply an increase in the diffusion barrier height with the sample potential.<sup>14</sup> In that case, the acceleration of Au island coarsening with the sample potential<sup>15</sup> as well as the transition between the layer-by-layer and step-flow growth mode as a function of sample potential observed in Ref. 9 would require alternative explanations beyond the sample potential dependence of the  $\text{Au}_{\text{ad}}$  diffusion energy barrier on the plain terraces. Such effects might include the energy barrier for the detachment of atoms from Au steps<sup>15,18</sup> and the sample potential dependence of island nucleation. However, an important feature of the electrochemical interface, the aqueous environment has, not been considered. Reaction and activation energies have been reported in the literature<sup>48–52</sup> to change in the presence of water. Zope *et al.*<sup>48</sup> have calculated reaction and activation energies for the elementary reaction steps involved in the oxidation of ethanol to acetic acid on Au(111) and Pt(111) with and without explicit solvent. The difference in the reaction energies for solvated case and the vacuum case ranges from  $-0.80$  eV to 0.39 eV on Au(111). The difference in activation energies ranges from  $-0.28$  eV to 0.27 eV on Au(111). Moreover, Iyemperumal and Deskins<sup>52</sup> have found that reaction energies (e.g., for oxygen reduction, formic acid oxidation, C–C cleave, and water gas shift) at the aqueous/Pt(111) interface change up to 0.23 eV with respect to vacuum/Pt(111). But the effect of water can also be less than 0.02 eV in the case of C–C cleavage.<sup>52</sup> To the best of our knowledge, there are no studies addressing the influence of water on activation barriers of halide covered coinage metal surfaces.

Previous work by various authors regarding the metal(111)-water interface (without halides) has shown that while the icelike

**TABLE IV.** Comparison of diffusion barriers  $\Delta E$  (eV) and variation of dipole moment  $\Delta\mu$  (eÅ) for  $\text{Au}_{\text{ad}}$  diffusion on Cl covered Au(001) surfaces with  $\Theta = 1/2$  and containing one Cl vacancy.

	$c(2 \times 2)\text{-Cl}$				$c(\sqrt{2} \times 2\sqrt{2})\text{R}45^\circ\text{-Cl}$		
	No vacancy		Cl vacancy		No vacancy	Cl vacancy	
	Concerted rotation	Via hollow	Path I	Path II	Via top	Path I	Path II
$\Delta E$ (eV)	0.52	0.44	0.26	0.25	0.77	0.35	0.34
$\Delta\mu$ (eÅ)	-0.10	-0.20	-0.08	-0.02	-0.09	-0.09	-0.06

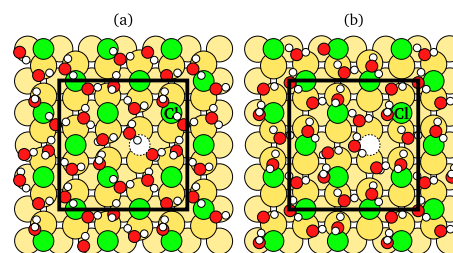
bilayer is not stable at room temperature, it is a good starting point.<sup>53–55</sup> DFT-MD simulations by *Le et al.*<sup>55</sup> have identified the presence of different local water configurations within the interface, and notably structural differences between inert surfaces (e.g., Ag and Au) and more reactive surfaces (e.g. Pt and Pd). Furthermore, DFT studies by Schnur and Groß<sup>53</sup> have shown that the H-up and H-down water bilayers on the (111) metal surfaces studied yield a strong difference in the dipole moments, despite the similarity of the adsorption energies. In the case of water clusters, water hexamers at metal surfaces have been studied intensely with various GGA's<sup>56,57</sup> and dispersion corrected GGA functionals.<sup>58,59</sup> Especially at noble metal surfaces, the buckling of the water hexamers has been found by *Dong et al.* to be sensitive to the choice of the functional.<sup>59</sup> In the case of the metal(001) surfaces, molecular dynamics simulations with classical potentials<sup>60,61</sup> have resulted in a structure of the water layer on Pt(001), which is rectangular. Lin and Groß<sup>62</sup> have investigated the structure of a water layer on Au(001) using DFT. They start from a rectangular structure in a  $(2 \times 2)$  SUC. In their BOMD simulations, the structure of the water changes largely (prior to desorption, depending on temperature). From a calculation of frequencies, they conclude, however, that the structure of their water layer seems not to be realistic.

To obtain a structure model for a static water layer that fits into our  $p(4 \times 4)$  Au(001) surface unit cell, we start from a rectangular structure as described in Ref. 62 with 16 water molecules. We introduce a structural perturbation by putting the  $\text{H}_2\text{O}$  layer on top of the Cl vacancy structure shown in Fig. 9. The relaxed water layer is characterized by hexagonal  $\text{H}_2\text{O}$  rings. This structure is different from the BOMD snapshot shown in Fig. 2(b) from Ref. 62, but a hexagonal  $\text{H}_2\text{O}$  structure also has been observed in the same reference for water on a clean stepped Au(511) surface. The two water structures in Figs. 9(a) and 9(b) are basically the same; they are only slightly displaced with respect to each other.

When placed on the clean Au(001) surface, the hexagon-like structure from Fig. 9 lowers the total energy with respect to the rectangular water structure by 80 meV per  $\text{H}_2\text{O}$  molecule. The nearest-neighbor O–O distances range from 2.55 to 2.94 Å (to be compared ~2.75 Å in Ref. 55, 2.80 Å in Ref. 62, and 2.63 and 2.76 Å in Ref. 56). The H–bond distances are between 1.51 and 1.99 Å (1.83 Å in Ref. 58).  $\Delta z_{\text{O–Au}}$  of the bottommost oxygen layer varies from 2.65 to 3.47 Å. In the case of the fully Cl covered surfaces,  $\Delta z_{\text{O–Cl}}$  ranges from 2.86 to 3.04 Å.

As the next step, we propose a rough estimate of the effect of water on the diffusion energy barrier, disregarding the influence of

the electrochemical interface and the cations from the electrolyte. As Au adatom diffusion is promoted by the presence of a neighboring Cl vacancy [see, in particular, Figs. 7(b) and 8], we here, for simplicity, focus only on the effect of a water layer on the Cl vacancy diffusion (see Fig. 5). Results are summarized in Table V. The diffusion path from the initial to the final configuration is symmetric with respect to the intermediate configuration, the initial and final state being equivalent in the absence of the water layer. The symmetry is broken by the water layer. Table V contains a rough estimate for the energy of the transition state both starting from the initial configuration and the final configuration of the Cl vacancy. For each configuration (initial, transition state, and intermediate in Fig. 5), the atomic geometry of the substrate and Cl adlayer was taken from the calculation without water and kept fixed, while the water layer has been ionically relaxed for each configuration. Both water adlayers as shown in Figs. 9(a) and 9(b) have been considered. Additionally, a NEB calculation has been performed for the diffusion of the Cl vacancy in the presence of the water adlayer shown in Fig. 9(a). Results are in agreement with Table V within the error bars. With regard to our approximate approach based on the frozen vacuum reaction path, we find that the diffusion energy barrier changes by less than 0.01 eV with respect to the energy barrier observed in vacuum if only the two water structures with the lowest energy of the initial configuration are considered. In this case, the dipole moment changes by less than 0.01 eÅ, which is to be compared to the

**FIG. 9.** Initial configuration of the diffusion of a Cl vacancy on the  $c(2 \times 2)\text{-Cl}$  Au(001) in contact with a local hexlike water adlayer. DFT calculation for the frozen substrate and Cl adlayer have been performed until the Hellmann-Feynman forces acting on the relaxed water molecules became smaller than 0.01 eV/Å. The Au substrate has been modeled with 6 layers and a vacuum thickness of ~13 Å. (a) and (b) show two water adlayer configurations, which are slightly displaced with respect to each other.

**TABLE V.** Comparison of energy variation  $\Delta E$  (units are given in the table) and variation of dipole moment  $\Delta\mu$  (units are given in the table) at the initial configuration and the transition state for Cl vacancy on  $c(2 \times 2)$ -Cl covered Au(001) surface.

	Initial		TS	
	$\Delta E$ (meV)	$\Delta\mu$ (meÅ)	$\Delta E$ (meV)	$\Delta\mu$ (meÅ)
Vacuum	0(ref.)	0(ref.)	187	-11
Figure 9(a)	0(ref.)	0(ref.)	190	-5
	88	-130	228	4
Figure 9(b)	12	-5	205	-7
	94	-173	287	-179

estimated accuracy of the calculated dipole moments of 0.01–0.02 eÅ. If also the water layer with higher initial energy is considered, the dipole moment change is +0.13 eÅ at the transition state. Thus, in the case of the water structures with minimum energy of the initial configuration, the effect of a water layer on the energy barrier of Cl vacancy diffusion and the induced dipole moment at the transition state is small. However, we emphasize that the validity of our hexagonal-like water structure requires further analysis (analog to the analysis of vibration frequencies in Ref. 62). The induced dipole moment has turned out to be extremely sensitive to the relaxation of the water molecules; this is ascribed to the large dipole moment of water molecules. The dipole moments will be affected by the dynamics of the water molecules.

While we have introduced a state-of-the-art explicit water layer, the counteractions from the electrolyte are not included in our simulations. Their effect on the diffusion barriers is not clear. From DFT calculations and X-ray diffraction experiments, Keller *et al.*<sup>63,64</sup> have derived a model for the interface between a Cu(001) electrode and  $\text{Cl}^-$  containing electrolytes where the electrochemical double layer contains a layer of anions adsorbed at the metal surface and a layer of counteractions with a water layer in between. Using X-ray diffraction, Nakamura *et al.*<sup>65,66</sup> have derived a model for the  $\text{Ag}(001)/\text{Br}^-/\text{water}/\text{Cs}^+$  interface. In those models, the water molecules are highly oriented with respect to the surface, and in Refs. 63 and 64, the halogen-water separation is distinctly smaller than in case of our water layer. It would be of interest to investigate the effect of the fluctuating distribution of cations at the interface on the diffusion properties of Au adatoms on the Au(001) surface in a  $\text{Cl}^-$  containing electrolyte. Such simulations are, however, beyond the scope of this paper.

#### IV. CONCLUSIONS

Our DFT calculations provide an atomistic view of the structure of the halide adlayer at the interface between the unreconstructed Au(001) surface and the chloride containing electrolyte, as well as the diffusion of  $\text{Au}_{\text{ad}}$  within this adlayer. Both experimentally observed reconstructions of the Cl adlayer,  $c(2 \times 2)$  and  $c(\sqrt{2} \times 2\sqrt{2})R45^\circ$ , come out very close in energy (with an energy difference below to the accuracy of our DFT calculations). They are therefore both considered in this paper. The Cl adlayer strongly modifies the adsorption properties and energies of  $\text{Au}_{\text{ad}}$ . On

Cl covered Au(001),  $\text{Au}_{\text{ad}}$  no longer adsorbs at the hollow site. It forms a  $\text{Au}_{\text{ad}}\text{Cl}_2$  complex, and  $\text{Au}_{\text{ad}}$  binds to the bridge site, as already suggested by other authors for Au(111)<sup>38</sup> and for Au(001).<sup>21</sup> On the completely Cl covered surface, the Au self-diffusion paths have energy barriers at least equal to 0.44 eV. It is only in the presence of a Cl vacancy that this diffusion energy barrier is drastically reduced to 0.26 eV in the case of  $c(2 \times 2)$ -Cl Au(001). Thus, we conclude that the presence of Cl vacancy is crucial to promote the Au self-diffusion at this electrochemical interface. The diffusion energy barrier of  $\text{Au}_{\text{ad}}\text{Cl}_2$  in our calculations is determined by the height of the Cl vacancy diffusion barrier on the respective surface. We note that, due to the complexity of the diffusion path in high-dimensional configuration space with a multitude of local energy minima, the probability of the suggested individual diffusion paths will be small. This is expected to affect the prefactor while the calculated activation energy still is meaningful. If all energy barriers for the elementary diffusion steps were equal, this barrier would determine how rapid the fluctuation is at a given temperature.

The dependence of the activation energy for  $\text{Au}_{\text{ad}}$  self-diffusion on sample potential, however, still poses an open problem for future research. Further DFT simulations are needed to investigate the effect of the electrolyte on the  $\text{Au}_{\text{ad}}$  diffusion barriers.

#### SUPPLEMENTARY MATERIAL

See [supplementary material](#) for (i) an analysis of the accuracy and convergence properties of total energy calculations presented in this paper, (ii) an overview of various low energy atomic configurations which have been considered as candidates for the atomic structure in the vicinity of an Au adatom adsorbed on the completely Cl covered Au(001) surfaces, as well as atomic configurations containing a single Cl vacancy in the neighborhood of  $\text{Au}_{\text{ad}}$ , and (iii) details concerning the calculations to estimate the effect of a water layer on the diffusion energy barrier in the case of Cl vacancy diffusion on the  $c(2 \times 2)$ -Cl Au(001) surface.

#### ACKNOWLEDGMENTS

The numerical computations have been performed at the Rechenzentrum der Christian-Albrechts-Universität zu Kiel. A. C. Dávila thanks PRONABEC-Perú for the financial support via Beca Presidente de la República. Helpful discussions with Professor Dr. O. Magnussen, Dr. J. Stettner, L. Deuchler, and Dr. J. Lück are gratefully acknowledged.

#### REFERENCES

- <sup>1</sup>D. M. Kolb, *Angew. Chem., Int. Ed.* **40**, 1162 (2001).
- <sup>2</sup>A. J. Bard, H. D. Abruna, C. E. Chidsey, L. R. Faulkner, S. W. Feldberg, K. Itaya, M. Majda, O. Melroy, and R. W. Murray, *J. Phys. Chem.* **97**, 7147 (1993).
- <sup>3</sup>J. Lipkowsky, Z. Shi, A. Chen, B. Pettinger, and C. Bilger, *Electrochim. Acta* **43**, 2875 (1998).
- <sup>4</sup>*Interfacial Electrochemistry: Theory, Experiment, and Applications*, edited by A. Więckowski (Marcel Dekker, New York, 1999).
- <sup>5</sup>O. M. Magnussen and A. Groß, *J. Am. Chem. Soc.* **141**, 4777 (2019).
- <sup>6</sup>A.-K. Henß, S. Sakong, P. K. Messer, J. Wiechers, R. Schuster, D. C. Lamb, A. Groß, and J. Wintterlin, *Science* **363**, 715 (2019).
- <sup>7</sup>O. M. Magnussen, J. Hageböck, J. Hotlos, and R. J. Behm, *Faraday Discuss.* **94**, 329 (1992).



- <sup>8</sup>A. S. Varela, W. Ju, T. Reier, and P. Strasser, *ACS Catal.* **6**, 2136 (2016).
- <sup>9</sup>K. Krug, J. Stettner, and O. M. Magnussen, *Phys. Rev. Lett.* **96**, 246101 (2006).
- <sup>10</sup>F. Golks, J. Stettner, Y. Gründer, K. Krug, J. Zegenhagen, and O. M. Magnussen, *Phys. Rev. Lett.* **108**, 256101 (2012).
- <sup>11</sup>B. Rahn, R. Wen, L. Deuchler, J. Stremme, A. Franke, E. Pehlke, and O. M. Magnussen, *Angew. Chem., Int. Ed.* **57**, 6065 (2018).
- <sup>12</sup>A. S. Dakkouri, *Solid State Ionics* **94**, 99 (1997).
- <sup>13</sup>S. Dieluweit and M. Giesen, *J. Phys.: Condens. Matter* **14**, 4211 (2002).
- <sup>14</sup>M. Giesen, G. Beltramo, S. Dieluweit, J. Müller, H. Ibach, and W. Schmickler, *Surf. Sci.* **595**, 127 (2005).
- <sup>15</sup>E. Pichardo-Pedrero, G. Beltramo, and M. Giesen, *Appl. Phys. A* **87**, 461 (2007).
- <sup>16</sup>O. M. Magnussen, K. Krug, A. H. Ayyad, and J. Stettner, *Electrochim. Acta* **53**, 3449 (2008).
- <sup>17</sup>K. Pötting, N. B. Luque, P. M. Quaino, H. Ibach, and W. Schmickler, *Electrochim. Acta* **54**, 4494 (2009).
- <sup>18</sup>J. E. Müller and H. Ibach, *Phys. Rev. B* **74**, 085408 (2006).
- <sup>19</sup>M. Mesgar, P. Kaghazchi, T. Jacob, E. Pichardo-Pedrero, M. Giesen, H. Ibach, N. B. Luque, and W. Schmickler, *ChemPhysChem* **14**, 233 (2013).
- <sup>20</sup>K. Pötting, W. Schmickler, and T. Jacob, *ChemPhysChem* **11**, 1395 (2010).
- <sup>21</sup>M. Mesgar, "Multi-scale modeling of island formation and surface dynamics on the Au(100) surface," Doctoral Thesis (Universität Ulm, 2015).
- <sup>22</sup>Y.-C. Yang, K. Hecker, and O. M. Magnussen, *Electrochim. Acta* **112**, 881 (2013).
- <sup>23</sup>O. M. Magnussen, *Chem. Rev.* **102**, 679 (2002).
- <sup>24</sup>M. Al-Shakran, L. A. Kibler, T. Jacob, H. Ibach, G. L. Beltramo, and M. Giesen, *Surf. Sci.* **651**, 84 (2016).
- <sup>25</sup>P. Giannozzi, S. Baroni, N. Bonini, M. Calandra, R. Car, C. Cavazzoni, D. Ceresoli, G. L. Chiarotti, M. Cococcioni, I. Dabo, A. D. Corso, S. de Gironcoli, S. Fabris, G. Fratesi, R. Gebauer, U. Gerstmann, C. Gougoussis, A. Kokalj, M. Lazzeri, L. Martin-Samos, N. Marzari, F. Mauri, R. Mazzarello, S. Paolini, A. Pasquarello, L. Paulatto, C. Sbraccia, S. Scandolo, G. Sclauzero, A. P. Seitsonen, A. Smogunov, P. Umari, and R. M. Wentzcovitch, *J. Phys.: Condens. Matter* **21**, 395502 (2009).
- <sup>26</sup>P. Giannozzi, O. Andreussi, T. Brumme, O. Bunau, M. B. Nardelli, M. Calandra, R. Car, C. Cavazzoni, D. Ceresoli, M. Cococcioni, N. Colonna, I. Carnimeo, A. D. Corso, S. de Gironcoli, P. Delugas, R. A. DiStasio, Jr., A. Ferretti, A. Floris, G. Fratesi, G. Fugallo, R. Gebauer, U. Gerstmann, F. Giustino, T. Gorni, J. Jia, M. Kawamura, H.-Y. Ko, A. Kokalj, E. Küçükbenli, M. Lazzeri, M. Marsili, N. Marzari, F. Mauri, N. L. Nguyen, H.-V. Nguyen, A. Otero-de-la-Roza, L. Paulatto, S. Poncè, D. Rocca, R. Sabatini, B. Santra, M. Schlipf, A. P. Seitsonen, A. Smogunov, I. Timrov, T. Thonhauser, P. Umari, N. Vast, X. Wu, and S. Baroni, *J. Phys.: Condens. Matter* **29**, 465901 (2017).
- <sup>27</sup>J. P. Perdew, K. Burke, and M. Ernzerhof, *Phys. Rev. Lett.* **77**, 3865 (1996).
- <sup>28</sup>D. Vanderbilt, *Phys. Rev. B* **41**, 7892 (1990).
- <sup>29</sup>K. F. Garrity, J. W. Bennett, K. M. Rabe, and D. Vanderbilt, *Comput. Mater. Sci.* **81**, 446 (2014).
- <sup>30</sup>L. Bengtsson, *Phys. Rev. B* **59**, 12301 (1999).
- <sup>31</sup>B. Meyer and D. Vanderbilt, *Phys. Rev. B* **63**, 205426 (2001).
- <sup>32</sup>H. J. Monkhorst and J. D. Pack, *Phys. Rev. B* **13**, 5188 (1976).
- <sup>33</sup>D. Sheppard, R. Terrell, and G. Henkelman, *J. Chem. Phys.* **128**, 134106 (2008).
- <sup>34</sup>G. Henkelman, B. P. Uberuaga, and H. Jónsson, *J. Chem. Phys.* **113**, 9901 (2000).
- <sup>35</sup>G. Henkelman and H. Jónsson, *J. Chem. Phys.* **113**, 9978 (2000).
- <sup>36</sup>M. Bonomi, D. Branduardi, G. Bussi, C. Camilloni, D. Provasi, P. Raiteri, D. Donadio, F. Marinelli, F. Pietrucci, R. A. Broglia, and M. Parrinello, *Comput. Phys. Commun.* **180**, 1961 (2009).
- <sup>37</sup>M. Giesen, *Prog. Surf. Sci.* **68**, 1 (2001).
- <sup>38</sup>B. V. Andryushechkin, V. V. Cherkez, E. V. Gladchenko, T. V. Pavlova, G. M. Zhidomirov, B. Kierren, C. Didiot, Y. Fagot-Reverat, D. Malterre, and K. N. Eltsov, *J. Phys. Chem. C* **117**, 24948 (2013).
- <sup>39</sup>B. D. Yu and M. Scheffler, *Phys. Rev. B* **56**, R15569 (1997).
- <sup>40</sup>P. Schwerdtfeger, P. D. W. Boyd, A. K. Burrell, W. T. Robinson, and M. J. Taylor, *Inorg. Chem.* **29**, 3593 (1990).
- <sup>41</sup>R. F. W. Bader, *Atoms in Molecules: A Quantum Theory*, International Series of Monographs on Chemistry (Oxford University Press, Oxford, New York, 1994).
- <sup>42</sup>W. Tang, E. Sanville, and G. Henkelman, *J. Phys.: Condens. Matter* **21**, 084204 (2009).
- <sup>43</sup>E. Sanville, S. D. Kenny, R. Smith, and G. Henkelman, *J. Comput. Chem.* **28**, 899 (2007).
- <sup>44</sup>G. A. Henkelman, A. Arnaldsson, and H. Jónsson, *Comput. Mater. Sci.* **36**, 354 (2006).
- <sup>45</sup>M. Yu and D. R. Trinkle, *J. Chem. Phys.* **134**, 064111 (2011).
- <sup>46</sup>W. Gao, T. A. Baker, L. Zhou, D. S. Pinnaduwa, E. Kaxiras, and C. M. Friend, *J. Am. Chem. Soc.* **130**, 3560 (2008).
- <sup>47</sup>M. Al-Shakran, G. Beltramo, and M. Giesen, *Phys. Chem. Chem. Phys.* **16**, 12143 (2014).
- <sup>48</sup>B. N. Zope, D. D. Hibbitts, M. Neurock, and R. J. Davis, *Science* **330**, 74 (2010).
- <sup>49</sup>A. Fortunelli, W. A. Goddard, Y. Sha, T. H. Yu, L. Sementa, G. Barcaro, and O. Andreussi, *Angew. Chem., Int. Ed.* **53**, 6669 (2014).
- <sup>50</sup>M. M. Montemore, O. Andreussi, and J. W. Medlin, *J. Chem. Phys.* **145**, 074702 (2016).
- <sup>51</sup>L. Sementa, O. Andreussi, W. A. Goddard III, and A. Fortunelli, *Catal. Sci. Technol.* **6**, 6901 (2016).
- <sup>52</sup>S. K. Iyemperumal and N. A. Deskins, *ChemPhysChem* **18**, 2171 (2017).
- <sup>53</sup>S. Schnur and A. Groß, *New J. Phys.* **11**, 125003 (2009).
- <sup>54</sup>L. S. Pedroza, A. Poissier, and M.-V. Fernández-Serra, *J. Chem. Phys.* **142**, 034706 (2015).
- <sup>55</sup>J. Le, A. Cuesta, and J. Cheng, *J. Electroanal. Chem.* **819**, 87 (2018).
- <sup>56</sup>A. Michaelides and K. Morgenstern, *Nat. Mater.* **6**, 597 (2007).
- <sup>57</sup>J. Carrasco, A. Hodgson, and A. Michaelides, *Nat. Mater.* **11**, 667 (2012).
- <sup>58</sup>J. Carrasco, J. Klimeš, and A. Michaelides, *J. Chem. Phys.* **138**, 024708 (2013).
- <sup>59</sup>A. Dong, L. Yan, L. Sun, S. Yan, X. Shan, Y. Guo, S. Meng, and X. Lu, *ACS Nano* **12**, 6452 (2018).
- <sup>60</sup>X. Xia and M. L. Berkowitz, *Phys. Rev. Lett.* **74**, 3193 (1995).
- <sup>61</sup>I. C. Yeh and M. L. Berkowitz, *J. Electroanal. Chem.* **450**, 313 (1998).
- <sup>62</sup>X. Lin and A. Groß, *Surf. Sci.* **606**, 886 (2012).
- <sup>63</sup>H. Keller, M. Saracino, H. M. T. Nguyen, and P. Broekmann, *Phys. Rev. B* **82**, 245425 (2010).
- <sup>64</sup>H. Keller, M. Saracino, H. M. T. Nguyen, T. M. T. Huynh, and P. Broekmann, *J. Phys. Chem. C* **116**, 11068 (2012).
- <sup>65</sup>M. Nakamura, N. Sato, N. Hoshi, and O. Sakata, *ChemPhysChem* **12**, 1430 (2011).
- <sup>66</sup>M. Nakamura, Y. Nakajima, N. Sato, N. Hoshi, and O. Sakata, *Phys. Rev. B* **84**, 165433 (2011).



# 5. | Initial Steps Toward Au<sub>ad</sub> Island Nucleation on a $c(2 \times 2)$ -Cl Au(001) Surface

In this chapter, our interest is focused on homoepitaxial growth on Au(001) under electrochemical conditions. Electrodeposition experiments for Au(001) in a Cl<sup>-</sup> containing electrolyte have shown transitions from 3D to layer-by-layer and to step-flow growth mode at positive potentials ( $V_{Ag/AgCl}$ ), where the unreconstructed substrate surface is stable [50]. While island nucleation is essential for layer-by-layer growth, a detailed atomic-scale description of the early steps leading to the formation of Au ad-structures on the  $c(2 \times 2)$ -Cl covered Au(001) electrode surface is still lacking. Therefore, the overall goal of the presented work is to investigate the binding topology of (Au<sub>ad</sub>)<sub>n</sub> adatom structures for  $n \leq 4$  on  $c(2 \times 2)$ -Cl Au(001) surface as well as their stability as a function of Cl chemical potential. The results from Sec. 5.1 have been published in Ref. [229].

In nucleation theory, it is often assumed that all clusters are not mobile [4]. However, the migration of small clusters *e.g.* dimers, trimers, may affect growth processes, specially if their diffusion occurs with low energy barriers [124]. In Sec. 5.2, diffusion processes of Au<sub>ad</sub> dimer on the otherwise clean unreconstructed Au(001) surface reported in the literature are summarized. To gain an insight of the effect of Cl adatom in the diffusion of a Au<sub>ad</sub> dimer, we discuss the diffusion of Au<sub>2</sub>Cl clean unreconstructed Au(001) surface. The activation barrier of Au<sub>2</sub>Cl dimer is  $\approx 6$  times the diffusion barrier of Au<sub>ad</sub>Cl<sub>2</sub> on the clean Au(001) surface and  $\approx 2$  times the barrier of Au<sub>ad</sub>Cl<sub>2</sub> on  $c(2 \times 2)$ -Cl surface in the presence of a Cl vacancy.

## 5.1. Au<sub>ad</sub> Small Clusters on $c(2 \times 2)$ -Cl Au(001)

In this Section our aim is to reveal the local binding topology at and around Au<sub>ad</sub> small clusters on a  $c(2 \times 2)$ -Cl Au(001) surface for Cl coverage  $\Theta$  from 7/18 to 1/2. Assuming that the  $c(2 \times 2)$ -Cl adlayer can exchange Cl<sup>-</sup> ions with the electrolyte the stability for Cl structures are derived for Au<sub>ad</sub> monomer and dimer as a function of Cl chemical potential  $\mu_{Cl}$ . Although our primary focus is on adsorbed clusters at high Cl coverage, we explore the energetics of various Au-Cl complexes adsorbed on the clean Au(001) surface, both cases resemble the system Au<sub>n</sub>/Au(001) at low Cl coverage.

To address Au<sub>n</sub> in the presence of  $c(2 \times 2)$ -Cl adlayer, DFT total energy calculations have been carried out for several configurations with a given number of Au adatoms at various Cl

coverage  $\Theta$  on a  $p(6 \times 6)$  SUC using Quantum Espresso package [117, 118]. The total energy of a configuration  $\mathcal{C}$  will be denoted by

$$E(n, N_{\text{site}}/2 - n_{\text{Vac}}, \mathcal{C}, N_{\text{site}}), \quad (5.1)$$

$n_{\text{Vac}}$  is the number of Cl vacancies in the adlayer.  $N_{\text{site}}$  denotes the number of Au atoms per layer in the  $(1 \times 1)$ -Au surface, which is 36 for a  $p(6 \times 6)$  SUC. Thus, the coverage is defined as the ratio of  $(N_{\text{site}}/2 - n_{\text{Vac}})/N_{\text{site}}$ . The minimum of  $E(n, N_{\text{site}}/2 - n_{\text{Vac}}, \mathcal{C}, N_{\text{site}})$  with respect all configurations  $\mathcal{C}$  at a given  $\Theta$  and  $N_{\text{site}}$  will be only taken into account

$$E_0(n, N_{\text{site}}/2 - n_{\text{Vac}}, N_{\text{site}}) = \min_{\mathcal{C}} E(n, N_{\text{site}}/2 - n_{\text{Vac}}, \mathcal{C}, N_{\text{site}}). \quad (5.2)$$

At a given  $\mu_{\text{Cl}}$  and  $Au_n$  the stable Cl structures results from the minimization of the energy

$$\Delta E_n(n_{\text{Vac}}, \mu_{\text{Cl}}) = E_0(n, N_{\text{site}}/2 - n_{\text{Vac}}, N_{\text{site}}) - E_0(n, N_{\text{site}}/2, N_{\text{site}}) + n_{\text{Vac}}(E_{\text{Cl}_2}/2 + \mu_{\text{Cl}}), \quad (5.3)$$

with respect Cl coverage  $\Theta$ . In Eq. (5.3) the total energy  $E_0(n, N_{\text{site}}/2, N_{\text{site}})$  has been taken as a reference energy, which corresponds to the lowest energy configuration for  $n$  Au adatoms at  $\Theta = 1/2$ . The energy per Cl atom in reservoir is given by  $E_{\text{Cl}_2}/2 + \mu_{\text{Cl}}$ . Following this approach, the equilibrium Cl configurations at and around  $Au_{ad}$  monomer and dimer are identified as a function of  $\mu_{\text{Cl}}$ . It should be noted that configurational entropy effects are not taken into account. Regarding  $\mu_{\text{Cl}}$ , the values of chemical potential are restricted to a range where the  $c(2 \times 2)$ -Cl adlayer at  $\Theta = 1/2$  is stable, see Chapter 3. Thus, the following discussions are valid within the range of  $\mu_{\text{Cl}}$  of -0.94 to -0.35 eV.

Analogously to high Cl coverage, adsorption configurations for Au-Cl complexes on clean unreconstructed Au(001) surface have been calculated by means of DFT. Following Eq. 5.1, the total energy of a configuration  $\mathcal{C}$  will be denoted by

$$E(n, n_{\text{Cl}}, \mathcal{C}, N_{\text{site}}), \quad (5.4)$$

where  $n_{\text{Cl}}$  is the number of Cl atoms in the complex. The lowest energy configuration for a given number of Au and Cl adatoms is given by

$$E_0(n, n_{\text{Cl}}, N_{\text{site}}) = \min_{\mathcal{C}} E(n, n_{\text{Cl}}, \mathcal{C}, N_{\text{site}}). \quad (5.5)$$

Assuming a Cl reservoir with  $\mu_{\text{Cl}}$ , a selection of stable Au-Cl complexes is the result of the minimization of the energy difference

$$E_{\text{diff},n}(n_{\text{Cl}}, \mu_{\text{Cl}}) = E_0(n, n_{\text{Cl}}, N_{\text{site}}) - E_0(n, 0, N_{\text{site}}) - n_{\text{Cl}}(E_{\text{Cl}_2}/2 + \mu_{\text{Cl}}). \quad (5.6)$$

In this case  $E_0(n, 0, N_{\text{site}})$  has been chosen as a reference energy. It corresponds to  $Au_n$  adatoms on Au(001) without coadsorbates, in which Au adatoms occupy epitaxial sites.

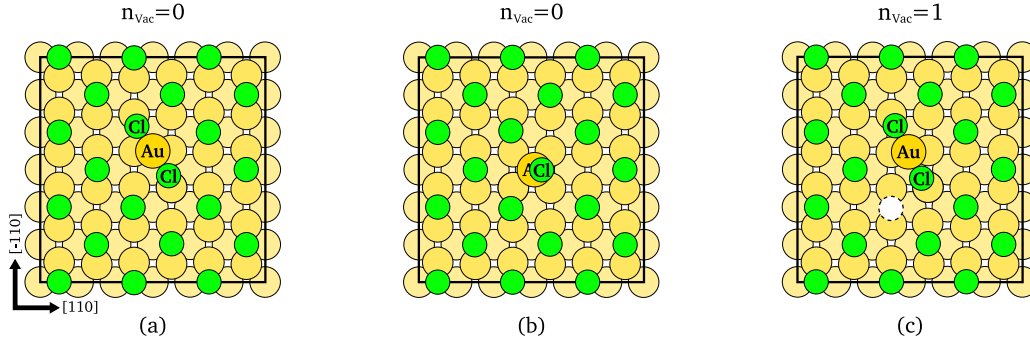


Figure 5.1.: Calculated adsorption configurations for  $Au_{ad}$  on  $c(2 \times 2)$ -Cl adlayer with  $n_{vac} = 0$  (a, b) and  $n_{vac} = 1$  (c). Configurations (a) and (c) correspond to the lowest energy structures for  $n_{vac} = 0$  and 1, respectively. The  $Au_{ad}-Cl_c$  bond lengths of the complex amounts to 2.31 Å for (a) and (c) and 2.27 Å for (b). The black squares denote the  $p(6 \times 6)$  SUC.

### 5.1.1. $Au_{ad}$ Monomer

The atomic configurations and energies of  $Au_{ad}$  adsorbed on  $c(2 \times 2)$ -Cl Au(001) surfaces with  $n_{vac}$  from 0 to 4 here considered are listed in Appendix A.2 and A.6, which have been published in the Supplementary Material of Ref. [158] and [229] respectively.

Among the calculated configurations for the monomer the  $Au_{ad}Cl_2$  complex has turned out to be the most stable structure. The complex is adsorbed at bridge site of the substrate; see Fig. 5.1(a),(c) for  $n_{vac} = 0$  and 1. Further electronic and geometric properties of the complex remain unaltered in the presence of Cl vacancies e.g. interatomic distances of the  $Au_{ad}Cl_2$  complex.

$\Delta E_n(n_{vac}, \mu_{Cl})$  vs.  $\mu_{Cl}$  is shown in Fig. 5.2 as published in Ref. [229]. In addition to the calculated configurations, the energy of a configuration with  $n_{vac}$  has been obtained from a system with  $(n_{vac} - 1)$  plus a Cl vacancy added far away from  $Au_{ad}$  by

$$\Delta E_1^*(n_{vac}, \mu_{Cl}) = \Delta E_1(n_{vac} - 1, \mu_{Cl}) + E_{vacCl}(\mu_{Cl}). \quad (5.7)$$

$E_{vacCl}(\mu_{Cl})$  represents the energy necessary to desorb a Cl adatom from a perfect  $c(2 \times 2)$ -Cl adlayer at a given  $\mu_{Cl}$ , see Eq. (6) in Ref. [229]. The difference between  $\Delta E_1^*(n_{vac}, \mu_{Cl})$  and  $\Delta E_1(\mu_{Cl})$  is a value independent from  $\mu_{Cl}$

$$\begin{aligned} \Delta E_1^*(n_{vac}, \mu_{Cl}) - \Delta E_1(n_{vac}, \mu_{Cl}) = & E_0(1, N_{site}/2 - (n_{vac} - 1), N_{site}) - E_0(0, N_{site}/2, N_{site}) \\ & - \left( E_0(1, N_{site}/2 - n_{vac}, N_{site}) - E_0(0, N_{site}/2 - 1, N_{site}) \right). \end{aligned} \quad (5.8)$$

We observe that  $\Delta E_1^*(n_{vac}, \mu_{Cl}) - \Delta E_1(\mu_{Cl})$  amounts to about is +0.04 and +0.03 eV for  $n_{vac} = 1$  and 2, respectively. In case of  $n_{vac} = 3$  and 4 the difference is negligible. This is attributed to the fact that additional vacancies do not bind to  $Au_{ad}Cl_2$  complex with 2 vacancies.

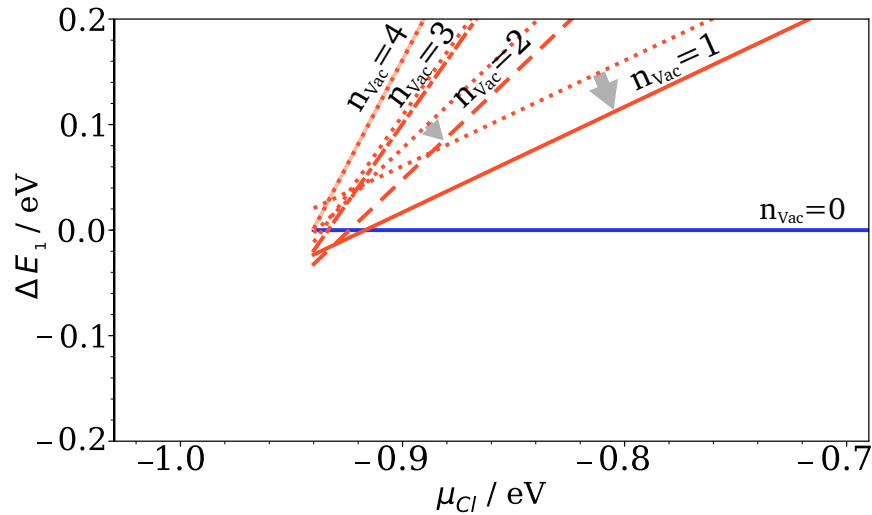


Figure 5.2.:  $\Delta E_1(n_{\text{Vac}}, \mu_{\text{Cl}})$  as a function of  $\mu_{\text{Cl}}$  at a fixed number of Cl vacancies  $n_{\text{Vac}}$  from 0 to 4. Dotted red lines correspond to  $\Delta E_1^*(n_{\text{Vac}}, \mu_{\text{Cl}})$  as defined in Eq. (5.7). Reproduced from J. Chem. Phys. 152, 084701 (2020) [229], with the permission of AIP Publishing.

Regarding stability, from Fig. 5.2 the creation of an additional vacancy on the Cl adlayer becomes only advantageous for values of Cl chemical potential  $\mu_{\text{Cl}}$  below -0.91 eV. For more positive values of  $\mu_{\text{Cl}}$  the  $\text{Au}_{\text{ad}}\text{Cl}_2$  complex with  $\Theta = 1/2$  remains stable.

Notably, Andryushechkin *et al.* have reported that the  $\text{Au}_{\text{ad}}\text{Cl}_2$  complex is stable on  $(\sqrt{3} \times \sqrt{3})R30^\circ$ -Cl Au(111) surface at chlorine coverage  $\Theta > 0.33$  ML [289]. In fact, they have shown that their calculated STM image of  $\text{Au}_{\text{ad}}\text{Cl}_2$  complex on Cl covered Au(111) surface is in agreement with the experimental image at low temperature [289]. Furthermore, other complexes such as AuCl,  $\text{AuCl}_3$  and  $\text{Au}_2\text{Cl}_6$  were not consistent with their experimental STM results.

### 5.1.2. $\text{Au}_{\text{ad}}$ Dimer

The structure and chemical bond of  $\text{Au}_{\text{ad}}$  dimer have been investigated under two conditions: at low and high Cl coverage. For the first case  $\text{Au}_2\text{Cl}_n$  for  $n_{\text{Cl}} \leq 4$  complexes adsorbed on clean unreconstructed Au(001) surface have been calculated. Adsorption configurations are depicted in Fig. 5.3, among these structures the Au adatoms are located on hollow site (see Fig. 5.3 (a),(b)) or bridge site (see Fig. 5.3 (c)-(e)) of the substrate. Detailed information regarding the calculations as well as interatomic distances of the complexes are presented in Appendix A.5. For high coverages a survey of adsorption configurations for  $\text{Au}_2$  on  $c(2 \times 2)$ -Cl Au(001) surfaces with  $n_{\text{Vac}}$  from 0 to 4 have been carried through, corresponding structures and energies are listed in Appendix A.6.

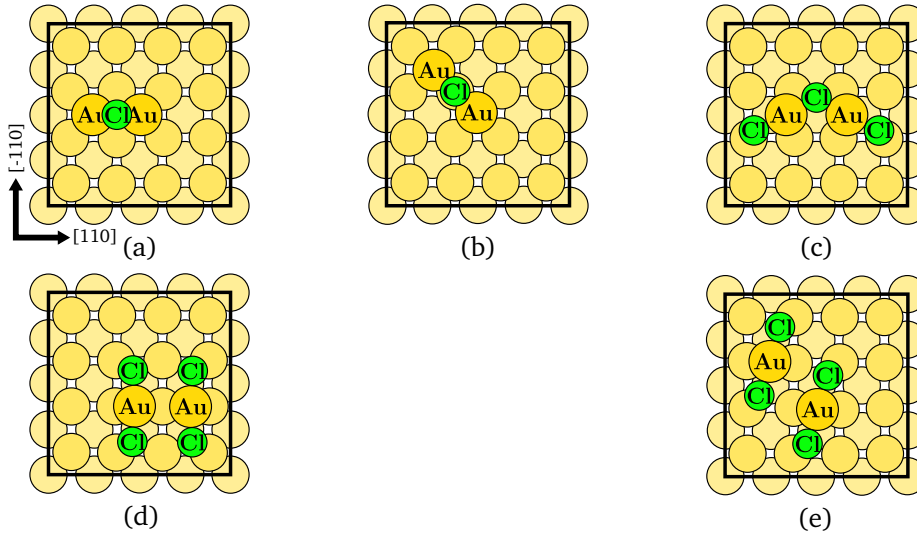


Figure 5.3.: The atomic geometries of the Au dimer adsorbed on the clean unreconstructed Au(001) surface. Following Eq. 5.9 the energy difference for  $\mu_{Cl} = -1.26$  eV ( $\Theta = 1/16$ ) amounts to: (a) -0.16 eV, (b) -0.09 eV, (c) +0.71 eV, (d) +0.70 eV and (e) +0.62 eV. Positive sign denotes that the formation of  $Au_2Cl_n$  complex costs energy. The black squares represent the  $p(4 \times 4)$  surface unit cell used in the calculation. Details regarding the computation are to be found in Appendix A.5.

### $Au_2$ -Cl Complexes

As a first step, we discuss the stability of  $Au_2$ -Cl complexes on the clean unreconstructed Au(001) surface. If a Cl reservoir is assumed with  $\mu_{Cl}$ , the selection of stable complexes is obtained by the minimization of  $E_{diff,2}$  at a given  $\mu_{Cl}$ .

$$E_{diff,2}(n_{Cl}, \mu_{Cl}) = E_0(2, n_{Cl}, N_{site}) - E_0(2, 0, N_{site}) - n_{Cl}(E_{Cl_2}/2 + \mu_{Cl}). \quad (5.9)$$

$E_{diff,2}(n_{Cl}, \mu_{Cl})$  vs.  $\mu_{Cl}$  is plotted in Fig. 5.4.

At equilibrium state between the Cl adlayer and the reservoir the value of  $\mu_{Cl}$  depends on the coverage *e.g.* at  $\Theta = 1/16$   $\mu_{Cl}$  amounts to -1.26 eV. For the complex  $Au_2Cl$  as depicted in Fig. 5.3 (a)  $E_{diff,2}$  amounts -0.16 eV at  $\Theta = 1/16$ . The negative sign indicates that there is an energy gain if a Cl atom is adsorbed on the bridge site of the  $Au_{ad}$  dimer rather than on the terrace at low coverage. This result is consistent with the result of Mesgar (-0.19 eV [60]), who has already pointed out this fact. For  $Au_2Cl$  structure in Fig. 5.3 (b)  $E_{diff,2}$  is about -0.09 eV at  $\Theta = 1/16$ . The absolute energy difference between both  $Au_2Cl$  configurations amounts to 0.07 eV (0.09 eV [60]), while in absence of Cl adatom the energy difference is about 0.20 eV (0.26 eV [186]). In this case the effect of Cl is significant and it is attributed to the  $Au_{ad}$ -Cl bond length, which only varies slightly with respect to  $Au_2Cl$  in Fig. 5.3 (a) Furthermore, the distance between Au adatoms amounts to 3.88 Å, which is 7% smaller than second nearest-neighbor separation. Other complexes such as  $Au_2Cl_3$  (configuration from Ref. [290]) and  $(Au_{ad}Cl_2)_2$  have been calculated, see Fig. 5.3 (c)-(e). At  $\Theta = 1/16$  these

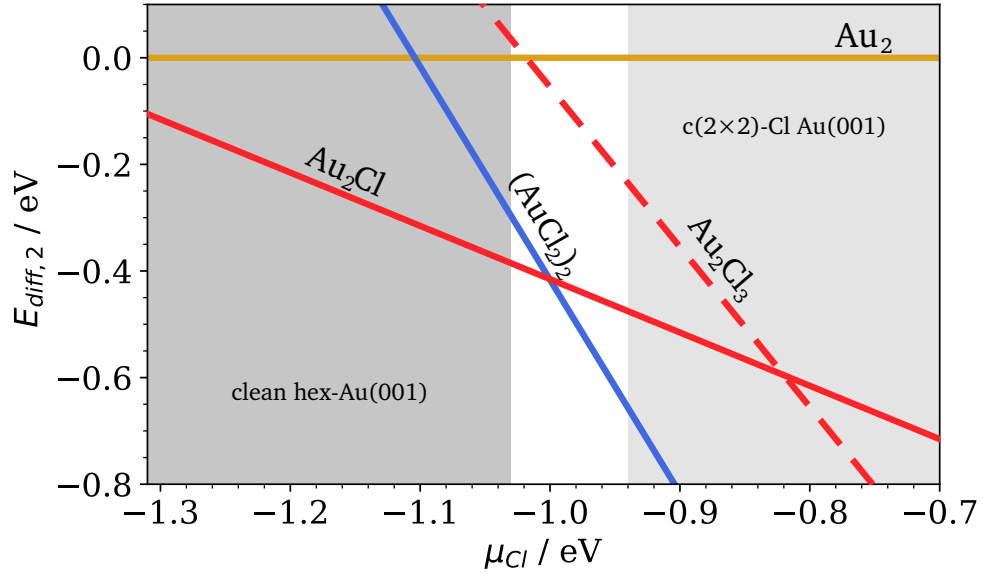


Figure 5.4.:  $E_{diff,2}$  for Au–Cl complexes in Fig. 5.3 (a),(c),(e) plotted as a function of  $\mu_{Cl}$ . Grey regions denote the stability range of the clean hex-Au(001) and  $c(2 \times 2)$ -Cl Au(001) with  $\Theta = 1/2$ .

complexes are energetically unstable *e.g.*  $E_{diff,2}$  amounts to +0.62 eV for  $(Au_{ad}Cl_2)_2$ .

Concerning stability,  $(Au_{ad}Cl_2)_2$  complex is the stable specie in the range of  $\mu_{Cl}$  of -0.94 to -0.35 eV, where the  $c(2 \times 2)$ -Cl adlayer at  $\Theta = 1/2$  is stable. Analogously to  $Au_{ad}$  monomer, for high Cl coverage a question arises: How will the specifically coadsorbed Cl atoms affect to the chemical bonding of  $Au_{ad}$  dimer?

#### **$Au_{ad}$ Dimer on $c(2 \times 2)$ -Cl Au(001)**

When the Cl adsorbates are in equilibrium with the reservoir, the repulsion of Cl adatoms will characterize the equilibrium structures in the vicinity of the  $Au_{ad}$  dimer. To select the equilibrium Cl structures, we employ Eq. (5.3) for  $n = 2$

$$\Delta E_2(n_{Vac}, \mu_{Cl}) = E_0(2, N_{site}/2 - n_{Vac}, N_{site}) - E_0(2, N_{site}/2, N_{site}) + n_{Vac}(E_{Cl_2}/2 + \mu_{Cl}). \quad (5.10)$$

Fig. 5.5 shows  $\Delta E_2$  as a function of  $\mu_{Cl}$  for  $n_{Vac} \leq 4$ . As a result of the minimization of Eq. (5.10) for  $\mu_{Cl} > -0.86$  eV, where the creation of an additional Cl vacancy is unfavorable, a chainlike  $(Au_{ad}Cl_2)_2$  structure along the [100] direction of the substrate is stable as shown in Fig. 5.6 (a). A similarity with the low Cl case is observed, the  $(Au_{ad}Cl_2)_2$  complex on the clean Au(001) is also stable for  $\mu_{Cl} > -0.86$  eV. The presence of the surroundings coadsorbates influences the separation between Au adatoms. At high coverage  $Au_{ad}$ - $Au_{ad}$  bond length is 2.6% smaller than the second nearest-neighbor separation on the unreconstructed Au(001) surface, while on clean surface  $Au_{ad}$ - $Au_{ad}$  bond length is 5% larger than the second nearest-neighbor separation. In this range of  $\mu_{Cl}$  adsorption configurations of  $Au_{ad}$  dimer on epitaxial



sites are energetically unfavorable with respect to the chainlike dimer *e.g.* structure depicted in Fig. 5.6 (b) is energetically unstable by 0.18 eV.

Similar chainlike structures have been reported in the literature *e.g.*  $(Au_{ad}Cl_2)_2$  on Cl covered Au(111) [289],  $(Au(CH_3S)_2)_2$  on methylthiolate covered Au(111) [291, 292].

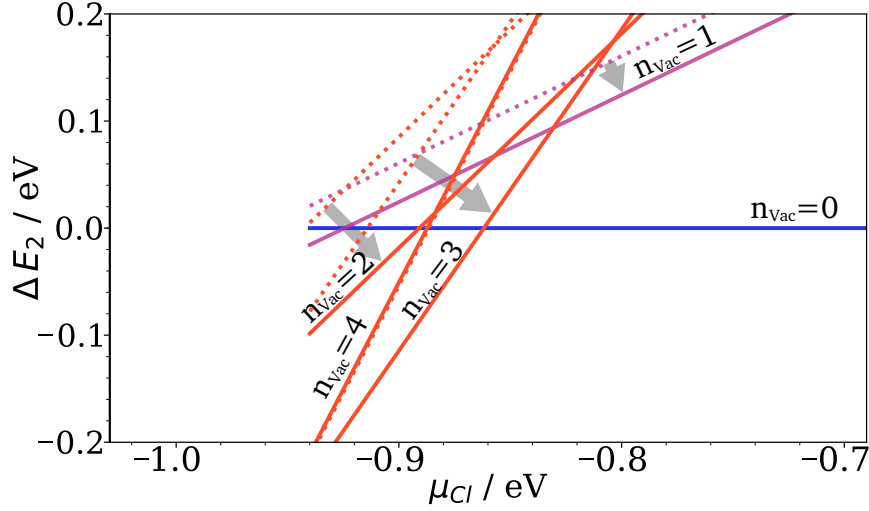


Figure 5.5.:  $\Delta E_2(n_{vac}, \mu_{Cl})$  as a function of  $\mu_{Cl}$  at a fixed number of Cl vacancies  $n_{vac}$  from 0 to 4. Analogously to  $\Delta E_1^*(n_{vac}, n_{vac}, \mu_{Cl})$ , dotted red lines represent the case of an additional Cl vacancy far away from the  $Au_{ad}$  dimer. Reproduced from J. Chem. Phys. 152, 084701 (2020) [229], with the permission of AIP Publishing.

At values of  $\mu_{Cl} < -0.86$  eV a  $Au_2Cl$  cluster, in which  $Au_{ad}$  adatoms occupy nearest-neighbor positions, is stable as shown in Fig. 5.5 ( $n_{vac} = 3$ ). Similarly, the  $Au_2Cl$  complex adsorbed on clean surface becomes stable for  $\mu_{Cl} < -1.0$  eV. The distance between Cl coadsorbates and the  $Au_2Cl$  could influence substantially in the energetics. For example, for  $n_{vac} = 3$  if the distance between  $Au_2Cl$  cluster and the coadsorbates reduces, adsorption configurations are energetically less favorable over a range from 0.07 to 0.17 eV.

From Sec. 5.1.1 we know that on the  $c(2 \times 2)$ -Cl covered Au(001) surface the binding of two  $Au_{ad}Cl_2$  monomers is the initial step towards  $Au_{ad}$  island formation. The binding energy of a  $Au_{ad}Cl_2$  monomer to another on the  $c(2 \times 2)$ -Cl Au(001) surface depends strongly on the Cl chemical potential, see Fig. 4 in [229]. The energy gain amounts only to 0.06 eV if the chainlike  $(Au_{ad}Cl_2)_2$  is formed, this occurs at  $\mu_{Cl} > -0.86$  eV. When Cl vacancies are available on the adlayer, the absolute value of the binding energy increases up to 0.23 eV for  $\mu_{Cl} \leq -0.86$  eV. This result implies that the nucleation of an Au ad-dimer is distinctly supported by the presence of vacancies in the halide adlayer. While there are of course various parameters that determine the growth mode, we note that a larger absolute value of the binding energy of the nucleus is expected to assist the transition from step-flow to layer-by-layer growth mode.

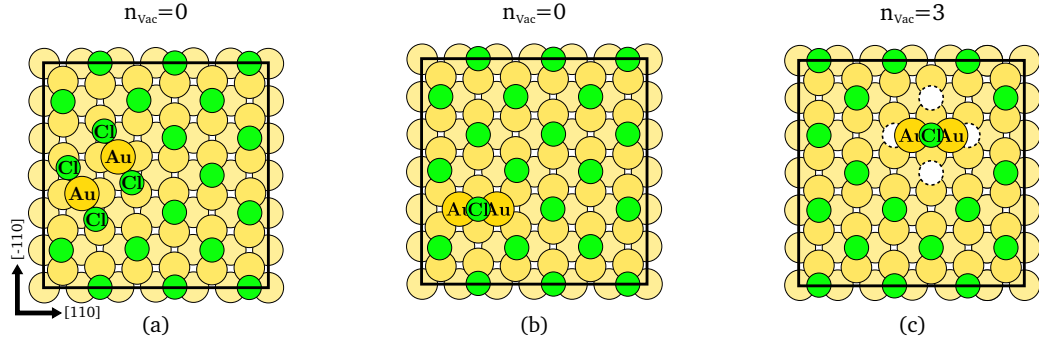


Figure 5.6.: Selected adsorption configurations for  $\text{Au}_{\text{ad}}$  on  $c(2 \times 2)$ -Cl adlayer with  $n_{\text{vac}} = 0$  (a,b) and  $n_{\text{vac}} = 3$  (c). Structures (a) and (c) correspond to the lowest energy configurations for  $n_{\text{vac}} = 0$  and 3, respectively. The surface unit cell is denoted by black squares.

### 5.1.3. Further Clusters of $\text{Au}_{\text{ad}}$

Analogously to the  $\text{Au}_{\text{ad}}$  dimer, calculations have been carried out with low and high Cl coverage. However, due to the large number of possible adsorptions configurations calculations have been restricted to the following cases:

- (i)  $\text{Au}_4\text{Cl}_n$  complexes on the clean  $\text{Au}(001)$  surface.
- (ii)  $\text{Au}_{\text{ad}}$  trimer and tetramer on  $c(2 \times 2)$ -Cl  $\text{Au}(001)$  surface with  $n_{\text{vac}} \leq 2$ .

#### $\text{Au}_4$ -Cl Complexes

The list of  $\text{Au}_4$ -Cl complexes here considered are detailed in Appendix A.7. Fig. 5.7 shows six types of  $\text{Au}_4$ -Cl complexes. The stable  $\text{Au}_4$ -Cl complex at a given  $\mu_{\text{Cl}}$  is selected by minimizing

$$E_{\text{diff},4}(n_{\text{Cl}}, \mu_{\text{Cl}}) = E_0(4, n_{\text{Cl}}, N_{\text{site}}) - E_0(4, 0, N_{\text{site}}) - n_{\text{Cl}}(E_{\text{Cl}_2}/2 + \mu_{\text{Cl}}) \quad (5.11)$$

over the number of Cl atoms  $n_{\text{Cl}}$ . Fig. 5.8 displays  $E_{\text{diff},4}$  as function of Cl chemical potential for a fixed number of Cl atoms.

At  $\mu_{\text{Cl}} = -1.26$  eV ( $\Theta = 1/16$ ) the most stable complex is the linear-like  $(\text{Au}_2\text{Cl})_2$  as depicted in Fig. 5.7 (a). The corresponding value of  $E_{\text{diff},4}$  amounts to -0.44 eV. Interestingly, for a compact complex shown in Fig. 5.7 (e) of  $E_{\text{diff},4}$  amounts only to -0.10 eV. Compact epitaxial clusters are expected for larger number of Au adatoms. For the chainlike structure  $E_{\text{diff},4}$  at  $\mu_{\text{Cl}} = -1.26$  eV amounts to +1.23 eV, while at values of  $\mu_{\text{Cl}} \geq -0.94$  eV the chainlike structure becomes the most stable complex as shown in Fig. 5.8.

#### $\text{Au}_{\text{ad}}$ Trimer and Tetramer on $c(2 \times 2)$ -Cl $\text{Au}(001)$

Energies and geometries of calculated configurations with  $n_{\text{vac}} \leq 2$  are listed in Appendix A.6.

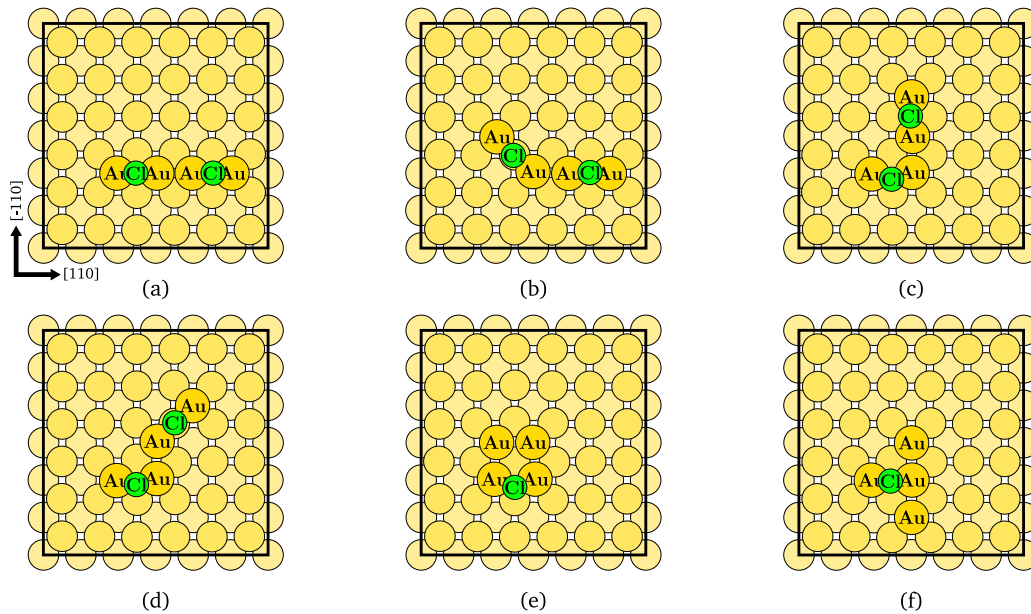


Figure 5.7.: The atomic geometries of the Au–Cl tetramer adsorbed on the clean unreconstructed Au(001) surface. For each  $Au_2$ –Cl complex  $E_{diff,4}$  at  $\mu_{Cl} = -1.26$  eV amounts to: (a)  $-0.44$  eV, (b)  $-0.33$  eV, (c)  $-0.25$  eV, (d)  $-0.18$  eV, (e)  $-0.10$  eV and (f)  $+1.23$  eV. The thickness of the Au slab is 4 layers. The black squares represent the  $p(6 \times 6)$  surface unit cell used in the calculation.

At the perfect  $c(2 \times 2)$ -Cl adlayer the chainlike structures of  $Au_{ad}Cl_2$  are found to be stable, see Fig. 5 (a) in Ref. [229]. The attachment of a successive  $Au_{ad}Cl_2$  results in an energy gain of about  $\approx 0.06$  eV per complex. In the presence of Cl vacancies the lowest energy configurations for trimer and tetramer are characterized by the juxtaposition of  $Au_{ad}Cl_2$  complexes and a  $Au_2Cl$  dimer, see Fig. 5 (b) in Ref. [229]. The separation between Au adatoms of the dimer and the  $Au_{ad}Cl_2$  complex corresponds approximately to the nearest neighbor distance, this occurs due to the adsorption of  $Au_{ad}Cl_2$  on bridge site of the substrate. Similarly to the dimer, we expect epitaxial  $Au_{ad}$  islands configurations for larger number of Cl vacancies.

Previous studies in the literature have found stable coinage metal-S clusters on metal surfaces *e.g.*  $Au_4S_5/Au(100)$  [290],  $Ag_3S_3/Ag(111)$  [293]. Interestingly, Walen *et al.* have pointed out that all Au–S complexes can be regarded as combinations of (near)linear S–Au–S. Although there are some similarities to our findings, the interaction of the adsorbates with the substrate is different as well as their chemical nature *e.g.* S atom occupies the hollow site on Au(001), while Cl adsorbs at the bridge site. For example a diamond-shaped cluster as identified for Au–S in Ref. [290] is not expected for Au–Cl.

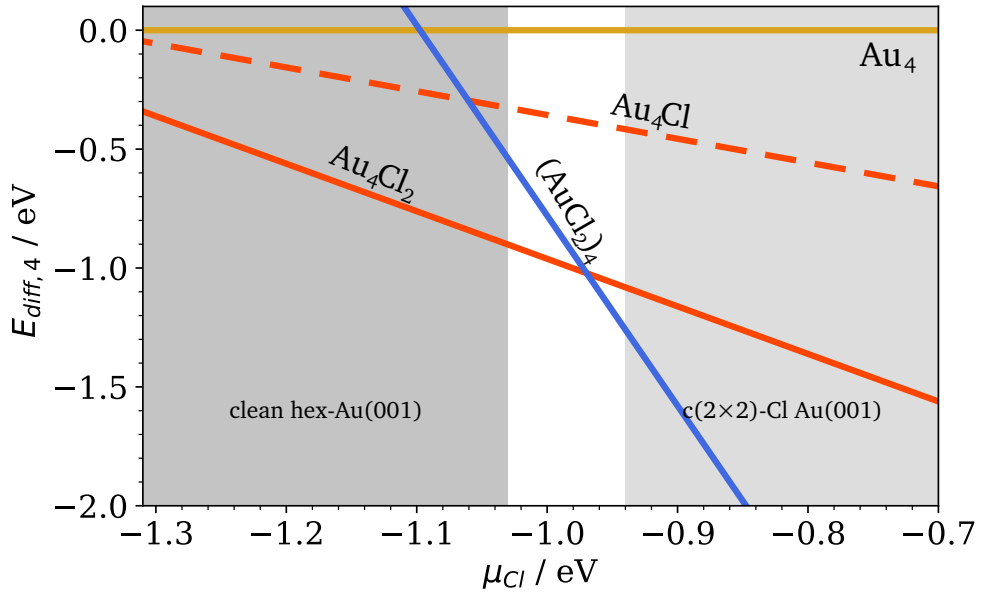


Figure 5.8.:  $E_{\text{diff},4}$  for  $\text{Au}_4$ -Cl complexes in Fig. 5.7 (a),(e),(f) plotted as a function of  $\mu_{\text{Cl}}$ . Grey regions denote the stability range of the clean hex-Au(001) and  $c(2 \times 2)$ -Cl Au(001) with  $\Theta = 1/2$ .

#### 5.1.4. Discussion of Induced Dipole Moments

Under electrochemical conditions the surface mobility can be tuned by the electrode sample potential [49, 294]. The dependence on sample potential can be explained by the coupling of the adsorbate's dipole moment  $\mu$  of hopping rates and the local electric field in the electrolyte at the surface  $\mathcal{E}$  [39, 47, 49, 173]. In a first step toward including the electrochemical environment, the impact of the local electric field in the electric double layer can be estimated by varying the external electric field. Potentially, including the local electric field could change adsorption energies and barriers substantially [28, 180].

In the present, the effect of an electric field has been assessed for the binding energy of the  $\text{Au}_{\text{ad}}$  dimer on Cl covered Au(001) surface by adding the interaction energy  $-\mu_z \mathcal{E}_z$  to the DFT total energies. The lowest energy configuration for a given number of Au adatoms and Cl vacancies on the adlayer remains unaltered within the range of  $-0.4$  to  $+0.4$  V/Å. For example, in case of  $n_{\text{vac}} = 0$  ( $\Theta = 1/2$ ) the energy and dipole moment differences between the  $\text{Au}_{\text{ad}}\text{Cl}$  (see Fig. 5.1 (b)) and the  $\text{Au}_{\text{ad}}\text{Cl}_2$  (see Fig. 5.1 (a)) configurations at  $\mathcal{E}_z = 0.0$  V/Å amount to 0.24 eV and  $-0.41$  eÅ, only for  $\mathcal{E}_z \leq -0.6$  V/Å the difference between both structures is negative *i.e.*  $\text{Au}_{\text{ad}}\text{Cl}_2$  becomes energetically unstable.

Concerning the binding energy, here we only consider the effect of the electric field in the formation of  $\text{Au}_{\text{ad}}$  dimer when there is no exchange of Cl with the electrolyte *i.e.* the number of coadsorbed anions in the initial and final states are the same. If two  $\text{Au}_{\text{ad}}\text{Cl}_2$  monomers, which are far away from each other, form a  $(\text{Au}_{\text{ad}}\text{Cl}_2)_2$  dimer at the perfect  $c(2 \times 2)$ -Cl adlayer, the dipole difference between the initial and final states amounts roughly to  $-0.02$  eÅ. The initial state corresponds to two unit cells with the  $\text{Au}_{\text{ad}}\text{Cl}_2$  at  $\Theta = 1/2$ , while

the final state is composed of a unit cell with the (Au<sub>ad</sub>Cl<sub>2</sub>)<sub>2</sub> dimer with  $\Theta = 1/2$  and another one with the perfect  $c(2 \times 2)$ -Cl Au(001) without Au adatoms.

We assume that Cl adlayer is a reservoir for vacancies. If two Au<sub>ad</sub>Cl<sub>2</sub> monomers, which are bound to one and two Cl vacancies respectively, form a dimer with  $n_{\text{vac}} = 3$  on the  $c(2 \times 2)$ -Cl Au(001) surface, the dipole moment the dipole difference between the initial and final states results in  $-0.18 \text{ e}\text{\AA}$ . This larger value is attributed to the Cl atom, which resides on the bridge site of the dimer. The interaction of such dipole moment with the electric field leads to significant variations in the binding energy *e.g.*  $\pm 0.07 \text{ eV}$  for  $\mathcal{E}_z = \pm 0.4 \text{ V/\AA}$ .

A rigorous treatment of the electrochemical interface, which requires the explicit (or implicit) simulation of the electrolyte (water molecules and ions), is beyond scope this work. Various theoretical studies have been focused on processes involving proton transfer. In particular, the CO dimerization in CO<sub>2</sub> electrochemical reduction on Cu(100) surface has been investigated by Montoya *et al.* [202]. They reported that the reaction energy for  $2^*\text{CO} \rightarrow ^*\text{OCCO}$  can be reduced by 0.2 eV if an uniform electric field of 0.9 V/Å is applied. Moreover, in contact with a single water layer and with an extra H to the water layer the reaction energy decreases by 0.6 and 1.0 eV respectively. The authors pointed out that the solvent stabilizes the dimer, both carbons atoms bound to the surface while at metal/vacuum interface only one carbon bounds to the surface. The stabilization of the dimer as well as the reduction of the corresponding energy barrier have been attributed to a combined effect of solvation and local electric field, which can not be reproduced by an external electric field. In comparison to our system Au adatoms bond to the surface, therefore we expect smaller energy changes for solvation conditions. Altogether, the effect of the electrolyte in an electrochemical environment and the dependence on sample potential still have to be accounted for and are issues for future research.

## 5.2. Diffusion of Au<sub>2</sub>Cl Dimer on Clean Au(001)

Small complexes can influence metal mass transport, for example, in the form of accelerated decay of smaller two-dimensional (2D) metal nanoclusters [293, 295]. Experimental evidence of such carriers on Cl covered Au(001) surface is not known to date. But in [158] the diffusion gold halide species on Cl covered Au(001) surfaces has been discussed. Furthermore, the stable configurations for Au<sub>ad</sub> dimer on  $c(2 \times 2)$ -Cl Au(001) as a function of Cl chemical potential have been identified in Sec. 5.1. To gain a very first insight about the migration of Au<sub>2</sub> on Cl covered, diffusion pathways and energy barriers for Au<sub>2</sub>Cl complex on clean unreconstructed Au(001) have been determined by using climbing image nudged elastic band method (CI-NEB) [145, 146, 296] with PWscf [117]. As a comparison we refer to the diffusion mechanisms of Au<sub>2</sub> on clean unreconstructed Au(001) surface from the literature, a survey is presented in Tab. 5.1.

Reported self-diffusion energy barriers for Au<sub>2</sub> on clean unreconstructed Au(001) surface range between 0.32 eV to 1.0 eV [124, 186, 194, 262, 297]. The two important mechanisms are exchange and shearing processes. The first mechanism is based on the exchange of one of the Au adatom with a first layer Au atom. The transition state is characterized by a Au<sub>ad</sub> trimer structure, and its corresponding energy barrier amounts to 0.24 eV [194]. In

Table 5.1.: Comparison with theoretical studies of diffusion barriers  $E_{act}$  for  $Au_{ad}$  dimer and  $Au_2Cl$  diffusion on the clean  $Au(001)$  surface. The variation of dipole moment  $\Delta \mu$  at transition state for  $Au_2Cl$ . Calculations in Ref. [262] have been performed by means of tight-binding second-moment approximation (TB-SMA). Energies and dipole moments are given in eV and eÅ respectively.

Mechanism	$Au_{ad}$ dimer	$Au_2Cl$	
	$E_{act} / eV$	$E_{act} / eV$	$\Delta \mu / e\text{\AA}$
Perpendicular hopping	0.53 [262]	0.86	-0.03
Collinear hopping	0.73 [262]	0.94	-0.06
Exchange	0.24 [194]	0.64	-0.11
Shearing	0.82 [194, 297], 0.74 [186]	0.45 (0.52 [60])	0.0

the shearing process, one  $Au_{ad}$  diffuses in a direction perpendicular to dimer axis to next neighbor site with an energy barrier of about 0.86 eV [194, 297].

For the  $Au_2Cl$  complex four diffusion mechanisms are shown in Fig. 5.9. In the initial state the  $Au_2Cl$  complex is arranged along the [110] direction of the substrate. Two concerted hopping moves, toward the collinear and perpendicular directions with respect the dimer, are displayed in Fig. 5.9 (a) and (b). The energy barrier for a concerted hopping along the direction [110] amounts to 0.94 eV, while the hopping along the direction [-110] requires 0.08 eV less energy for diffusion. This trend has been observed for  $Au_2$  without a Cl atom, but with a larger difference [262]. The exchange process is depicted in Fig. 5.9 (c). Similarly to the  $Au_{ad}$  dimer, here the transition state is characterized by a  $Au_{ad}$  trimer structure. The Cl is adsorbed at the hollow site of the trimer. In contrast to the exchange mechanism for  $Au_2$  (0.24 eV [194]), the activation barrier amounts to 0.64 eV for  $Au_2Cl$ . The large increase of energy barrier is attributed to the stretching of  $Au_{ad}-Cl$  bond, from 2.46 to 3.04 Å. The lowest activation barrier corresponds to the shearing process and amounts to 0.45 eV, see Fig. 5.9(d). Along this mechanism a local minimum is encountered, which is only 0.07 eV energetically unfavorable with respect the initial state. In this intermediate state the  $Au_2Cl$  complex is oriented toward the direction [100] of the substrate. It should be noted that the  $Au_2Cl$  complex can diffuse to any adsorption site via shearing and exchange process, while the concerted hopping paths promote only one direction of diffusion separately.

In Tab. 5.1, the results for  $Au_2Cl$  are summarized and compared to  $Au_{ad}$  dimer from the literature. Only for the shearing process the activation barrier is reduced by the presence of Cl atom.

The dissociation of  $Au_2Cl$  complex results in  $Au_{ad} + Au_{ad}Cl$ . Furthermore, Mesgar has pointed out that the  $Au_2Cl$  dimer on the clean unreconstructed  $Au(001)$  surface is expected to migrate rather than dissociate [60]. However, at higher Cl coverage it is not clear how the the dissociation of  $Au_2Cl$  into two  $Au_{ad}Cl_2$  monomers proceeds.

In contrast to  $Au_2Cl$  complex, the average number of successful translations for the  $Au_{ad}Cl_2$  complex on clean surface (given by  $\approx \nu_0 e^{-0.07eV/k_B T}$ ) is six orders of magnitude

higher at room temperature. The hopping rate  $Au_{ad}Cl_2$  complex at Cl coverage  $\Theta \approx 0.47$  (given by  $\approx \nu_0 e^{-0.26e\bar{V}/k_B T}$ ) is roughly three orders of magnitude higher at room temperature. Therefore, the  $Au_2Cl$  complex can be considered immobile.

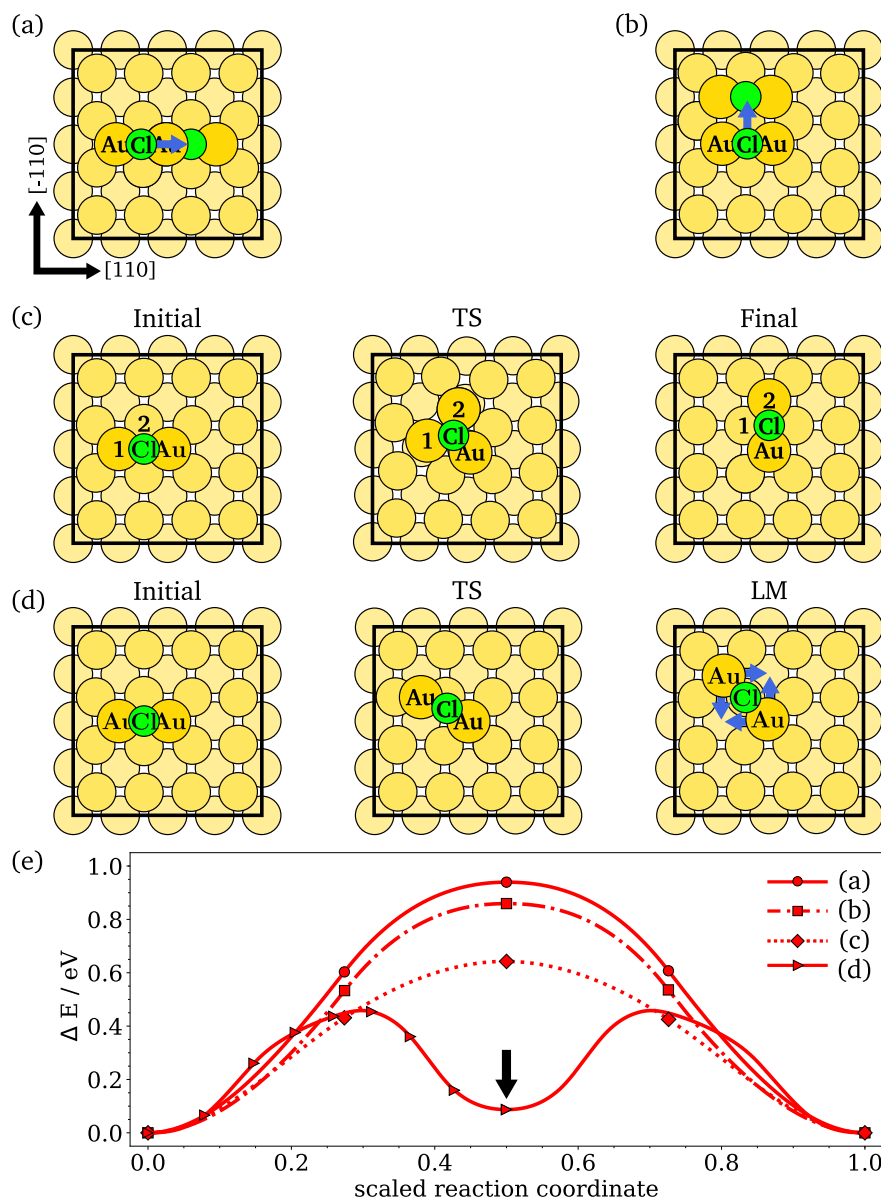


Figure 5.9.: Diffusion paths for the  $\text{Au}_2\text{Cl}$  dimer on the clean unreconstructed  $\text{Au}(001)$  surface. Concerted hopping of the  $\text{Au}_2\text{Cl}$  dimer in the direction (a)  $[110]$  and (b)  $[-110]$  of the substrate. (c) Exchange mechanism, interchange of Au atoms denoted by 1 and 2. (d) Shearing diffusion analog to path in Ref. [60]. Along this path a local minimum (denoted by an arrow) is encountered. The first half of the path has been calculated, while the second half has been obtained by applying symmetry operations. (e) Variation of the energy along the diffusion path, with the adsorption minimum ( $\text{Au}_{\text{ad}}$  at hollow site) taken as a reference. The slabs have been modeled by 4 Au layers. The black squares represent the  $p(4 \times 4)$  surface unit cell used in the calculation.



**5.3. Publication *J. Chem. Phys.* 152, 084701 (2020),  
Copyright (2020) by AIP Publishing**

# Initial steps toward Au<sub>ad</sub> island nucleation on a $c(2 \times 2)$ -Cl Au(001) surface investigated by DFT

Cite as: J. Chem. Phys. 152, 084701 (2020); doi: 10.1063/1.5140244

Submitted: 26 November 2019 • Accepted: 31 January 2020 •

Published Online: 24 February 2020



View Online



Export Citation



CrossMark

Alexandra Celinda Dávila López<sup>a)</sup>  and Eckhard Pehlke<sup>b)</sup>

## AFFILIATIONS

Institut für Theoretische Physik und Astrophysik, Christian-Albrechts-Universität zu Kiel, 24098 Kiel, Germany

<sup>a)</sup> Author to whom correspondence should be addressed: [davila@theo-physik.uni-kiel.de](mailto:davila@theo-physik.uni-kiel.de)

<sup>b)</sup> [pehlke@theo-physik.uni-kiel.de](mailto:pehlke@theo-physik.uni-kiel.de)

## ABSTRACT

Density functional theory calculations are reported that elucidate the initial steps toward Au ad-island nucleation on  $c(2 \times 2)$ -Cl covered Au(001) surfaces, which is relevant for Au electrodeposition in  $\text{Cl}^-$  containing electrolytes. The atomic geometry of  $(\text{Au}_{\text{ad}})_n$  adatom structures for  $n \leq 4$ , as well as their stability as a function of Cl chemical potential, has been determined. The electrolyte, however, has not been accounted for in the computation. We find a weakly bonded  $(\text{Au}_{\text{ad}}\text{Cl}_2)$ -chain as the most stable structure in the case of Cl chemical potentials such that Cl vacancies are suppressed. In the range of Cl chemical potential, where Cl vacancies occur in equilibrium and bind to an (modified) Au<sub>ad</sub> induced ad-structure, the formation of a dimer from two monomers is accompanied by an energy gain between 0.06 and 0.23 eV. For Au<sub>ad</sub> trimer and tetramer formation, the calculations suggest a similar tendency. This suggests that on  $c(2 \times 2)$ -Cl covered Au(001) surfaces, the Au ad-island nucleation is supported by the presence of vacancies in the Cl adlayer.

Published under license by AIP Publishing. <https://doi.org/10.1063/1.5140244>

## I. INTRODUCTION

Electrochemical deposition is a scientifically and technologically important process.<sup>1,2</sup> In general, the growth kinetics is known to depend on the electrolyte,<sup>3</sup> additives,<sup>4</sup> and the sample potential.<sup>5,6</sup> In order to proceed toward a microscopic understanding of the observed growth modes, and ultimately the morphology of the deposited film, detailed knowledge of the atomic-scale processes at the interface is a prerequisite, which may serve as a basis for the investigation of growth kinetics.<sup>7–9</sup> In this paper, we focus on a well-studied model system, Au-deposition on Au(001) in a  $\text{Cl}^-$  containing electrolyte,<sup>5,10–15</sup> and investigate the initial steps toward Au<sub>ad</sub> island nucleation using density functional total energy calculations (not including, however, the effect of water, solvated ions, and sample potential).

For the unreconstructed Au(001) substrate surface in the  $\text{Cl}^-$  containing electrolyte, a  $c(\sqrt{2} \times 2\sqrt{2})\text{R}45^\circ$ -Cl adlayer has been reported in surface x-ray scattering (SXS) experiments.<sup>16</sup> Furthermore, using *in situ* scanning tunneling microscopy (STM),

a defective ordered  $c(2 \times 2)$ -Cl adlayer has been observed by Yang *et al.* in the sample voltage range 0–0.4 V<sub>Ag/AgCl</sub>.<sup>17</sup> At a more positive sample potential, larger than  $\sim 0.71$  V<sub>SCE</sub>, a uniaxially compressed incommensurate  $c(\sqrt{2} \times p)\text{R}45^\circ$ -Cl structure has been observed in STM by Cuesta and Kolb.<sup>18</sup> At a more negative sample potential, below 0.08 V<sub>Ag/AgCl</sub>,<sup>17</sup> the Au(001)-substrate surface becomes hexagonally reconstructed. The calculations presented in this paper refer to the  $c(2 \times 2)$ -Cl adlayer on the unreconstructed Au(001) substrate surface.

*In situ* SXS experiments by Krug *et al.*<sup>5</sup> have revealed a growth mode for Au electrodeposition on Au(001) in a  $\text{Cl}^-$  containing electrolyte that is dependent on the sample potential. Within the potential range, where the hexagonally reconstructed Au(001) substrate is stable, Krug *et al.* have observed a transition from 2D to 3D growth mode. At a more positive sample potential, where the unreconstructed Au(001) surface is stable, a transition from 3D to layer-by-layer growth and, finally, to a step-flow growth mode has been found. The transition from 3D to layer-by-layer growth mode has been attributed to a sample potential dependence of the

Ehrlich–Schwoebel barrier of Au adatoms, which is lowered by the presence of coadsorbed Cl.<sup>5,19</sup> The transition from layer-by-layer to step-flow growth mode has been noted<sup>5</sup> to be consistent with electrochemical STM observations,<sup>3</sup> which showed an increase in the decay rate of Au islands with the sample potential in the Ostwald ripening process.

Concerning theory, Au self-diffusion on clean and Cl covered Au(001) surfaces has been studied in detail. The self-diffusion on clean (1 × 1)-Au(001) surfaces and over steps has been described by various authors in Refs. 20–22, as well as the Au<sub>ad</sub> dimer formation.<sup>22,23</sup> The influence of Cl coadsorbates on the Au<sub>ad</sub> self-diffusion has been calculated with density functional theory (DFT) by Mesgar *et al.*,<sup>14,15</sup> mostly for small Cl coverages. Additionally, in Ref. 15, Mesgar has presented a formation mechanism of a Au<sub>ad</sub> dimer in the presence of a single Cl atom. The present authors<sup>24</sup> have investigated the diffusion paths and diffusion energy barriers for Au self-diffusion on Cl covered Au(001) at a chlorine coverage of  $\Theta = 1/2$  and found Cl vacancies to distinctly assist the Au<sub>ad</sub> diffusion. We note, however, that despite these computational efforts, the dependence of diffusion rate on the sample potential is still an open question.

Moreover, Ostwald ripening of Au islands has been simulated with Kinetic Monte Carlo (KMC) supported by ReaxFF calculations<sup>25</sup> by Kleiner *et al.*<sup>13</sup> Following Ref. 13, Mesgar *et al.*<sup>14</sup> have investigated the effect of chlorine on island ripening by considering the diffusion energy barriers of the Au<sub>ad</sub>Cl complex (at low Cl coverages).

What is still missing for the description of Au(001) growth by electrodeposition is a detailed knowledge about the initial steps of Au island nucleation on the  $c(2 \times 2)$ -Cl covered Au substrate surface. For this purpose, we have performed DFT total energy calculations for various Cl configurations including one or two (up to 4) Au<sub>ad</sub> adatoms and investigated the stability.

The paper is structured as follows: We summarize the computational methods in Sec. II. The Cl coverage and the corresponding equilibrium adsorption structures of Cl on the unreconstructed Au(001) substrate surface are discussed in Sec. III A. In Sec. III B, the most stable configuration of Cl adatoms as a function of Cl chemical potential is derived for the case of a single Au adatom on the (Cl covered) Au(001) substrate. This is an extension of our previous work.<sup>24</sup> In Sec. III C, the calculations are generalized to the Au<sub>ad</sub> dimer, and we calculate its binding energy as a function of Cl chemical potential. Finally, we present selected qualitative results for the Au<sub>ad</sub> trimer and tetramer.

## II. COMPUTATIONAL DETAILS

For this work, the same computational approach as described in Ref. 24 has been applied. Calculations have been carried out in the framework of DFT using PWscf from the Quantum ESPRESSO package<sup>26,27</sup> with the generalized gradient approximation by Perdew, Burke, and Ernzerhof (PBE-GGA)<sup>28</sup> for  $E_{XC}[n]$ . We used the pseudopotential method for all atoms, with ultrasoft pseudopotentials<sup>29</sup> from the open-source GBRV library.<sup>30</sup> The Au(001) surfaces were simulated by using a slab geometry with six metal layers. The substrate surface is unreconstructed (1 × 1). The slabs were separated by a vacuum region with a thickness of about 13 Å. Atoms were

adsorbed on one side, a dipole correction<sup>31,32</sup> has been used. The two Au lower layers were fixed at their ideal bulk positions, and the remaining Au layers and the adsorbate layer were allowed to relax. Geometry optimizations have been carried through until the residual forces acting on the relaxed atoms became smaller than 0.01 eV/Å. The plane-wave cutoff energy is 30 Ry. Brillouin-zone integrations have been performed using a (4 × 4 × 1) Monkhorst–Pack grid of special  $k$ -points<sup>33</sup> for the  $p(6 \times 6)$  surface unit cell (SUC). For Sec. III A, simulations have been carried out with different SUC's dependence on Cl coverage with a  $k$ -point density in the reciprocal space corresponding approximately to a (4 × 4 × 1)  $k$ -point mesh in the full Brillouin zone of a  $p(6 \times 6)$  SUC.

## III. RESULTS AND DISCUSSION

The surface unit cells of the Au slabs are  $p(N \times N)$  or  $c(N \times N)$ , with the number of Au atoms per layer  $N_{\text{site}} = N^2$  or  $N^2/2$ , respectively. The energy of the respective slabs with a clean surface is denoted by  $E_{\text{clean}}(N_{\text{site}})$ . In addition, the unit cell may contain  $m$  Cl atoms. In that case, the Cl coverage amounts to  $\Theta = m/N_{\text{site}}$ . In the  $c(2 \times 2)$ -Cl Au(001) adlayer, the Cl adatoms are adsorbed at Au bridge sites. The number of Cl vacancies refers to a perfect  $c(2 \times 2)$ -Cl adlayer, i.e.,  $n_{\text{vac}} = N_{\text{site}}/2 - m$ . The various possible Cl adsorption configurations at a given  $m$  (or Cl coverage) are enumerated by  $\mathcal{C}$ . Furthermore,  $n$  Au adatoms may be included in the top surface. In that case,  $\mathcal{C}$  also includes the atomic configurations of the Au adatoms. The total energy of the corresponding slab will be denoted as

$$E(n, m, \mathcal{C}, N_{\text{site}}). \quad (1)$$

The minimum of  $E(n, m, \mathcal{C}, N_{\text{site}})$  with respect to all configurations  $\mathcal{C}$  at a given Cl coverage  $\Theta$  and  $n$  Au adatoms will be written as

$$E_0(n, m, N_{\text{site}}) = \min_{\mathcal{C}} E(n, m, \mathcal{C}, N_{\text{site}}). \quad (2)$$

$n = 0$  corresponds to a surface without Au adatoms.

### A. Cl adlayer on Au(001)

As a prerequisite for our study, we first discuss the equilibrium chlorine coverage and Cl adsorption structure on the unreconstructed Au(001) substrate surface as a function of Cl chemical potential  $\mu_{\text{Cl}}$ .

DFT calculations have been performed for a single Cl adatom on  $p(4 \times 4)$ ,  $p(3 \times 3)$ , and  $c(4 \times 4)$  SUCs, corresponding to small Cl coverages 0.063, 0.11, and 0.125. In this case, only one Cl adsorption configuration is considered for each coverage. For  $\Theta = 0.25$ , two configurations have been calculated with a  $p(2 \times 2)$  and a  $p(2 \times 4)$  SUC (configuration from Ref. 34) with 1 and 2 adsorbed chlorines, respectively. In addition,  $c(2 \times 2)$ -Cl adlayer surfaces without and with  $n_{\text{vac}} = 1, 2, 3, 4$ , and 6 Cl vacancies have been calculated within a  $p(6 \times 6)$  SUC, corresponding to Cl coverages 0.47, 0.44, 0.42, 0.39, and 0.33. For  $n_{\text{vac}} \geq 2$ , several configurations  $\mathcal{C}$  of Cl vacancies have been considered. The results are given in the [supplementary material](#).

The stable Cl adsorption structure<sup>35,36</sup> at chemical potential  $\mu_{\text{Cl}}$  has been obtained by minimizing the adsorption energy per substrate surface site,

$$E_{\text{ads}}(\Theta, \mu_{\text{Cl}}) = \left[ E_0(0, m, N_{\text{site}}) - E_{\text{clean}}(N_{\text{site}}) - m(E_{\text{Cl}_2}/2 + \mu_{\text{Cl}}) \right] \frac{1}{N_{\text{site}}}, \quad (3)$$

with respect to the coverage  $\Theta$ . In this equation, the energy per Cl atom in the reservoir is  $E_{\text{Cl}_2}/2 + \mu_{\text{Cl}}$ . Defined in this way,  $E_{\text{ads}}$  is equal to the change in surface energy due to Cl adsorption times the area of the  $(1 \times 1)$  surface unit cell. Note that, in general, the Gibbs free energy of adsorption should be minimized,<sup>36–38</sup> and thus, Eq. (3) is an approximation. The contribution from configurational entropy is neglected, as well as differences between the contributions of differently adsorbed Cl atoms to the vibrational free energy (including zero point energies). The vibrational free energy per Cl atom in the  $c(2 \times 2)$  reconstruction can be incorporated into the chemical potential term. It results in a shift in the value of  $\mu_{\text{Cl}}$ .

$E_{\text{ads}}(\Theta, \mu_{\text{Cl}})$  vs  $\mu_{\text{Cl}}$  is plotted in Fig. 1 for various coverages. The adsorption energy corresponding to the equilibrium coverage is given by the lower envelope of the curves. Moreover, disregarding the presence of Cl coadsorbates, the surface energy of hex-Au(001) is lower than the corresponding value of the  $(1 \times 1)$ -Au(001) surface by  $0.077 \text{ J/m}^2$  ( $0.060 \text{ J/m}^2$  in Ref. 39) for PBE-GGA without an electric field. This competes with the lowering of surface energy of the unreconstructed substrate by Cl adsorption. If the clean hexagonal reconstructed Au(001) surface were considered, the range of stability of the Cl covered Au(001) surfaces with unreconstructed Au(001) substrate surface were cut off at about  $\mu_{\text{Cl}} \approx -1.03 \text{ eV}$ . For this reason, the plot range of  $\mu_{\text{Cl}}$  starts at  $-1.03 \text{ eV}$ . However, this value is uncertain due to the limited number of low coverage Cl adlayers that we have considered here, the neglect of electric field effects, as well as the known sensitivity of the surface energy difference to the approximation of  $E_{\text{XC}}[n]$  as pointed out by Feng *et al.*<sup>39</sup>

The  $c(2 \times 2)$ -Cl adlayer with  $\Theta = 1/2$  becomes stable for  $\mu_{\text{Cl}} \geq -0.94 \text{ eV}$ . In fact, it stays stable as long as  $\mu_{\text{Cl}} \leq -0.35 \text{ eV}$ , where a  $c(\sqrt{2} \times p)\text{R}^{45}$ -Cl structure appears with  $\Theta > 1/2$ . Calculations for  $\Theta = 0.63$  have been performed in a  $p(8\sqrt{2} \times \sqrt{2})\text{SUC}$ .<sup>40</sup> This means that the experimentally observed<sup>17,18</sup> compressed Cl layers only become stable at the Cl chemical potential

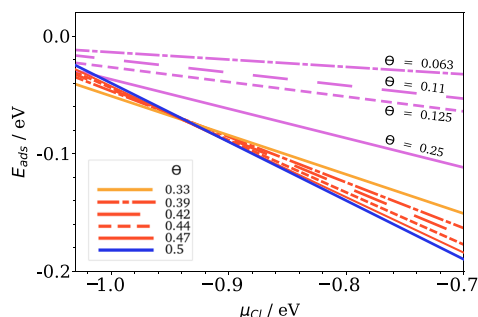


**FIG. 1.** Adsorption energy  $E_{\text{ads}}$  per substrate surface site defined in Eq. (3) at given values of  $\Theta$  is plotted as a function of Cl chemical potential.

beyond the range of  $\mu_{\text{Cl}}$  shown in Fig. 1 and discussed in this paper.

Among those structures that we have calculated, for values of  $\mu_{\text{Cl}}$  below  $-0.94 \text{ eV}$ , a  $c(2 \times 2)$ -Cl adlayer with vacancies with  $\Theta = 0.33$  is stable (see Fig. 1 and structures in Table S3 in the supplementary material). Note that the particular value of  $\Theta$  is supposed to change, if further striped vacancy structures were considered. The equilibrium Cl coverage as a function of  $\mu_{\text{Cl}}$  decreases abruptly. This is attributed to the attractive interaction of Cl vacancies if they occupy nearest neighbor sites of the  $c(2 \times 2)$  lattice and develop straight lines (vacancy chains). There is no net energy gain if, e.g., three vacancies form an L-like structure. The formation energy of the  $2 \text{ Vac}_{\text{Cl}}$ -chain amounts to  $7 \text{ meV}$  ( $\approx 0.3 k_{\text{B}} T_{\text{room}}$ ) per vacancy with respect to separated Cl vacancies. For longer straight chains, the energy gain increases to, e.g.,  $17 \text{ meV}$  ( $\approx 0.7 k_{\text{B}} T_{\text{room}}$ ) per vacancy for  $6 \text{ Vac}_{\text{Cl}}$ -chain. By contrast, other vacancy distributions yield energies consistent with the repulsion of Cl vacancies. To gain an insight into this issue, further calculations have been carried out for a fully and a partially (only  $z$  coordinate) relaxed Cl adlayer. In both cases, the atomic coordinates of the Au substrate have been kept frozen to the case of  $\Theta = 1/2$ . For both calculations, the formation energy of  $6 \text{ Vac}_{\text{Cl}}$ -chain amounts to  $13 \text{ meV}$  ( $\approx 0.5 k_{\text{B}} T_{\text{room}}$ ) per Cl vacancy with respect to separate Cl vacancies. This indicates that the gain of energy may be attributed neither to elastic interactions via the substrate nor to local stresses of the adsorbate layer, but to the change in the electronic structure due to the adsorbate–surface bond.<sup>41</sup> LEED patterns showing  $(p\sqrt{2} \times \sqrt{2})\text{R}45^\circ$  superstructures of the Cl adlayers on unreconstructed Au(001) for Cl coverages well below the saturation coverage have been observed by Iwai *et al.*<sup>42</sup> at a low temperature (below  $150 \text{ K}$ ). At room temperature, only streaks in the direction of the superlattice peaks remain. The chains are oriented in the  $[010]$  (or the  $[100]$ ) direction of the Au substrate,<sup>42</sup> which is identical to the direction of the vacancy chains in our calculation. At a saturation coverage, Iwai *et al.* found that the LEED pattern finally conforms with a  $c(2 \times 2)$ -Cl adlayer at low and room temperatures. In the electrochemical environment at  $T_{\text{room}}$ , the experiments in Ref. 43 yield a smooth variation of the Cl coverage as a function of sample potential. We presume that at  $T_{\text{room}}$ , the vacancy chain configurations will show a small statistical weight. Thus, the smoothness of  $E_{\text{ads}}$  can be recovered at  $T_{\text{room}}$ . Further studies, e.g., lattice-gas model in combination with DFT,<sup>44–47</sup> would be needed to assess a larger number of configurations as well as the effect of temperature.

For simplicity, in what follows, we restrict ourselves to chemical potential  $\mu_{\text{Cl}} > -0.94 \text{ eV}$ , where the  $c(2 \times 2)$ -Cl adlayer without vacancies is stable (at  $T = 0 \text{ K}$ ) within the set of structures that we have calculated.

## B. Au<sub>ad</sub> monomer

As a next step, we investigate the equilibrium Cl adsorption configuration at and around a single Au adatom on the  $c(2 \times 2)$ -Cl covered Au(001) surface as a function of  $\mu_{\text{Cl}}$ . From Refs. 15 and 24, it is known that an Au<sub>ad</sub>Cl<sub>2</sub> complex (put on the, otherwise, clean unreconstructed Au(001) surface) becomes more stable than an Au<sub>ad</sub>Cl complex or a plain Au<sub>ad</sub> adatom if a Cl reservoir is assumed with  $\mu_{\text{Cl}}$  in the range of the Cl chemical potential considered in this paper. To address Au<sub>ad</sub> in the presence of a  $c(2 \times 2)$ -Cl adlayer, total energy

calculations have been carried out for several configurations (which have been relaxed electronically and with respect to the atomic positions) at a given Cl coverage  $\Theta$  on a  $p(6 \times 6)$  SUC. For  $n_{\text{vac}} = 0, 1$  Cl vacancies, we refer to our previous work,<sup>24</sup> which we extend here to  $n_{\text{vac}} = 2, 3$ , and 4 Cl vacancies. The results for specific configurations can be found in the [supplementary material](#).

The  $c(2 \times 2)$ -Cl Au(001) surface can exchange  $\text{Cl}^-$  ions with the electrolyte. The thermodynamically stable Cl structure for an  $\text{Au}_{\text{ad}}$  on the surface at a given  $\mu_{\text{Cl}}$  is the result of the minimization of the energy,

$$\Delta E_1(n_{\text{vac}}, \mu_{\text{Cl}}) = E_0(1, N_{\text{site}}/2 - n_{\text{vac}}, N_{\text{site}}) - E_0(1, N_{\text{site}}/2, N_{\text{site}}) + n_{\text{vac}}(E_{\text{Cl}_2}/2 + \mu_{\text{Cl}}), \quad (4)$$

with respect to coverage  $\Theta$ . In this equation,  $E_0(1, N_{\text{site}}/2, N_{\text{site}})$  has been chosen as a reference energy. It corresponds to the lowest energy configuration at a fixed coverage  $\Theta = 1/2$  ( $n_{\text{vac}} = 0$ ), which is depicted in [Fig. 2\(b\)](#).  $\Delta E_1$  as a function of  $\mu_{\text{Cl}}$  is plotted for several values of  $\Theta$  in [Fig. 2\(a\)](#). Furthermore, the energy of a configuration with  $n_{\text{vac}} - 1$  Cl vacancies, to which another Cl vacancy has been added far away from the  $\text{Au}_{\text{ad}}$  adatom, is given by

$$\Delta E_1^*(n_{\text{vac}}, \mu_{\text{Cl}}) = \Delta E_1(n_{\text{vac}} - 1, \mu_{\text{Cl}}) + E_{\text{VacCl}}(\mu_{\text{Cl}}). \quad (5)$$

In the range of  $\mu_{\text{Cl}} > -0.94$  eV, the energy necessary to desorb a Cl adatom from the  $c(2 \times 2)$ -Cl adlayer  $E_{\text{VacCl}}(\mu_{\text{Cl}})$  at a given  $\mu_{\text{Cl}}$  is

$$E_{\text{VacCl}}(\mu_{\text{Cl}}) = E_0(0, N_{\text{site}}/2 - 1, N_{\text{site}}) - E_0(0, N_{\text{site}}/2, N_{\text{site}}) + (E_{\text{Cl}_2}/2 + \mu_{\text{Cl}}). \quad (6)$$

In [Fig. 2\(a\)](#), dotted lines denote  $\Delta E_1^*$  as a function of chemical potential for given  $n_{\text{vac}}$ . The most stable configurations and Cl coverages

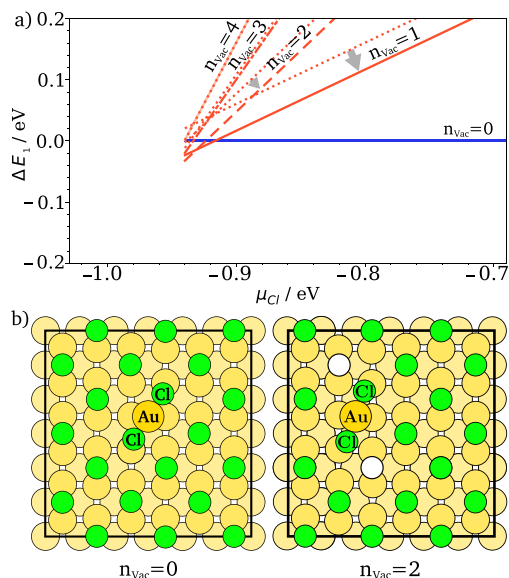


**FIG. 2.** (a)  $\Delta E_1$  for a fixed number of Cl vacancies plotted as a function of  $\mu_{\text{Cl}}$ . Dotted lines denote  $\Delta E_1^*(n_{\text{vac}}, \mu_{\text{Cl}})$  from Eq. (5). The atomic geometries of the lowest energy configurations for an Au adatom in the presence of  $n_{\text{vac}} = 0$  and 2 Cl vacancies (denoted by white circles) are shown in (b).

as a function of  $\mu_{\text{Cl}}$  can be derived from the lower envelope of the curves  $\Delta E_1(n_{\text{vac}}, \mu_{\text{Cl}})$ .

We find that the  $\text{Au}_{\text{ad}}\text{Cl}_2$  complex stays stable as the number of Cl vacancies is increased. When a Cl vacancy, which has been created far away from the  $\text{Au}_{\text{ad}}\text{Cl}_2$  complex, binds to the  $\text{Au}_{\text{ad}}\text{Cl}_2$  complex with  $n_{\text{vac}} = 0$  or 1, the energy decreases by 40 ( $\approx 1.5 k_B T_{\text{room}}$ ) or 30 ( $\approx 1.2 k_B T_{\text{room}}$ ) meV, respectively. In the case of additional Cl vacancies, the energy gain becomes smaller or even negligible, i.e., the additional Cl vacancy no longer binds to the  $\text{Au}_{\text{ad}}\text{Cl}_2$  complex with two vacancies. From [Fig. 2](#), we read that the configuration with  $\Theta = 1/2$  is the most stable one for  $\mu_{\text{Cl}} > -0.91$  eV. In this range of  $\mu_{\text{Cl}}$ , the creation of an additional Cl vacancy is disadvantageous as it would cost energy (in our calculation, disregarding finite temperature configuration entropy effects). At a more negative  $\mu_{\text{Cl}}$ , configurations in which Cl vacancies attach to the  $\text{Au}_{\text{ad}}\text{Cl}_2$  complex become more stable than the one with  $\Theta = 1/2$ . Atomic configurations are shown in [Fig. 2\(b\)](#).

### C. $\text{Au}_{\text{ad}}$ dimer

The initial step toward  $\text{Au}_{\text{ad}}$  island formation is the binding of two  $\text{Au}_{\text{ad}}\text{Cl}_2$  monomers. In this section, we analyze the equilibrium Cl adsorption configuration in the vicinity of an  $\text{Au}_{\text{ad}}$  dimer on the  $c(2 \times 2)$ -Cl Au(001) surface and its binding energy with respect to two separate  $\text{Au}_{\text{ad}}\text{Cl}_2$  monomers. Processes and binding energies depend on  $\mu_{\text{Cl}}$ . At a low Cl coverage, Mesgar<sup>15</sup> has found that a Cl atom adsorbs on the bridge site of the  $\text{Au}_{\text{ad}}$  dimer. The bond length of the  $\text{Au}_{\text{ad}}$  dimer amounts to 3.09 Å,<sup>15</sup> which is 5% larger than the nearest neighbor distance. For the  $c(2 \times 2)$ -Cl Au(001) surface, we have performed DFT calculations for various configurations with  $n_{\text{vac}} = 0$  to 4 Cl vacancies within a  $p(6 \times 6)$  SUC. Different adsorption configurations at a given  $n_{\text{vac}}$  and their energies are listed in the [supplementary material](#).

Analogously to [Sec. III B](#), in order to identify the most stable Cl adsorption configuration, we minimize the energy,

$$\Delta E_2(n_{\text{vac}}, \mu_{\text{Cl}}) = E_0(2, N_{\text{site}}/2 - n_{\text{vac}}, N_{\text{site}}) - E_0(2, N_{\text{site}}/2, N_{\text{site}}) + n_{\text{vac}}(E_{\text{Cl}_2}/2 + \mu_{\text{Cl}}). \quad (7)$$

$E_0(2, N_{\text{site}}/2, N_{\text{site}})$  has been chosen as a reference energy. It corresponds to the lowest energy configuration for the  $\text{Au}_{\text{ad}}$  dimer on the Cl covered Au(001) surface with  $\Theta = 1/2$ . Similar to [Eq. \(5\)](#), the energy of a configuration with  $n_{\text{vac}} - 1$  Cl vacancies plus an additional Cl vacancy, which is far away from the  $\text{Au}_{\text{ad}}$  dimer, can be written as

$$\Delta E_2^*(n_{\text{vac}}, \mu_{\text{Cl}}) = \Delta E_2(n_{\text{vac}} - 1, \mu_{\text{Cl}}) + E_{\text{VacCl}}(\mu_{\text{Cl}}). \quad (8)$$

[Figure 3\(a\)](#) displays  $\Delta E_2$  as a function of  $\mu_{\text{Cl}}$  for fixed values of  $n_{\text{vac}}$ . Dashed lines correspond to the energy  $\Delta E_2^*$  in [Eq. \(8\)](#). The equilibrium Cl coverage and configurations for the  $\text{Au}_{\text{ad}}$  dimer follow from the lower envelope of the curves.

The data are summarized in [Fig. 3](#), together with lowest energy configurations. We find a chain-like  $(\text{Au}_{\text{ad}}\text{Cl}_2)_2$  structure to be stable for  $\mu_{\text{Cl}} > -0.86$  eV, with the two  $\text{Au}_{\text{ad}}$  atoms residing on bridge positions of the Au substrate lattice (the separation between the Au adatoms of the two  $\text{Au}_{\text{ad}}\text{Cl}_2$  amounts to 4.05 Å, which is distinctly larger than the Au–Au nearest neighbor separation of the epitaxial

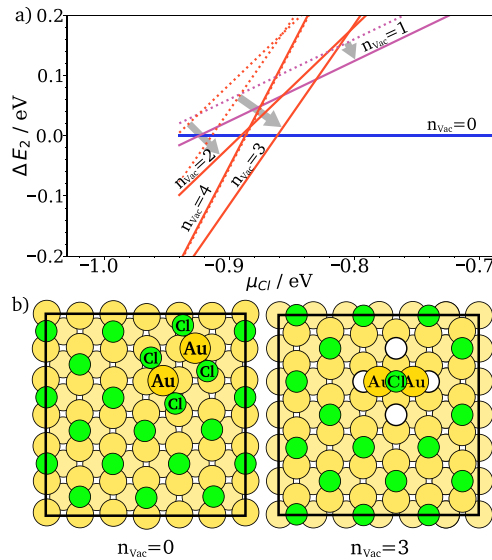


**FIG. 3.** (a)  $\Delta E_2$  at a fixed number of Cl vacancies as a function of  $\mu_{\text{Cl}}$ . Dotted lines denote  $\Delta E_2^*(n_{\text{vac}}, \mu_{\text{Cl}})$  from Eq. (8). The atomic geometries of the lowest energy configurations for the  $\text{Au}_{\text{ad}}$  dimer in the presence of  $n_{\text{vac}} = 0$  and 3 Cl vacancies are shown in (b). Four white circles denote the positions of the vacancies.  $n_{\text{vac}}$  is equal to 3 due to the additional Cl adsorbed at the  $\text{Au}_{\text{ad}}\text{-Au}_{\text{ad}}$  bridge site.

sites on the unreconstructed Au(001) surface and only 2.6% smaller than the Au–Au second nearest neighbor separation).  $\text{Au}_{\text{ad}}\text{Cl}_2$  forming dimers and chain-like structures has been observed by STM on the  $(\sqrt{3} \times \sqrt{3})R^\circ 30\text{-Cl Au}(111)$  surface by Andryushechkin *et al.*<sup>48</sup> Due to the different substrate orientation, their  $\text{Au}_{\text{ad}}\text{-Au}_{\text{ad}}$  separation, calculated with DFT, amounts to 3.56 Å. Most importantly, we find for the Au(001) surface that the equilibrium structure of the  $\text{Au}_{\text{ad}}$  dimer and the adsorbed Cl atoms changes drastically for Cl chemical potential  $\mu_{\text{Cl}} < -0.86$  eV. At these more negative values of  $\mu_{\text{Cl}}$ , the separation between the Au adatoms amounts to 3.04 Å, i.e., they occupy epitaxial nearest neighbor positions on the Au(001) surface (the separation is 3.6% larger than the Au–Au nearest neighbor distance on the unreconstructed clean Au(001) surface). A single Cl atom is adsorbed at the bridge site of the dimer. This geometry is consistent with the one described by Mesgar<sup>15</sup> for low Cl coverages.  $\text{Au}_{\text{ad}}$  dimers without an adsorbed Cl atom are, by far, unstable (see the [supplementary material](#)).

For one Cl vacancy, the difference between  $\Delta E_2$  and  $\Delta E_2^*$  is about 40 meV. In the case of two and three Cl vacancies, the difference amounts to 100 meV and 160 meV. This difference decreases to –5 meV for the case of four Cl vacancies; in this case, the dotted line lies below the calculated curve. While this implies for  $n_{\text{vac}} = 4$  that there are other adsorption configurations (maybe in a larger SUC) which have a lower energy, the difference between  $\Delta E_2$  and  $\Delta E_2^*$  is too small to be relevant.

To this point, we have calculated the stability of the Cl structures as a function of  $\mu_{\text{Cl}}$ . Now one question arises: How large is the binding energy of the  $\text{Au}_{\text{ad}}$  dimer on the  $c(2 \times 2)\text{-Cl Au}(001)$  surface? We consider two  $\text{Au}_{\text{ad}}\text{Cl}_2$  monomer complexes, initially far away from each other, that diffuse on the  $c(2 \times 2)\text{-Cl Au}(001)$  surface

and eventually form an  $\text{Au}_{\text{ad}}$  dimer. The binding energy is given by the energy difference between the equilibrium structures of the  $\text{Au}_{\text{ad}}$  dimer plus the Cl covered surface without any Au adatom minus the energy of two  $\text{Au}_{\text{ad}}$  monomers,

$$E_{\text{bind}}(\mu_{\text{Cl}}) = \min_{n_{\text{vac}}} [E_0(2, N_{\text{site}}/2 - n_{\text{vac}}, N_{\text{site}}) + n_{\text{vac}}(E_{\text{Cl}_2}/2 + \mu_{\text{Cl}})] \\ + \min_{n'_{\text{vac}}} [E_0(0, N_{\text{site}}/2 - n'_{\text{vac}}, N_{\text{site}}) + n'_{\text{vac}}(E_{\text{Cl}_2}/2 + \mu_{\text{Cl}})] \\ - 2 \min_{n''_{\text{vac}}} [E_0(1, N_{\text{site}}/2 - n''_{\text{vac}}, N_{\text{site}}) \\ + n''_{\text{vac}}(E_{\text{Cl}_2}/2 + \mu_{\text{Cl}})]. \quad (9)$$

Here,  $E_{\text{bind}}$  is negative for an exothermic reaction. Equation (9) can be rewritten as

$$E_{\text{bind}}(\mu_{\text{Cl}}) = \min_{n_{\text{vac}}} [\Delta E_2(n_{\text{vac}}, \mu_{\text{Cl}}) + E_0(2, N_{\text{site}}/2, N_{\text{site}})] \\ + \min_{n'_{\text{vac}}} [\Delta E_0(n'_{\text{vac}}, \mu_{\text{Cl}}) + E_0(0, N_{\text{site}}/2, N_{\text{site}})] \\ - 2 \min_{n''_{\text{vac}}} [\Delta E_1(n''_{\text{vac}}, \mu_{\text{Cl}}) + E_0(1, N_{\text{site}}/2, N_{\text{site}})], \quad (10)$$

where  $\Delta E_0(n_{\text{vac}}, \mu_{\text{Cl}})$  is defined as

$$\Delta E_0(n_{\text{vac}}, \mu_{\text{Cl}}) = E_0(0, N_{\text{site}}/2 - n_{\text{vac}}, N_{\text{site}}) - E_0(0, N_{\text{site}}/2, N_{\text{site}}) \\ + n_{\text{vac}}(E_{\text{Cl}_2}/2 + \mu_{\text{Cl}}). \quad (11)$$

$E_0(0, N_{\text{site}}/2, N_{\text{site}})$  is chosen a reference energy and corresponds to the total energy of the  $c(2 \times 2)\text{-Cl Au}(001)$  surface with  $\Theta = 1/2$ , i.e.,  $n_{\text{vac}} = 0$ . This is the equilibrium coverage (in the case of our  $T = 0$  K calculation) for  $\mu_{\text{Cl}} > -0.94$  eV; thus,  $\Delta E_0$  is equal to zero in this range. At values of  $\mu_{\text{Cl}} > -0.86$  eV, where the most stable configurations of the  $\text{Au}_{\text{ad}}$  monomer and  $\text{Au}_{\text{ad}}$  dimer have no Cl vacancies (i.e.,  $n_{\text{vac}} = 0$ ),  $E_{\text{bind}}$  simplifies to

$$E_{\text{bind}}(\mu_{\text{Cl}} > -0.86\text{eV}) = E_0(2, N_{\text{site}}/2, N_{\text{site}}) + E_0(0, N_{\text{site}}/2, N_{\text{site}}) \\ - 2 E_0(1, N_{\text{site}}/2, N_{\text{site}}). \quad (12)$$

The binding energy as a function of  $\mu_{\text{Cl}}$  is shown in [Fig. 4](#).

For  $\mu_{\text{Cl}} > -0.86$  eV, the absolute value of the binding energy of the  $(\text{Au}_{\text{ad}}\text{Cl}_2)_2$  dimer amounts to only 0.064 eV ( $\approx 2.5 k_B T_{\text{room}}$ ). For more negative values of  $\mu_{\text{Cl}}$ , the absolute value of the binding energy of the dimer increases up to 0.23 eV ( $\approx 9 k_B T_{\text{room}}$ ). This means

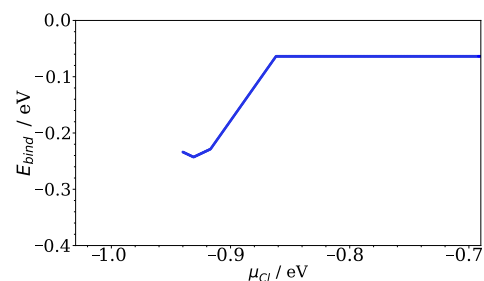


**FIG. 4.** Binding energy of an  $\text{Au}_{\text{ad}}$  dimer on the  $c(2 \times 2)\text{-Cl Au}(001)$  surface as a function of  $\mu_{\text{Cl}}$ .

that the  $\text{Au}_{\text{ad}}$  dimer is distinctly stabilized by the presence of Cl vacancies.

For processes at solid–liquid interfaces, activation energies depend on the electrode potential.<sup>6,49,50</sup> This can be taken into consideration via an interaction energy  $-\mu_z \mathcal{E}_z$  between the dipole moment  $\mu$  of the surface defect with the electric field in the electrolyte at the surface.<sup>6,50,51</sup> Using our calculated electric dipole moments, we have investigated the relative energy variation among the adsorbate configurations on Au(001) with the same number of Cl and Au adatoms. If we restrict ourselves to those structures, i.e., the number of Cl vacancies  $n_{\text{vac}}$ , that occur as equilibrium structures in Figs. 2 and 3 (hence omit, e.g., the Au ad-dimer with  $n_{\text{vac}} = 1$ ), we find that for an electric field  $\mathcal{E}_z$  between about  $-0.4 \text{ V/\AA}$  and  $+0.4 \text{ V/\AA}$ ,<sup>51,52</sup> the lowest energy atomic configuration does not change. However, for larger  $|\mathcal{E}_z|$ ,<sup>3,53,54</sup> the lowest energy configuration changes in some cases. Roughly speaking, the main effect is that the energy of structures with Cl on top of  $\text{Au}_{\text{ad}}$  adatoms or at the bridge site of  $\text{Au}_{\text{ad}}$  ad-dimers decreases with respect to the energy of respective  $(\text{Au}_{\text{ad}}\text{Cl}_2)_n$  ad-structures in the case of sample potential more negative than the potential of zero charge. For a correction of the binding energy in Fig. 4 with respect to the electric field at the surface, the interrelations between Cl chemical potential, ion activities in the electrolyte, electric field, and sample potential would be required.<sup>44,55–57</sup> In the following, we confine ourselves to the simpler case of two reactions, where two  $\text{Au}_{\text{ad}}\text{Cl}_2$  monomers form an ad-dimer without exchange of Cl with the electrolyte. Furthermore, we restrict ourselves to a small absolute value of the electric field (e.g.,  $|\mathcal{E}_z| < 0.4 \text{ V/\AA}$ ) such that the equilibrium Cl adsorption configuration does not change. If a  $(\text{Au}_{\text{ad}}\text{Cl}_2)_2$  chain is formed without any Cl vacancy in the  $c(2 \times 2)$ -Cl adlayer (i.e., neither in the case of the surface without an Au adatom nor in the case of the monomer nor the dimer), the dipole moment change is small,  $-0.02 \text{ e\AA}$ , and the effect on the binding energy is negligible. We remark that this will not hold true anymore when the electric field  $-\mathcal{E}_z$  is sufficiently large so that other local Cl adsorption structures are preferred. If two  $\text{Au}_{\text{ad}}\text{Cl}_2$  monomers with  $n_{\text{vac}} = 1$  and  $n_{\text{vac}} = 2$  bind and form a dimer with  $n_{\text{vac}} = 3$  on an, otherwise, fully  $c(2 \times 2)$ -Cl covered Au(001) surface, the dipole moment change amounts to  $-0.18 \text{ e\AA}$ . In this case, the energy variation is not negligible, it amounts to about  $\pm 0.07 \text{ eV}$  for  $\mathcal{E}_z = \pm 0.4 \text{ V/\AA}$ . Within the present paper, however, we have to omit these effects evoked by the electric field at the electrochemical surface.

#### D. $\text{Au}_{\text{ad}}$ trimer and tetramer

Island formation requires the attachment of further Au adatoms. Therefore, calculations for small  $\text{Au}_{\text{ad}}$  nanoclusters are worthwhile. Due to the large number of possible atomic configurations of the Au and Cl adatoms, a comprehensive sampling of the configuration space is computationally not feasible. We present DFT calculations for selected structures of  $\text{Au}_{\text{ad}}$  trimers and tetramers on the  $c(2 \times 2)$ -Cl Au(001) surface, which have been inspired by the calculated equilibrium structures of the  $\text{Au}_{\text{ad}}$  monomer and dimer presented above. Due to computational limitations, we restrict  $n_{\text{vac}}$  to 0, 1, and 2 Cl vacancies. We emphasize that larger number of vacancies attached to the trimer or tetramer are to be expected in equilibrium configurations. Nonetheless, despite the limited range of  $n_{\text{vac}}$  investigated here, there are

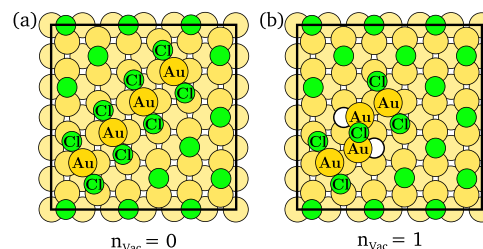


FIG. 5. Ground state adsorption configurations for the  $\text{Au}_{\text{ad}}$  tetramer with  $n_{\text{vac}} = 0$  (a) and  $n_{\text{vac}} = 1$  (b) Cl vacancies.

trends for the binding energy which can be derived from the present results.

On the Cl covered surface with  $n_{\text{vac}} = 0$ , we still find chain-like structures of  $\text{Au}_{\text{ad}}\text{Cl}_2$  monomers as depicted in Fig. 5(a) to be stable. The attachment of an  $\text{Au}_{\text{ad}}\text{Cl}_2$  monomer to an  $(\text{Au}_{\text{ad}}\text{Cl}_2)_2$  dimer results in an energy gain of  $0.065 \text{ eV}$  ( $\approx 2.5 k_B T_{\text{room}}$ ). The energy gain by attachment of an  $\text{Au}_{\text{ad}}\text{Cl}_2$  monomer to a trimer amounts to  $0.062 \text{ eV}$  ( $\approx 2.4 k_B T_{\text{room}}$ ). We did not find any configurations for the  $\text{Au}_{\text{ad}}$  tetramer, where all Au adatoms occupy epitaxial nearest neighbor positions, that were stable in comparison to the  $(\text{Au}_{\text{ad}}\text{Cl}_2)_4$  in Fig. 5. Energies and geometries of calculated configurations are listed in the [supplementary material](#).

In the presence of Cl vacancies, the lowest energy configurations of the  $\text{Au}_{\text{ad}}$  trimer and tetramer follow a trend already observed in the case of the dimer: A single Cl adatom is adsorbed on the bridge site of the  $\text{Au}_{\text{ad}}$  dimer. Additional  $\text{Au}_{\text{ad}}\text{Cl}_2$  monomers bind to the  $\text{Au}_{\text{ad}}$  dimer, see, e.g., the  $\text{Au}_{\text{ad}}$  tetramer with  $n_{\text{vac}} = 1$  in Fig. 5(b). The separation between Au adatoms of the dimer and the  $\text{Au}_{\text{ad}}\text{Cl}_2$  amounts to  $3.11 \text{ \AA}$ , which is 6% larger than the Au–Au nearest neighbor distance. The energy gain due to the attachment of an  $\text{Au}_{\text{ad}}$  tends to increase, and this is attributed to the presence of Cl vacancies.

For  $n_{\text{vac}} \leq 2$  Cl vacancies, we could not find any ground state structures resembling compact epitaxial  $\text{Au}_{\text{ad}}$  islands. Analogously to the dimer, one may speculate that more compact Au adatom structures might occur in the presence of a larger number of Cl vacancies. We observe a trend that there is a transition from  $\text{Au}_{\text{ad}}\text{Cl}_2$  chain-like configurations at  $n_{\text{vac}} = 0$  to structures, in which some of the Au adatoms occupy Au–Au nearest neighbor positions on the Au(001) surface, in the presence of Cl vacancies.

#### IV. CONCLUSIONS

Using density functional total energy calculations, we have investigated the ground state configurations for  $(\text{Au}_{\text{ad}})_n$  clusters for  $n \leq 4$  on the  $c(2 \times 2)$ -Cl Au(001) surface including Cl vacancies for a selected set of configurations (see the [supplementary material](#)). Water layers and effects of the electric field at the surface are not included in the calculations. The equilibrium structures in the case of the number of vacancies  $n_{\text{vac}} = 0$  consist of  $(\text{Au}_{\text{ad}}\text{Cl}_2)$ -chains. The energy gain due to the attachment of an  $\text{Au}_{\text{ad}}\text{Cl}_2$  monomer to another monomer or cluster is about  $0.06 \text{ eV}$ . This implies a weak bonding between the  $\text{Au}_{\text{ad}}\text{Cl}_2$  monomers with the Au adatoms staying on the Au(001) bridge sites.

At more negative values of  $\mu_{\text{Cl}}$ , where Cl vacancies exist in equilibrium and bind to the  $(\text{Au}_{\text{ad}})_n$  cluster, the energy gain due to the attachment of a monomer increases significantly, e.g., two Au monomers bind and form a dimer on the surface with an energy gain of up to 0.23 eV. This is accompanied by a change in  $\text{Au}_{\text{ad}}$  adsorption positions and local Cl adsorption sites.

This result implies that the nucleation of an Au ad-dimer is distinctly supported by the presence of vacancies in the halide adlayer. While there are, of course, various parameters that determine the growth mode, we note that a larger absolute value of the binding energy of the nucleus is expected to assist the transition from step-flow to layer-by-layer growth mode. The complete path to the formation of compact Au islands, however, is an issue for future research. Furthermore, the effect of the electrolyte in an electrochemical environment and the dependence on sample potential still have to be accounted for. Nonetheless, this work highlights the differences and complications which arise due to the presence of the halide coadsorbates—as opposed to the case of Au island nucleation in molecular beam epitaxy on the clean surface—and emphasizes the decisive role the halide vacancy concentration may play not only for diffusion<sup>24</sup> but also for the energetics of island nucleation.

## SUPPLEMENTARY MATERIAL

See the [supplementary material](#) for (i) an overview of several atomic configurations of Cl adlayers for chlorine coverage between 1/16 and 1/2, and (ii) a survey of calculated atomic configurations of  $(\text{Au}_{\text{ad}})_n$  with  $n \leq 4$  on a  $c(2 \times 2)$ -Cl Au(001) surface.

## ACKNOWLEDGMENTS

The calculations were performed at the Rechenzentrum der Christian-Albrechts-Universität zu Kiel. A. Dávila thanks PRONABEC-Perú for the financial support via Beca Presidente de la República Beca Presidente de la República- Convocatoria 2014-3. Helpful discussions with Professor Dr. O. Magnussen, Dr. J. Stettner, and L. Deuchler are gratefully acknowledged.

## REFERENCES

- S. Kowarik, *J. Phys.: Condens. Matter* **29**, 043003 (2016).
- O. M. Magnussen and A. Groß, *J. Am. Chem. Soc.* **141**, 4777 (2019).
- E. Pichardo-Pedrero, G. Beltramo, and M. Giesen, *Appl. Phys. A* **87**, 461 (2007).
- D. Josell, D. Wheeler, W. H. Huber, and T. P. Moffat, *Phys. Rev. Lett.* **87**, 016102 (2001).
- K. Krug, J. Stettner, and O. M. Magnussen, *Phys. Rev. Lett.* **96**, 246101 (2006).
- O. M. Magnussen, *Chem. - Eur. J.* **25**, 12865 (2019).
- A. Pimpinelli and J. Villain, *Physics of Crystal Growth*, Collection Alea-Saclay: Monographs and Texts in Statistical Physics (Cambridge University Press, 1998).
- A. P. J. Jansen, *An Introduction to Kinetic Monte Carlo Simulations of Surface Reactions*, Lecture Notes in Physics (Springer-Verlag, Berlin Heidelberg, 2012).
- M. Andersen, C. Panosetti, and K. Reuter, *Front. Chem.* **7**, 202 (2019).
- A. H. Ayyad, J. Stettner, and O. M. Magnussen, *Phys. Rev. Lett.* **94**, 066106 (2005).
- O. M. Magnussen, K. Krug, A. H. Ayyad, and J. Stettner, *Electrochim. Acta* **53**, 3449 (2008).
- K. Krug, D. Kaminski, F. Golks, J. Stettner, and O. M. Magnussen, *J. Phys. Chem. C* **114**, 18634 (2010).
- K. Kleiner, A. Comas-Vives, M. Naderian, J. E. Mueller, D. Fantauzzi, M. Mesgar, J. A. Keith, J. Anton, and T. Jacob, *Adv. Phys. Chem.* **2011**, 252591 (2012).
- M. Mesgar, P. Kaghazchi, T. Jacob, E. Pichardo-Pedrero, M. Giesen, H. Ibach, N. B. Luque, and W. Schmickler, *ChemPhysChem* **14**, 233 (2013).
- M. Mesgar, “Multi-scale modeling of island formation and surface dynamics on the Au(100) surface,” Ph.D. thesis, Universität Ulm, 2015.
- O. M. Magnussen, *Chem. Rev.* **102**, 679 (2002).
- Y.-C. Yang, K. Hecker, and O. M. Magnussen, *Electrochim. Acta* **112**, 881 (2013).
- A. Cuesta and D. M. Kolb, *Surf. Sci.* **465**, 310 (2000).
- M. Al-Shakran, L. A. Kibler, and T. Jacob, *Surf. Sci.* **631**, 130 (2015).
- B. D. Yu and M. Scheffler, *Phys. Rev. B* **56**, R15569 (1997).
- J. E. Müller and H. Ibach, *Phys. Rev. B* **74**, 085408 (2006).
- K. Pötting, W. Schmickler, and T. Jacob, *ChemPhysChem* **11**, 1395 (2010).
- G. Antczak and G. Ehrlich, *Surface Diffusion: Metals, Metal Atoms, and Clusters* (Cambridge University Press, 2010).
- A. C. Dávila López and E. Pehlke, *J. Chem. Phys.* **151**, 064709 (2019).
- J. A. Keith, D. Fantauzzi, T. Jacob, and A. C. T. van Duin, *Phys. Rev. B* **81**, 235404 (2010).
- P. Giannozzi, S. Baroni, N. Bonini, M. Calandra, R. Car, C. Cavazzoni, D. Ceresoli, G. L. Chiarotti, M. Cococcioni, I. Dabo, A. Dal Corso, S. de Gironcoli, S. Fabris, G. Fratesi, R. Gebauer, U. Gerstmann, C. Gougoussis, A. Kokalj, M. Lazzeri, L. Martin-Samos, N. Marzari, F. Mauri, R. Mazzarello, S. Paolini, A. Pasquarello, L. Paulatto, C. Sbraccia, S. Scandolo, G. Sclauzero, A. P. Seitsonen, A. Smogunov, P. Umari, and R. M. Wentzcovitch, *J. Phys.: Condens. Matter* **21**, 395502 (2009).
- P. Giannozzi, O. Andreussi, T. Brumme, O. Bunau, M. B. Nardelli, M. Calandra, R. Car, C. Cavazzoni, D. Ceresoli, M. Cococcioni, N. Colonna, I. Carnimeo, A. D. Corso, S. de Gironcoli, P. Delugas, R. A. D. Jr, A. Ferretti, A. Floris, G. Fratesi, G. Fugallo, R. Gebauer, U. Gerstmann, F. Giustino, T. Gorni, J. Jia, M. Kawamura, H.-Y. Ko, A. Kokalj, E. Küçükbenli, M. Lazzeri, M. Marsili, N. Marzari, F. Mauri, N. L. Nguyen, H.-V. Nguyen, A. Otero-de-la-Rozza, L. Paulatto, S. Poncè, D. Rocca, R. Sabatini, B. Santra, M. Schlipf, A. P. Seitsonen, A. Smogunov, I. Timrov, T. Thonhauser, P. Umari, N. Vast, X. Wu, and S. Baroni, *J. Phys.: Condens. Matter* **29**, 465901 (2017).
- J. P. Perdew, K. Burke, and M. Ernzerhof, *Phys. Rev. Lett.* **77**, 3865 (1996).
- D. Vanderbilt, *Phys. Rev. B* **41**, 7892 (1990).
- K. F. Garrity, J. W. Bennett, K. M. Rabe, and D. Vanderbilt, *Comput. Mater. Sci.* **81**, 446 (2014).
- L. Bengtsson, *Phys. Rev. B* **59**, 12301 (1999).
- B. Meyer and D. Vanderbilt, *Phys. Rev. B* **63**, 205426 (2001).
- H. J. Monkhorst and J. D. Pack, *Phys. Rev. B* **13**, 5188 (1976).
- C. G. M. Hermse, A. P. van Bavel, M. T. M. Koper, J. J. Lukkien, R. A. van Santen, and A. P. J. Jansen, *Phys. Rev. B* **73**, 195422 (2006).
- S. Peljhan and A. Kokalj, *J. Phys. Chem. C* **113**, 14363 (2009).
- F. Gossenberger, T. Roman, and A. Groß, *Surf. Sci.* **631**, 17 (2015).
- K. Reuter and M. Scheffler, *Phys. Rev. B* **65**, 035406 (2001).
- J. Rogal, K. Reuter, and M. Scheffler, *Phys. Rev. B* **75**, 205433 (2007).
- Y. J. Feng, K. P. Bohnen, and C. T. Chan, *Phys. Rev. B* **72**, 125401 (2005).
- A. C. Dávila López and E. Pehlke (unpublished).
- A. Krishnamoorthy and B. Yildiz, *Phys. Chem. Chem. Phys.* **17**, 22227 (2015).
- H. Iwai, M. Okada, K. Fukutani, and Y. Murata, *J. Phys.: Condens. Matter* **7**, 5163 (1995).
- M. Al-Shakran, L. A. Kibler, T. Jacob, H. Ibach, G. L. Beltramo, and M. Giesen, *Surf. Sci.* **651**, 84 (2016).
- I. Abou Hamad, S. J. Mitchell, T. Wandlowski, P. A. Rikvold, and G. Brown, *Electrochim. Acta* **50**, 5518 (2005).
- S. J. Mitchell and M. T. M. Koper, *Surf. Sci.* **563**, 169 (2004).
- T. Juwono, I. Abou Hamad, P. A. Rikvold, and S. Wang, *J. Electroanal. Chem.* **662**, 130 (2011).
- H. Walen, D.-J. Liu, J. Oh, H. Lim, J. W. Evans, Y. Kim, and P. A. Thiel, *J. Chem. Phys.* **143**, 014704 (2015).
- B. V. Andryushechkin, V. V. Cherkez, E. V. Gladchenko, T. V. Pavlova, G. M. Zhidomirov, B. Kierren, C. Didiot, Y. Fagot-Reverat, D. Malterre, and K. N. Eltsov, *J. Phys. Chem. C* **117**, 24948 (2013).



- <sup>49</sup>M. Giesen, M. Dietterle, D. Stapel, H. Ibach, and D. M. Kolb, *Surf. Sci.* **384**, 168 (1997).
- <sup>50</sup>M. Giesen, G. Beltramo, S. Dieluweit, J. Müller, H. Ibach, and W. Schmickler, *Surf. Sci.* **595**, 127 (2005).
- <sup>51</sup>J. K. Nørskov, J. Rossmeisl, A. Logadottir, L. Lindqvist, J. R. Kitchin, T. Bligaard, and H. Jónsson, *J. Phys. Chem. B* **108**, 17886 (2004).
- <sup>52</sup>G. S. Karlberg, J. Rossmeisl, and J. K. Nørskov, *Phys. Chem. Chem. Phys.* **9**, 5158 (2007).
- <sup>53</sup>J.-L. Fraikin, M. V. Requa, and A. N. Cleland, *Phys. Rev. Lett.* **102**, 156601 (2009).
- <sup>54</sup>B. Rahn and O. M. Magnussen, *ChemElectroChem* **5**, 3073 (2018).
- <sup>55</sup>F. Gossenberger, T. Roman, and A. Groß, *Electrochim. Acta* **216**, 152 (2016).
- <sup>56</sup>P. A. Rikvold, T. Wandlowski, I. Abou Hamad, S. J. Mitchell, and G. Brown, *Electrochim. Acta* **52**, 1932 (2007).
- <sup>57</sup>M. M. Waagele, C. M. Gunathunge, J. Li, and X. Li, *J. Chem. Phys.* **151**, 160902 (2019).



# 6. | Summary and Outlook

The atomic-scale structure of the metal/electrolyte interface can affect the surface transport of deposited atoms, hence the growth behavior and the resulting morphology of a thin film. The role of adsorbing species (*e.g.* halides) from the electrolyte during electrodeposition processes is of particular interest. The enhancement of surface mobility has been attributed to the coadsorbed halide species along with the sample potential. Due to the high mobility of metallic atoms in electrochemical conditions, atomic-scale processes such as self-diffusion of metal atoms cannot be studied by direct STM observation as in the case of sulfide diffusion. Thus, available information from experiments are scarce about the kinetics mechanisms for metal adatoms at electrochemical environment which determine thin film growth *e.g.* self-diffusion rates, formation of a nuclei and adsorption positions. Model calculations of elemental processes from first principles are therefore of great importance to elucidate the influence of coadsorbed species during electrodeposition.

The objective of this thesis was to investigate growth and nucleation for Au(001) homoepitaxial electrodeposition in Cl containing electrolytes by means of density functional theory (DFT) calculations. Especially, the core of this work were the effect of Cl coadsorbates on the atomic-scale processes: self-diffusion of Au adatom ( $\text{Au}_{\text{ad}}$ ) and nucleation of Au islands. This work conveys the evolution of the potential energy landscape of Au adatoms due to the presence of Cl coadsorbates, which results in more complex atomic processes than in the clean surface.

The rapid diffusion of Au adatoms on the terrace supports the step-flow growth mode. Thus, DFT calculations of diffusion mechanisms for Au adsorbed on Cl covered Au(001) surfaces were carried out. Concerning nucleation, the stable structures of small  $\text{Au}_{\text{ad}}$  clusters on Cl covered surfaces were identified. For self-diffusion and nucleation processes the knowledge of the equilibrium Cl coverage and adlayer reconstructions, as well as the local binding topology of Au adatoms on Cl covered unreconstructed Au(001) surfaces are prerequisite. Based on experimental evidence, two ordered Cl adlayers  $c(2 \times 2)$  and  $c(\sqrt{2} \times 2\sqrt{2})R45^\circ$  with Cl coverage of 1/2 have been addressed. DFT calculations confirmed that the lowest energy adsorption site for  $c(2 \times 2)$ -Cl adlayer is the bridge position of the unreconstructed Au(001) surface. The difference between both adlayer structures relies on the distances to neighboring Cl adatoms. Furthermore, experimental surface chloride coverage increases steeply within the potential range of homoepitaxial growth. Therefore, the presence of Cl vacancies in the adlayer structures was considered. The adsorption energy per Cl amounts to -1.08 eV for  $c(2 \times 2)$ -Cl and -1.06 eV for  $c(\sqrt{2} \times 2\sqrt{2})R45^\circ$ -Cl. The small difference between the energies are below the accuracy of the DFT calculations. Regarding

the stability of Cl adlayer structures, these represent the minimum energy and are therefore expected to arise along the values of Cl chemical potential ranging from -0.94 to -0.35 eV.

As small metal complexes (e.g.  $\text{Ag}_3\text{S}_3$  complex [293]) have been related as carriers in mass transport, low total energy structures and diffusion paths of Au-Cl complexes have been evaluated on unreconstructed Au(001) surfaces disregarding the presence of Cl coadsorbates. Among these simple systems the  $\text{AuCl}_2$  complex becomes stable for values of  $\mu_{\text{Cl}}$  from -1.03 to -0.35 eV, and diffuses with an activation barrier of 0.07 eV. The formation of a  $\text{AuCl}_2$  complex leads to a significant reduction of the diffusion barriers of single Au and Cl adatoms on the clean unreconstructed Au(001) surface, which amount to 0.27 and 0.14 eV respectively.

To account for the specific adsorption of Cl atoms, low total energy configurations of a Au adsorbed on Cl covered Au(001) surfaces with  $\Theta = 1/2$  were examined. Both structures  $c(2 \times 2)$  and  $c(\sqrt{2} \times 2\sqrt{2})R45^\circ$  were considered. This survey has revealed that the energetically preferred configurations for both ordered adlayers comprise those with  $\text{Au}_{\text{ad}}$  located at bridge site of the substrate. In the presence of Cl coadsorbates a  $\text{Au}_{\text{ad}}\text{Cl}_2$  complex is formed. Conversely, the lowest energy position of  $\text{Au}_{\text{ad}}$  on the clean surface is the hollow site. This difference illustrates the strong influence of the Cl adlayer on the binding properties and energies of a  $\text{Au}_{\text{ad}}$ . Additionally, the presence of Cl vacancies was considered which also resulted in a  $\text{Au}_{\text{ad}}\text{Cl}_2$  complex at bridge site of the substrate for the lowest energy configurations. Due to the presence of a Cl vacancy the potential energy surface exhibits a multitude of local energy minima. For example in the  $c(2 \times 2)$ -Cl adlayer local energy minima are within a range up to 0.19 eV of the lowest energy configuration.

During the diffusion of a  $\text{Au}_{\text{ad}}$  from a lowest energy site to another the surrounding Cl coadsorbates can form Au-Cl complexes as well as rearrange their positions in the vicinity of  $\text{Au}_{\text{ad}}$ . The lowest activation barriers  $E_{\text{act}}$  calculated for diffusion of  $\text{Au}_{\text{ad}}$  on  $c(2 \times 2)$ -Cl and  $c(\sqrt{2} \times 2\sqrt{2})R45^\circ$ -Cl Au(001) surfaces at coverage of 1/2 and in the presence of a Cl vacancy are summarized in Tab. 6.1. An increase in the activation barriers is observed with respect to the energy barrier for  $\text{Au}_{\text{ad}}\text{Cl}_2$  complex on the clean surface, which can be attributed to the repulsion between Cl adsorbates. In particular, for the diffusion of  $\text{Au}_{\text{ad}}$  on the fully covered  $c(2 \times 2)$ -Cl Au(001) surface the lowest activation barrier corresponds to the dissociation of  $\text{AuCl}_2$  complex into a AuCl complex and a Cl adatom. The activation barrier  $E_{\text{act}}$  for this diffusion mechanism amounts to 0.44 eV. If a Cl vacant site is considered in the Cl adlayer, the diffusion mechanisms involve elementary movement of  $\text{Au}_{\text{ad}}\text{Cl}_2$  complex and Cl vacancy separately which results in several diffusion steps. The related activation barriers are approximately half as large as those for fully covered Cl adlayers. For the  $c(2 \times 2)$ -Cl Au(001) surface with a Cl vacancy  $E_{\text{act}}$  amounts to 0.26 eV. Hence, the presence of a Cl vacancy promotes the Au self-diffusion.

In electrochemical experiments [50, 57, 298] an increase of Au surface mobility in the potential regime of the unreconstructed Au(001) surface has been attributed to a change of the applied sample potential towards positive values. The effect of electric field in the electrolyte has been estimated from the change of the adsorbate dipole moment relative to the adsorption site along the diffusion paths. The electrostatic contribution due to an electric field and the change of dipole moment at the transition state is added non-self-consistently to the DFT activation barriers. The dipole moment change at transition state comes out negative for all diffusion paths of Au adatom on Cl covered Au(001) surfaces

Table 6.1.: Comparison of activation barriers  $E_{\text{act}}$  (eV) and variation of dipole moment  $\Delta\mu$  (eÅ) at transition state for  $\text{Au}_{\text{ad}}$  on Cl covered  $(1 \times 1)$ -Au(001) surfaces with  $\Theta = 1/2$  and containing one Cl vacancy and for  $\text{Au}_{\text{ad}}\text{Cl}_2$  on the clean  $(1 \times 1)$ -Au(001) surface.  $\text{vac}_{\text{Cl}}$  refers to one Cl vacancy.

Au(001) surface		$E_{\text{act}}$ (eV)	$\Delta\mu$ (eÅ)	
$\text{Au}_{\text{ad}}\text{Cl}_2$	clean	0.07	-0.12	
$\text{Au}_{\text{ad}}$	$c(2 \times 2)$ -Cl	No $\text{vac}_{\text{Cl}}$	0.44	-0.20
		$\text{vac}_{\text{Cl}}$	0.26	-0.08
	$c(\sqrt{2} \times 2\sqrt{2})\text{R}45^\circ$ -Cl	No $\text{vac}_{\text{Cl}}$	0.25	-0.02
		$\text{vac}_{\text{Cl}}$	0.77	-0.09
		$\text{vac}_{\text{Cl}}$	0.35	-0.09
		$\text{vac}_{\text{Cl}}$	0.34	-0.06

within this work, which implies an increase of the energy barrier with the sample voltage. In that case the acceleration of Au island coarsening with the sample potential [57] as well as the transition between layer-by-layer and step-flow growth mode as a function of sample potential observed in [50] would require alternative explanations beyond the sample potential dependence of the  $\text{Au}_{\text{ad}}$  diffusion energy barrier on terraces. The sample voltage dependence of the dissociation of Au adatoms from islands as well as the island nucleation could play a role.

The nucleation of Au islands on the Cl covered Au(001) electrode surface starts with the binding of two  $\text{Au}_{\text{ad}}\text{Cl}_2$  complexes. As a first step, low total energy configurations of  $\text{Au}_{\text{ad}}$  dimer on  $c(2 \times 2)$ -Cl Au(001) with Cl coverage 1/2 and with several number of Cl vacancies in the Cl adlayer have been evaluated. In the absence of vacant sites in the Cl adlayer  $\text{AuCl}_2$ -chains are formed on the surface with a Au–Au separation of about a lattice constant. If Cl vacant sites become part of the equilibrium atomic adsorption structure, structural changes take place *i.e.* Au adatoms occupy epitaxial sites of the substrate with a Cl on the bridge site of the dimer. In this case, the energy gain due to the addition of a Au monomer increases from about 0.06 eV to about 0.23 eV. Hence, the presence of Cl vacancies tends to promote Au ad-structure formation. The raise of energy gain may support the transition from step-flow to layer-by-layer growth mode.

This work evidences the formation of equilibrium Au–Cl structures on Cl covered unreconstructed Au(001) surfaces. These illustrate that coadsorbates can form metal complexes as well as participate actively in the diffusion mechanisms. Therefore, strong differences between Cl covered and clean Au(001) surfaces are manifested, for example, low energy adsorption sites and diffusion paths. This study reveals that the density of Cl vacancies in the adlayer affects the self-diffusion of  $\text{Au}_{\text{ad}}$  and nucleation of Au islands on Cl covered Au(001) surfaces.

A natural way to extend the studies presented in this thesis are to include the effects of explicit water layers and cations. These features will be necessary to understand the dependence on sample potential and the role of the electrochemical environment in atomic processes during deposition. First insights of water effects within this work pointed out that lowest energy configurations of water on  $c(2 \times 2)$ -Cl Au(001) surfaces are hexagon-like. Model calculation of further elemental processes such as diffusion across a step and detachment from an island will be necessary to examine the effect of Cl coadsorbates in epitaxial growth. The results of such model calculations and the ones presented here could lead to the generation of rate constant data for large scale kMC simulations of Au(001) homoepitaxial growth in electrochemical environment.

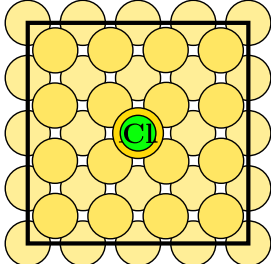
# A. | Appendix

## A.1. Au–Cl Complex on Clean Unreconstructed Au(001)

Table A.1 lists the configurations of Au–Cl complexes with  $n_{\text{Cl}} = 1, 2, 4$  adsorbed on clean unreconstructed Au(001). Energy differences  $E_{\text{diff},1}$  are calculated using Eq. (4.1) defined in Chapter 4 for values of  $\mu_{\text{Cl}}$  corresponding to  $\Theta = 1/16$ .

The adsorption configurations have been calculated by means of DFT using Quantum Espresso package [117, 118]. The Au surfaces have been modeled by six metal layers. The periodically repeated slabs are separated by a vacuum region of 13 Å. Asymmetric slabs have been chosen, *i.e.*, the adsorbate binds to a single side of the slab only. A dipole correction is applied in order to account for the work function difference between the opposite surfaces of the slab [111, 112]. A  $p(4 \times 4)$  surface unit cell (SUC) has been used with  $(4 \times 4 \times 1)$  Monkhorst-Pack grid of special  $k$ -points [107]. Denser  $k$ -point meshes produce a variation of  $E_{\text{diff},1}$  of about 0.01 eV.

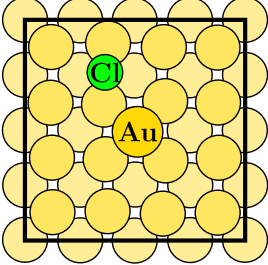
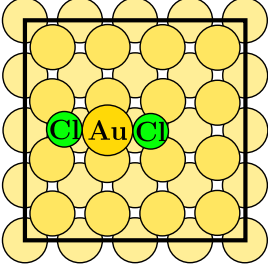
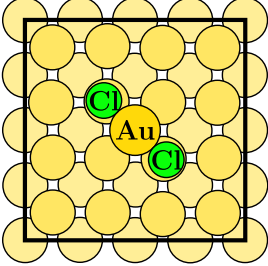
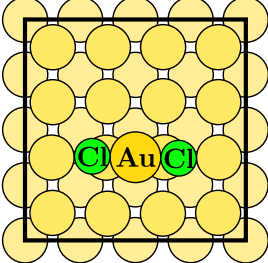
Table A.1.: Adsorption configurations of AuCl on Au(001) surface. Black squares denote the  $p(4 \times 4)$  SUC.

$n_{\text{Cl}}$	Configuration	$E_{\text{diff},1}(\mu_{\text{Cl},\Theta=1/16})$ (eV)
1		-0.01 (+0.01 <sup>1</sup> )

*Continued on next page*

<sup>1</sup>Result obtained with  $(6 \times 6 \times 1)$  Monkhorst-Pack grid of special  $k$ -points

Table A.1 - Continued from previous page

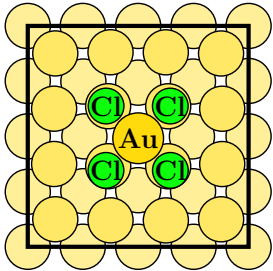
$n_{\text{Cl}}$	Configuration	$E_{\text{diff},1}(\mu_{\text{Cl},\Theta=1/16})$ (eV)
1		0.15 (0.16 <sup>2</sup> )
2		0.14
2		0.21
2		0.48

Continued on next page

<sup>2</sup>Result obtained with  $(6 \times 6 \times 1)$  Monkhorst-Pack grid of special  $k$ -points



Table A.1 - Continued from previous page

$n_{\text{Cl}}$	Configuration	$E_{\text{diff},1}(\mu_{\text{Cl},\theta=1/16})$ (eV)
4		1.57

**A.2. Supplementary Material from Publication J. Chem. Phys.  
151, 064709 (2019), Copyright (2019) by AIP Publishing**

DFT study of Au self-diffusion on Au(001)  
at a Cl<sup>-</sup> electrochemical interface:  
supplementary material

A. C. Dávila López<sup>1\*</sup> and E. Pehlke<sup>1†</sup>

<sup>1</sup>Institut für Theoretische Physik und Astrophysik, Christian-Albrechts-Universität zu Kiel

Leibnizstr. 15, 24098 Kiel, Germany

\*E-mail: davila@theo-physik.uni-kiel.de

†E-mail: pehlke@theo-physik.uni-kiel.de

July 17, 2019

## Contents

<b>S.1 Convergence analysis</b>	<b>2</b>
S.1.A Au <sub>ad</sub> / c(2 × 2)-Cl Au(001) . . . . .	2
S.1.B Cl vacancy / c(2 × 2)-Cl Au(001) . . . . .	4
S.1.C Au <sub>ad</sub> / c(2 × 2)-Cl Au(001) with Cl vacancy . . . . .	6
<b>S.2 Adsorption configurations of Au<sub>ad</sub> on Cl covered Au(001)</b>	<b>8</b>
S.2.A Cl covered Au(001) without a Cl vacancy . . . . .	8
S.2.A.1 Au <sub>ad</sub> / c(2 × 2)-Cl . . . . .	8
S.2.A.2 Au <sub>ad</sub> / c(√2 × 2√2)R45°-Cl . . . . .	9
S.2.B Cl covered Au(001) with a Cl vacancy . . . . .	10
S.2.B.1 Au <sub>ad</sub> / c(2 × 2)-Cl . . . . .	10
S.2.B.2 Au <sub>ad</sub> / c(√2 × 2√2)R45°-Cl . . . . .	12
<b>S.3 Water adlayer on Cl covered Au(001)</b>	<b>14</b>
S.3.A Rectangular water layer . . . . .	14
S.3.B Water adlayer on Cl covered Au(001) with a vacancy . . . . .	16
S.3.B.1 Structure of the water layer . . . . .	16
S.3.B.2 Diffusion of Cl vacancy on c(2 × 2)-Cl Au(001) in contact with water . . . . .	17

## S.1 Convergence analysis

The density functional calculations in this work have been carried through with the program PWscf from the Quantum ESPRESSO package [1, 2] (together with PLUMED [3] for metadynamics). The calculations are described in the main paper.

All relaxations have been carried through at a plane-wave cutoff energy of 30 Ry (a lower cutoff energy was used for molecular dynamics or metadynamics simulations only). Larger values of the cutoff energy produce a variation in energy less than 2 meV for the diffusion of Cl vacancy on  $c(2 \times 2)$ -Cl Au(001) surface. Convergence tests (with respect to the number of layers, k-points and surface unit cell (SUC)) have been carried through in order to estimate the accuracy of the energy differences along the diffusion paths. Three different diffusion mechanisms have been chosen for the convergence analysis: diffusion of  $\text{Au}_{\text{ad}}$  on  $c(2 \times 2)$ -Cl via hollow site (see Fig. 3(b) in main text), Cl vacancy diffusion on  $c(2 \times 2)$ -Cl (see Fig. 5), and a step of the diffusion path of  $\text{Au}_{\text{ad}}$  on  $c(2 \times 2)$ -Cl with a Cl vacancy (see Fig.7(b)).

### S.1.A $\text{Au}_{\text{ad}}$ / $c(2 \times 2)$ -Cl Au(001)

The hopping of  $\text{Au}_{\text{ad}}$  via hollow on the Cl covered Au(001) surface yields an activation energy of 0.44 eV. The  $\text{Cl}_{\text{c}}$  atom, bound to the  $\text{Au}_{\text{ad}}$ , moves towards the top position of the  $\text{Au}_{\text{ad}}$  along the diffusion path (see local minimum Fig. 3(b)). In Fig.S1, the variation of the total energy between the initial and local minimum (LM) configuration computed with a  $(4 \times 4)$  and a  $(6 \times 6)$  SUC are compared. We observe the largest difference  $\sim 0.07$  eV between the calculations with 4 and 6 Au layers and a  $(6 \times 6)$  SUC. At a fixed number (4 or 6) of layers, the calculations yield an error  $\sim 0.03$  eV with respect to the convergent value. Denser k-point meshes produce a variation of roughly 0.01 eV for each SUC. Increasing the vacuum thickness to  $17\text{\AA}$   $\Delta E$  varies less than 5 meV. In Fig.S2 the variation of energy along the diffusion path is presented, the results are summarized in Tab.S1. The largest difference of the energy barrier  $E_{\text{B}}$  is between 4 and 6 layer with the  $(6 \times 6)$  SUC and amounts to roughly 0.03 eV. In case of the induced dipole moment the difference between both SUC is about  $0.02 \text{ e}\text{\AA}$ , as well as for the difference at transition state presented in Tab. S1 .

Path	# of layers	k-points	SUC	$E_{\text{B}}$ /meV	$\Delta \mu_{\text{B}}$ / meÅ
$\text{Au}_{\text{ad}}\text{Cl}_2 \rightarrow \text{Au}_{\text{ad}}\text{Cl}$	4	$(4 \times 4 \times 1)$	$(4 \times 4)$	420	-173
	6	$(4 \times 4 \times 1)$	$(4 \times 4)$	424	-176
	4	$(3 \times 3 \times 1)$	$(6 \times 6)$	445	-193
	6	$(3 \times 3 \times 1)$	$(6 \times 6)$	417	-198

**Table S1:** Energy barrier and dipole moment difference at the transition state for the configurations presented in Fig. S2.

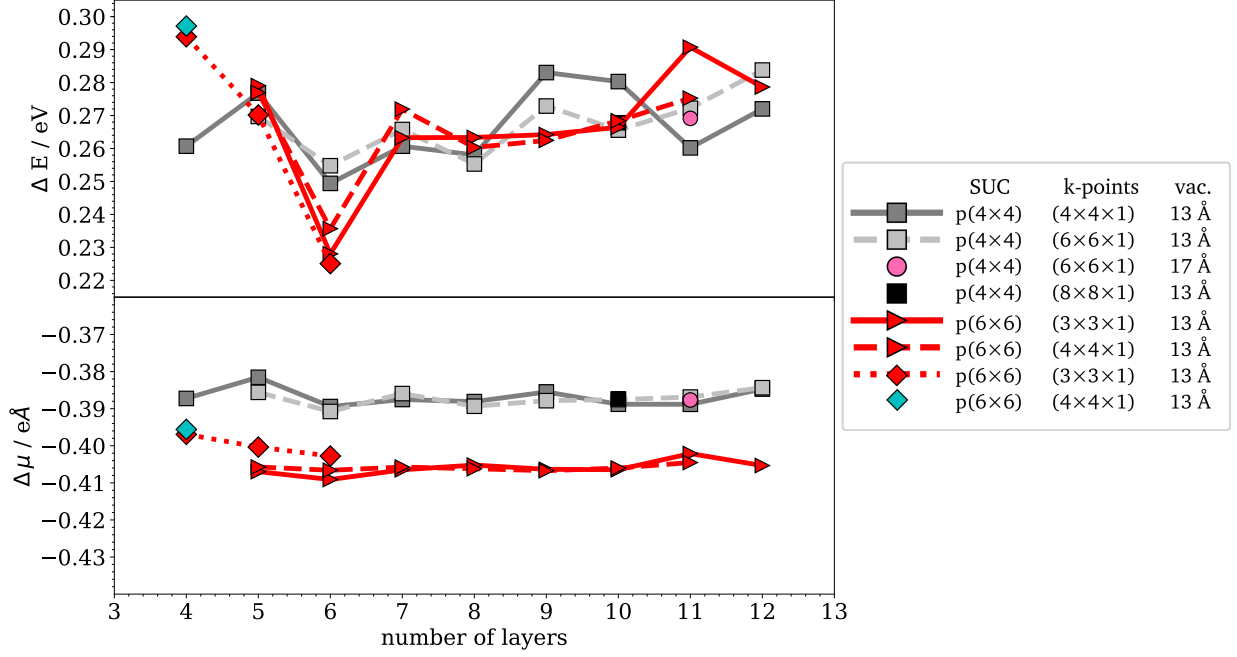


**Figure S1:** Convergence test for hopping of  $\text{Au}_{\text{ad}}$  via hollow on  $c(2 \times 2)$ -Cl Au(001). Top: energy difference between the local minimum and the initial configuration in Fig. 3(b) of the main text versus the number of layers in the Au substrate. Bottom: dipole moment difference between the local minimum and the initial configuration. In case of the 4 layer Au slab the topmost 2 Au layers have been relaxed, as well as the adatoms positions. In case of the 6 layers Au slab the topmost 4 layers have been relaxed. For  $(6 \times 6)$  SUC two 5 layer slabs have been created by either adding a bulk layer to 4 layer slab or removing the bottommost Au layer from the 6 layer slab. All slabs with more than 6 layers have been created by adding bulk layers, while all atomic positions have been kept fixed.

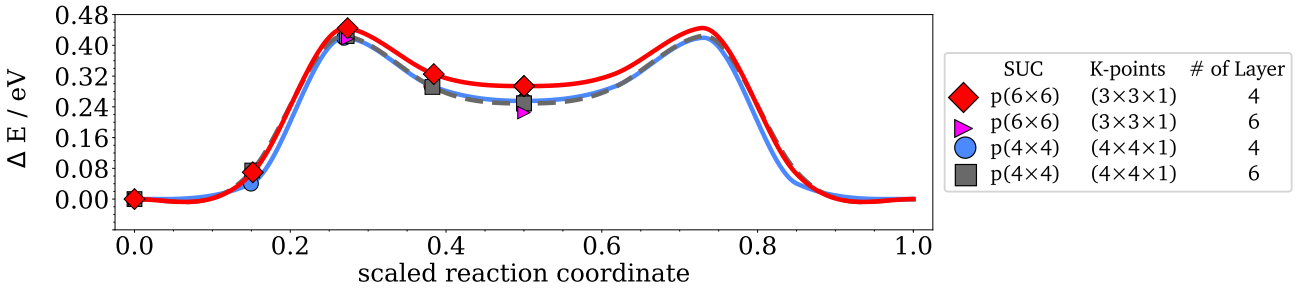


**Figure S2:** Convergence test with respect to the substrate layer thickness and k-point mesh. Diffusion path of the  $\text{Au}_{\text{ad}}$  on  $c(2 \times 2)$ -Cl Au(001) via a hollow site of the substrate. Variation of the energy along the path has been obtained by a Nudged Elastic Band (NEB) calculation for the 4 and the 6 layer Au slabs with a  $(4 \times 4)$  SUC and for the 4 layer Au slab with a  $(6 \times 6)$  SUC. A DFT calculation for frozen atomic coordinates was performed for the 6 layer Au slab in a  $(6 \times 6)$  SUC by adding two bulk layers to the 4 layer Au slab. 30 Ry plane-waves cutoff energy, 13 Å vacuum layer thickness.

### S.1.B Cl vacancy / $c(2 \times 2)$ -Cl Au(001)

The diffusion path of a Cl adatom into a neighboring vacant site is displayed in Fig. 5 of the main text. The calculation with a 6 layer Au slab and  $(6 \times 6)$  SUC gives a diffusion energy barrier of 0.18 eV and a very small energy difference between the initial and the local minimum (LM) configurations of 0.04 eV at these convergence parameters. In Fig. S3, the total energy difference between the initial and the local minimum (LM) configurations calculated with a  $(4 \times 4)$  and a  $(6 \times 6)$  SUC are compared. The values for  $\Delta E$  are roughly 12 meV with 10 Au layers slab for both surface unit cells. Denser k-point meshes produce a variation less than 0.01 eV for each SUC, while a thicker vacuum region of  $\sim 21 \text{ \AA}$  produces only minimal variations. The uncertainty for the 6 layers Au slab with a  $(6 \times 6)$  SUC is roughly 0.03 eV, which is larger than the converged value of  $\Delta E \approx 0.01 \text{ eV}$ . However, an accuracy of 0.03-0.04 eV is sufficient for the calculation of the energy barrier. The values of dipole moment differences are between  $-20 \text{ me\AA}$  to  $-10 \text{ me\AA}$ . The variation of energy along the diffusion path is shown in Fig. S4, activation energy barrier and the variation of the dipole moment at the transition state are summarized in Tab. S2. The accuracy of the energy barrier amounts to 15 meV for a 6 layers Au slab with a  $(6 \times 6)$  SUC. In case of the induced dipole moment, the estimated accuracy amounts to about 15 me\AA.

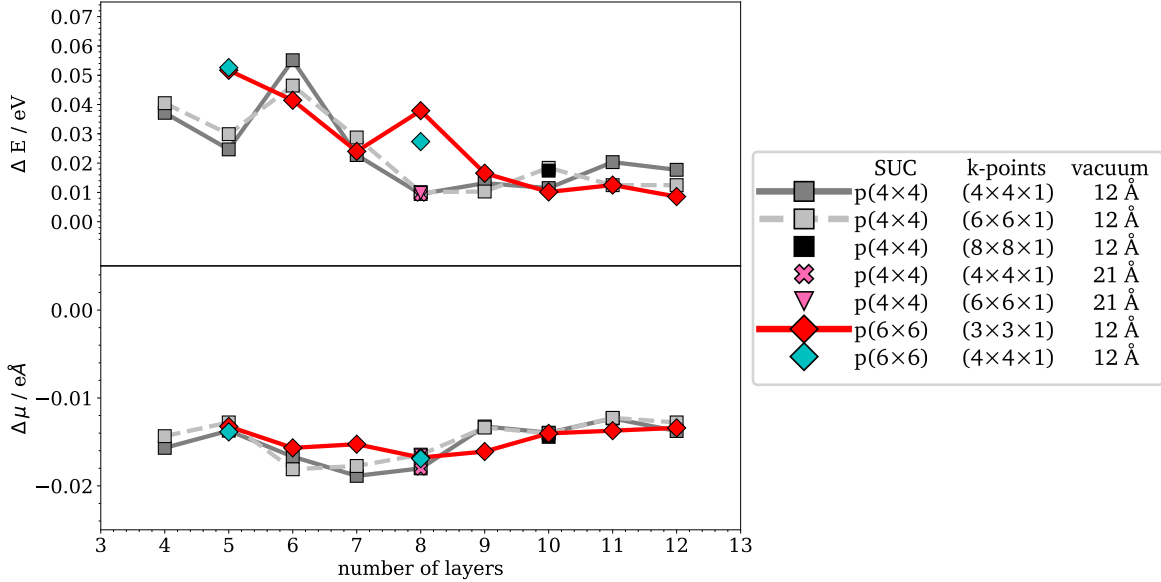


**Figure S3:** Convergence tests for diffusion of a Cl vacancy on  $c(2 \times 2)$ -Cl Au(001) (see Fig. 5 in the main text). Top: energy difference between the initial and the intermediate configuration versus the number of layers. Bottom: dipole moment difference between the initial and intermediate configurations. In case of the 4 layers Au slab the topmost 2 layers have been relaxed. In case of the 6 layers Au slab the topmost 4 layers have been relaxed. Configurations of 5 layer slabs have been created by removing the bottommost Au layer from the 6 layer slab. All slabs with more than 6 layers have been created by adding bulk layers, while all atomic positions have been kept fixed.

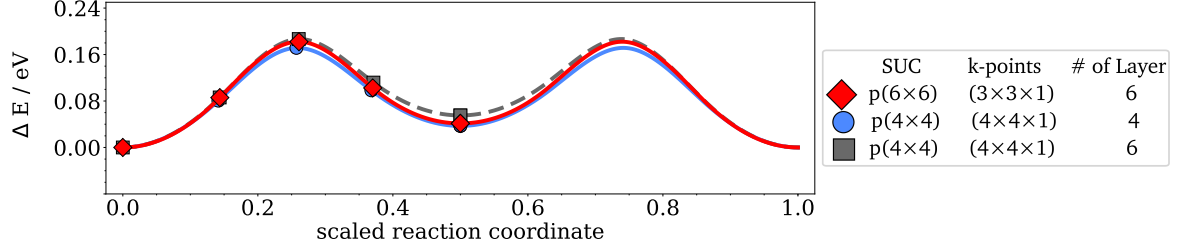


**Figure S4:** Convergence test with respect to the substrate layer thickness and k-point mesh. Diffusion path of the Cl vacancy on  $c(2 \times 2)$ -Cl Au(001). The variation of energy along the path has been obtained by a Nudged Elastic Band (NEB) calculation for a 4 and a 6 Au layers slab with a  $(4 \times 4)$  SUC, and a 6 Au layers slab with a  $(6 \times 6)$  SUC. 30 Ry cutoff energy, 13 Å vacuum.

Path	# of layers	k-points	SUC	$E_B$ /meV	$\Delta\mu$ / meÅ
Initial $\rightarrow$ Intermediate	4	$(4 \times 4 \times 1)$	$(4 \times 4)$	171	-15
	6	$(4 \times 4 \times 1)$	$(4 \times 4)$	187	-11
	6	$(3 \times 3 \times 1)$	$(6 \times 6)$	182	-6
	8	$(3 \times 3 \times 1)$	$(6 \times 6)$	175	-21
	10	$(3 \times 3 \times 1)$	$(6 \times 6)$	168	-20

**Table S2:** Energy barrier and dipole moment difference at the transition state for the configurations presented in Fig.S4. For the 8 and the 10 Au layers slabs DFT calculations for frozen atomic coordinates have been performed in a  $(6 \times 6)$  SUC by adding two bulk layers to the 6 Au layers slab.

### S.1.C $\text{Au}_{\text{ad}} / \text{c}(2 \times 2)\text{-Cl Au}(001)$ with Cl vacancy

Furthermore, convergence has been tested for the diffusion step depicted in Fig. S5, which is part of the diffusion path of  $\text{Au}_{\text{ad}}$  on the  $\text{c}(2 \times 2)\text{-Cl Au}(001)$  surface in the presence of a Cl vacancy as shown in Fig. 7(b) of the main text. In Fig. S6 the energy difference between the initial and the intermediate configuration is plotted versus the number of layers. The largest difference with respect to the converged value amounts to 0.04 eV and the dipole moment difference ranges between -5 to +5  $\text{me}\text{\AA}$ . The variation of energy along the diffusion path is shown in Fig. S7, energy barrier and variation of the dipole moment at the transition state are summarized in Tab. S3. It is observed that the energy barrier has an accuracy better than 15 meV. The variation of the dipole moment at the transition state has an accuracy of 5  $\text{me}\text{\AA}$ .

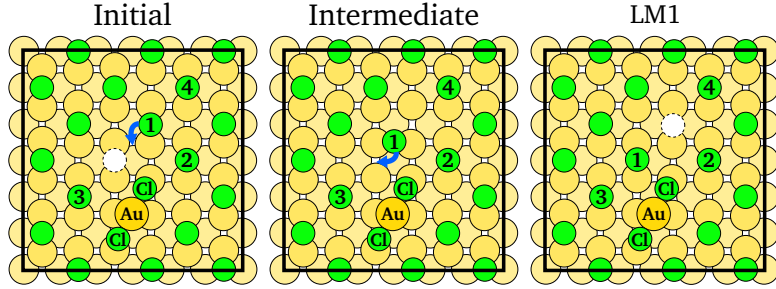


**Figure S5:** Diffusion of  $\text{Cl}_{\text{ad}}$  to a vacant site in the presence of  $\text{Au}_{\text{ad}}\text{Cl}_2$  complex on  $\text{c}(2 \times 2)\text{-Cl Au}(001)$  from Fig. 7(b) in the main text. The squares represent the  $(6 \times 6)$  SUC. The diffusion path is indicated schematically by arrows.

Path	# of layers	k-points	SUC	$E_B / \text{meV}$	$\Delta\mu_B / \text{me}\text{\AA}$
Initial $\rightarrow$ Intermediate	4	$(3 \times 3 \times 1)$	$(6 \times 6)$	168	-12
	6	$(3 \times 3 \times 1)$	$(6 \times 6)$	180	-10
	8	$(3 \times 3 \times 1)$	$(6 \times 6)$	174	-14
	10	$(3 \times 3 \times 1)$	$(6 \times 6)$	167	-10

**Table S3:** Convergence test of the energy barrier and the variation of dipole moment at the transition state. For the 8 and the 10 Au layers slabs DFT calculations for frozen atomic coordinates have been performed in a  $(6 \times 6)$  SUC by adding two and four bulk layers, respectively, to the 6 layer Au slab calculation, see Fig. S7



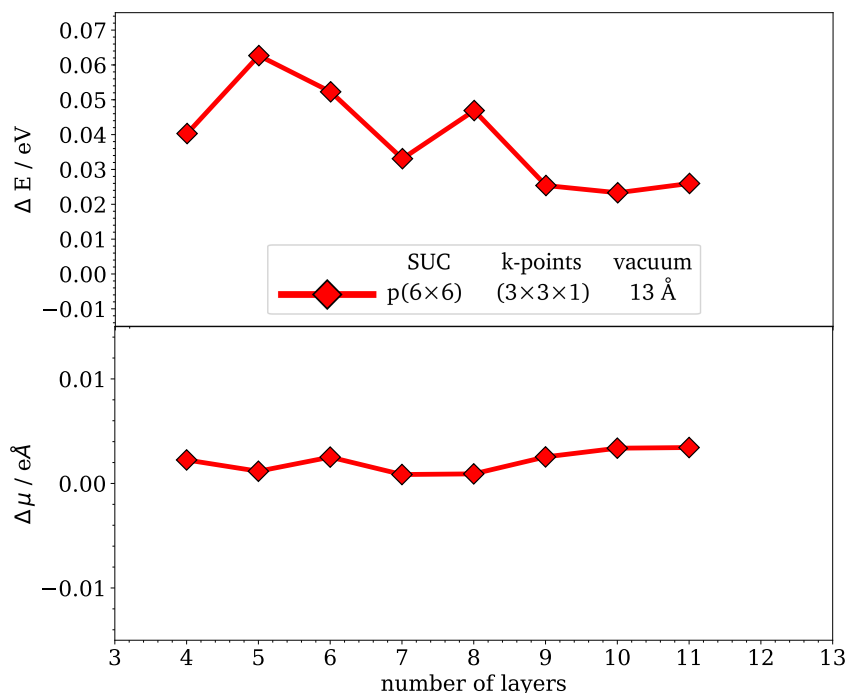


**Figure S6:** Convergence test with respect to the substrate thickness. Top: energy difference between the initial and the intermediate configuration (see Fig. S5) versus the number of layers. Bottom: dipole moment difference between the initial and the intermediate configurations. In case of the 4 layer Au slab the topmost 2 Au layers have been relaxed. In case of the 6 layer Au slab the topmost 4 Au layers have been relaxed. The 5 layer Au slab configuration has been created by removing the bottommost Au layer from the 6 layer Au slab. All slabs with more than 6 layers have been created by adding bulk layers, with all atomic positions fixed.

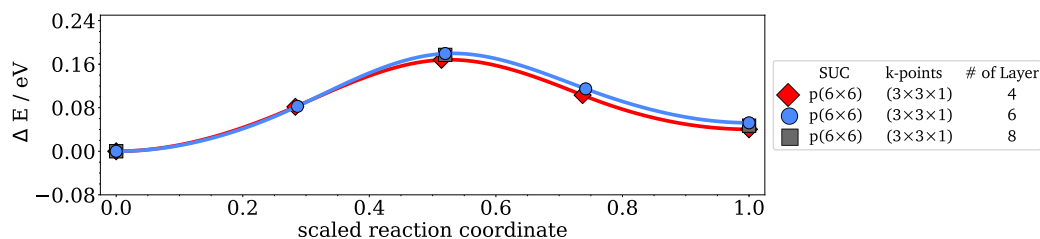


**Figure S7:** Convergence test with respect to the layer thickness of the substrate. Diffusion energy path of the  $\text{Cl}_{\text{ad}}$  on  $c(2 \times 2)\text{-Cl Au}(001)$  in the presence of a  $\text{Au}_{\text{ad}}\text{Cl}_2$  complex (see Fig. S5). The variation of energy along the path has been obtained by NEB calculation for the 4 and the 6 layer Au slabs. 30 Ry cutoff energy. The 8 layers Au slab has been created by adding bulk layers, with all atomic positions fixed.

## S.2 Adsorption configurations of Au<sub>ad</sub> on Cl covered Au(001)

In order to find the global and local minimum energy configurations we have performed Metadynamic-MD simulations in combination with ionic relaxations to find adsorption configurations in addition to configurations chosen by chemical intuition. Metadynamic-MD simulations have been performed for the fully Cl covered Au(001) surface and a Cl covered Au(001) surface with a Cl vacancy. For each case we have started from a local minimum energy configuration. Also adsorption configurations with different local number of Cl adatoms on the chlorine covered Au(001) surface have been calculated, results will be summarized elsewhere. In this paper we present only two cases: fully Cl covered Au(001) and Cl covered Au(001) surface with a Cl vacancy.

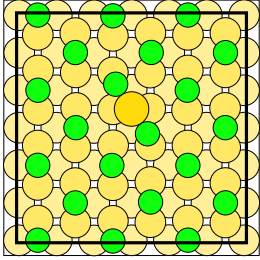
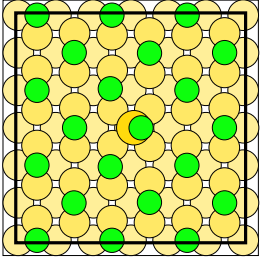
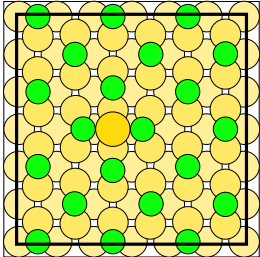
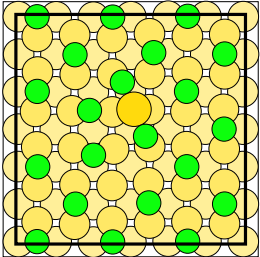
### S.2.A Cl covered Au(001) without a Cl vacancy

In the present section we give an overview of the most relevant calculated adsorption configurations of a Au adatom on a  $c(2 \times 2)$ -Cl and a  $c(\sqrt{2} \times 2\sqrt{2})R45^\circ$ -Cl covered Au(001) surface. Calculations for both adlayer reconstructions have been performed for a Cl coverage  $\Theta = 1/2$ . The adsorption configurations in Tab. S4 and S5 have been calculated with 4 Au layers and  $(3 \times 3 \times 1)$  k-points, 30 Ry of cutoff energy and 13 Å vacuum region.

#### S.2.A.1 Au<sub>ad</sub> / $c(2 \times 2)$ -Cl

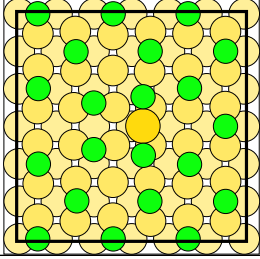
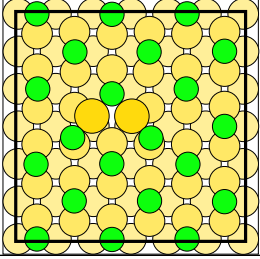
In Tab. S4 the energy for a Au<sub>ad</sub> on  $c(2 \times 2)$ -Cl Au(001) with reference to the lowest adsorption configuration is presented. For this coverage and Cl adlayer the configuration **1** was identified as the global energy minimum.

**Table S4:** Adsorption configurations for Au adatom on  $c(2 \times 2)$ -Cl covered Au(001) with  $\Theta = 1/2$ .

Configuration	$\Delta E / \text{meV}$	Configuration	$\Delta E / \text{meV}$
	0(ref.)		294
	369		404

*Continued on next page*

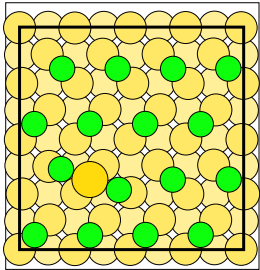
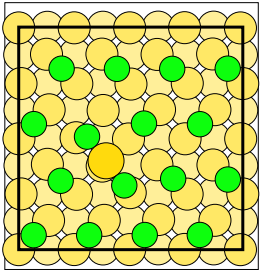
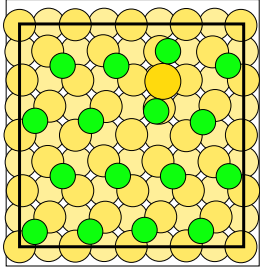
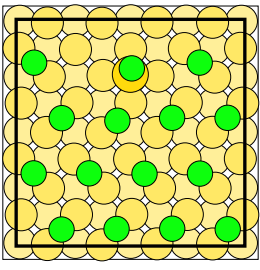
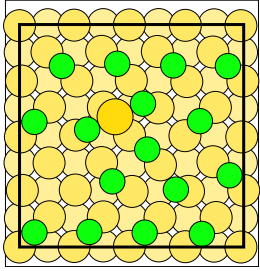
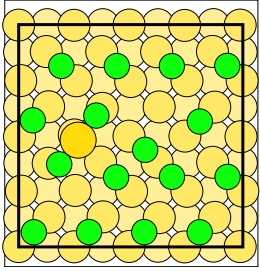
Table S4 - Continued from previous page

Configuration	$\Delta E / \text{meV}$	Configuration	$\Delta E / \text{meV}$
	520		571

### S.2.A.2 $\text{Au}_{\text{ad}} / c(\sqrt{2} \times 2\sqrt{2})\text{R}45^\circ\text{-Cl}$

In Tab. S5 the energy for a Au adatom on a  $c(\sqrt{2} \times 2\sqrt{2})\text{R}45^\circ\text{-Cl}$  covered Au(001) surface with reference to the lowest adsorption configuration is presented. For this coverage and Cl adlayer the configuration **1** was identified as the global minimum.

**Table S5:** Adsorption configurations for Au adatom on  $c(\sqrt{2} \times 2\sqrt{2})\text{R}45^\circ\text{-Cl}$  covered Au(001) with  $\Theta = 1/2$ .

Configuration	$\Delta E / \text{meV}$	Configuration	$\Delta E / \text{meV}$
	0(ref.)		83
	155		370
	686		1317

## S.2.B Cl covered Au(001) with a Cl vacancy

The adsorption configurations in Tab. S6 and S7 have been calculated with 4 Au layers and  $(3 \times 1)$  k-points, 30 Ry cutoff energy and 13 Å vacuum region.

### S.2.B.1 Au<sub>ad</sub> / c(2 × 2)-Cl

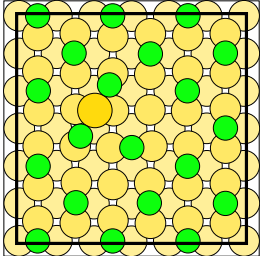
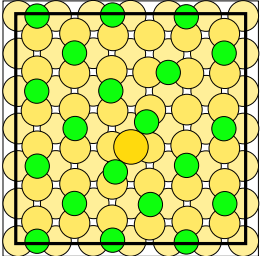
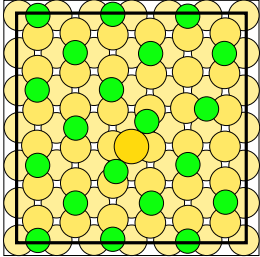
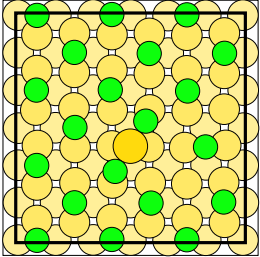
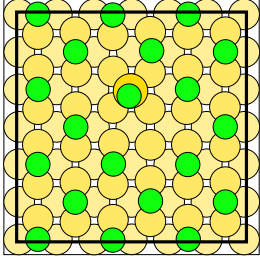
In Tab. S6 the energy of the local minimum energy configurations with reference to the proposed global minimum configuration is presented for a Au adatom on the c(2 × 2)-Cl covered Au(001) surface with a Cl-vacancy.

**Table S6:** Adsorption configurations for Au adatom on c(2 × 2)-Cl covered Au(001) with a Cl vacancy.

Configuration	$\Delta E / \text{meV}$	Configuration	$\Delta E / \text{meV}$
	0(ref.)		13
	40		40
	41		55
	60		64

*Continued on next page*

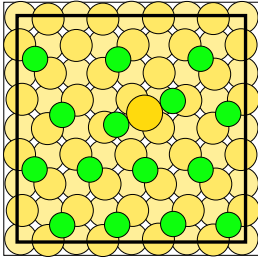
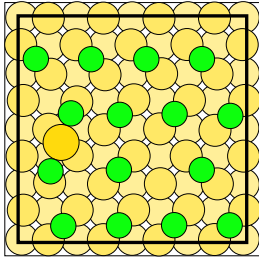
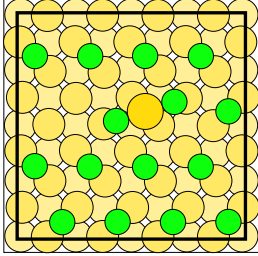
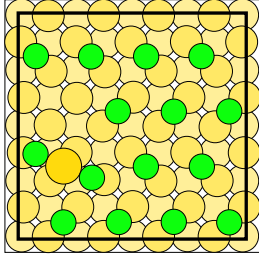
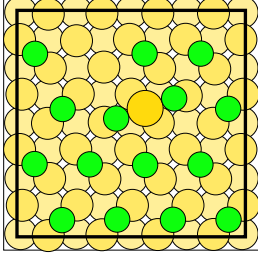
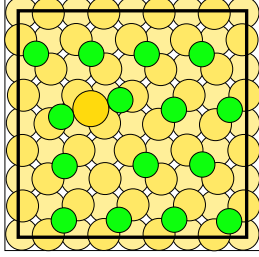
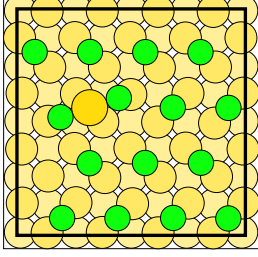
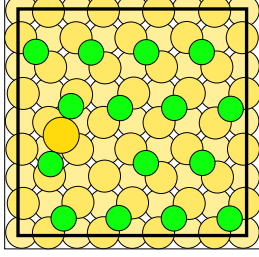
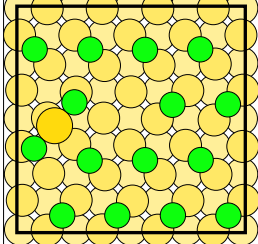
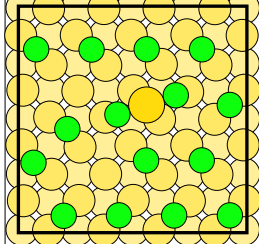
Table S6 - *Continued from previous page*

Configuration	$\Delta E/$ meV	Configuration	$\Delta E/$ meV
	69		89
	100		100
	190		

### S.2.B.2 Au<sub>ad</sub> / c( $\sqrt{2} \times 2\sqrt{2}$ )R45°-Cl

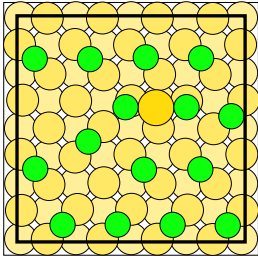
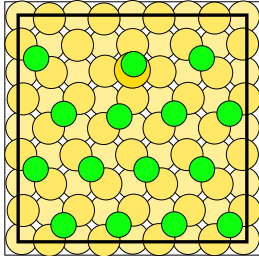
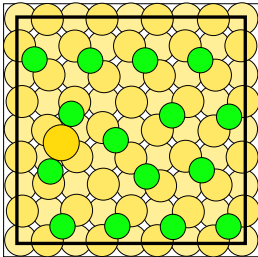
In Tab. S7 the energy of the local minimum energy configurations with reference to the proposed global minimum configuration is presented for a Au adatom on the c( $\sqrt{2} \times 2\sqrt{2}$ )R45°-Cl covered Au(001) surface with a Cl vacancy.

**Table S7:** Adsorption configurations for Au adatom on c( $\sqrt{2} \times 2\sqrt{2}$ )R°45-Cl covered Au(001) with a Cl vacancy.

Configuration	$\Delta E$ / meV	Configuration	$\Delta E$ / meV
	0(ref.)		8
	52		58
	66		68
	79		82
	113		125

*Continued on next page*

Table S7 - *Continued from previous page*

Configuration	$\Delta E/$ meV	Configuration	$\Delta E/$ meV
	193		287
	335		

### S.3 Water adlayer on Cl covered Au(001)

#### S.3.A Rectangular water layer

We started from the rectangular water structure as described by Lin and Groß in Ref. 4. The H and O atoms, as well as the halogens and metals atoms, are represented by ultrasoft pseudopotentials from the open-source GBRV library [5]. These pseudopotentials are different from those used in the VASP calculations in Ref. 4 and the cutoff energy required for the present calculation needs to be determined. We have put the rectangular water layer on top of the clean and Cl covered Au(001) surface as depicted in Fig. S8. The adsorption energy of water molecules has been defined:

$$E_{\text{ads}}^{H_2O} = \left( E^{x \text{Cl} + n \text{H}_2\text{O} / \text{Au}(001)} - E^{x \text{Cl} / \text{Au}(001)} - n E^{H_2O} \right) / n \quad (1)$$

where  $x$  is the number of Cl atoms in the SUC, and  $n$  is the number of water molecules. Similarly, the adsorption energy of Cl has been defined:

$$E_{\text{ads}}^{\text{Cl}} = \left( E^{x \text{Cl} + n \text{H}_2\text{O} / \text{Au}(001)} - E^{n \text{H}_2\text{O} / \text{Au}(001)} - x \frac{E^{\text{Cl}_2}}{2} \right) / x \quad (2)$$

There are two adsorption positions for water molecules on the clean Au(001) surface, bridge and top sites. It has been pointed out in Ref. 4 that the adsorption energy difference between both sites is very small. We found an analogous result for the Cl covered Au(001) surface. For simplicity we have considered only the top site for the determination of the converge parameters.

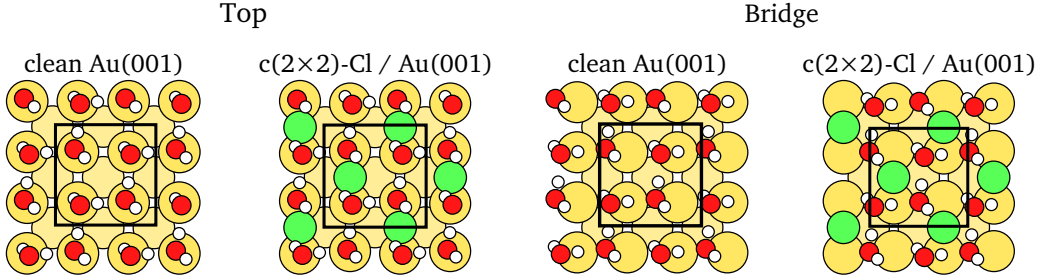


**Figure S8:** Water adlayer structures with  $\text{H}_2\text{O}$  molecules on top (t) and bridge (b) site of the clean Au(001) and Cl covered Au(001) surfaces. Black squares denote the  $(2 \times 2)$  SUC. The two bottommost Au layers have been fixed, the remaining Au layers and adsorbates have been allowed to relax.

The adsorption energy as a function of the plane-wave cutoff energy is shown in Fig. S9. A calculation with 30 Ry results in an accuracy of 0.01 eV for  $E_{\text{ads}}^{H_2O}$ , which refers to one  $\text{H}_2\text{O}$  molecule. In Fig. S10 the  $\text{H}_2\text{O}$  and Cl adsorption energy defined above are shown as a function of the number of Au layers in the slab. Due to the ionicity of the  $\text{Cl}^-$  the Cl adsorption energy is more susceptible to the number of substrate layers. For a 6 layer Au slab the calculation yields an error  $\sim 15$  meV with respect to the converged value.



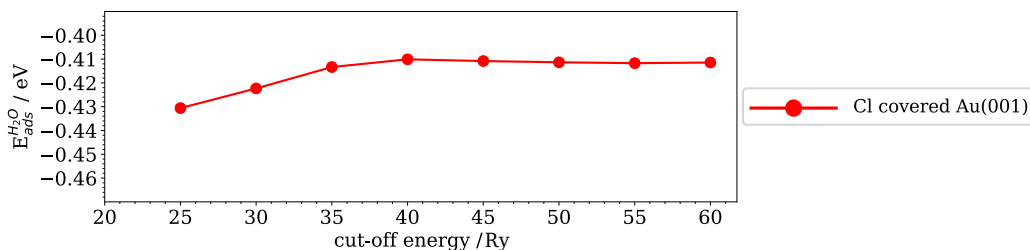


**Figure S9:** Convergence test with respect to the cutoff energy. Adsorption energy of  $\text{H}_2\text{O}$  on a  $c(2 \times 2)$ -Cl Au(001) surface for a 4 layer Au slab and a  $(2 \times 2)$  SUC with a k-point mesh of  $(12 \times 12 \times 1)$  and a vacuum thickness of  $17 \text{ \AA}$ . In case of the calculation with 30 Ry cutoff the topmost 2 Au layers as well as the adsorbates (Cl and  $\text{H}_2\text{O}$  molecules) have been ionically relaxed. For all other calculations in this diagram the atomic positions have been kept fixed at this geometry.

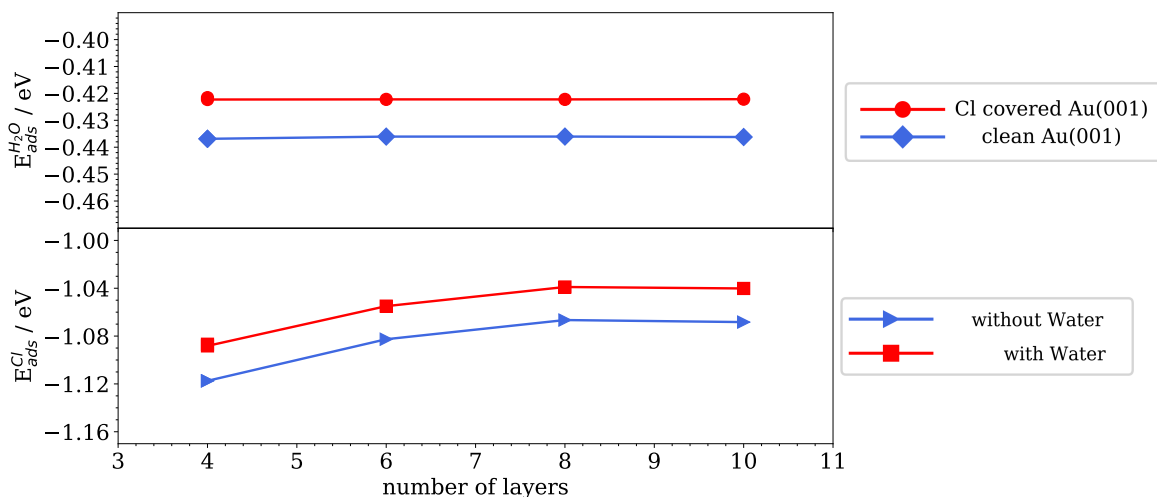
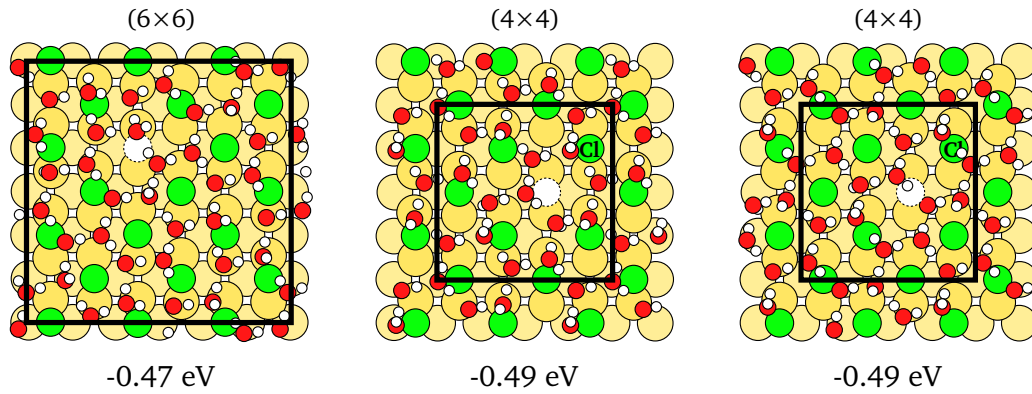


**Figure S10:** Top: Adsorption energy of  $\text{H}_2\text{O}$  versus number of layers. Bottom: Adsorption energy of Cl versus number of layers. For each calculation the two bottommost Au layers have been fixed to their bulk position, the remaining Au layers and adsorbates have been ionically relaxed in a  $(2 \times 2)$  SUC with  $(12 \times 12 \times 1)$  k-points mesh and a vacuum thickness of  $17 \text{ \AA}$ . In case of the 10 layers slab a DFT calculation for frozen atomic coordinates has been performed by adding two bulk layers to the 8 Au layers slab.

### S.3.B Water adlayer on Cl covered Au(001) with a vacancy

#### S.3.B.1 Structure of the water layer

To allow for different relaxation patterns, we have performed calculations within a  $(4 \times 4)$  SUC with 16 water molecules and a  $(6 \times 6)$  SUC with 36 water molecules. For both unit cells the atomic geometry of the substrate and the Cl adlayer has been fixed, while water molecules have been ionically relaxed. In Fig. S11 water configurations with their corresponding adsorption energies are presented. Both unit cells contain hexagonal  $\text{H}_2\text{O}$  rings, in case of the  $(6 \times 6)$  SUC rectangular  $\text{H}_2\text{O}$  rings are also present. In the  $(6 \times 6)$  SUC water molecules adsorb with an energy of 0.47 eV, and they adsorb with an energy of 0.49 eV per  $\text{H}_2\text{O}$  molecule in the  $(4 \times 4)$  SUC.

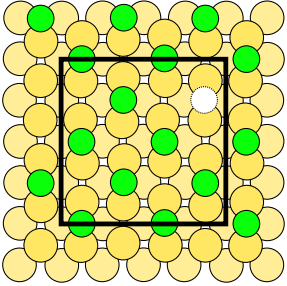
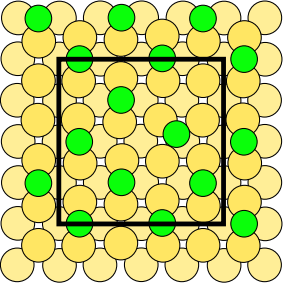
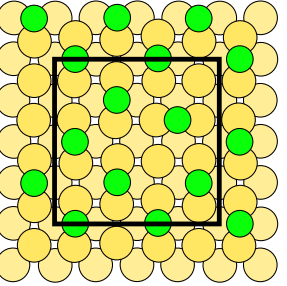
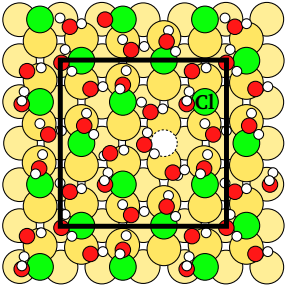
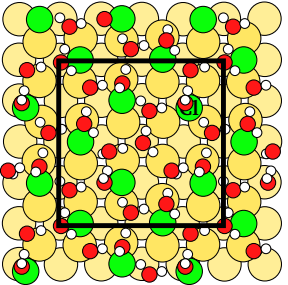
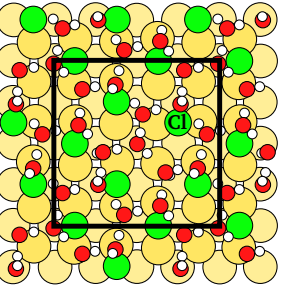


**Figure S11:** Water structure on Cl covered Au(001) with a Cl vacancy. The black squares represent the surface unit cell. The Au slabs contain 6 layers and a vacuum layer with a thickness of 13 Å. For the Brillouin zone integration a  $(4 \times 4 \times 1)$  k-point mesh for the  $(4 \times 4)$  SUC, and a  $(3 \times 3 \times 1)$  k-point mesh for the  $(6 \times 6)$  SUC have been used. For  $(4 \times 4)$  SUC we obtain two water layers, which are slightly displaced from each other.

### S.3.B.2 Diffusion of Cl vacancy on $c(2 \times 2)$ -Cl Au(001) in contact with water

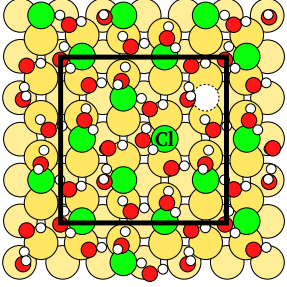
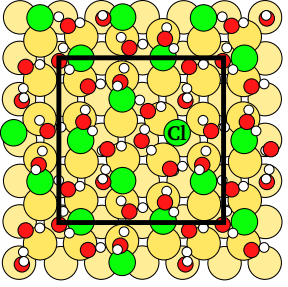
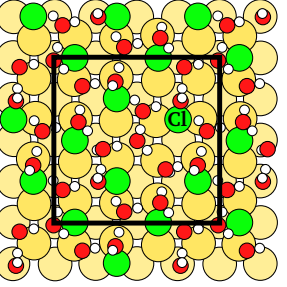
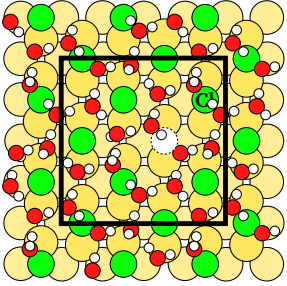
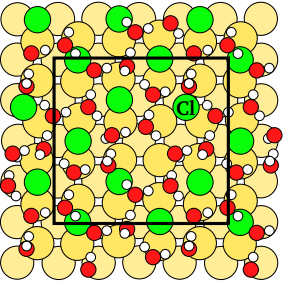
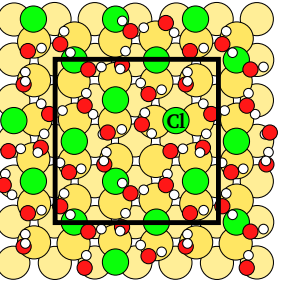
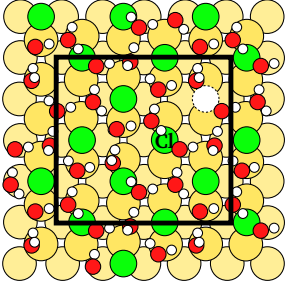
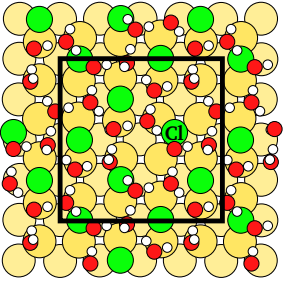
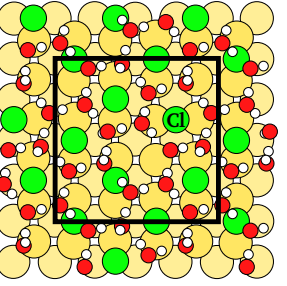
In vacuum the diffusion path of a Cl adatom into a neighboring vacant site is symmetric with respect to the intermediate state as shown in Fig. 5 of the main text. However, in contact with the water layer the diffusion path of the Cl adatom no longer possesses this symmetry. For this reason, in this work we have calculated the diffusion of the Cl adatom for two different initial positions of the Cl vacancy as shown in Tab.S8. Specially, the difference consists in the orientation of the water molecules close to the diffusing Cl adatom. Furthermore, two positions of the water layer, slightly displaced with respect to each other, have been considered, resulting in a total of four diffusion paths. In Tab.S8 the energy and dipole moment with respect to the lowest energy configuration of the initial state are presented for configurations along the diffusion path of the Cl adatom. For all configurations the atomic geometries of the substrate and the Cl adlayer have been fixed, while the water molecules have been relaxed ionically. The vacuum thickness is about 13 Å, increasing the vacuum region to 20 Å  $\Delta E$  varies less than 3 meV and  $\Delta \mu$  only 2 meÅ.

**Table S8:** Diffusion of a Cl vacancy on  $c(2 \times 2)$ -Cl Au(001) in contact with water. The black squares represent the  $(4 \times 4)$  SUC. The Au slabs contain 6 layers. The two bottommost layers have been fixed to bulk positions. For the Brillouin zone integration a  $(4 \times 4 \times 1)$  k-points mesh has been used. Energy and dipole moment differences correspond to calculations with a vacuum thickness of 13 Å.

	Initial	Transition State	Intermediate
No Water			
$\Delta E / \text{meV}$	0	187	55
$\Delta \mu / \text{meÅ}$	0	-11	-17
Water 01			
$\Delta E / \text{meV}$	0 (ref.)	190	68
$\Delta \mu / \text{meÅ}$	0 (ref.)	-5	4

*Continued on next page*

Table S8 - Continued from previous page

	Initial	Transition State	Intermediate
Water 01			
$\Delta E / \text{meV}$	88	228	68
$\Delta \mu / \text{me\AA}$	-130	4	4
Water 02			
$\Delta E / \text{meV}$	12	205	98
$\Delta \mu / \text{me\AA}$	-5	-8	-12
Water 02			
$\Delta E / \text{meV}$	94	287	98
$\Delta \mu / \text{me\AA}$	-173	-179	-12

## References

- [1] P. Giannozzi, S. Baroni, N. Bonini, M. Calandra, R. Car, C. Cavazzoni, D. Ceresoli, G. L. Chiarotti, M. Cococcioni, I. Dabo, A. Dal Corso, S. de Gironcoli, S. Fabris, G. Fratesi, R. Gebauer, U. Gerstmann, C. Gougousis, A. Kokalj, M. Lazzeri, L. Martin-Samos, N. Marzari, F. Mauri, R. Mazzarello, S. Paolini, A. Pasquarello, L. Paulatto, C. Sbraccia, S. Scandolo, G. Sclauzero, A. P. Seitsonen, A. Smogunov, P. Umari, and R. M. Wentzcovitch. QUANTUM ESPRESSO: a modular and open-source software project for quantum simulations of materials. *J. Phys.: Condens. Matter*, 21(39):395502, 2009. ISSN 0953-8984. doi: 10.1088/0953-8984/21/39/395502. URL <http://stacks.iop.org/0953-8984/21/i=39/a=395502>.
- [2] P. Giannozzi, O. Andreussi, T. Brumme, O. Bunau, M. Buongiorno Nardelli, M. Calandra, R. Car,

- C. Cavazzoni, D. Ceresoli, M. Cococcioni, N. Colonna, I. Carnimeo, A. Dal Corso, S. de Gironcoli, P. Delugas, R. A. DiStasio Jr, A. Ferretti, A. Floris, G. Fratesi, G. Fugallo, R. Gebauer, U. Gerstmann, F. Giustino, T. Gorni, J. Jia, M. Kawamura, H-Y Ko, A. Kokalj, E. Küçükbenli, M. Lazzeri, M. Marsili, N. Marzari, F. Mauri, N. L. Nguyen, H.-V. Nguyen, A. Otero-de-la-Roza, L. Paulatto, S. Poncé, D. Rocca, R. Sabatini, B. Santra, M. Schlipf, A. P. Seitsonen, A. Smogunov, I. Timrov, T. Thonhauser, P. Umari, N. Vast, X. Wu, and S. Baroni. Advanced capabilities for materials modelling with Quantum ESPRESSO. *Journal of Physics: Condensed Matter*, 29(46):465901, 2017. ISSN 0953-8984. doi: 10.1088/1361-648X/aa8f79. URL <http://stacks.iop.org/0953-8984/29/i=46/a=465901>.
- [3] M. Bonomi, D. Branduardi, G. Bussi, C. Camilloni, D. Provasi, P. Raiteri, D. Donadio, F. Marinelli, F. Pietrucci, R. A. Broglia, and M. Parrinello. PLUMED: A portable plugin for free-energy calculations with molecular dynamics. *Computer Physics Communications*, 180(10):1961–1972, October 2009. ISSN 0010-4655. doi: 10.1016/j.cpc.2009.05.011. URL <http://www.sciencedirect.com/science/article/pii/S001046550900157X>.
- [4] X. Lin and A. Groß. First-principles study of the water structure on flat and stepped gold surfaces. *Surface Science*, 606(1112):886–891, June 2012. ISSN 0039-6028. doi: 10.1016/j.susc.2011.12.015. URL <http://www.sciencedirect.com/science/article/pii/S0039602811004845>.
- [5] K. F. Garrity, J. W. Bennett, K. M. Rabe, and D. Vanderbilt. Pseudopotentials for high-throughput DFT calculations. *Computational Materials Science*, 81: 446–452, January 2014. ISSN 0927-0256. doi: 10.1016/j.commatsci.2013.08.053. URL <http://www.sciencedirect.com/science/article/pii/S0927025613005077>.

### A.3. Molecular Dynamics Trajectories

In order to explore the potential energy surface (PES) of  $\text{Au}_{\text{ad}}$  on Cl covered Au(001) surfaces metadynamics method was chosen to accelerate the sampling of traditional ab initio molecular dynamics (BOMD). In metadynamics, an additional bias potential is added to the system at regular intervals during the simulation time, which allows the system to escape beyond high energy barriers. The sampling of the free energy surface (FES) is performed over a set of collective variables (CVs), and the bias potential takes the form of Gaussian functions.

Metadynamic-BOMD simulations were carried out using PLUMED [122] plugin with PWscf [117, 118] at finite temperature. Intermediate configurations of the Metadynamic-BOMD simulations were ionically relaxed with more accurate parameters. It should be stressed that Metadynamic-BOMD simulations were employed to identified different adsorption configurations rather than to sample the FES. The slabs have been modeled by 4 Au layers, and were separated by 13 Å. The bottom two layers were frozen in all calculations, adsorbates are placed on one side of the surface. Thus, dipole corrections are used. For the Brillouin zone integration, we have used a  $(4 \times 4 \times 1)$  Monkhorst-Pack grid of special  $k$ -points [107] for the  $p(4 \times 4)$  surface unit cells (SUs). Kinetic energy cutoffs were 25 and 100 Ry for the wave functions and charge density, respectively. The Berendsen thermostat was used. A time step of 2.4 fs was taken for all Metadynamic-BOMD simulations. Three CVs were selected, the  $(x, y)$  coordinates of  $\text{Au}_{\text{ad}}$  and the coordination number of  $\text{Au}_{\text{ad}}$  with Cl atoms. No constraints were placed on the systems. The bias potential was applied after 10 time steps.

Table A.2.: Parameters for PLUMED plugin used in the test simulations. A time step of 2.4 fs was employed for all calculations. Every ten time steps a bias potential was applied.

	Test	Temp. (K)	CV	Sigma	Height (eV)
Fig. A.1	1	300	$\text{Au}_{\text{ad}}(x, y)$ ,	0.4 Å, 0.4 Å, 0.04	0.05
Fig. A.3	2	400	$\text{Au}_{\text{ad}}\text{-Cl}$		0.05
Fig. A.5	3	400	coordination number	0.2 Å, 0.2 Å, 0.02	0.01

Figures A.1, A.3 and A.5 show three trajectories of the corresponding Au and Cl adatoms performed with the parameters in Tab. A.2. The variation of  $z$  coordinate of selected Cl adatoms relative to  $z_0$  and the variation of the distance between  $\text{Au}_{\text{ad}}$  and selected Cl adatoms relative to  $d_0$  along the simulations are shown in Fig. A.2 and A.4.  $\Delta z$  and  $\Delta d$  are plotted in  $a$  units (nearest-neighbor distance equals to 2.94 Å).  $z_0$  represents the  $z$  coordinate of Cl adatoms in the  $c(2 \times 2)$  adlayer in the absence of a  $\text{Au}_{\text{ad}}$  at  $T = 0$  K.  $d_0$  is the Au-Cl bond length in  $\text{Au}_{\text{ad}}\text{Cl}_2$  complex in the Cl covered surface, which amounts to 2.31 Å at  $T = 0$  K.

In Fig. A.1 the initial configuration is characterized by a  $\text{Au}_{\text{ad}}\text{Cl}$  complex at the hollow

site of the substrate. During the simulation it is observed that six Cl adatoms are oscillating around their initial  $(x, y)$  positions. Cl adatoms are also oscillating around their initial  $z$  coordinate, see Fig. A.2  $\Delta z$  vs iterations (cyan and pink curves). The remaining two Cl adatoms and the  $\text{Au}_{\text{ad}}$  participate in the formation and dissociation of a  $\text{Au}_{\text{ad}}\text{Cl}_2$  complex, which is approximately arranged along the  $[010]$  direction of the substrate. It should be pointed out that  $\Delta z$  for a Cl atom in the  $\text{Au}_{\text{ad}}\text{Cl}_2$  complex amounts to  $0.2 a$  at  $T = 0$  K. In Fig. A.2 it is observed that the values of  $\Delta z$  oscillate around  $0.2 a$  for the Cl adatoms with blue and orange trajectories between the iterations 500 (1.2 ps) and 2500 (6 ps). In the same interval of time the values of  $\Delta d$  oscillate around zero. At iteration 2500 (6 ps) the Cl adatom with blue trajectory diffuses to the top of the  $\text{Au}_{\text{ad}}$  and then descends to the surface. Within this interval of time the values of  $\Delta z$  increase for the blue curve, as well as the values of  $\Delta d$  for the orange curve *i.e* the Cl adatom detaches from the  $\text{Au}_{\text{ad}}$ . The simulation results in the diffusion of the  $\text{Au}_{\text{ad}}$  along the  $[\bar{1}10]$  direction of the substrate.

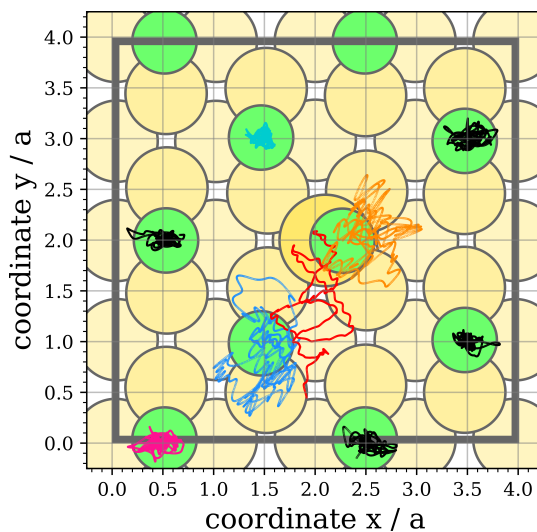


Figure A.1.: Trajectories of the Au and Cl adatoms taken from the metadynamic-BOMD of an adsorption configuration of  $\text{Au}_{\text{ad}}$  on the  $c(2 \times 2)$ -Cl covered  $\text{Au}(001)$  surface with  $\Theta = 1/2$  at 300 K. Coordinates are given in  $a$  units ( $a$  is the nearest-neighbor distance and amounts to  $2.94 \text{ \AA}$ ). The trajectory of  $\text{Au}_{\text{ad}}$  is colored by red. Calculations were carried out with 25 Ry and a 4 Au layer slab. Atomic geometry for the initial configuration in a  $p(4 \times 4)$  surface unit cell (SUC) is shown.

Similar results are obtained for the trajectory shown in Fig. A.3 at 400 K, which is started from an unstable  $\text{Au}_{\text{ad}}\text{Cl}_2$  configuration. However, a  $\text{Au}_{\text{ad}}\text{Cl}_2$  complex arranged along the  $[110]$  direction of the substrate is formed.

The trajectories in Fig. A.5 are the result of a simulation with small value of height (0.01 eV) for the deposited Gaussian functions. For this parameter the  $\text{Au}_{\text{ad}}\text{Cl}_2$  complex moves around its initial position rather than dissociate. This movement causes the diffusion of neighboring Cl adatoms to the next bridge sites of the substrate as shown in Fig. A.5.

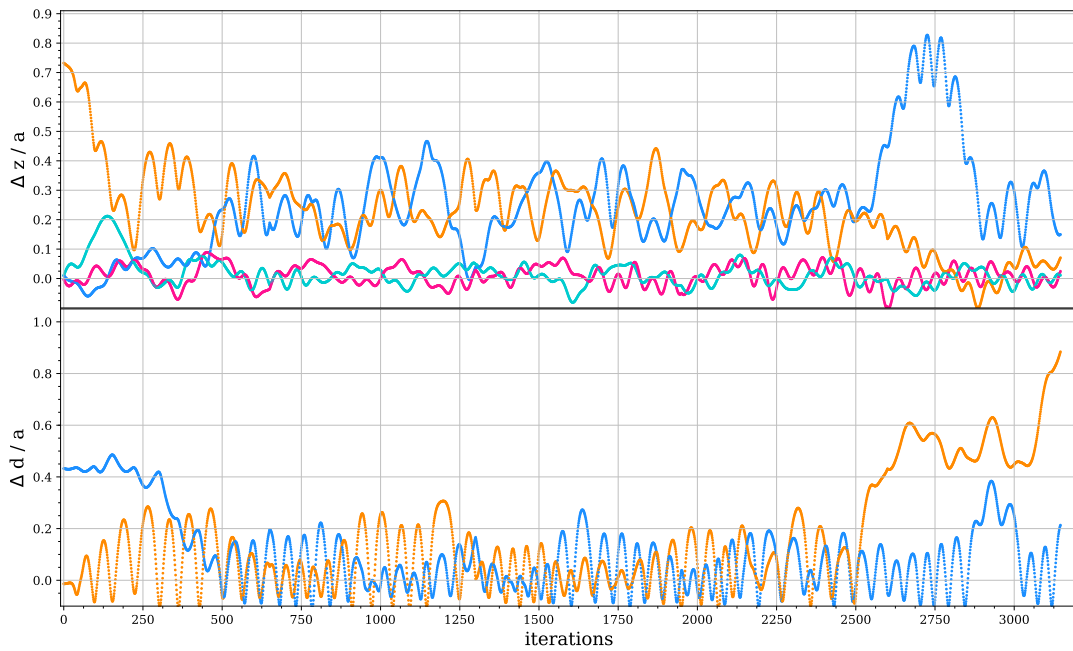


Figure A.2.: Top: Variation of  $z$  coordinate of selected Cl adatoms relative to the  $z$  coordinate of a Cl adatom in a  $c(2 \times 2)$  adlayer without a  $\text{Au}_{\text{ad}}$ ,  $\Delta z$ , along the metadynamic-BOMD simulation. Bottom: Variation of the distance between  $\text{Au}_{\text{ad}}$  and selected Cl adatoms relative to Au–Cl bond length of the  $\text{Au}_{\text{ad}}\text{Cl}_2$  in the Cl covered Au(001) surface ( $2.31\text{\AA}$ ),  $\Delta d$ , along the simulation.  $\Delta z$  and  $\Delta d$  are plotted in  $a$  units. Colors are referred to Fig A.1.



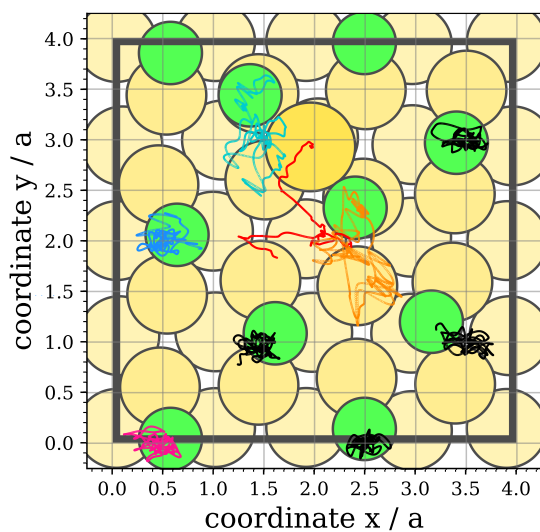


Figure A.3.: Trajectories of the Au and Cl adatoms taken from the metadynamic-BOMD of an adsorption configuration of Au<sub>ad</sub> on the  $c(2 \times 2)$ -Cl covered Au(001) surface with  $\Theta = 1/2$  at 400 K. Coordinates are given in  $a$  units. The trajectory of Au<sub>ad</sub> is colored by red. Atomic geometry for the start configuration in a  $p(4 \times 4)$  SUC is shown.

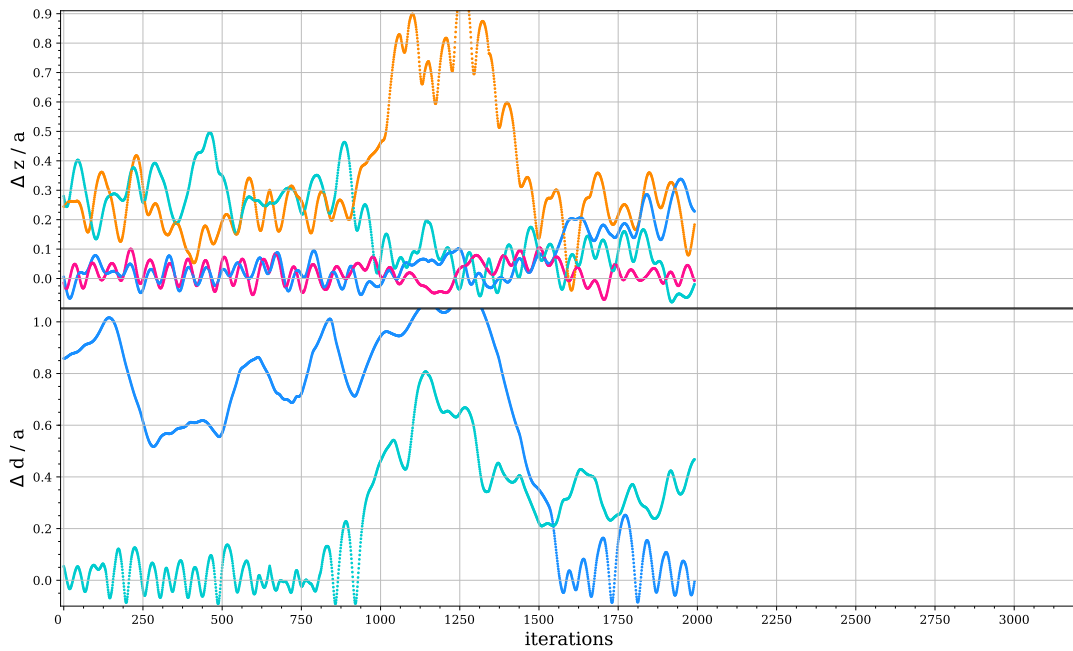


Figure A.4.: Top: Variation of  $z$  coordinate of selected Cl adatoms relative to the  $z$  coordinate of a Cl adatom in a  $c(2 \times 2)$  adlayer without a  $\text{Au}_{\text{ad}}$ ,  $\Delta z$ , along the metadynamic-BOMD simulation. Bottom: Variation of the distance between  $\text{Au}_{\text{ad}}$  and selected Cl adatoms relative to Au-Cl bond length of the  $\text{Au}_{\text{ad}}\text{Cl}_2$  in the Cl covered Au(001) surface ( $2.31\text{\AA}$ ),  $\Delta d$ , along the simulation. Colors are referred to Fig A.3.  $\Delta z$  and  $\Delta d$  are plotted in  $a$  units.

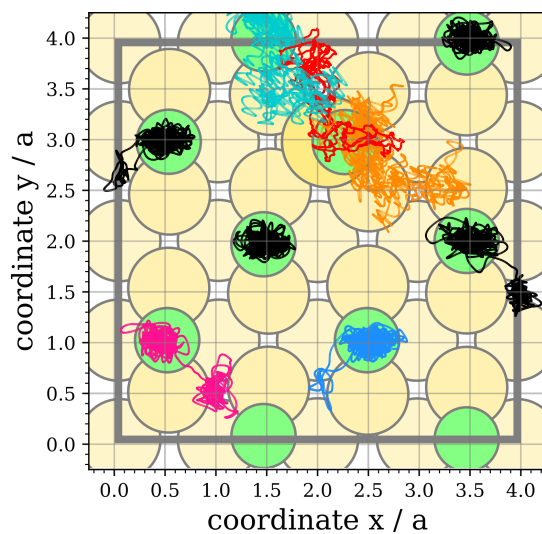
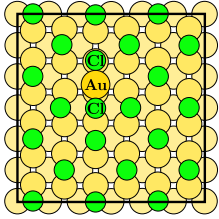
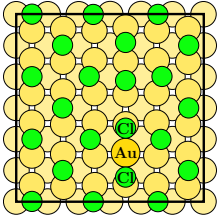
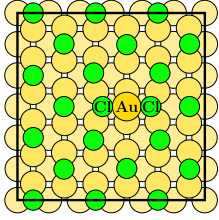
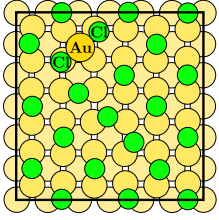
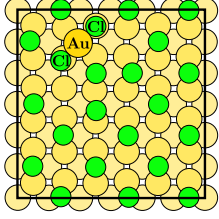
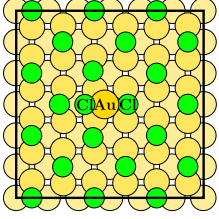
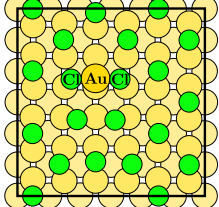
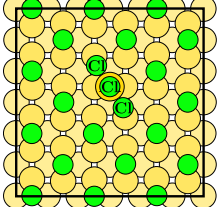


Figure A.5.: Trajectories of the Au and Cl adatoms taken from the metadynamic-BOMD of an adsorption configuration of Au<sub>ad</sub> on the  $c(2 \times 2)$ -Cl covered Au(001) surface with  $\Theta = 1/2$  at 400 K. Coordinates are given in  $a$  units. The trajectory of Au<sub>ad</sub> is colored by red. Atomic geometry for the initial configuration in a  $p(4 \times 4)$  SUC is shown.

### A.4. Adsorption Configurations of $\text{Au}_{\text{ad}}$ on $c(2 \times 2)\text{-Cl Au}(001)$ with an Additional Cl Atom

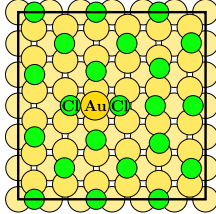
In Tab. A.4 the energy of the local minimum energy configurations with reference to the proposed global minimum configuration is presented for a Au adatom on the  $c(2 \times 2)\text{-Cl}$  covered Au(001) surface in the presence of an additional Cl atom. The adsorption configurations in Tab. A.4 have been calculated with 4 Au layers and  $(3 \times 3 \times 1)$   $k$ -points, 30 Ry of cutoff energy and 13 Å vacuum region.

Table A.3.: Adsorption configurations for Au adatom on  $c(2 \times 2)\text{-Cl Au}(001)$  with an additional Cl atom. Black squares denote the  $p(6 \times 6)$  SUC.

Configuration	$\Delta E$ (eV)	Configuration	$\Delta E$ (eV)
	0(ref.)		0.09
	0.11		0.14
	0.21		0.29
	0.34		0.38

*Continued on next page*

Table A.3 - Continued from previous page

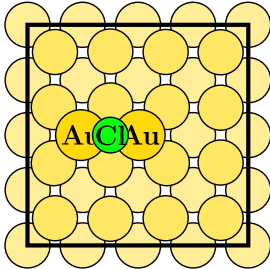
Configuration	$\Delta E$ (eV)	Configuration	$\Delta E$ (eV)
	0.57		

### A.5. $Au_2Cl_n$ Complex on Clean Unreconstructed $Au(001)$

Here we provide a list of all possible configurations of  $Au_2Cl_n$  for  $n = 1, 3, 4$  on clean unreconstructed  $Au(001)$  surface. A special selection of configurations has been calculated by means of DFT using Quantum Espresso package [117, 118].

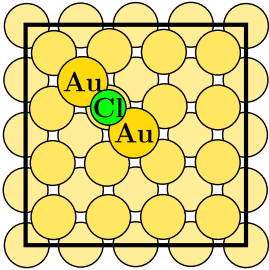
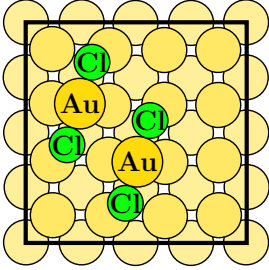
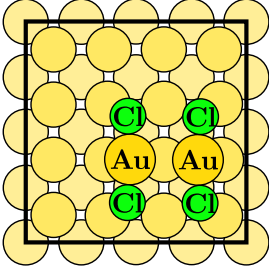
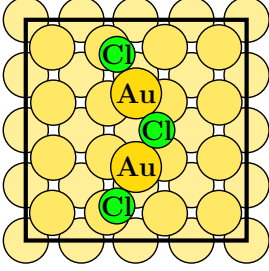
Energy differences are calculated using Eq. 5.9 defined in Chapter 5 for values of  $\mu_{Cl}$  corresponding to  $\Theta = 1/16$ . The parameters chosen for the calculations are less accurate, but sufficient to distinguish the ground state configuration with the lowest total energy. The parameters chosen for  $Au_2Cl_x/Au(001)$  are less accurate, but sufficient to distinguish the ground state configuration with the lowest total energy. The adsorption configurations have been modeled in four slab geometry, and a  $p(4 \times 4)$  SUC with  $(4 \times 4 \times 1)$  Monkhorst-Pack grid of special  $k$ -points [107].

Table A.4.: Adsorption configurations of  $Au_2Cl_n$  for  $n = 1, 3, 4$  on  $Au(001)$  surface. Black squares denote the  $p(4 \times 4)$  SUC.

$n_{Cl}$	Configuration	$E_{diff}(\mu_{Cl, \Theta=1/16})$ (eV)	$d_{Au-Au}$ (Å)
1		-0.16	3.13

Continued on next page

Table A.4 - Continued from previous page

$n_{\text{Cl}}$	Configuration	$E_{\text{diff}}(\mu_{\text{Cl},\theta=1/16})$ (eV)	$d_{\text{Cl-Cl}}$
1		-0.09	3.88
4		+0.62	4.37
4		+0.70	3.62
3		+0.71	3.92

**A.6. Supplementary Material from Publication J. Chem. Phys.  
152, 084701 (2020), Copyright (2020) by AIP Publishing**

# Initial steps towards $\text{Au}_{\text{ad}}$ island nucleation on a $c(2 \times 2)$ -Cl Au(001) surface investigated by DFT

## Supplementary Material

Alexandra Celinda Dávila López\* and Eckhard Pehlke†  
*Institut für Theoretische Physik und Astrophysik, Christian-Albrechts-Universität zu Kiel, 24098 Kiel, Germany*

### CONTENTS

	2
S.1. Convergence tests	2
S.1.A. Adsorption of Cl on Au(001) surface	2
S.1.B. $(\text{Au}_{\text{ad}}\text{Cl}_2)_2$ on $c(2 \times 2)$ -Cl Au(001) surface	4
S.2. Energy of a Cl vacancy on a $c(2 \times 2)$ -Cl Au(001) surface	5
S.3. Adsorption configurations of small $\text{Au}_{\text{ad}}$ clusters on a $c(2 \times 2)$ -Cl Au(001) surface	7
S.3.A. $\text{Au}_{\text{ad}}$ monomer	7
1. $n_{\text{Vac}} = 2$ Cl vacancies	7
2. $n_{\text{Vac}} = 3$ Cl vacancies	8
3. $n_{\text{Vac}} = 4$ Cl vacancies	9
S.3.B. $\text{Au}_{\text{ad}}$ dimer	10
1. $n_{\text{Vac}} = 0$ Cl vacancy	10
2. $n_{\text{Vac}} = 1$ Cl vacancy	11
3. $n_{\text{Vac}} = 2$ Cl vacancies	12
4. $n_{\text{Vac}} = 3$ Cl vacancies	13
5. $n_{\text{Vac}} = 4$ Cl vacancies	14
S.3.C. $\text{Au}_{\text{ad}}$ trimer	15
1. $n_{\text{Vac}} = 0$ Cl vacancy	15
2. $n_{\text{Vac}} = 1$ Cl vacancy	16
3. $n_{\text{Vac}} = 2$ Cl vacancies	17
S.3.D. $\text{Au}_{\text{ad}}$ tetramer	18
1. $n_{\text{Vac}} = 0$ Cl vacancy	18
2. $n_{\text{Vac}} = 1$ Cl vacancy	19
3. $n_{\text{Vac}} = 2$ Cl vacancies	20
References	21

---

\* [davila@theo-physik.uni-kiel.de](mailto:davila@theo-physik.uni-kiel.de)

† [pehlke@theo-physik.uni-kiel.de](mailto:pehlke@theo-physik.uni-kiel.de)



All density functional calculations in this work have been performed with the program PWscf from the Quantum ESPRESSO package [1, 2] using ultrasoft pseudopotentials [3] from the open-source GBRV library [4]. Adsorption configurations have been simulated by using asymmetric slabs with 6 Au layers. A vacuum region of 13 Å including a dipole correction [5, 6] was used. Total energies have been calculated using a plane-waves basis set of 30 Ry cutoff energy. For all further computational details see the main text.

## S.1. CONVERGENCE TESTS

Convergence tests (with respect to the number of  $k$ -points and surface unit cell (SUC)) have been carried through in order to estimate the accuracy of the adsorption energy of chlorine on Au(001) surface, as well as the accuracy and the numerical error of the binding energy of the Au<sub>ad</sub> dimer. Further convergence tests with respect to the number of Au layers, plane-wave cutoff energy can be found in the Supplementary Material from Ref. [7].

### S.1.A. Adsorption of Cl on Au(001) surface

The adsorption energy of Cl on the unreconstructed Au(001) surface per site,  $E_{ads}$ , as a function of the Cl chemical potential yields the  $c(2 \times 2)$ -Cl adlayer as equilibrium structure for  $\mu_{Cl}$  in the range of  $[-0.94, -0.35]$  eV, see Fig. 1 in the main text. In Tab. S1 and Tab. S2, the adsorption energies  $E_{ads}$  and  $\epsilon_{ads}$  for several SUC's with Cl coverage  $\Theta = 1/2$  and  $\Theta < 1/2$  are presented.  $\epsilon_{ads}$  denotes the adsorption energy per adsorbed Cl atom:

$$\epsilon_{ads} = \left[ E(0, m, \mathcal{C}, N_{site}) - E_{clean}(N_{site}) - m E_{Cl_2}/2 \right] \frac{1}{m} = E_{ads} \frac{N_{site}}{m}. \quad (1)$$

We observe that denser  $k$ -points produce a variation of roughly 0.01 eV for each SUC.

TABLE S1. Comparison of  $k$ -points density for  $c(2 \times 2)$ -Cl/Au(001) with  $\Theta = 1/2$ .

SUC	$k$ -points	$\epsilon_{ads}$ / eV	$E_{ads}(\Theta, 0)$ / eV
$c(2 \times 2)$	$(16 \times 16 \times 1)$	-1.085	-0.543
$c(2 \times 2)$	$(18 \times 18 \times 1)$	-1.080	-0.540
$p(2 \times 2)$	$(12 \times 12 \times 1)$	-1.083	-0.541
$p(4 \times 4)$	$(4 \times 4 \times 1)$	-1.089	-0.545
$p(4 \times 4)$	$(6 \times 6 \times 1)$	-1.083	-0.542
$p(6 \times 6)$	$(4 \times 4 \times 1)$	-1.083	-0.542

TABLE S2. List of adsorption energies for  $\Theta < 1/2$ . For  $\Theta = 0.125$   $\epsilon_{ads}$  and  $E_{ads}$  have been calculated for identical adsorption geometries with  $(8 \times 8 \times 1)$  and  $(10 \times 10 \times 1)$   $k$ -points meshes. The two structures for  $\Theta = 0.25$  differ from each other, see Fig. S1(a). The same is true for the two structures for  $\Theta = 0.33$  in Fig. S1(b).

SUC	$k$ -points	$\Theta$	$\epsilon_{ads}$ / eV	$E_{ads}(\Theta, 0)$ / eV
$p(4 \times 4)$	$(6 \times 6 \times 1)$	0.0625	-1.220	-0.076
$p(3 \times 3)$	$(8 \times 8 \times 1)$	0.11	-1.179	-0.131
$c(4 \times 4)$	$(8 \times 8 \times 1)$	0.125	-1.221	-0.153
$c(4 \times 4)$	$(10 \times 10 \times 1)$	0.125	-1.213	-0.152
$p(2 \times 2)$	$(12 \times 12 \times 1)$	0.25	-1.116	-0.279
$p(2 \times 4)$	$(12 \times 6 \times 1)$	0.25	-1.147	-0.287
$p(3 \times 3)$	$(8 \times 8 \times 1)$	0.33	-1.130	-0.377
$p(6 \times 6)$	$(4 \times 4 \times 1)$	0.33	-1.153	-0.384
$p(6 \times 6)$	$(4 \times 4 \times 1)$	0.39	-1.120	-0.436
$p(6 \times 6)$	$(4 \times 4 \times 1)$	0.42	-1.109	-0.462
$p(6 \times 6)$	$(4 \times 4 \times 1)$	0.44	-1.099	-0.488
$p(6 \times 6)$	$(4 \times 4 \times 1)$	0.47	-1.090	-0.515

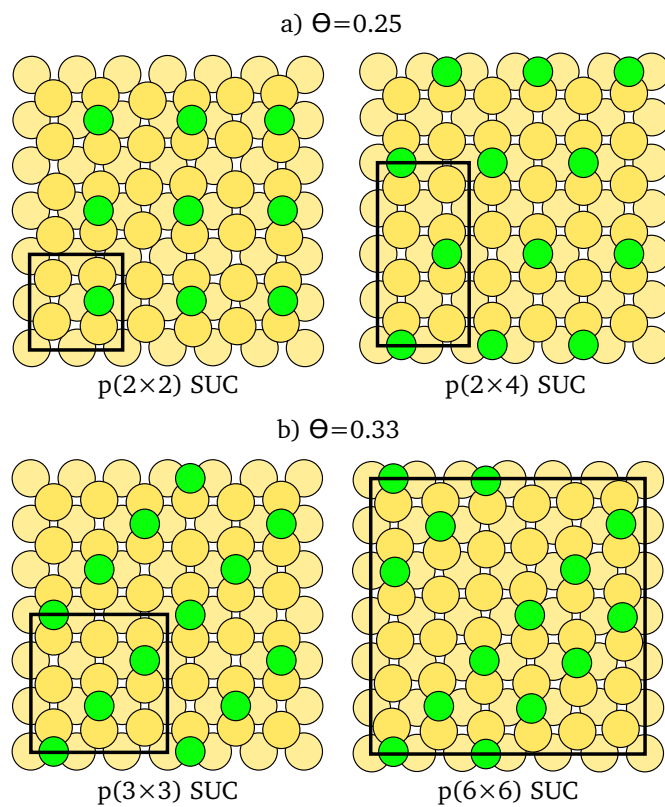


FIG. S1. Ground state adsorption configurations for  $\Theta = 0.25$  (a) and  $\Theta = 0.33$  (b). Black squares represent the surface unit cells used in the calculations.

### S.1.B. $(\text{Au}_{\text{ad}}\text{Cl}_2)_2$ on $c(2 \times 2)$ -Cl Au(001) surface

For two  $\text{Au}_{\text{ad}}\text{Cl}_2$  complexes, which are far away from each other, the binding energy must approach to zero. We restrict ourselves to Cl chemical potentials  $\mu_{\text{Cl}}$ , where the equilibrium configuration of  $\text{Au}_{\text{ad}}$  monomer does not contain any Cl vacancy. In this case the binding energy of the monomers is

$$E_{\text{bind}}^*(\mathcal{C}, N_{\text{site}}) = E(2, N_{\text{site}}/2, \mathcal{C}, N_{\text{site}}) + E_0(0, N_{\text{site}}/2, N_{\text{site}}/2) - 2E_0(1, N_{\text{site}}/2, N_{\text{site}}/2). \quad (2)$$

In the  $p(6 \times 6)$  SUC the binding energy of two  $\text{Au}_{\text{ad}}\text{Cl}_2$  far away from each other (Fig. S2(a)) amounts to 3 meV, this value is less than the accuracy and the numerical error of the calculation.

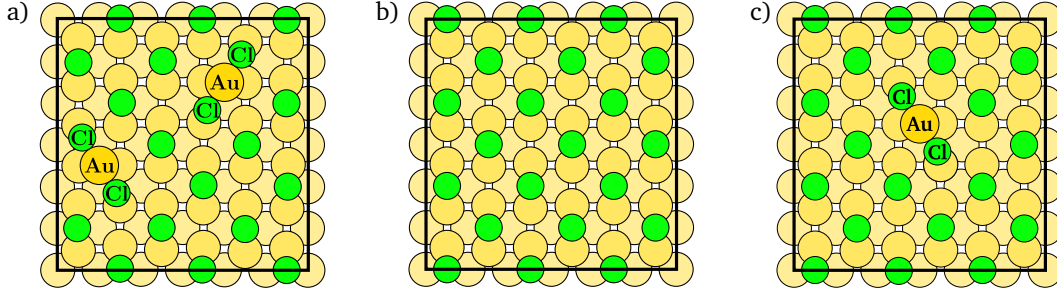


FIG. S2. Atomic structures of two  $\text{Au}_{\text{ad}}\text{Cl}_2$  complexes on the  $c(2 \times 2)$ -Cl Au(001) surface (a),  $c(2 \times 2)$ -Cl Au(001) surface (b) and a  $\text{Au}_{\text{ad}}\text{Cl}_2$  complex on the  $c(2 \times 2)$ -Cl Au(001) surface (c). All configurations have  $\Theta = 1/2$ .

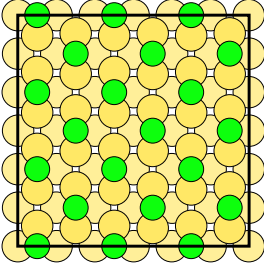
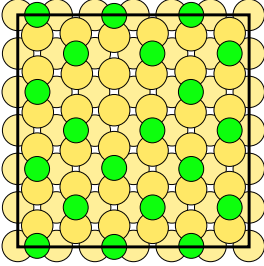
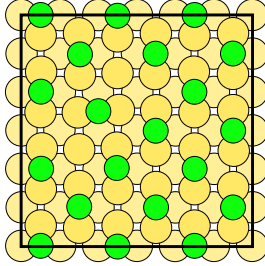
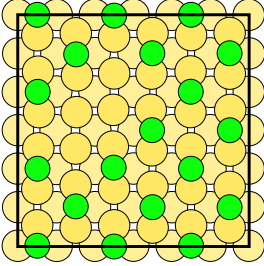
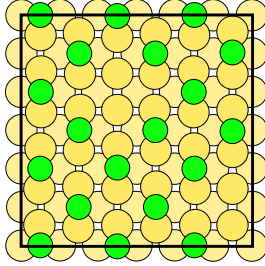
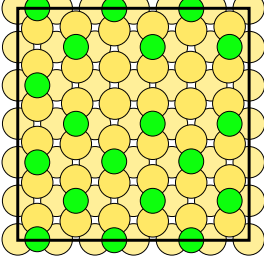
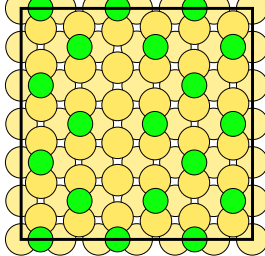
## S.2. ENERGY OF A Cl VACANCY ON A $c(2 \times 2)$ -Cl Au(001) SURFACE

In Table S3 the vacancy energies of the most relevant adsorption configurations for  $c(2 \times 2)$ -Cl Au(001) with  $n_{\text{vac}}=1, 2, 3, 4, 6$  Cl vacancies within a  $p(6 \times 6)$  SUC are presented. The energy per Cl vacancy at a given number  $m$  of Cl atoms within a configuration  $\mathcal{C}$  is

$$E_{\text{Vac}}^*(n_{\text{Vac}}) = \frac{1}{n_{\text{Vac}}} \left[ E(0, m, \mathcal{C}, N_{\text{site}}) - E_0(0, N_{\text{site}}/2, N_{\text{site}}) + n_{\text{Vac}} E_{\text{Cl}_2}/2 \right]. \quad (3)$$

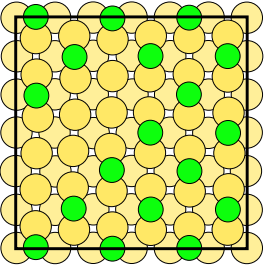
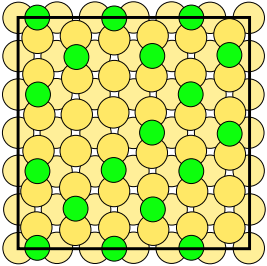
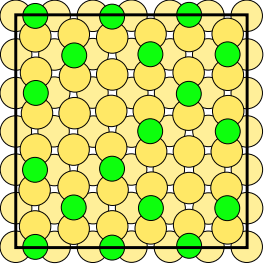
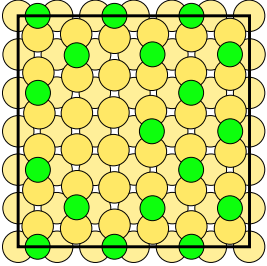
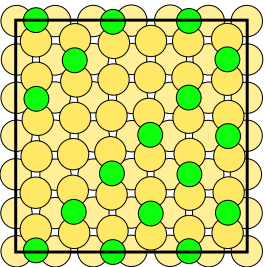
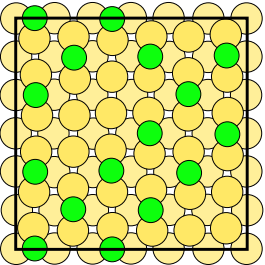
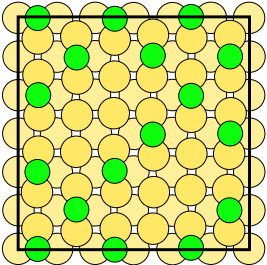
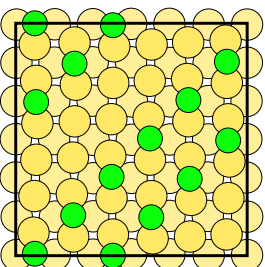
$E_0(0, N_{\text{site}}/2, N_{\text{site}})$  is the total energy of a  $c(2 \times 2)$ -Cl Au(001) slab for  $\Theta = 1/2$ .

TABLE S3: Adsorption configurations of  $c(2 \times 2)$ -Cl Au(001) structures with  $n_{\text{vac}}$  Cl vacancies.

$n_{\text{Vac}}$	Configuration	$E_{\text{Vac}}^* / \text{eV}$	Configuration	$E_{\text{Vac}}^* / \text{eV}$
0		0(ref.)	-	-
1		0.960		1.00
2		0.953		0.961
		0.974		0.985

*Continued on next page*

TABLE S3 - *Continued from previous page*

$n_{\text{Vac}}$	Configuration	$E_{\text{Vac}}^* / \text{eV}$	Configuration	$E_{\text{Vac}_1}^* / \text{eV}$
3		0.950		0.956
		0.965		0.972
4		0.948		
		0.953		0.963
6		0.943		

### S.3. ADSORPTION CONFIGURATIONS OF SMALL $\text{Au}_{\text{ad}}$ CLUSTERS ON A $c(2 \times 2)$ -Cl $\text{Au}(001)$ SURFACE

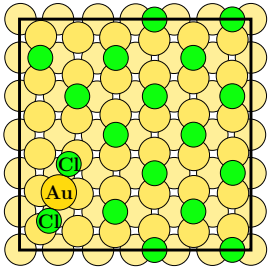
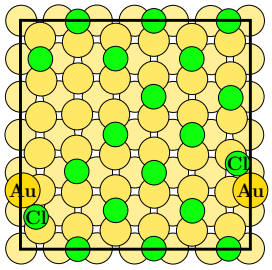
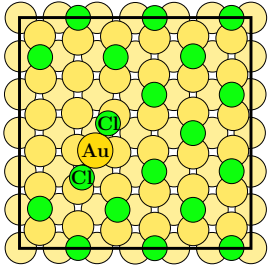
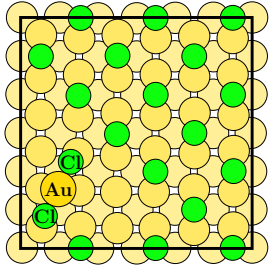
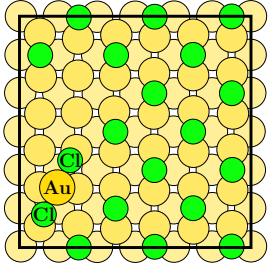
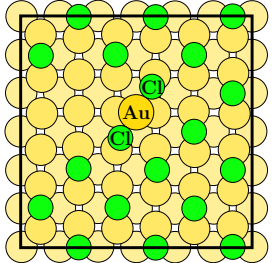
In the present section we give an overview of the calculated adsorption configurations of Cl in the vicinity of a  $\text{Au}_{\text{ad}}$  monomer, dimer, trimer and tetramer on unreconstructed  $\text{Au}(001)$  surface for various number of Cl vacancies  $n_{\text{vac}}$  within a  $p(6 \times 6)$  SUC.

#### S.3.A. $\text{Au}_{\text{ad}}$ monomer

For a given number of Cl vacancies  $n_{\text{vac}}$  the energy of a slab containing a Au adatom on  $c(2 \times 2)$ -Cl  $\text{Au}(001)$  surface with reference to the lowest energy adsorption configuration is presented in Tab. S4 ( $n_{\text{vac}} = 2$ ), Tab. S5 ( $n_{\text{vac}} = 3$ ) and Tab. S6 ( $n_{\text{vac}} = 4$ ). The configurations for  $n_{\text{vac}} = 0, 1$  are not listed here, as they can be found in the Supplementary Material of Ref. [7].

##### 1. $n_{\text{vac}} = 2$ Cl vacancies

TABLE S4: Adsorption configurations for  $\text{Au}_{\text{ad}}$  on a  $c(2 \times 2)$ -Cl covered  $\text{Au}(001)$  with  $n_{\text{vac}} = 2$  Cl vacancies.

Configuration	$\Delta E / \text{meV}$	Configuration	$\Delta E / \text{meV}$
	0(ref.)		19
	32		33
	59		88

*Continued on next page*

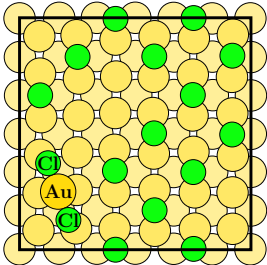
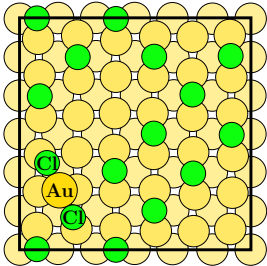
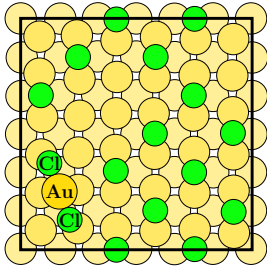
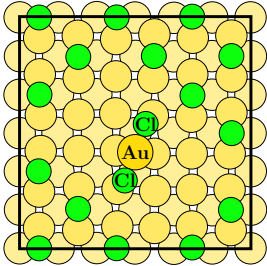
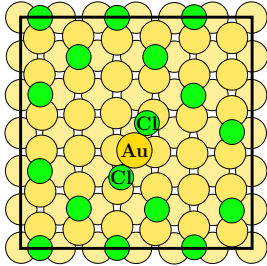
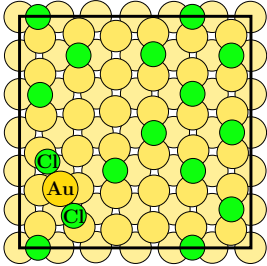
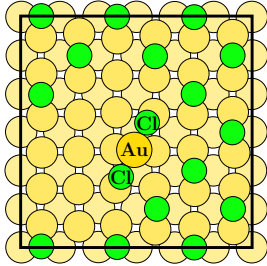
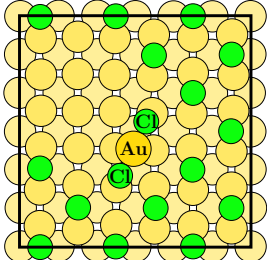
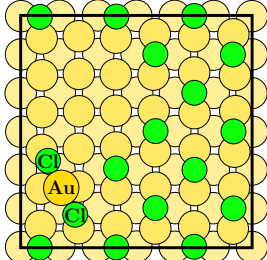
TABLE S5 - Continued from previous page

Configuration	$\Delta E / \text{meV}$	Configuration	$\Delta E / \text{meV}$
	193		402

2.  $n_{\text{vac}} = 3 \text{ Cl vacancies}$ TABLE S5: Adsorption configurations for  $\text{Au}_{\text{ad}}$  on  $c(2 \times 2)$ -Cl covered Au(001) for  $n_{\text{vac}} = 3 \text{ Cl vacancies}$ .

Configuration	$\Delta E / \text{meV}$	Configuration	$\Delta E / \text{meV}$
	0(ref.)		12
	53		62
	71		

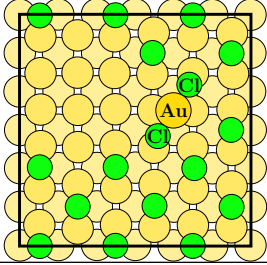
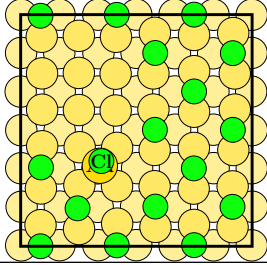
3.  $n_{\text{Vac}} = 4$  Cl vacanciesTABLE S6: Adsorption configurations for  $\text{Au}_{\text{ad}}$  monomer on  $c(2 \times 2)$ -Cl covered  $\text{Au}(001)$  for  $n_{\text{Vac}} = 4$ .

Configuration	$\Delta E / \text{meV}$	Configuration	$\Delta E / \text{meV}$
	0(ref.)		
	12		19
	36		92
	101		107
	114		156

*Continued on next page*



TABLE S6 - Continued from previous page

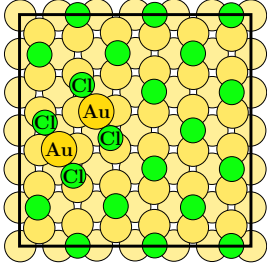
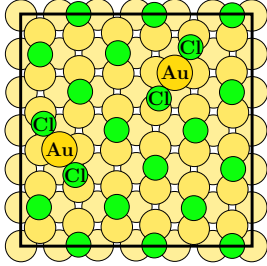
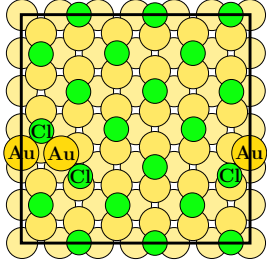
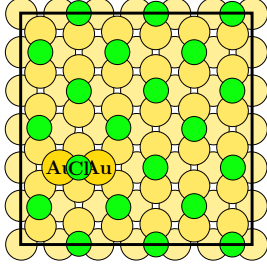
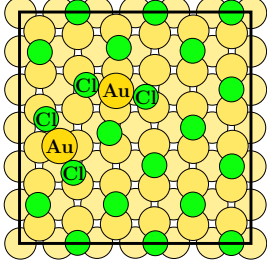
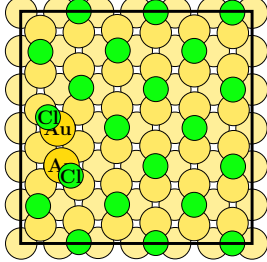
Configuration	$\Delta E / \text{meV}$	Configuration	$\Delta E / \text{meV}$
	198		238

### S.3.B. Au<sub>ad</sub> dimer

At a given number of Cl vacancies  $n_{\text{vac}}$  the energy of a Au<sub>ad</sub> dimer on a  $c(2 \times 2)$ -Cl Au(001) surface with reference to the lowest adsorption configuration is presented in Tab. S7 ( $n_{\text{vac}} = 0$ ) – Tab. S11 ( $n_{\text{vac}} = 4$ ).

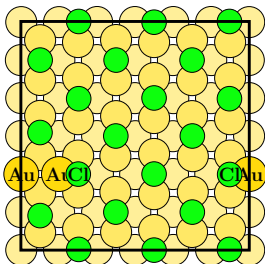
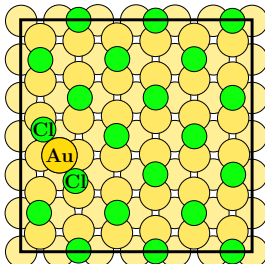
#### 1. $n_{\text{vac}} = 0$ Cl vacancy

TABLE S7: Adsorption configurations for Au<sub>ad</sub> dimer on  $c(2 \times 2)$ -Cl covered Au(001) for  $n_{\text{vac}} = 0$ .

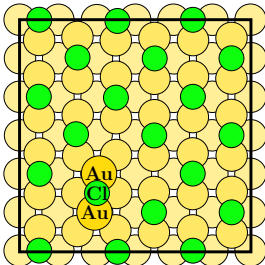
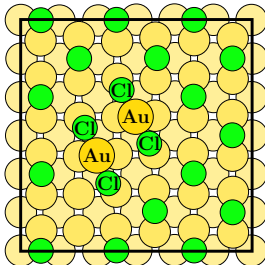
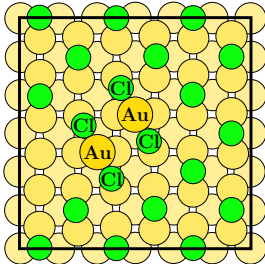
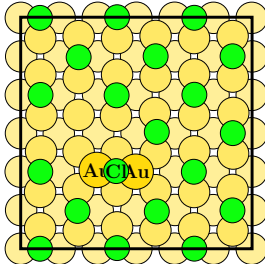
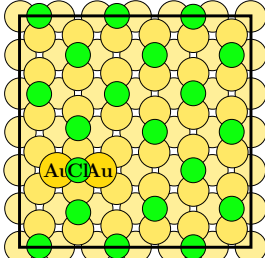
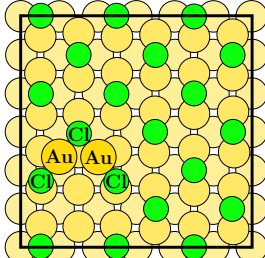
Configuration	$\Delta E / \text{meV}$	Configuration	$\Delta E / \text{meV}$
	0(ref.)		61
	172		180
	389		423

Continued on next page

TABLE S7 - Continued from previous page

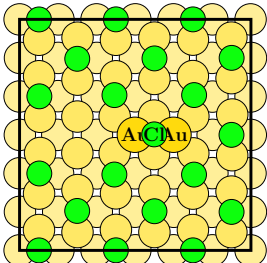
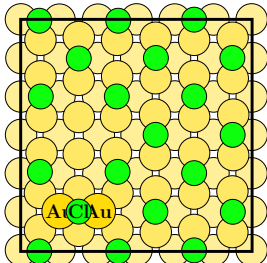
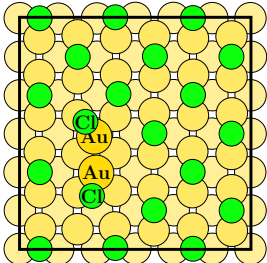
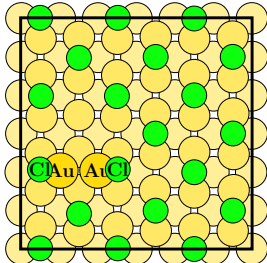
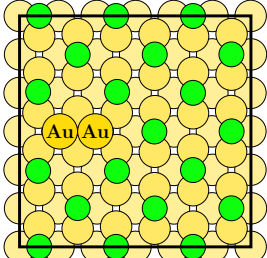
Configuration	$\Delta E / \text{meV}$	Configuration	$\Delta E / \text{meV}$
	564		1982

2.  $n_{\text{vac}} = 1$  Cl vacancyTABLE S8: Adsorption configurations for  $\text{Au}_{\text{ad}}$  on  $c(2 \times 2)$ -Cl covered Au(001) for  $n_{\text{vac}} = 1$ .

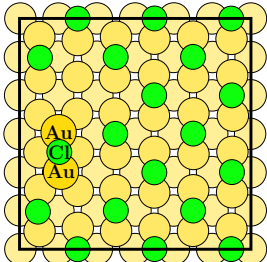
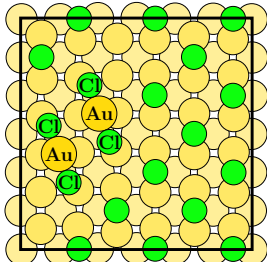
Configuration	$\Delta E / \text{meV}$	Configuration	$\Delta E / \text{meV}$
	0(ref.)		0
	46		96
	173		190

Continued on next page

TABLE S8 - Continued from previous page

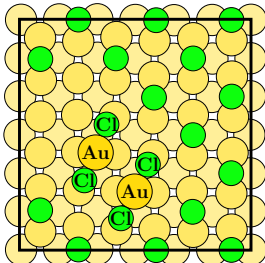
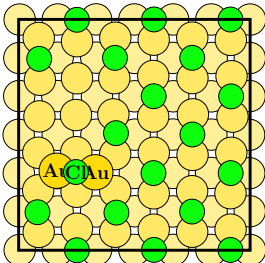
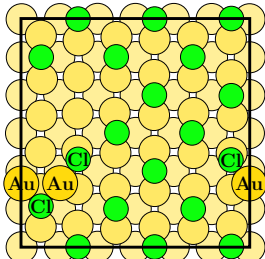
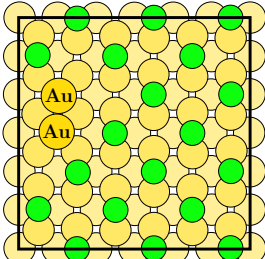
Configuration	$\Delta E / \text{meV}$	Configuration	$\Delta E / \text{meV}$
	234		236
	238		308
	724		

3.  $n_{\text{Vac}} = 2$  Cl vacanciesTABLE S9: Adsorption configurations for  $\text{Au}_{\text{ad}}$  dimer on  $c(2 \times 2)$ -Cl covered Au(001) for  $n_{\text{Vac}} = 2$ .

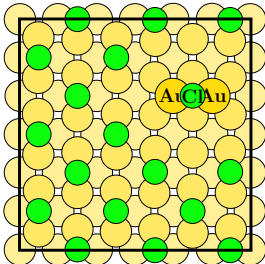
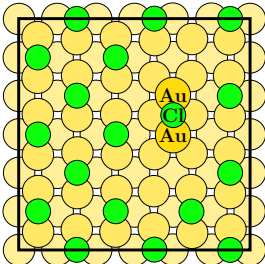
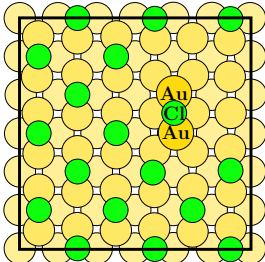
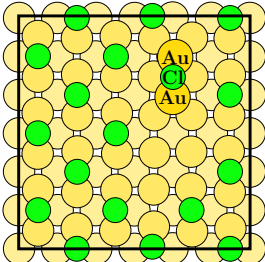
Configuration	$\Delta E / \text{meV}$	Configuration	$\Delta E / \text{meV}$
	0(ref.)		54

Continued on next page

TABLE S9 - Continued from previous page

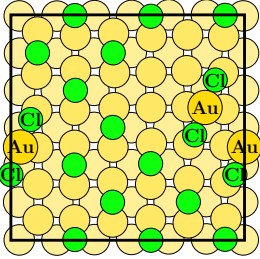
Configuration	$\Delta E / \text{meV}$	Configuration	$\Delta E / \text{meV}$
	105		209
	320		613

4.  $n_{\text{vac}} = 3 \text{ Cl vacancies}$ TABLE S10: Adsorption configurations for  $\text{Au}_{\text{ad}}$  on  $c(2 \times 2)\text{-Cl}$  covered  $\text{Au}(001)$  for  $n_{\text{vac}} = 3$ .

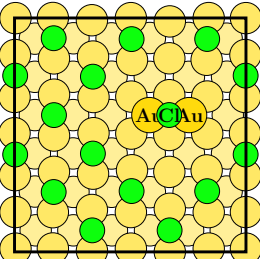
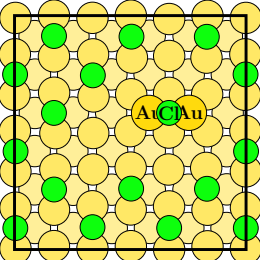
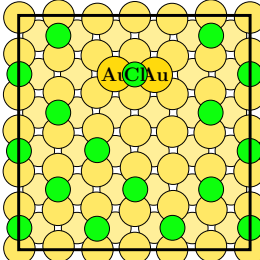
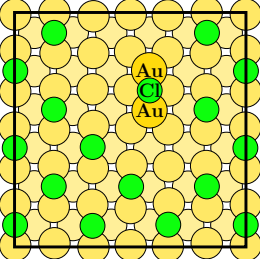
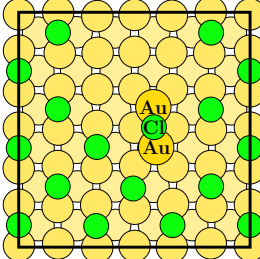
Configuration	$\Delta E / \text{meV}$	Configuration	$\Delta E / \text{meV}$
	0(ref.)		65
	158		174

Continued on next page

TABLE S10 - *Continued from previous page*

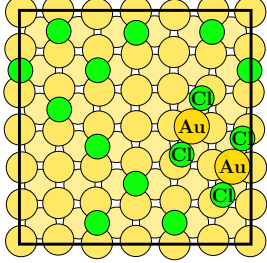
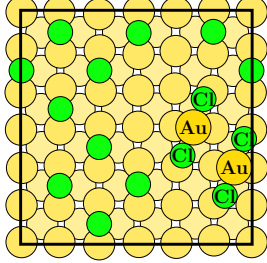
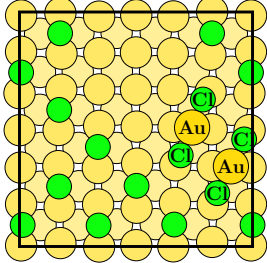
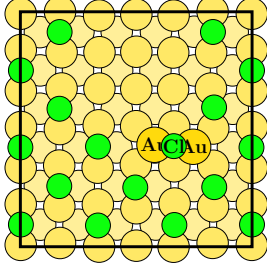
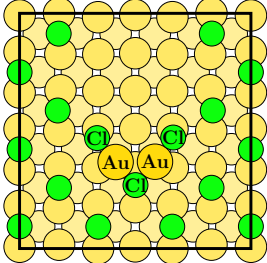
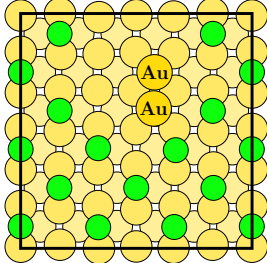
Configuration	$\Delta E / \text{meV}$	Configuration	$\Delta E / \text{meV}$
	218		

5.  $n_{\text{vac}} = 4 \text{ Cl vacancies}$ TABLE S11: Adsorption configurations for  $\text{Au}_{\text{ad}}$  dimer on  $c(2 \times 2)$ -Cl covered  $\text{Au}(001)$  for  $n_{\text{vac}} = 4$ .

Configuration	$\Delta E / \text{meV}$	Configuration	$\Delta E / \text{meV}$
	0(ref.)		
	16		50
	65		173

*Continued on next page*

TABLE S11 - *Continued from previous page*

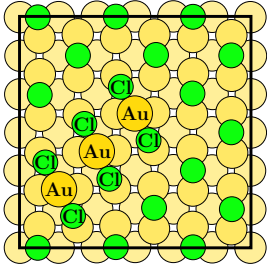
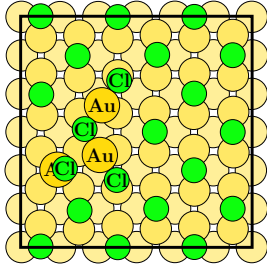
Configuration	$\Delta E / \text{meV}$	Configuration	$\Delta E / \text{meV}$
	220		330
	333		408
	616		667

### S.3.C. $\text{Au}_{\text{ad}}$ trimer

At a given number of Cl vacancies  $n_{\text{vac}}$  the energy of a  $\text{Au}_{\text{ad}}$  trimer on a  $c(2 \times 2)$ -Cl Au(001) surface with reference to the lowest adsorption configuration is presented in Tab. S12 ( $n_{\text{vac}} = 0$ ) – Tab. S14 ( $n_{\text{vac}} = 2$ ).

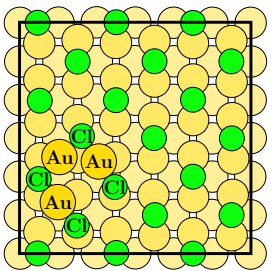
#### 1. $n_{\text{vac}} = 0$ Cl vacancy

TABLE S12: Adsorption configurations for  $\text{Au}_{\text{ad}}$  trimer on  $c(2 \times 2)$ -Cl covered Au(001) for  $n_{\text{vac}} = 0$ .

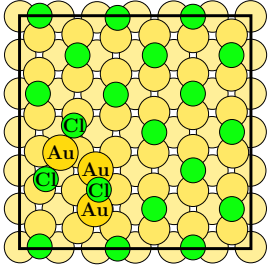
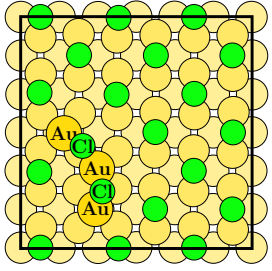
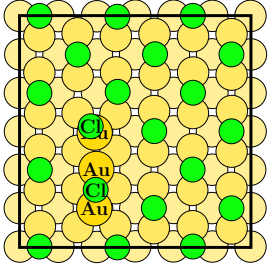
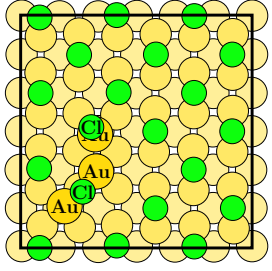
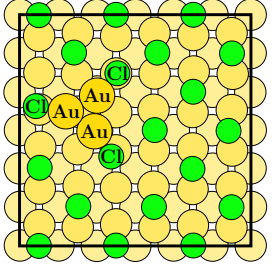
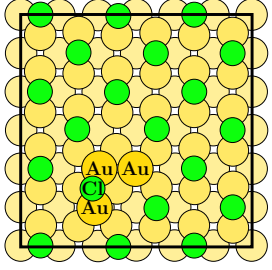
Configuration	$\Delta E / \text{meV}$	Configuration	$\Delta E / \text{meV}$
	0(ref.)		254

*Continued on next page*

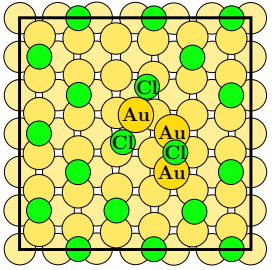
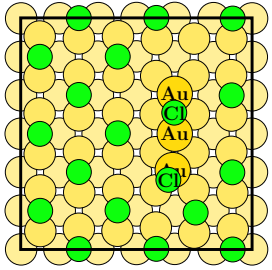
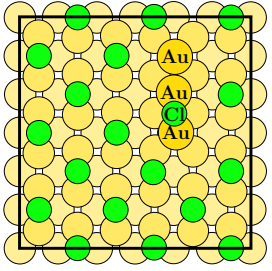
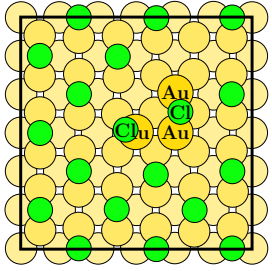
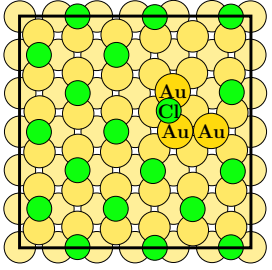
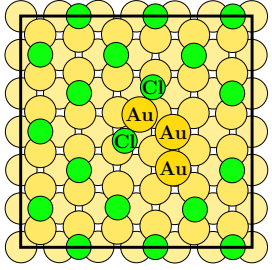
TABLE S12 - *Continued from previous page*

Configuration	$\Delta E / \text{meV}$	Configuration	$\Delta E / \text{meV}$
	347		

2.  $n_{\text{vac}} = 1$  Cl vacancyTABLE S13: Adsorption configurations for Au<sub>ad</sub> trimer on  $c(2 \times 2)$ -Cl covered Au(001) for  $n_{\text{vac}} = 1$ .

Configuration	$\Delta E / \text{meV}$	Configuration	$\Delta E / \text{meV}$
	0(ref.)		62
	97		179
	293		520

3.  $n_{\text{Vac}} = 2$  Cl vacanciesTABLE S14: Adsorption configurations for  $\text{Au}_{\text{ad}}$  trimer on  $c(2 \times 2)$ -Cl covered  $\text{Au}(001)$  for  $n_{\text{Vac}} = 2$ .

Configuration	$\Delta E / \text{meV}$	Configuration	$\Delta E / \text{meV}$
	0(ref.)		21
	201		260
	437		502

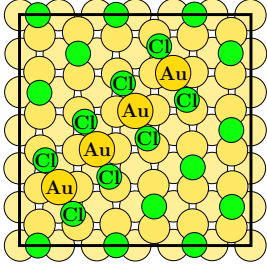
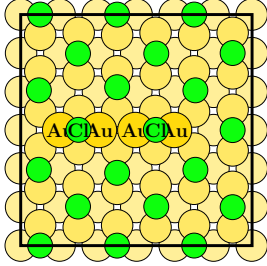
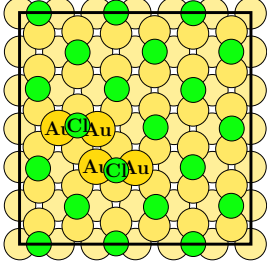
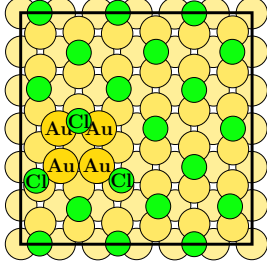
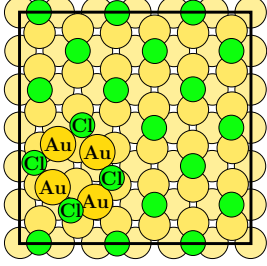
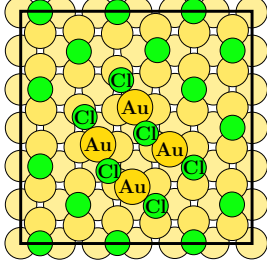


### S.3.D. Au<sub>ad</sub> tetramer

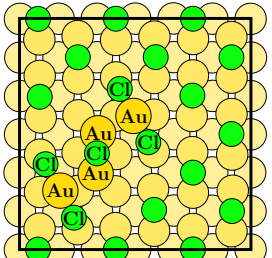
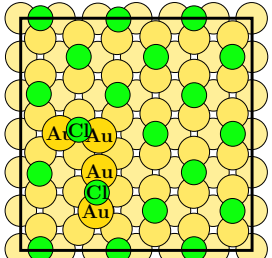
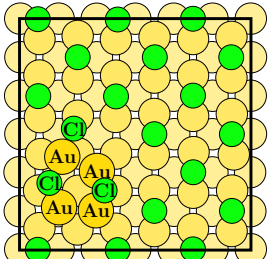
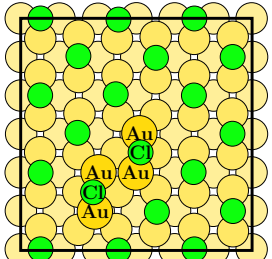
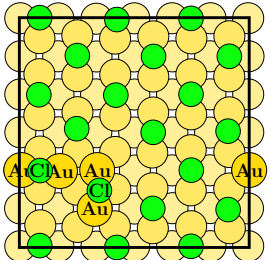
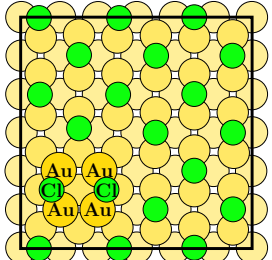
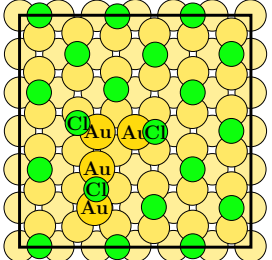
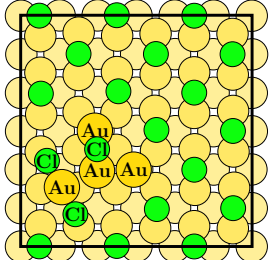
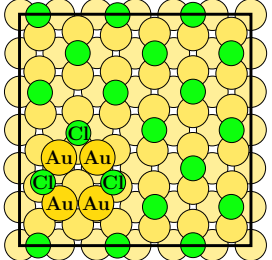
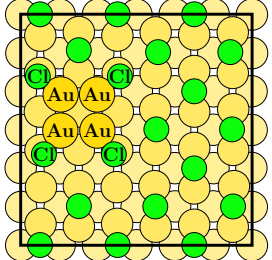
At a given number of Cl vacancies  $n_{\text{vac}}$  the energy of a Au<sub>ad</sub> tetramer on a  $c(2 \times 2)$ -Cl Au(001) surface with reference to the lowest adsorption configuration is presented in Tab. S15 ( $n_{\text{vac}} = 0$ ) – Tab. S17 ( $n_{\text{vac}} = 2$ ).

#### 1. $n_{\text{vac}} = 0$ Cl vacancy

TABLE S15: Adsorption configurations for Au<sub>ad</sub> tetramer on  $c(2 \times 2)$ -Cl covered Au(001) for  $n_{\text{vac}} = 0$ .

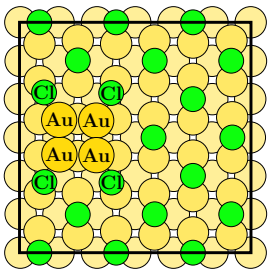
Configuration	$\Delta E / \text{meV}$	Configuration	$\Delta E / \text{meV}$
	0(ref.)		232
	251		423
	425		574

2.  $n_{\text{vac}} = 1$  Cl vacancyTABLE S16: Adsorption configurations for  $\text{Au}_{\text{ad}}$  tetramer on  $c(2 \times 2)$ -Cl covered Au(001) for  $n_{\text{vac}} = 1$ .

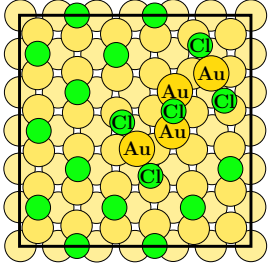
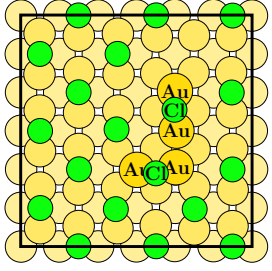
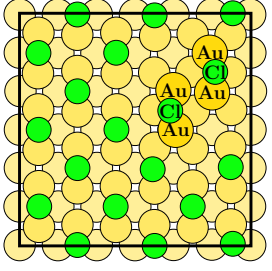
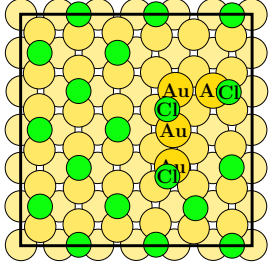
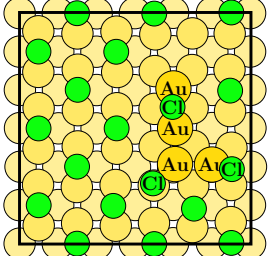
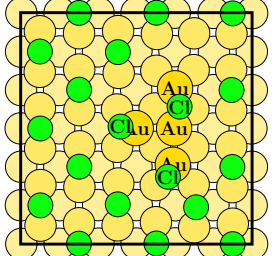
Configuration	$\Delta E / \text{meV}$	Configuration	$\Delta E / \text{meV}$
	0(ref.)		147
	201		276
	311		319
	386		505
	577		612

Continued on next page

TABLE S16 - *Continued from previous page*

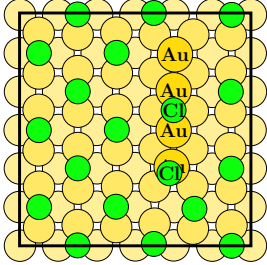
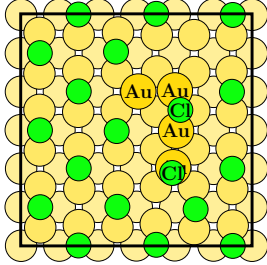
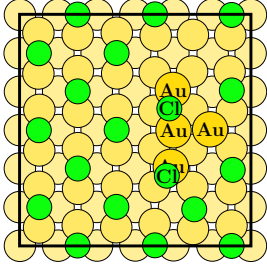
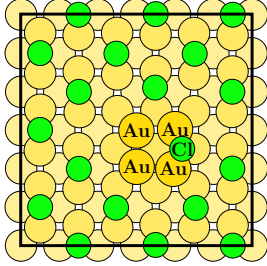
Configuration	$\Delta E / \text{meV}$	Configuration	$\Delta E / \text{meV}$
	1158		

3.  $n_{\text{vac}} = 2$  Cl vacanciesTABLE S17: Adsorption configurations for  $\text{Au}_{\text{ad}}$  tetramer on  $c(2 \times 2)$ -Cl covered Au(001) for  $n_{\text{vac}} = 2$ .

Configuration	$\Delta E / \text{meV}$	Configuration	$\Delta E / \text{meV}$
	0(ref.)		72
	115		202
	236		251

*Continued on next page*

TABLE S17 - *Continued from previous page*

Configuration	$\Delta E/ \text{meV}$	Configuration	$\Delta E/ \text{meV}$
	264		533
	539		694

- [1] P. Giannozzi, S. Baroni, N. Bonini, M. Calandra, R. Car, C. Cavazzoni, D. Ceresoli, G. L. Chiarotti, M. Cococcioni, I. Dabo, A. Dal Corso, S. de Gironcoli, S. Fabris, G. Fratesi, R. Gebauer, U. Gerstmann, C. Gougoussis, A. Kokalj, M. Lazzeri, L. Martin-Samos, N. Marzari, F. Mauri, R. Mazzarello, S. Paolini, A. Pasquarello, L. Paulatto, C. Sbraccia, S. Scandolo, G. Sclauzero, A. P. Seitsonen, A. Smogunov, P. Umari, and R. M. Wentzcovitch, *J. Phys.: Condens. Matter* **21**, 395502 (2009).
- [2] P. Giannozzi, O. Andreussi, T. Brumme, O. Bunau, M. B. Nardelli, M. Calandra, R. Car, C. Cavazzoni, D. Ceresoli, M. Cococcioni, N. Colonna, I. Carnimeo, A. D. Corso, S. de Gironcoli, P. Delugas, R. A. D. Jr, A. Ferretti, A. Floris, G. Fratesi, G. Fugallo, R. Gebauer, U. Gerstmann, F. Giustino, T. Gorni, J. Jia, M. Kawamura, H-Y Ko, A. Kokalj, E. Küçükbenli, M. Lazzeri, M. Marsili, N. Marzari, F. Mauri, N. L. Nguyen, H.-V. Nguyen, A. Otero-de-la-Roza, L. Paulatto, S. Poncé, D. Rocca, R. Sabatini, B. Santra, M. Schlipf, A. P. Seitsonen, A. Smogunov, I. Timrov, T. Thonhauser, P. Umari, N. Vast, X. Wu, and S. Baroni, *Journal of Physics: Condensed Matter* **29**, 465901 (2017).
- [3] D. Vanderbilt, *Physical Review B* **41**, 7892 (1990).
- [4] K. F. Garrity, J. W. Bennett, K. M. Rabe, and D. Vanderbilt, *Computational Materials Science* **81**, 446 (2014).
- [5] L. Bengtsson, *Physical Review B* **59**, 12301 (1999).
- [6] B. Meyer and D. Vanderbilt, *Physical Review B* **63**, 205426 (2001).
- [7] A. C. Dávila López and E. Pehlke, *The Journal of Chemical Physics* **151**, 064709 (2019).

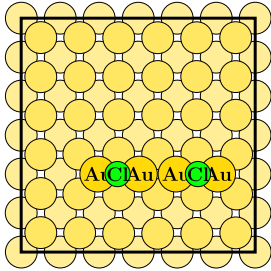
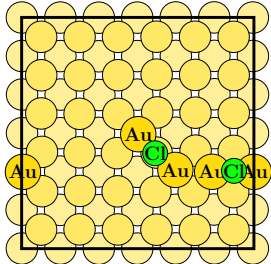
## A.7. $Au_4Cl_n$ Complex on Clean Unreconstructed $Au(001)$

Here we provide a list of all possible configurations of  $Au_4Cl_n$  for  $n = 1, 2$  on clean unreconstructed  $Au(001)$  surface. Adsorption configurations have been selected with the following criterion:

- (i) Au adatoms reside at hollow site
- (ii) Cl-Cl separation is larger than  $3a/2$  ( $\approx 4.41$  Å).

A special selection of configurations has been calculated by means of DFT using Quantum Espresso package [117, 118]. Calculated structures are labeled by the symbol  $\checkmark$ , otherwise configurations are denoted by  $\times$ . Energy differences are calculated using Eq. 5.11 defined in Chapter 5 for values of  $\mu_{Cl}$  corresponding to  $\Theta = 1/16$ . The parameters chosen for the calculations are less accurate, but sufficient to distinguish the ground state configuration with the lowest total energy. The slabs have been modeled by 4 Au layers, and were separated by 13 Å. For the Brillouin zone integration, we have used a  $(3 \times 3 \times 1)$  Monkhorst-Pack grid of special  $k$ -points [107] for the  $p(6 \times 6)$  surface unit cells.

Table A.5.: Adsorption configurations of  $Au_4Cl_n$  for  $n = 1, 2$  on  $Au(001)$  surface. Black squares denote the  $p(6 \times 6)$  SUC.

$n_{Cl}$	Configuration	$E_{diff}(\mu_{Cl, \Theta=1/16})$ (eV)	$d_{Cl-Cl}$ (Å)	
2		-0.44	6.06	$\checkmark$
2		-0.33	6.18	$\checkmark$

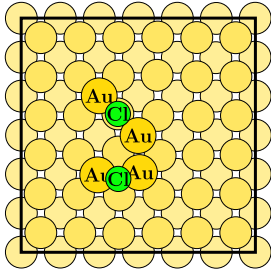
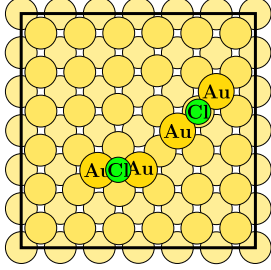
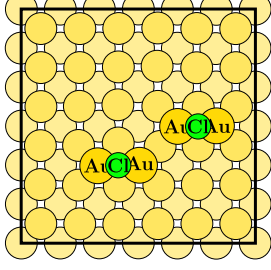
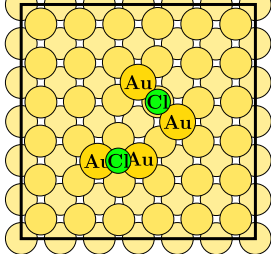
*Continued on next page*

Table A.5 - *Continued from previous page*

$n_{\text{Cl}}$	Configuration	$E_{\text{diff}}(\mu_{\text{Cl},\Theta=1/16})$ (eV)	$d_{\text{Cl-Cl}}$	
2		-0.25	5.18	✓
2		-0.20	6.29	✓
2		-0.18	5.70	✓
2		-0.12	4.77	✓

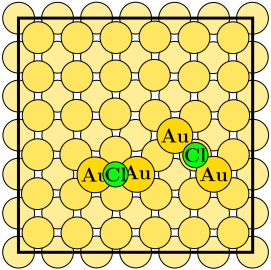
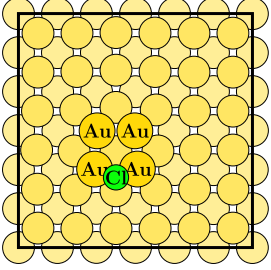
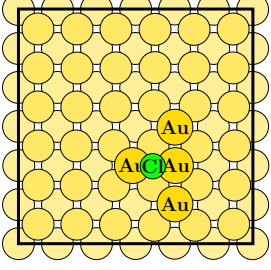
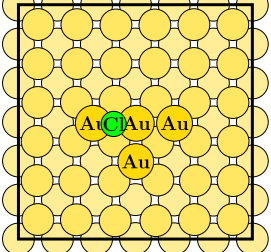
*Continued on next page*

Table A.5 - Continued from previous page

$n_{Cl}$	Configuration	$E_{diff}(\mu_{Cl, \Theta=1/16})$ (eV)	$d_{Cl-Cl}$
2		-	~ 4.40 ✗
2		-	~ 7.34 ✗
2		-	~ 6.57 ✗
2		-	~ 5.30 ✗

Continued on next page

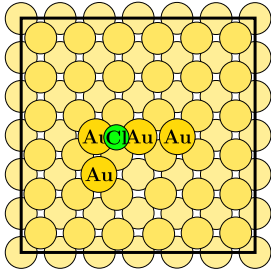
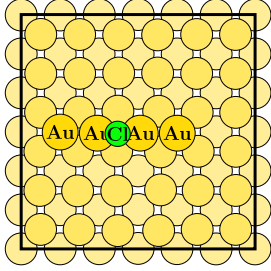
Table A.5 - Continued from previous page

$n_{\text{Cl}}$	Configuration	$E_{\text{diff}}(\mu_{\text{Cl}, \Theta=1/16})$ (eV)	$d_{\text{Cl-Cl}}$	
2		-	$\sim 6.06$	✗
1		-0.10	-	✓
1		+0.02	-	✓
1		-	-	✗

Continued on next page



Table A.5 - Continued from previous page

$n_{Cl}$	Configuration	$E_{diff}(\mu_{Cl, \Theta=1/16})$ (eV)	$d_{Cl-Cl}$
1		-	-
1		-	-



# Bibliography

- [1] P. M. Vereecken, R. A. Binstead, H. Deligianni, and P. C. Andricacos, "The chemistry of additives in damascene copper plating," *IBM Journal of Research and Development* **49**, 3 (2005).
- [2] S. Naghdi, K. Y. Rhee, D. Hui, and S. J. Park, "A Review of Conductive Metal Nanomaterials as Conductive, Transparent, and Flexible Coatings, Thin Films, and Conductive Fillers: Different Deposition Methods and Applications," *Coatings* **8**, 278 (2018).
- [3] J. Pu, Z. Shen, C. Zhong, Q. Zhou, J. Liu, J. Zhu, and H. Zhang, "Electrodeposition Technologies for Li-Based Batteries: New Frontiers of Energy Storage," *Advanced Materials* **32**, 1903808 (2020).
- [4] T. Michely and J. Krug, *Islands, Mounds and Atoms*, Springer Series in Surface Sciences (Springer-Verlag, Berlin Heidelberg, 2004).
- [5] G. Rosenfeld, B. Poelsema, and G. Comsa, "Chapter 3 Epitaxial growth modes far from equilibrium," in *The Chemical Physics of Solid Surfaces*, Vol. 8, edited by D. A. King and D. P. Woodruff, Growth and Properties of Ultrathin Epitaxial Layers (Elsevier, Jan. 1997), pp. 66–101.
- [6] H. Brune and K. Kern, "Chapter 5 Heteroepitaxial metal growth: the effects of strain," in *The Chemical Physics of Solid Surfaces*, Vol. 8, edited by D. A. King and D. P. Woodruff, Growth and Properties of Ultrathin Epitaxial Layers (Elsevier, Jan. 1997), pp. 149–206.
- [7] T. Pearsall, ed., *Quantum Semiconductor Devices and Technologies*, Electronic Materials Series (Springer US, 2000).
- [8] Y. Suzuki, H. Kikuchi, and N. Koshizuka, "Observation of RHEED Intensity Oscillation in the Growth of Ag on Ag(100) Single Crystals," *Japanese Journal of Applied Physics* **27**, L1175 (1988).
- [9] P. Bedrossian, B. Poelsema, G. Rosenfeld, L. C. Jorritsma, N. N. Lipkin, and G. Comsa, "Electron density contour smoothing for epitaxial Ag islands on Ag(100)," *Surface Science* **334**, 1 (1995).
- [10] J. Vrijmoeth, H. A. van der Vegt, J. A. Meyer, E. Vlieg, and R. J. Behm, "Surfactant-Induced Layer-by-Layer Growth of Ag on Ag(111): Origins and Side Effects," *Physical Review Letters* **72**, 3843 (1994).
- [11] B. D. Yu and M. Scheffler, "Anisotropy of Growth of the Close-Packed Surfaces of Silver," *Physical Review Letters* **77**, 1095 (1996).
- [12] B. D. Yu and M. Scheffler, "Ab initio study of step formation and self-diffusion on Ag(100)," *Physical Review B* **55**, 13916 (1997).

- [13] P. A. Thiel and J. W. Evans, "Nucleation, Growth, and Relaxation of Thin Films: Metal(100) Homoepitaxial Systems," *The Journal of Physical Chemistry B* **104**, 1663 (2000).
- [14] D. G. Fedak and N. A. Gjostein, "On the anomalous surface structures of gold," *Surface Science* **8**, 77 (1967).
- [15] S. Günther, E. Kopatzki, M. C. Bartelt, J. W. Evans, and R. J. Behm, "Anisotropy in Nucleation and Growth of Two-Dimensional Islands during Homoepitaxy on "Hex" Reconstructed Au(100)," *Physical Review Letters* **73**, 553 (1994).
- [16] L. Bönig, S. Liu, and H. Metiu, "An effective medium theory study of Au islands on the Au(100) surface: reconstruction, adatom diffusion, and island formation," *Surface Science* **365**, 87 (1996).
- [17] M. Nomura and X.-Q. Wang, "Hexagonally Reconstructed Islands and Anisotropic Diffusion for Au/Au(100)," *Physical Review Letters* **81**, 2739 (1998).
- [18] F. Ercolessi, E. Tosatti, and M. Parrinello, "Au (100) Surface Reconstruction," *Physical Review Letters* **57**, 719 (1986).
- [19] P. Ruggerone, C. Ratsch, and M. Scheffler, "Chapter 13 density-functional theory of epitaxial growth of metals," in *Growth and properties of ultrathin epitaxial layers*, Vol. 8, edited by D. King and D. Woodruff, *The Chemical Physics of Solid Surfaces* (Elsevier, 1997), pp. 490–544.
- [20] P. Kratzer and M. Scheffler, "Reaction-Limited Island Nucleation in Molecular Beam Epitaxy of Compound Semiconductors," *Physical Review Letters* **88**, 036102 (2002).
- [21] G. Henkelman and H. Jónsson, "Long time scale kinetic Monte Carlo simulations without lattice approximation and predefined event table," *The Journal of Chemical Physics* **115**, 9657 (2001).
- [22] A. F. Voter and S. P. Chen, "Accurate Interatomic Potentials for Ni, Al and Ni<sub>3</sub>Al," *MRS Proceedings* **82**, 175 (1986).
- [23] J. M. Hawkins, J. F. Weaver, and A. Asthagiri, "Density functional theory study of the initial oxidation of the Pt(111) surface," *Physical Review B* **79**, 125434 (2009).
- [24] X. Lian, P. Xiao, R. Liu, and G. Henkelman, "Calculations of Oxygen Adsorption-Induced Surface Reconstruction and Oxide Formation on Cu(100)," *Chemistry of Materials* **29**, 1472 (2017).
- [25] Q. Zhu, W. A. Saidi, and J. C. Yang, "Step-Induced Oxygen Upward Diffusion on Stepped Cu(100) Surface," *The Journal of Physical Chemistry C* **119**, 251 (2015).
- [26] Q. Zhu, W. A. Saidi, and J. C. Yang, "Step-Edge Directed Metal Oxidation," *The Journal of Physical Chemistry Letters* **7**, 2530 (2016).
- [27] A. J. Bard and L. R. Faulkner, *Electrochemical methods: fundamentals and applications*, 2nd edition (Wiley, 2001).
- [28] J. Nørskov, F. Studt, F. Abild-Pedersen, and T. Bligaard, *Fundamental concepts in heterogeneous catalysis* (Wiley-Blackwell, United Kingdom, 2014).

- [29] D. M. Kolb, "Electrochemical Surface Science," *Angewandte Chemie International Edition* **40**, 1162 (2001).
- [30] W. Schmickler and E. Santos, *Interfacial Electrochemistry*, 2nd ed. (Springer-Verlag, Berlin Heidelberg, 2010).
- [31] A. Groß, "Theory of Solid/Electrolyte Interfaces," in *Surface and Interface Science* (John Wiley & Sons, Ltd, 2020), pp. 471–515.
- [32] O. M. Magnussen and A. Groß, "Toward an Atomic-Scale Understanding of Electrochemical Interface Structure and Dynamics," *Journal of the American Chemical Society* **141**, 4777 (2019).
- [33] C. S. Cucinotta and M. Kosa, "Electrochemical Interfaces for Energy Storage and Conversion," in *Encyclopedia of Nanotechnology*, edited by B. Bhushan (Springer Netherlands, Dordrecht, 2014), pp. 1–14.
- [34] O. M. Magnussen, J. Hageböck, J. Hotlos, and R. J. Behm, "In situ scanning tunnelling microscopy observations of a disorder–order phase transition in hydrogensulfate adlayers on Au(111)," *Faraday Discussions* **94**, 329 (1992).
- [35] O. M. Magnussen, "Ordered Anion Adlayers on Metal Electrode Surfaces," *Chemical Reviews* **102**, 679 (2002).
- [36] M. R. Vogt, A. Lachenwitzer, O. M. Magnussen, and R. J. Behm, "In-situ STM study of the initial stages of corrosion of Cu(100) electrodes in sulfuric and hydrochloric acid solution," *Surface Science* **399**, 49 (1998).
- [37] M. Al-Shakran, L. A. Kibler, T. Jacob, H. Ibach, G. L. Beltramo, and M. Giesen, "Repulsive interactions induced by specific adsorption: Anomalous step diffusivity and inadequacy of nearest-neighbor Ising model: (part I experimental)," *Surface Science* **651**, 84 (2016).
- [38] Y.-C. Yang, K. Hecker, and O. M. Magnussen, "In situ video-scanning tunneling microscopy studies of the structure and dynamics of Cl adlayers on Au(1 0 0) electrodes," *Electrochimica Acta* **112**, 881 (2013).
- [39] J. K. Nørskov, J. Rossmeisl, A. Logadottir, L. Lindqvist, J. R. Kitchin, T. Bligaard, and H. Jónsson, "Origin of the Overpotential for Oxygen Reduction at a Fuel-Cell Cathode," *The Journal of Physical Chemistry B* **108**, 17886 (2004).
- [40] F. Gossenberger, T. Roman, and A. Groß, "Equilibrium coverage of halides on metal electrodes," *Surface Science, Surface Science and Electrochemistry - 20 years later* **631**, 17 (2015).
- [41] F. Gossenberger, T. Roman, and A. Groß, "Hydrogen and halide co-adsorption on Pt(111) in an electrochemical environment: a computational perspective," *Electrochimica Acta* **216**, 152 (2016).
- [42] I. Abou Hamad, T. Wandlowski, G. Brown, and P. A. Rikvold, "Electrosorption of Br and Cl on Ag(100): experiments and computer simulations," *Journal of Electroanalytical Chemistry, Special issue in memory of Professor M.J. Weaver* **554-555**, 211 (2003).

- [43] I. Abou Hamad, S. J. Mitchell, T. Wandlowski, P. A. Rikvold, and G. Brown, "Cl electrosorption on Ag(100): Lateral interactions and electrosorption valency from comparison of Monte Carlo simulations with chronocoulometry experiments," *Electrochimica Acta* **50**, 5518 (2005).
- [44] P. A. Rikvold, T. Wandlowski, I. Abou Hamad, S. J. Mitchell, and G. Brown, "Reply to "Remarks on the simulation of Cl electrosorption on Ag(100) reported in *Electrochimica Acta* 50 (2005) 5518"," *Electrochimica Acta* **52**, 1932 (2007).
- [45] T. Tansel and O. M. Magnussen, "Video STM Studies of Adsorbate Diffusion at Electrochemical Interfaces," *Physical Review Letters* **96**, 026101 (2006).
- [46] T. Tansel, A. Taranovskyy, and O. M. Magnussen, "In Situ Video-STM Studies of Adsorbate Dynamics at Electrochemical Interfaces," *ChemPhysChem* **11**, 1438 (2010).
- [47] M. Giesen, G. Beltramo, S. Dieluweit, J. Müller, H. Ibach, and W. Schmickler, "The thermodynamics of electrochemical annealing," *Surface Science* **595**, 127 (2005).
- [48] B. Rahn, R. Wen, L. Deuchler, J. Stremme, A. Franke, E. Pehlke, and O. M. Magnussen, "Coadsorbate-Induced Reversal of Solid-Liquid Interface Dynamics," *Angewandte Chemie International Edition* **57**, 6065 (2018).
- [49] O. M. Magnussen, "Atomic-Scale Insights into Electrode Surface Dynamics by High-Speed Scanning Probe Microscopy," *Chemistry – A European Journal* **25**, 12865 (2019).
- [50] K. Krug, J. Stettner, and O. M. Magnussen, "In Situ Surface X-Ray Diffraction Studies of Homoepitaxial Electrochemical Growth on Au(100)," *Physical Review Letters* **96**, 246101 (2006).
- [51] F. Golks, J. Stettner, Y. Gründer, K. Krug, J. Zegenhagen, and O. M. Magnussen, "Anomalous Potential Dependence in Homoepitaxial Cu(001) Electrodeposition: An In Situ Surface X-Ray Diffraction Study," *Physical Review Letters* **108**, 256101 (2012).
- [52] F. Golks, Y. Gründer, J. Stettner, K. Krug, J. Zegenhagen, and O. M. Magnussen, "In situ surface x-ray diffraction studies of homoepitaxial growth on Cu(001) from aqueous acidic electrolyte," *Surface Science, Surface Science and Electrochemistry - 20 years later* **631**, 112 (2015).
- [53] T. M. T. Huynh, F. Weiss, N. T. M. Hai, W. Reckien, T. Bredow, A. Fluegel, M. Arnold, D. Mayer, H. Keller, and P. Broekmann, "On the role of halides and thiols in additive-assisted copper electroplating," *Electrochimica Acta* **89**, 537 (2013).
- [54] C. Vaz-Domínguez and A. Cuesta, "In situ STM study of homoepitaxial electrodeposition on Au(100)," *Electrochimica Acta* **56**, 6847 (2011).
- [55] M. Labayen, C. Ramirez, W. Schattke, and O. M. Magnussen, "Quasi-collective motion of nanoscale metal strings in metal surfaces," *Nature Materials* **2**, 783 (2003).
- [56] K. G. Krug, *In-situ Surface X-ray Diffraction Studies of Homoepitaxial Growth and Dissolution at Gold Single Crystal Electrodes*, PhD thesis (2009).

- 
- [57] E. Pichardo-Pedrero, G. Beltramo, and M. Giesen, "Electrochemical annealing and its relevance in metal electroplating: an atomistic view," *Applied Physics A* **87**, 461 (2007).
- [58] J. E. Müller and H. Ibach, "Migration of point defects at charged Cu, Ag, and Au (100) surfaces," *Physical Review B* **74**, 085408 (2006).
- [59] M. Mesgar, P. Kaghazchi, T. Jacob, E. Pichardo-Pedrero, M. Giesen, H. Ibach, N. B. Luque, and W. Schmickler, "Chlorine-Enhanced Surface Mobility of Au(100)," *Chem-PhysChem* **14**, 233 (2013).
- [60] M. Mesgar, *Multi-scale modeling of island formation and surface dynamics on the Au(100) surface*, Doctoral Thesis (Universität Ulm, July 2015).
- [61] P. Hohenberg and W. Kohn, "Inhomogeneous Electron Gas," *Physical Review* **136**, B864 (1964).
- [62] R. M. Martin, *Electronic structure: basic theory and practical methods* (Cambridge University Press, 2004).
- [63] E. Engel and R. M. Dreizler, *Density Functional Theory: An Advanced Course*, en, *Theoretical and Mathematical Physics* (Springer-Verlag, Berlin Heidelberg, 2011).
- [64] W. Kohn and L. J. Sham, "Self-Consistent Equations Including Exchange and Correlation Effects," *Physical Review* **140**, A1133 (1965).
- [65] A. D. Becke, "Perspective: Fifty years of density-functional theory in chemical physics," *The Journal of Chemical Physics* **140**, 18A301 (2014).
- [66] N. Mardirossian and M. Head-Gordon, "Thirty years of density functional theory in computational chemistry: an overview and extensive assessment of 200 density functionals," *Molecular Physics* **115**, 2315 (2017).
- [67] L. Goerigk and N. Mehta, "A Trip to the Density Functional Theory Zoo: Warnings and Recommendations for the User\*," *Australian Journal of Chemistry* **72**, 563 (2019).
- [68] J. P. Perdew and K. Schmidt, "Jacob's ladder of density functional approximations for the exchange-correlation energy," *AIP Conference Proceedings* **577**, 1 (2001).
- [69] K. Burke, "Perspective on density functional theory," *The Journal of Chemical Physics* **136**, 150901 (2012).
- [70] L. Li, J. C. Snyder, I. M. Pelaschier, J. Huang, U.-N. Niranjana, P. Duncan, M. Rupp, K.-R. Müller, and K. Burke, "Understanding machine-learned density functionals," *International Journal of Quantum Chemistry* **116**, 819 (2016).
- [71] P. A. M. Dirac, "Note on Exchange Phenomena in the Thomas Atom," *Mathematical Proceedings of the Cambridge Philosophical Society* **26**, 376 (1930).
- [72] D. M. Ceperley and B. J. Alder, "Ground State of the Electron Gas by a Stochastic Method," *Physical Review Letters* **45**, 566 (1980).
- [73] J. P. Perdew and A. Zunger, "Self-interaction correction to density-functional approximations for many-electron systems," *Physical Review B* **23**, 5048 (1981).

- [74] M. Fuchs, M. Bockstedte, E. Pehlke, and M. Scheffler, "Pseudopotential study of binding properties of solids within generalized gradient approximations: The role of core-valence exchange correlation," *Physical Review B* **57**, 2134 (1998).
- [75] V. N. Staroverov, G. E. Scuseria, J. Tao, and J. P. Perdew, "Tests of a ladder of density functionals for bulk solids and surfaces," *Physical Review B* **69**, 075102 (2004).
- [76] D. C. Patton and M. R. Pederson, "Application of the generalized-gradient approximation to rare-gas dimers," *Physical Review A* **56**, R2495 (1997).
- [77] D. Rappoport, N. R. M. Crawford, F. Furche, and K. Burke, "Approximate Density Functionals: Which Should I Choose?" In *Encyclopedia of Inorganic Chemistry* (American Cancer Society, 2009).
- [78] Y.-M. Juan, E. Kaxiras, and R. G. Gordon, "Use of the generalized gradient approximation in pseudopotential calculations of solids," *Physical Review B* **51**, 9521 (1995).
- [79] C. Ratsch, A. P. Seitsonen, and M. Scheffler, "Strain dependence of surface diffusion: Ag on Ag(111) and Pt(111)," *Physical Review B* **55**, 6750 (1997).
- [80] A. D. Becke, "Density-functional exchange-energy approximation with correct asymptotic behavior," *Physical Review A* **38**, 3098 (1988).
- [81] A. D. Becke, "Density functional calculations of molecular bond energies," *The Journal of Chemical Physics* **84**, 4524 (1986).
- [82] A. D. Becke, "Density-functional thermochemistry. I. The effect of the exchange-only gradient correction," *The Journal of Chemical Physics* **96**, 2155 (1992).
- [83] J. P. Perdew and Y. Wang, "Accurate and simple analytic representation of the electron-gas correlation energy," *Physical Review B* **45**, 13244 (1992).
- [84] J. P. Perdew, K. Burke, and M. Ernzerhof, "Generalized Gradient Approximation Made Simple," *Physical Review Letters* **77**, 3865 (1996).
- [85] M. Bühl and H. Kabrede, "Geometries of Transition-Metal Complexes from Density-Functional Theory," *Journal of Chemical Theory and Computation* **2**, 1282 (2006).
- [86] M. P. Waller, H. Braun, N. Hojdis, and M. Bühl, "Geometries of Second-Row Transition-Metal Complexes from Density-Functional Theory," *Journal of Chemical Theory and Computation* **3**, 2234 (2007).
- [87] M. Bühl, C. Reimann, D. A. Pantazis, T. Bredow, and F. Neese, "Geometries of Third-Row Transition-Metal Complexes from Density-Functional Theory," *Journal of Chemical Theory and Computation* **4**, 1449 (2008).
- [88] L. Schimka, R. Gaudoin, J. Klimeš, M. Marsman, and G. Kresse, "Lattice constants and cohesive energies of alkali, alkaline-earth, and transition metals: Random phase approximation and density functional theory results," *Physical Review B* **87**, 214102 (2013).
- [89] A. Patra, J. E. Bates, J. Sun, and J. P. Perdew, "Properties of real metallic surfaces: Effects of density functional semilocality and van der Waals nonlocality," *Proceedings of the National Academy of Sciences of the United States of America* **114**, E9188 (2017).



- [90] P. Sony, P. Puschnig, D. Nabok, and C. Ambrosch-Draxl, "Importance of Van Der Waals Interaction for Organic Molecule-Metal Junctions: Adsorption of Thiophene on Cu(110) as a Prototype," *Physical Review Letters* **99**, 176401 (2007).
- [91] J. Hermann, R. A. DiStasio, and A. Tkatchenko, "First-Principles Models for van der Waals Interactions in Molecules and Materials: Concepts, Theory, and Applications," *Chemical Reviews* **117**, 4714 (2017).
- [92] A. Ambrosetti, N. Ferri, R. A. DiStasio, and A. Tkatchenko, "Wavelike charge density fluctuations and van der Waals interactions at the nanoscale," *Science* **351**, 1171 (2016).
- [93] J. F. Dobson, T. Gould, and G. Vignale, "How Many-Body Effects Modify the van der Waals Interaction between Graphene Sheets," *Physical Review X* **4**, 021040 (2014).
- [94] K. Berland, V. R. Cooper, K. Lee, E. Schröder, T. Thonhauser, P. Hyldgaard, and B. I. Lundqvist, "van der Waals forces in density functional theory: a review of the vdW-DF method," *Rep. Prog. Phys.* **78**, 066501 (2015).
- [95] S. Grimme, "Semiempirical GGA-type density functional constructed with a long-range dispersion correction," *J. Comput. Chem.* **27**, 1787 (2006).
- [96] S. Grimme, S. Ehrlich, and L. Goerigk, "Effect of the damping function in dispersion corrected density functional theory," *J. Comput. Chem.* **32**, 1456 (2011).
- [97] A. Tkatchenko and M. Scheffler, "Accurate Molecular Van Der Waals Interactions from Ground-State Electron Density and Free-Atom Reference Data," *Physical Review Letters* **102**, 073005 (2009).
- [98] M. Dion, H. Rydberg, E. Schröder, D. C. Langreth, and B. I. Lundqvist, "Van der Waals Density Functional for General Geometries," *Physical Review Letters* **92**, 246401 (2004).
- [99] S. D. Chakarova-Käck, E. Schröder, B. I. Lundqvist, and D. C. Langreth, "Application of van der Waals Density Functional to an Extended System: Adsorption of Benzene and Naphthalene on Graphite," *Physical Review Letters* **96**, 146107 (2006).
- [100] T. Thonhauser, V. R. Cooper, S. Li, A. Puzder, P. Hyldgaard, and D. C. Langreth, "Van der Waals density functional: Self-consistent potential and the nature of the van der Waals bond," *Physical Review B* **76**, 125112 (2007).
- [101] G. Román-Pérez and J. M. Soler, "Efficient Implementation of a van der Waals Density Functional: Application to Double-Wall Carbon Nanotubes," *Physical Review Letters* **103**, 096102 (2009).
- [102] K. Lee, É. D. Murray, L. Kong, B. I. Lundqvist, and D. C. Langreth, "Higher-accuracy van der Waals density functional," *Physical Review B* **82**, 081101 (2010).
- [103] J. Klimeš, D. R. Bowler, and A. Michaelides, "Chemical accuracy for the van der Waals density functional," *Journal of Physics: Condensed Matter* **22**, 022201 (2009).
- [104] A. Ambrosetti and P. L. Silvestrelli, "Cohesive properties of noble metals by van der Waals-corrected density functional theory: Au, Ag, and Cu as case studies," *Physical Review B* **94**, 045124 (2016).

- [105] J. Park, B. D. Yu, and S. Hong, “Van der Waals density functional theory study for bulk solids with BCC, FCC, and diamond structures,” *Current Applied Physics* **15**, 885 (2015).
- [106] M. Methfessel and A. T. Paxton, “High-precision sampling for Brillouin-zone integration in metals,” *Physical Review B* **40**, 3616 (1989).
- [107] H. J. Monkhorst and J. D. Pack, “Special points for Brillouin-zone integrations,” *Physical Review B* **13**, 5188 (1976).
- [108] H. Hellmann, *Einführung in die Quantenchemie* (J.W. Edwards, Ann Arbor, Mich, 1944).
- [109] R. P. Feynman, “Forces in Molecules,” *Physical Review* **56**, 340 (1939).
- [110] G. P. Francis and M. C. Payne, “Finite basis set corrections to total energy pseudopotential calculations,” *Journal of Physics: Condensed Matter* **2**, 4395 (1990).
- [111] L. Bengtsson, “Dipole correction for surface supercell calculations,” *Physical Review B* **59**, 12301 (1999).
- [112] B. Meyer and D. Vanderbilt, “Ab initio study of BaTiO<sub>3</sub> and PbTiO<sub>3</sub> surfaces in external electric fields,” *Physical Review B* **63**, 205426 (2001).
- [113] N. Troullier and J. L. Martins, “Efficient pseudopotentials for plane-wave calculations,” *Physical Review B* **43**, 1993 (1991).
- [114] D. Vanderbilt, “Soft self-consistent pseudopotentials in a generalized eigenvalue formalism,” *Physical Review B* **41**, 7892 (1990).
- [115] P. E. Blöchl, “Projector augmented-wave method,” *Physical Review B* **50**, 17953 (1994).
- [116] K. F. Garrity, J. W. Bennett, K. M. Rabe, and D. Vanderbilt, “Pseudopotentials for high-throughput DFT calculations,” *Computational Materials Science* **81**, 446 (2014).
- [117] P. Giannozzi et al., “QUANTUM ESPRESSO: a modular and open-source software project for quantum simulations of materials,” *Journal of Physics: Condensed Matter* **21**, 395502 (2009).
- [118] P. Giannozzi et al., “Advanced capabilities for materials modelling with Quantum ESPRESSO,” *Journal of Physics: Condensed Matter* **29**, 465901 (2017).
- [119] P. Giannozzi et al., “Quantum ESPRESSO toward the exascale,” *The Journal of Chemical Physics* **152**, 154105 (2020).
- [120] <https://www.quantum-espresso.org>.
- [121] <http://www.gnu.org/licenses>.
- [122] G. A. Tribello, M. Bonomi, D. Branduardi, C. Camilloni, and G. Bussi, “PLUMED 2: New feathers for an old bird,” *Computer Physics Communications* **185**, 604 (2014).
- [123] O. Andreussi, I. Dabo, and N. Marzari, “Revised self-consistent continuum solvation in electronic-structure calculations,” *The Journal of Chemical Physics* **136**, 064102 (2012).

- [124] G. Antczak and G. Ehrlich, *Surface diffusion: metals, metal atoms, and clusters* (Cambridge University Press, 2010).
- [125] S. Arrhenius, "Über die Dissociationswärme und den Einfluss der Temperatur auf den Dissociationsgrad der Elektrolyte," *Zeitschrift für Physikalische Chemie* **4U**, 96 (1889).
- [126] G. H. Vineyard, "Frequency factors and isotope effects in solid state rate processes," *Journal of Physics and Chemistry of Solids* **3**, 121 (1957).
- [127] D. G. Truhlar and B. C. Garrett, "Variational Transition State Theory," *Annual Review of Physical Chemistry* **35**, 159 (1984).
- [128] P. Hänggi, P. Talkner, and M. Borkovec, "Reaction-rate theory: fifty years after Kramers," *Reviews of Modern Physics* **62**, 251 (1990).
- [129] J. L. Bao and D. G. Truhlar, "Variational transition state theory: theoretical framework and recent developments," *Chemical Society Reviews* **46**, 7548 (2017).
- [130] M.-C. Marinica, C. Barreateau, D. Spanjaard, and M.-C. Desjonquères, "Diffusion rates of Cu adatoms on Cu(111) in the presence of an adisland nucleated at fcc or hcp sites," *Physical Review B* **72**, 115402 (2005).
- [131] G. Mills, G. K. Schenter, D. E. Makarov, and H. Jónsson, "RAW quantum transition state theory," in *Classical and Quantum Dynamics in Condensed Phase Simulations* (WORLD SCIENTIFIC, June 1998), pp. 405–421.
- [132] L. Messina, T. Schuler, M. Nastar, M.-C. Marinica, and P. Olsson, "Solute diffusion by self-interstitial defects and radiation-induced segregation in ferritic Fe-X (X=Cr, Cu, Mn, Ni, P, Si) dilute alloys," arXiv:1910.11440 [cond-mat, physics:physics] (2019).
- [133] W. Meyer and H. Neldel, "Concerning the relationship between the energy constant epsilon and the quantum constant alpha in the conduction-temperature formula in oxydising semi-conductors," *Physikalische Zeitschrift* **38**, 1014 (1937).
- [134] O. Sharia and G. Henkelman, "Analytic dynamical corrections to transition state theory," *New Journal of Physics* **18**, 013023 (2016).
- [135] S. T. Chill, J. Stevenson, V. Rühle, C. Shang, P. Xiao, J. D. Farrell, D. J. Wales, and G. Henkelman, "Benchmarks for Characterization of Minima, Transition States, and Pathways in Atomic, Molecular, and Condensed Matter Systems," *Journal of Chemical Theory and Computation* **10**, 5476 (2014).
- [136] G. Henkelman and H. Jónsson, "A dimer method for finding saddle points on high dimensional potential surfaces using only first derivatives," *The Journal of Chemical Physics* **111**, 7010 (1999).
- [137] R. Malek and N. Mousseau, "Dynamics of Lennard-Jones clusters: A characterization of the activation-relaxation technique," *Physical Review E* **62**, 7723 (2000).
- [138] G. M. Torrie and J. P. Valleau, "Nonphysical sampling distributions in Monte Carlo free-energy estimation: Umbrella sampling," *Journal of Computational Physics* **23**, 187 (1977).

- [139] J. Kästner, "Umbrella sampling," *Wiley Interdisciplinary Reviews: Computational Molecular Science* **1**, 932 (2011).
- [140] G. Ciccotti and M. Ferrario, "Blue Moon Approach to Rare Events," *Molecular Simulation* **30**, 787 (2004).
- [141] J. A. Herron, Y. Morikawa, and M. Mavrikakis, "Ab initio molecular dynamics of solvation effects on reactivity at electrified interfaces," *Proceedings of the National Academy of Sciences of the United States of America* **113**, E4937 (2016).
- [142] A. Laio and M. Parrinello, "Escaping free-energy minima," *PNAS* **99**, 12562 (2002).
- [143] K. M. Bal and E. C. Neyts, "Merging Metadynamics into Hyperdynamics: Accelerated Molecular Simulations Reaching Time Scales from Microseconds to Seconds," *Journal of Chemical Theory and Computation* **11**, 4545 (2015).
- [144] R. J. Shannon, S. Amabilino, M. O'Connor, D. V. Shalishilin, and D. R. Glowacki, "Adaptively Accelerating Reactive Molecular Dynamics Using Boxed Molecular Dynamics in Energy Space," *Journal of Chemical Theory and Computation* **14**, 4541 (2018).
- [145] G. Henkelman, B. P. Uberuaga, and H. Jónsson, "A climbing image nudged elastic band method for finding saddle points and minimum energy paths," *The Journal of Chemical Physics* **113**, 9901 (2000).
- [146] G. Henkelman and H. Jónsson, "Improved tangent estimate in the nudged elastic band method for finding minimum energy paths and saddle points," *The Journal of Chemical Physics* **113**, 9978 (2000).
- [147] H. Jónsson, G. Mills, and K. W. Jacobsen, "Nudged elastic band method for finding minimum energy paths of transitions," in *Classical and quantum dynamics in condensed phase simulations* (WORLD SCIENTIFIC, 2011), pp. 385–404.
- [148] S. Smidstrup, A. Pedersen, K. Stokbro, and H. Jónsson, "Improved initial guess for minimum energy path calculations," *The Journal of Chemical Physics* **140**, 214106 (2014).
- [149] S. A. Trygubenko and D. J. Wales, "A doubly nudged elastic band method for finding transition states," *The Journal of Chemical Physics* **120**, 2082 (2004).
- [150] N. A. Zarkevich and D. D. Johnson, "Nudged-elastic band method with two climbing images: Finding transition states in complex energy landscapes," *The Journal of Chemical Physics* **142**, 024106 (2015).
- [151] E. L. Kolsbjerg, M. N. Groves, and B. Hammer, "An automated nudged elastic band method," *The Journal of Chemical Physics* **145**, 094107 (2016).
- [152] J. A. Garrido Torres, P. C. Jennings, M. H. Hansen, J. R. Boes, and T. Bligaard, "Low-Scaling Algorithm for Nudged Elastic Band Calculations Using a Surrogate Machine Learning Model," *Physical Review Letters* **122**, 156001 (2019).
- [153] S. R. Bahn and K. W. Jacobsen, "An object-oriented scripting interface to a legacy electronic structure code," *Comput. Sci. Eng.* **4**, 56 (2002).

- [154] A. H. Larsen et al., “The atomic simulation environment—a Python library for working with atoms,” *Journal of Physics: Condensed Matter* **29**, 273002 (2017).
- [155] A. Laio and F. Gervasio, “Metadynamics: A method to simulate rare events and reconstruct the free energy in biophysics, chemistry and material science,” *Reports on Progress in Physics* **71**, 126601 (2008).
- [156] P. Tiwary and M. Parrinello, “From Metadynamics to Dynamics,” *Physical Review Letters* **111**, 230602 (2013).
- [157] A.-K. Henß, S. Sakong, P. K. Messer, J. Wiechers, R. Schuster, D. C. Lamb, A. Groß, and J. Wintterlin, “Density fluctuations as door-opener for diffusion on crowded surfaces,” *Science* **363**, 715 (2019).
- [158] A. C. Dávila López and E. Pehlke, “DFT study of Au self-diffusion on Au(001) in the presence of a Cl adlayer,” *The Journal of Chemical Physics* **151**, 064709 (2019).
- [159] B. V. Andryushechkin, T. V. Pavlova, and K. N. Eltsov, “Adsorption of halogens on metal surfaces,” *Surface Science Reports* **73**, 83 (2018).
- [160] I. A. Suleiman, M. W. Radny, M. J. Gladys, P. V. Smith, J. C. Mackie, E. M. Kennedy, and B. Z. Dlugogorski, “Interaction of Chlorine and Oxygen with the Cu(100) Surface,” *The Journal of Physical Chemistry C* **114**, 19048 (2010).
- [161] H. Fu, L. Jia, W. Wang, and K. Fan, “The first-principle study on chlorine-modified silver surfaces,” *Surface Science* **584**, 187 (2005).
- [162] Y. Wang, W. Wang, K. Fan, and J. Deng, “The first-principle study of the iodine-modified silver surfaces,” *Surface Science* **487**, 77 (2001).
- [163] S. Wang and P. A. Rikvold, “*Ab initio* calculations for bromine adlayers on the Ag(100) and Au(100) surfaces: The  $c(2 \times 2)$  structure,” *Physical Review B* **65**, 155406 (2002).
- [164] A. Migani and F. Illas, “A Systematic Study of the Structure and Bonding of Halogens on Low-Index Transition Metal Surfaces,” *The Journal of Physical Chemistry B* **110**, 11894 (2006).
- [165] D. Rampulla, A. Gellman, and D. S. Sholl, “Bromine atom diffusion on stepped and kinked copper surfaces,” *Surface Science* **600**, 2171 (2006).
- [166] J. Björk, F. Hanke, and S. Stafström, “Mechanisms of Halogen-Based Covalent Self-Assembly on Metal Surfaces,” *Journal of the American Chemical Society* **135**, 5768 (2013).
- [167] T. V. Pavlova, B. V. Andryushechkin, and G. M. Zhidomirov, “First-Principle Study of Adsorption and Desorption of Chlorine on Cu(111) Surface: Does Chlorine or Copper Chloride Desorb?” *The Journal of Physical Chemistry C* **120**, 2829 (2016).
- [168] Y. Santiago-Rodríguez, J. A. Herron, M. C. Curet-Arana, and M. Mavrikakis, “Atomic and molecular adsorption on Au(111),” *Surface Science* **627**, 57 (2014).
- [169] P. S. Bagus, A. Wieckowski, and C. Wöll, “Ionic adsorbates on metal surfaces,” *International Journal of Quantum Chemistry* **110**, 2844 (2010).

- [170] T. Roman and A. Groß, "Periodic Density-Functional Calculations on Work-Function Change Induced by Adsorption of Halogens on Cu(111)," *Physical Review Letters* **110**, 156804 (2013).
- [171] N. Reimann, private communication, Jan. 2017.
- [172] S. Buttenschön, private communication, Mar. 2016.
- [173] M. Giesen, M. Dietterle, D. Stapel, H. Ibach, and D. M. Kolb, "Step fluctuations on metals in contact with an electrolyte: a new access to dynamical processes at the solid/liquid interface," *Surface Science* **384**, 168 (1997).
- [174] J. Rossmeisl, E. Skúlason, M. E. Björketun, V. Tripkovic, and J. K. Nørskov, "Modeling the electrified solid-liquid interface," *Chemical Physics Letters* **466**, 68 (2008).
- [175] E. Skúlason, V. Tripkovic, M. E. Björketun, S. Gudmundsdóttir, G. Karlberg, J. Rossmeisl, T. Bligaard, H. Jónsson, and J. K. Nørskov, "Modeling the Electrochemical Hydrogen Oxidation and Evolution Reactions on the Basis of Density Functional Theory Calculations," *The Journal of Physical Chemistry C* **114**, 18182 (2010).
- [176] M. H. Hansen, A. Nilsson, and J. Rossmeisl, "Modelling pH and potential in dynamic structures of the water/Pt(111) interface on the atomic scale," *Physical Chemistry Chemical Physics* **19**, 23505 (2017).
- [177] J. Le, Q. Fan, L. Perez-Martinez, A. Cuesta, and J. Cheng, "Theoretical insight into the vibrational spectra of metal-water interfaces from density functional theory based molecular dynamics," *Physical Chemistry Chemical Physics* **20**, 11554 (2018).
- [178] R. Khatib, A. Kumar, S. Sanvito, M. Sulpizi, and C. S. Cucinotta, "The nanoscale structure of the Pt-water double layer under bias revealed," arXiv:1905.11850 [cond-mat, physics:physics] (2019).
- [179] A. Groß and S. Sakong, "Modelling the electric double layer at electrode/electrolyte interfaces," *Current Opinion in Electrochemistry* **14**, 1 (2019).
- [180] G. S. Karlberg, J. Rossmeisl, and J. K. Nørskov, "Estimations of electric field effects on the oxygen reduction reaction based on the density functional theory," *Physical Chemistry Chemical Physics* **9**, 5158 (2007).
- [181] S. Schnur and A. Groß, "Properties of metal-water interfaces studied from first principles," *New Journal of Physics* **11**, 125003 (2009).
- [182] S. Sakong and A. Groß, "The electric double layer at metal-water interfaces revisited based on a charge polarization scheme," *The Journal of Chemical Physics* **149**, 084705 (2018).
- [183] E. Bauer, "Phänomenologische Theorie der Kristallabscheidung an Oberflächen. I," *Zeitschrift für Kristallographie - Crystalline Materials* **110**, 372 (1958).
- [184] W. K. Burton, N. Cabrera, F. C. Frank, and N. F. Mott, "The growth of crystals and the equilibrium structure of their surfaces," *Philosophical Transactions of the Royal Society of London. Series A, Mathematical and Physical Sciences* **243**, 299 (1951).

- [185] R. Stumpf and M. Scheffler, "Ab initio calculations of energies and self-diffusion on flat and stepped surfaces of Al and their implications on crystal growth," *Physical Review B* **53**, 4958 (1996).
- [186] K. Pötting, W. Schmickler, and T. Jacob, "Self-Diffusion on Au(100): A Density Functional Theory Study," *ChemPhysChem* **11**, 1395 (2010).
- [187] G. Ehrlich and F. G. Hudda, "Atomic View of Surface Self-Diffusion: Tungsten on Tungsten," *The Journal of Chemical Physics* **44**, 1039 (1966).
- [188] R. L. Schwoebel and E. J. Shipsey, "Step Motion on Crystal Surfaces," *Journal of Applied Physics* **37**, 3682 (1966).
- [189] S. K. Xiang and H. Huang, "Ab initio determination of Ehrlich–Schwoebel barriers on Cu{111}," *Applied Physics Letters* **92**, 101923 (2008).
- [190] Y. Han, J. W. Evans, and F. Liu, "Energy barriers for Pb adatom diffusion on stepped ultrathin Pb(111) quantum nanofilms: First-principles calculations," *Physical Review B* **100**, 195405 (2019).
- [191] R. Stumpf and M. Scheffler, "Theory of self-diffusion at and growth of Al(111)," *Physical Review Letters* **72**, 254 (1994).
- [192] H. Yildirim and T. S. Rahman, "Diffusion barriers for Ag and Cu adatoms on the terraces and step edges on Cu(100) and Ag(100): An ab initio study," *Physical Review B* **80**, 235413 (2009).
- [193] M. Benlattar, E. Elkoraychy, K. Sbiaai, M. Mazroui, and Y. Boughaleb, "Ehrlich–Schwoebel barriers and adsorption of Au, Cu and Ag stepped (100) surfaces," *Modern Physics Letters B* **31**, 1750037 (2017).
- [194] C. M. Chang and C. M. Wei, "Self-diffusion of Adatoms and Dimers on fcc (100) Surfaces," *Chinese Journal of Physics* **43**, 169 (2005).
- [195] Q. Liu, Z. Sun, X. Ning, Y. Li, L. Liu, and J. Zhuang, "Systematical study of dimer diffusion on metal fcc(001) surfaces," *Surface Science* **554**, 25 (2004).
- [196] A. Kara, O. Trushin, H. Yildirim, and T. S. Rahman, "Off-lattice self-learning kinetic Monte Carlo: application to 2D cluster diffusion on the fcc(111) surface," *Journal of Physics: Condensed Matter* **21**, 084213 (2009).
- [197] H. Choi, S.-G. Lee, and Y.-C. Chung, "Atomic structures and behaviors of a fcc Cu(111) surface with submonolayer Pb coverage," *Computational Materials Science* **47**, 693 (2010).
- [198] Y. Han, C. R. Stoldt, P. A. Thiel, and J. W. Evans, "Ab Initio Thermodynamics and Kinetics for Coalescence of Two-Dimensional Nanoislands and Nanopits on Metal (100) Surfaces," *The Journal of Physical Chemistry C* **120**, 21617 (2016).
- [199] O. Trushin, A. Karim, A. Kara, and T. S. Rahman, "Self-learning kinetic Monte Carlo method: Application to Cu(111)," *Physical Review B* **72**, 115401 (2005).
- [200] S. I. Shah, G. Nandipati, A. Karim, and T. S. Rahman, "Self-learning kinetic Monte Carlo simulations of self-diffusion of small Ag islands on the Ag(111) surface," *Journal of Physics: Condensed Matter* **28**, 025001 (2015).

- [201] S. R. Acharya, S. I. Shah, and T. S. Rahman, "Diffusion of small Cu islands on the Ni(111) surface: A self-learning kinetic Monte Carlo study," *Surface Science* **662**, 42 (2017).
- [202] J. H. Montoya, C. Shi, K. Chan, and J. K. Nørskov, "Theoretical Insights into a CO Dimerization Mechanism in CO<sub>2</sub> Electroreduction," *The Journal of Physical Chemistry Letters* **6**, 2032 (2015).
- [203] L. D. Chen, M. Urushihara, K. Chan, and J. K. Nørskov, "Electric Field Effects in Electrochemical CO<sub>2</sub> Reduction," *ACS Catalysis* **6**, 7133 (2016).
- [204] H. Helmholtz, "Ueber einige Gesetze der Vertheilung elektrischer Ströme in körperlichen Leitern mit Anwendung auf die thierisch-elektrischen Versuche," *Annalen der Physik* **165**, 211 (1853).
- [205] M. Gouy, "Sur la constitution de la charge électrique à la surface d'un électrolyte," *Journal de Physique Théorique et Appliquée* **9**, 457 (1910).
- [206] D. L. Chapman, "LI. A contribution to the theory of electrocapillarity," *The London, Edinburgh, and Dublin Philosophical Magazine and Journal of Science* **25**, 475 (1913).
- [207] O. Stern, "Zur theorie der elektrolytischen doppelschicht," *Zeitschrift für Elektrochemie und angewandte physikalische Chemie* **30**, 508 (1924).
- [208] D. C. Grahame, "The Electrical Double Layer and the Theory of Electrocapillarity.," *Chemical Reviews* **41**, 441 (1947).
- [209] K. Reuter and M. Scheffler, "Composition, structure, and stability of RuO<sub>2</sub>(110) as a function of oxygen pressure," *Physical Review B* **65**, 035406 (2001).
- [210] J. Rogal, K. Reuter, and M. Scheffler, "CO oxidation at Pd(100): A first-principles constrained thermodynamics study," *Physical Review B* **75**, 205433 (2007).
- [211] K. Reuter, "Ab Initio Thermodynamics and First-Principles Microkinetics for Surface Catalysis," *Catalysis Letters* **146**, 541 (2016).
- [212] M. W. J. Chase, *NIST-JANAF Thermochemical Tables, 4th Edition* (American Institute of Physics, New York, 1998).
- [213] A. Y. Lozovoi, A. Alavi, J. Kohanoff, and R. M. Lynden-Bell, "Ab initio simulation of charged slabs at constant chemical potential," *The Journal of Chemical Physics* **115**, 1661 (2001).
- [214] E. Skúlason, G. S. Karlberg, J. Rossmeisl, T. Bligaard, J. Greeley, H. Jónsson, and J. K. Nørskov, "Density functional theory calculations for the hydrogen evolution reaction in an electrochemical double layer on the Pt(111) electrode," *Physical Chemistry Chemical Physics* **9**, 3241 (2007).
- [215] K. Chan and J. K. Nørskov, "Electrochemical Barriers Made Simple," *The Journal of Physical Chemistry Letters* **6**, 2663 (2015).
- [216] S. Sakong, K. Forster-Tonigold, and A. Groß, "The structure of water at a Pt(111) electrode and the potential of zero charge studied from first principles," *The Journal of Chemical Physics* **144**, 194701 (2016).



- [217] J. Le, M. Iannuzzi, A. Cuesta, and J. Cheng, "Determining Potentials of Zero Charge of Metal Electrodes versus the Standard Hydrogen Electrode from Density-Functional-Theory-Based Molecular Dynamics," *Physical Review Letters* **119**, 016801 (2017).
- [218] S. Surendralal, M. Todorova, M. W. Finnis, and J. Neugebauer, "First-Principles Approach to Model Electrochemical Reactions: Understanding the Fundamental Mechanisms behind Mg Corrosion," *Physical Review Letters* **120**, 246801 (2018).
- [219] A. Bouzid and A. Pasquarello, "Atomic-Scale Simulation of Electrochemical Processes at Electrode/Water Interfaces under Referenced Bias Potential," *The Journal of Physical Chemistry Letters* **9**, 1880 (2018).
- [220] H. A. Hansen, I. C. Man, F. Studt, F. Abild-Pedersen, T. Bligaard, and J. Rossmeisl, "Electrochemical chlorine evolution at rutile oxide (110) surfaces," *Physical Chemistry Chemical Physics* **12**, 283 (2010).
- [221] K. J. Vetter and J. W. Schultze, "Potentialabhängigkeit von Elektrosorptionsgleichgewichten und die Elektrosorptionswertigkeit  $\gamma$ ," *Berichte der Bunsengesellschaft für physikalische Chemie* **76**, 920 (1972).
- [222] K. J. Vetter and J. W. Schultze, "Stromfluß bei Elektrosorptionsprozessen und Elektrosorptionswertigkeit  $\gamma$ ," *Berichte der Bunsengesellschaft für physikalische Chemie* **76**, 927 (1972).
- [223] W. Schmickler and R. Guidelli, "The partial charge transfer," *Electrochimica Acta* **127**, 489 (2014).
- [224] M. M. Waegle, C. M. Gunathunge, J. Li, and X. Li, "How cations affect the electric double layer and the rates and selectivity of electrocatalytic processes," *The Journal of Chemical Physics* **151**, 160902 (2019).
- [225] J. Lipkowski, Z. Shi, A. Chen, B. Pettinger, and C. Bilger, "Ionic adsorption at the Au(111) electrode," *Electrochimica Acta* **43**, 2875 (1998).
- [226] T. Wandlowski, J. X. Wang, and B. M. Ocko, "Adsorption of bromide at the Ag(100) electrode surface," *Journal of Electroanalytical Chemistry* **500**, 418 (2001).
- [227] R. Jinnouchi, T. Hatanaka, Y. Morimoto, and M. Osawa, "First principles study of sulfuric acid anion adsorption on a Pt(111) electrode," *Physical Chemistry Chemical Physics* **14**, 3208 (2012).
- [228] K. Schwarz, B. Xu, Y. Yan, and R. Sundararaman, "Partial oxidation of step-bound water leads to anomalous pH effects on metal electrode step-edges," *Physical Chemistry Chemical Physics* **18**, 16216 (2016).
- [229] A. C. Dávila López and E. Pehlke, "Initial steps toward  $\text{Au}_{\text{ad}}$  island nucleation on a  $c(2 \times 2)\text{-Cl Au}(001)$  surface investigated by DFT," *The Journal of Chemical Physics* **152**, 084701 (2020).
- [230] D. G. Fedak, "Structure and Stability of the (100) Surface of Gold," *Physical Review Letters* **16**, 171 (1966).

- [231] M. A. Van Hove, R. J. Koestner, P. C. Stair, J. P. Bibérian, L. L. Kesmodel, I. Bartoš, and G. A. Somorjai, "The surface reconstructions of the (100) crystal faces of iridium, platinum and gold: I. Experimental observations and possible structural models," *Surface Science* **103**, 189 (1981).
- [232] R. Hammer, A. Sander, S. Förster, M. Kiel, K. Meinel, and W. Widdra, "Surface reconstruction of Au(001): High-resolution real-space and reciprocal-space inspection," *Physical Review B* **90**, 035446 (2014).
- [233] P. Havu, V. Blum, V. Havu, P. Rinke, and M. Scheffler, "Large-scale surface reconstruction energetics of Pt(100) and Au(100) by all-electron density functional theory," *Physical Review B* **82**, 161418 (2010).
- [234] D. M. Kolb and J. Schneider, "The study of reconstructed electrode surfaces: Au(100)-(5 × 20)," *Surface Science* **162**, 764 (1985).
- [235] D. M. Kolb and J. Schneider, "Surface reconstruction in electrochemistry: Au(100)-(5 × 20), Au(111)-(1 × 23) and Au(110)-(1 × 2)," *Electrochimica Acta* **31**, 929 (1986).
- [236] A. S. Dakkouri, "Reconstruction phenomena at gold/electrolyte interfaces: an in-situ STM study of Au(100)," *Solid State Ionics, Papers from the International Workshop* **94**, 99 (1997).
- [237] H. Striegler, P. Skoluda, and D. M. Kolb, "On the stability of unreconstructed Au(100)-(1 × 1) at negative potentials in aqueous sulfate solution," *Journal of Electroanalytical Chemistry* **471**, 9 (1999).
- [238] E. Santos and W. Schmickler, "Changes in the surface energy during the reconstruction of Au(100) and Au(111) electrodes," *Chemical Physics Letters* **400**, 26 (2004).
- [239] Y. J. Feng, K. P. Bohnen, and C. T. Chan, "First-principles studies of Au(100)-hex reconstruction in an electrochemical environment," *Physical Review B* **72**, 125401 (2005).
- [240] T. Jacob, "Potential-induced lifting of the Au(1 0 0)-surface reconstruction studied with DFT," *Electrochimica Acta, Selection of papers from the Third Gerischer Symposium Berlin, Germany, 6-8 July 2005* **52**, 2229 (2007).
- [241] S. Venkatachalam, P. Kaghazchi, L. A. Kibler, D. M. Kolb, and T. Jacob, "First principles studies of the potential-induced lifting of the Au(1 0 0) surface reconstruction," *Chemical Physics Letters* **455**, 47 (2008).
- [242] N. G. Hörmann, O. Andreussi, and N. Marzari, "Grand canonical simulations of electrochemical interfaces in implicit solvation models," *The Journal of Chemical Physics* **150**, 041730 (2019).
- [243] A. Cuesta and D. M. Kolb, "The structure of bromide and chloride adlayers on Au(100) electrodes: an in situ STM study," *Surface Science* **465**, 310 (2000).
- [244] H. Iwai, M. Okada, K. Fukutani, and Y. Murata, "Chlorine-induced de-reconstruction on Au(001) and Cl-adsorbed layers," *Journal of Physics: Condensed Matter* **7**, 5163 (1995).

- [245] Y. Zhang and W. Yang, "Comment on "Generalized Gradient Approximation Made Simple"," Physical Review Letters **80**, 890 (1998).
- [246] T. Thonhauser, S. Zuluaga, C. A. Arter, K. Berland, E. Schröder, and P. Hyldgaard, "Spin Signature of Nonlocal Correlation Binding in Metal-Organic Frameworks," Physical Review Letters **115**, 136402 (2015).
- [247] A. Dal Corso, "Pseudopotentials periodic table: From H to Pu," Computational Materials Science **95**, 337 (2014).
- [248] M. M. Montemore, O. Andreussi, and J. W. Medlin, "Hydrocarbon adsorption in an aqueous environment: A computational study of alkyls on Cu(111)," The Journal of Chemical Physics **145**, 074702 (2016).
- [249] K. Lejaeghere et al., "Reproducibility in density functional theory calculations of solids," Science **351**, aad3000 (2016).
- [250] F. Tran, J. Stelzl, and P. Blaha, "Rungs 1 to 4 of DFT Jacob's ladder: Extensive test on the lattice constant, bulk modulus, and cohesive energy of solids," The Journal of Chemical Physics **144**, 204120 (2016).
- [251] B. B. Blizanac, C. A. Lucas, M. E. Gallagher, P. N. Ross, and N. M. Marković, "Surface Structures and Phase Transitions at the Au(100)-Br Interface: pH and CO Effects," The Journal of Physical Chemistry B **108**, 5304 (2004).
- [252] T. Wandlowski, J. X. Wang, O. M. Magnussen, and B. M. Ocko, "Structural and Kinetic Aspects of Bromide Adsorption on Au(100)," The Journal of Physical Chemistry **100**, 10277 (1996).
- [253] E. Bertel and F. F. Netzer, "Adsorption of bromine on the reconstructed Au(100) surface: LEED, thermal desorption and work function measurements," en, Surface Science **97**, 409 (1980).
- [254] X. Gao, G. J. Edens, F.-C. Liu, M. J. Weaver, and A. Hamelin, "Sensitivity of Electrochemical Adlayer Structure to the Metal Crystallographic Orientation: Potential-Dependent Iodide Adsorption on Au(100) in Comparison with Other Low-Index Surfaces," The Journal of Physical Chemistry **98**, 8086 (1994).
- [255] C. G. M. Hermse, A. P. van Bavel, M. T. M. Koper, J. J. Lukkien, R. A. van Santen, and A. P. J. Jansen, "Bridge-bonded adsorbates on fcc(100) and fcc(111) surfaces: A kinetic Monte Carlo study," Physical Review B **73**, 195422 (2006).
- [256] J. Valenzuela-Benavides and M. Herrera-Zaldívar, "Structural transitions of chemisorbed iodine on Au(1 0 0): A STM and LEED study," Surface Science **592**, 150 (2005).
- [257] O. M. Magnussen, "Moving through the crowd," Science **363**, 695 (2019).
- [258] A. S. Varela, W. Ju, T. Reier, and P. Strasser, "Tuning the Catalytic Activity and Selectivity of Cu for CO<sub>2</sub> Electroreduction in the Presence of Halides," ACS Catalysis **6**, 2136 (2016).
- [259] B. D. Yu and M. Scheffler, "Physical origin of exchange diffusion on fcc(100) metal surfaces," Physical Review B **56**, R15569 (1997).

- [260] S. Mishra, V. Vallet, and W. Domcke, "Importance of Spin–Orbit Coupling for the Assignment of the Photodetachment Spectra of AuX<sub>2</sub>– (X=Cl, Br, and I)," *ChemPhysChem* **7**, 723 (2006).
- [261] J. Lee, T. L. Windus, P. A. Thiel, J. W. Evans, and D.-J. Liu, "Coinage Metal–Sulfur Complexes: Stability on Metal(111) Surfaces and in the Gas Phase," *The Journal of Physical Chemistry C* **123**, 12954 (2019).
- [262] S. Y. Kim, I.-H. Lee, and S. Jun, "Transition-pathway models of atomic diffusion on fcc metal surfaces. I. Flat surfaces," *Physical Review B* **76**, 245407 (2007).
- [263] R. v. Gastel, E. Somfai, W. v. Saarloos, and J. W. M. Frenken, "A giant atomic slide-puzzle," *Nature* **408**, 665 (2000).
- [264] J. Frenken, R. van Gastel, S. van Albada, E. Somfai, and W. van Saarloos, "Diffusion in a surface: the atomic slide puzzle," *Applied Physics A* **75**, 11 (2002).
- [265] R. van Gastel, E. Somfai, S. B. van Albada, W. van Saarloos, and J. W. M. Frenken, "Vacancy diffusion in the Cu(001) surface I: an STM study," *Surface Science* **521**, 10 (2002).
- [266] J. B. Hannon, C. Klünker, M. Giesen, H. Ibach, N. C. Bartelt, and J. C. Hamilton, "Surface Self-Diffusion by Vacancy Motion: Island Ripening on Cu(001)," *Physical Review Letters* **79**, 2506 (1997).
- [267] B. Rahn and O. M. Magnussen, "Formation and Diffusion of Subsurface Adsorbates at Electrodes," *Journal of the American Chemical Society* **140**, 9066 (2018).
- [268] L. Deuchler, *DFT study of the diffusion of S adsorbates on a Br pre-covered Cu(100)-surface*, MA thesis (Christian-Albrechts-Universität zu Kiel, Germany, 2016).
- [269] J. Stremme, *Dichtefunktionalrechnungen zu S- und Cl-Adsorbaten auf der Cu(100)-Oberfläche: Adsorption und Diffusion*, MA thesis (Christian-Albrechts-Universität zu Kiel, Germany, 2009).
- [270] B. N. Zope, D. D. Hibbitts, M. Neurock, and R. J. Davis, "Reactivity of the Gold/Water Interface During Selective Oxidation Catalysis," *Science* **330**, 74 (2010).
- [271] A. Fortunelli, W. A. Goddard, Y. Sha, T. H. Yu, L. Sementa, G. Barcaro, and O. Andreussi, "Dramatic Increase in the Oxygen Reduction Reaction for Platinum Cathodes from Tuning the Solvent Dielectric Constant," *Angewandte Chemie International Edition* **53**, 6669 (2014).
- [272] L. Sementa, O. Andreussi, W. A. G. Iii, and A. Fortunelli, "Catalytic activity of Pt 38 in the oxygen reduction reaction from first-principles simulations," *Catalysis Science & Technology* **6**, 6901 (2016).
- [273] S. K. Iyemperumal and N. A. Deskins, "Evaluating Solvent Effects at the Aqueous/Pt(111) Interface," *ChemPhysChem* **18**, 2171 (2017).
- [274] M. Saracino, P. Broekmann, K. Gentz, M. Becker, H. Keller, F. Janetzko, T. Bredow, K. Wandelt, and H. Dosch, "Surface relaxation phenomena at electrified interfaces: Revealing adsorbate, potential, and solvent effects by combined x-ray diffraction, STM and DFT studies," *Physical Review B* **79**, 115448 (2009).

- [275] Y. Gründer, D. Kaminski, F. Golks, K. Krug, J. Stettner, O. M. Magnussen, A. Franke, J. Stremme, and E. Pehlke, "Reversal of chloride-induced Cu(001) subsurface buckling in the electrochemical environment: An in situ surface x-ray diffraction and density functional theory study," *Physical Review B* **81**, 174114 (2010).
- [276] M. Nakamura, N. Sato, N. Hoshi, and O. Sakata, "Outer Helmholtz Plane of the Electrical Double Layer Formed at the Solid Electrode–Liquid Interface," *ChemPhysChem* **12**, 1430 (2011).
- [277] H. Keller, M. Saracino, H. M. Nguyen, T. M. T. Huynh, and P. Broekmann, "Competitive Anion/Water and Cation/Water Interactions at Electrified Copper/Electrolyte Interfaces Probed by in Situ X-ray Diffraction," *The Journal of Physical Chemistry C* **116**, 11068 (2012).
- [278] R. Sundararaman, W. A. Goddard III, and T. A. Arias, "Grand canonical electronic density-functional theory: Algorithms and applications to electrochemistry," *The Journal of Chemical Physics* **146**, 114104 (2017).
- [279] M. M. Melander, M. J. Kuisma, T. E. K. Christensen, and K. Honkala, "Grand-canonical approach to density functional theory of electrocatalytic systems: Thermodynamics of solid-liquid interfaces at constant ion and electrode potentials," *The Journal of Chemical Physics* **150**, 041706 (2018).
- [280] S. Ringe, E. L. Clark, J. Resasco, A. Walton, B. J. Seger, A. T. Bell, and K. Chan, "Understanding Cation Effects in Electrochemical CO<sub>2</sub> Reduction," *Energy & Environmental Science* (2019).
- [281] J. Carrasco, A. Hodgson, and A. Michaelides, "A molecular perspective of water at metal interfaces," *Nature Materials* **11**, 667 (2012).
- [282] L. Bellarosa, R. García-Muelas, G. Revilla-López, and N. López, "Diversity at the Water–Metal Interface: Metal, Water Thickness, and Confinement Effects," *ACS Central Science* **2**, 109 (2016).
- [283] S. Gim, K. J. Cho, H.-K. Lim, and H. Kim, "Structure, Dynamics, and Wettability of Water at Metal Interfaces," *Scientific Reports* **9**, 1 (2019).
- [284] L. S. Pedroza, A. Poissier, and M.-V. Fernández-Serra, "Local order of liquid water at metallic electrode surfaces," *The Journal of Chemical Physics* **142**, 034706 (2015).
- [285] J. Le, A. Cuesta, and J. Cheng, "The structure of metal-water interface at the potential of zero charge from density functional theory-based molecular dynamics," *Journal of Electroanalytical Chemistry* **819**, 87 (2018).
- [286] I. -. Yeh and M. L. Berkowitz, "Structure and dynamics of water at water|Pt interface as seen by molecular dynamics computer simulation," *Journal of Electroanalytical Chemistry* **450**, 313 (1998).
- [287] X. Lin and A. Groß, "First-principles study of the water structure on flat and stepped gold surfaces," *Surface Science* **606**, 886 (2012).

- [288] H. Keller, M. Saracino, H. M. T. Nguyen, and P. Broekmann, "Templating the near-surface liquid electrolyte: In situ surface x-ray diffraction study on anion/cation interactions at electrified interfaces," *Physical Review B* **82**, 245425 (2010).
- [289] B. V. Andryushechkin, V. V. Cherkez, E. V. Gladchenko, T. V. Pavlova, G. M. Zhidomirov, B. Kierren, C. Didiot, Y. Fagot-Revurat, D. Malterre, and K. N. Eltsov, "Self-Organization of Gold Chloride Molecules on Au(111) Surface," *The Journal of Physical Chemistry C* **117**, 24948 (2013).
- [290] H. Walen, D.-J. Liu, J. Oh, H. J. Yang, Y. Kim, and P. A. Thiel, "Identification of Au-S complexes on Au(100)," *Physical Chemistry Chemical Physics* **18**, 4891 (2016).
- [291] O. Voznyy, J. J. Dubowski, J. T. Yates, and P. Maksymovych, "The Role of Gold Adatoms and Stereochemistry in Self-Assembly of Methylthiolate on Au(111)," *Journal of the American Chemical Society* **131**, 12989 (2009).
- [292] J. Lee, J. S. Boschen, T. L. Windus, P. A. Thiel, and D.-J. Liu, "Stabilization of X-Au-X Complexes on the Au(111) Surface: A Theoretical Investigation and Comparison of X = S, Cl, CH<sub>3</sub>S, and SiH<sub>3</sub>S," *The Journal of Physical Chemistry C* **121**, 3870 (2017).
- [293] M. Shen, D.-J. Liu, C. J. Jenks, P. A. Thiel, and J. W. Evans, "Accelerated coarsening of Ag adatom islands on Ag(111) due to trace amounts of S: Mass-transport mediated by Ag-S complexes," *The Journal of Chemical Physics* **130**, 094701 (2009).
- [294] M. Giesen, "Step and island dynamics at solid/vacuum and solid/liquid interfaces," *Progress in Surface Science* **68**, 1 (2001).
- [295] H. Walen, D.-J. Liu, J. Oh, H. Lim, J. W. Evans, C. M. Aikens, Y. Kim, and P. A. Thiel, "Cu<sub>2</sub>S<sub>3</sub> complex on Cu(111) as a candidate for mass transport enhancement," *Physical Review B* **91**, 045426 (2015).
- [296] D. Sheppard, R. Terrell, and G. Henkelman, "Optimization methods for finding minimum energy paths," *The Journal of Chemical Physics* **128**, 134106 (2008).
- [297] A. Bogicevic, "Atom-by-atom and concerted hopping of adatom pairs on an open metal surface," *Physical Review B* **61**, R2456 (2000).
- [298] K. Kubo, N. Hirai, and S. Hara, "Decay of nano-islands on Au(100) electrode in sulfuric acid solution with Cl<sup>-</sup> anions," *Applied Surface Science, Proceedings of the Seventh International Symposium on Atomically Controlled Surfaces, Interfaces and Nanostructures* **237**, 301 (2004).

## Publications

- [1] A. C. Dávila López and E. Pehlke, “DFT study of Au self-diffusion on Au(001) in the presence of a Cl adlayer,” *The Journal of Chemical Physics* **151**, 064709 (2019).
- [2] A. C. Dávila López and E. Pehlke, “Initial steps toward Au<sub>ad</sub> island nucleation on a c(2×2)-Cl Au(001) surface investigated by DFT,” *The Journal of Chemical Physics* **152**, 084701 (2020).





# Acknowledgements

Firstly, I would like to express my sincere gratitude to my advisor Prof. Dr. Eckhard Pehlke for the opportunity to be part of his research group, for the continuous and intensive support during my doctoral studies, and for our many and frequent discussions. His guidance helped me in all the time of research and writing of this thesis.

I would like to thank PRONABEC-Perú for the financial support and the staff at the Rechenzentrum der Universität Kiel, where the calculations published in this work have been carried through.

My sincere thanks also goes to Prof. Dr. Olaf M. Magnussen and Dr. Jochim Stettner for their helpful discussions.

I thank my colleagues from AG Pehlke: Sönke Buttenschön, Nico Reinmann, Svenja Hövelmann, Phillip Lauwen, Oliver Heyen, Christopher Makait and Lukas Deuchler for the stimulating discussions, and for the time we were working together and for all the fun we have had during my stay in Kiel. Specially, I am very thankful to Lukas Deuchler for the fruitful discussions about my research, for helping me proof read this thesis, and for the enjoyable time we shared in our office. Also I thank Dr. Tim Schoof for his technical support and advice.

My gratitude also goes to Dr. Patrick Ludwig, Frau Doris Schulz and Herr Frank-Peter Hohmann for their help with everything about administration.

Last but not the least, I wish to thank Prof. Holger Valqui †, whose excitement for quantum physics sparkled during my studies in the Universidad Nacional de Ingeniería, Lima-Perú. I would like to thank Anna Maria Haase for her love and support during all this time. I am indebted grateful to my beloved husband Benjamin Tews for his patience and understanding, specially during the writing phase.



# Sworn Declaration

I hereby declare that – apart from the guidance of my supervisor Prof. Dr. Eckhard Pehlke – the content and design of this thesis is my own work. No other sources than those stated have been used. This work or parts of it have not been submitted as part of a doctoral examination procedure to another examining body. The thesis was prepared adhering to the Rules of Good Scientific Practice of the German Research Foundation. None of my academic degrees have ever been withdrawn. Part of this work is already published, see page 205.

Gifhorn, 7th August 2020,

---

Alexandra Celinda Dávila López